# High Load Limits of the Controlled Autoignition Engine

by

Craig B. E. Wildman



M.S. Mechanical Engineering
Massachusetts Institute of Technology, 2005

B.S. Mechanical Engineering
Massachusetts Institute of Technology, 2003

Submitted to the Department of Mechanical Engineering in Partial Fulfillment of the Requirements for the Degree of

Doctor of Philosophy

at the

Massachusetts Institute of Technology

June 2009





Signature of Author _____
Department of Mechanical Engineering
May 22, 2009

Certified by _____
Wai K. Cheng
Professor of Mechanical Engineering
Thesis Supervisor

Approved by_____
David Hardt
Ralph E. & Eloise F. Cross Professorship of Mechanical Engineering
Chairman, Departmental Graduate Committee

(This page was intentionally left blank.)

**High Load Limits of the Controlled Autoignition Engine**

by

Craig B.E. Wildman

Submitted to the Department of Mechanical Engineering on
May 22, 2009 in partial fulfillment of the
requirements for the Degree of Doctor of Philosophy in
Mechanical Engineering

# Abstract

The controlled autoignition (CAI) engine is an engine concept that features very low soot and $NO_X$ emissions while achieving diesel-like efficiency. The CAI combustion process is characterized by a fast, volumetric burn of a premixed fuel and air mixture that is heavily diluted with either excess air or burned gas. One problem that limits the engine's introduction into the market is that the rate of combustion can be fast to the point that it is very loud and is destructive to the mechanical components of the engine. The nature of this problem is akin to spark-ignition knock and presents a high-load limit to the operating range. Misfire presents a second high-load limit.

This work seeks to understand how various engine parameters affect the high-load knock limit and the high-load misfire limit of a CAI engine operating in the negative-valve-overlap mode. Valve timing, and therefore trapped residual gas fraction, turbocharging, intake air heating, and exhaust gas recirculation (EGR) are all explored for their effects on the high load limit. A single-cylinder research engine is used to assess each of these effects. 91 RON gasoline is used for all tests.

The first part of the study explores the effects of boost, intake air temperature, and trapped residual fraction on the rate of pressure rise, which was used as the metric for knock, and on NIMEP. It was shown that if operation is constrained by maximum pressure rise rate ($PRR_{max}$), the maximum load condition always lies at the misfire limit. The dependencies of misfire on boost, intake air temperature, and residual fraction were also explored.

The second part of the study examined how the use of EGR affected the high-load limit. Again, the high-load limit, constrained by maximum pressure rise rate, was maximized at the misfire limit. Varying boost and intake temperature did not materially change the high load limit because the misfire limit and the $PRR_{max}$ changed simultaneously in such a way that the NIMEP at the new limit point did not change appreciably from the original value. Correlations were developed for the misfire limit, for the burn duration, and for combustion phasing.

Thesis Supervisor: Wai K. Cheng

Title: Professor of Mechanical Engineering

(This page was intentionally left blank.)

# Acknowledgements

In August of 2005, I enrolled at UC, San Diego as a graduate student pursuing a doctorate in mechanical engineering. By November, I came to the realization that things were not going as I had hoped. I ran up a shocking phone bill talking over the predicament with various people. Two calls proved pivotal. First, Ferran Ayala convinced me to reapply to MIT to do a Ph.D. back at the Sloan Automotive Laboratory. Second, Professor Wai Cheng agreed to write a recommendation for my application. Later, he found a project for me that I found practically ideal. I believe the return to MIT was an excellent move, and I am thankful to them both for their help in my return.

I found my experience at MIT over the last three years by-and-large enjoyable and fulfilling. I credit the positive experience first to my advisor, Professor Cheng. He empowered me to succeed, challenged me to improve as a researcher, and never ceased to teach me about various research topics and the larger problems to which they applied. R.J. Scaringe and I worked closely together on our projects sharing everything from hardware to ideas on the proper theoretical approach. While I had heard many stories of students struggling to get along with each other, R.J. proved to be a reliable and congenial work partner and was far more helpful than I could have hoped for.

Furthermore, I appreciate the effective and supportive culture in the Sloan Lab. Professor John Heywood's leadership and forty odd years of devoted service to the laboratory set a tone of professionalism and high standard of performance. Thane DeWitt and Raymond Phan helped with sundry challenges with the experimental apparatus. Vikram Mittal and Sean Pont each tangibly contributed to my data processing tasks. Professor Bill Green's positive outlook on life never failed to inspire me onward in my work.

I appreciate the financial support from the U.S. Department of Energy for the research project. I never had to think about funding nor serve as a teaching assistant during my time during this project. I do not take the certainty of funding for granted.

I appreciate the love and support of my family, the encouragement, and the understanding they have shown me over the years. They set me up to succeed in school and in life and to enjoy it in the process.

I appreciate the blessings in all of this I have received from God, and I hope to use them to serve others in the future.

# Table of Contents

# List of Figures

# Nomenclature

SI – Spark Ignition
CAI – Controlled Auto-Ignition
HLL – High Load Limit
FTP – Federal Test Procedure
CFR – Cooperative Fuels Research
HCCI – Homogeneous Charge Compression Ignition

**Engine Timing:**
CAD – Crank Angle Degree
BDC – Bottom Dead Center
TDC – Top Dead Center
ABC – After Bottom Center
BBC – Before Bottom Center
ATC – After Top Center
BTC – Before Top Center

**Combustion Metrics:**
NIMEP – Net Indicated Mean Effective Pressure
BMEP – Brake Mean Effective Pressure
RPM – Revolutions per Minute
COV of NIMEP – Coefficient of Variation of NIMEP
$PRR_{max}$ – Maximum Pressure Rise Rate
COV of $PRR_{max}$ – Coefficient of Variation of $PRR_{max}$
ISFC – Indicated Specific Fuel Consumption
EGR – Exhaust Gas Recirculation

**Burn Duration:**
SOC – Start of Combustion
EOC – End of Combustion
CA10 – Crank Angle when 10% of the fuel mass has burned
CA50 – Crank Angle when 50% of the fuel mass has burned
CA90 – Crank Angle when 90% of the fuel mass has burned
BD10-90% – Duration from CA10 to CA90
LTHR – Low Temperature Heat Release (sometimes called the Cool Flame)
HTHR – High Temperature Heat Release

**Experimental Techniques:**
LDA – Laser Doppler Anemometry
LIF – Laser Induced Florescence
PLIF – Planar Laser Induced Florescence
RCM – Rapid Compression Machine

# Chapter 1 Introduction

The controlled auto-ignition (CAI) engine has garnered much interest recently for its better fuel economy and lower oxides of nitrogen ($NO_X$) emissions compared to the spark-ignition (SI) engine. In CAI combustion, the fuel and air are premixed and then compressed to the point of auto-ignition, resulting in a fast, volumetric burn. The comparatively short burn, the ability to operate unthrottled, and the use of a higher compression ratio contribute to efficiency gains. A higher compression ratio may be possible because this combustion process is not limited by spark-ignition knock although the limit is still constrained by the rate of pressure rise. The CAI engine produces much less $NO_X$ because of low combustion temperatures since the charge is either highly lean or dilute with exhaust.

## 1.1 Challenges

Two significant challenges slow this engine's path to market. First, to achieve the high temperature necessary for auto-ignition, a great deal of residual gas is trapped, perhaps 60%, from one cycle to the next. This means that the combustion characteristics of one cycle depends heavily on the combustion characteristics of the previous two or three cycles, thus making transient control difficult. Next, several factors limit the operating range of this combustion process. The low-load limit is governed by a misfire limit. Fuel rate determines, in part, the temperature of the residual gas. If the residual gas temperature is not hot enough, the charge will not attain a high enough temperature for auto-ignition. As this misfire limit is approached, cyclic torque variations and unburned hydrocarbon and CO emissions increase as well. A WAVE simulation result from Morgan Andreae's Ph.D. thesis is reprinted in Figure 1.1 in which compression temperature at 30° BTC is plotted against residual mass fraction. The result shows that as residual fraction is increased past 57%, compression temperature drops eventually below a critical temperature for auto-ignition [1].

The high-load limit (HLL) is governed by two phenomena. First, the heat release rate can be fast to the point that pressure waves develop thus causing the engine structure to vibrate. This results in unacceptable noise as well as conditions that might damage the engine. This engine knock occurs because a burning kernel of gas expands faster than the rate at which the cylinder volume can equilibrate pressure. Misfire can determine the HLL, as well. In this scenario, the

residual gas fraction is decreased to allow an increase in air and therefore fuel and load. As the fraction of residual gas is decreased, the trapped energy in the charge can become insufficient to initiate autoignition.

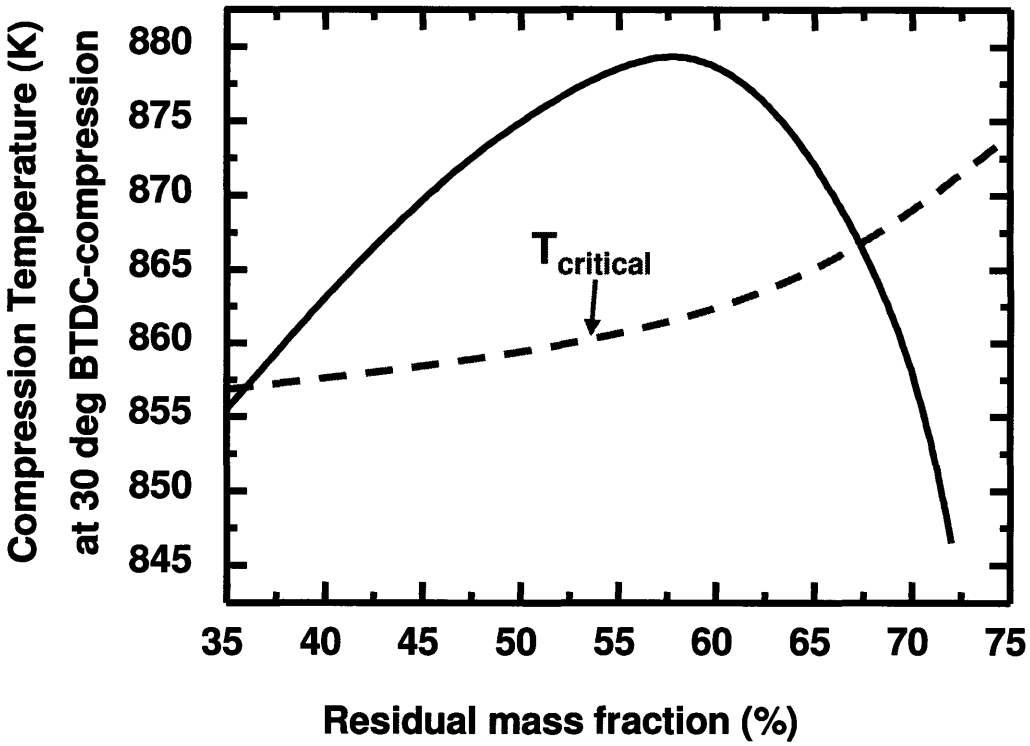


**Figure 1.1.** Compression Temperature at 30° BTC vs. Residual Fraction. Compression temperature drops below a critical temperature for auto-ignition both at high residual gas fraction levels and low residual gas fraction levels.

As shown in Figure 1.1, compression temperature 30° BTC drops as residual fraction is decreased from 57%. Eventually, it drops below a critical threshold where the charge is not hot enough to initiate combustion. Note that there is substantial uncertainty in this critical temperature. This critical temperature would depend heavily on fuel chemistry. Also, the critical temperature is a function of availability of oxygen, which is why it is curved. For turbocharged and supercharged engines, usually the HLL is dominated by knock.

One strategy to use CAI combustion in an automobile application is for an engine to operate as a dual mode SI-CAI engine, using the spark-ignition process during engine start and during high load operation [2]. If controlled effectively, the engine could dynamically switch back and forth seamlessly between combustion modes. The occurrence of a CAI high-load limit is unfortunate because it limits the range of operation in the CAI mode; hence, the CAI benefit is not fully utilized. Furthermore, if SI combustion is required for high-load operation, the compression ratio must be kept low to avoid SI knock, which limits the efficiency benefits of

implementing CAI combustion. In Figure 1.2, a second-by-second load/speed map of the U.S. Federal Test Procedure (FTP) Urban Fuel Economy Drive Cycle is plotted with a typical CAI operating regime overlaid.

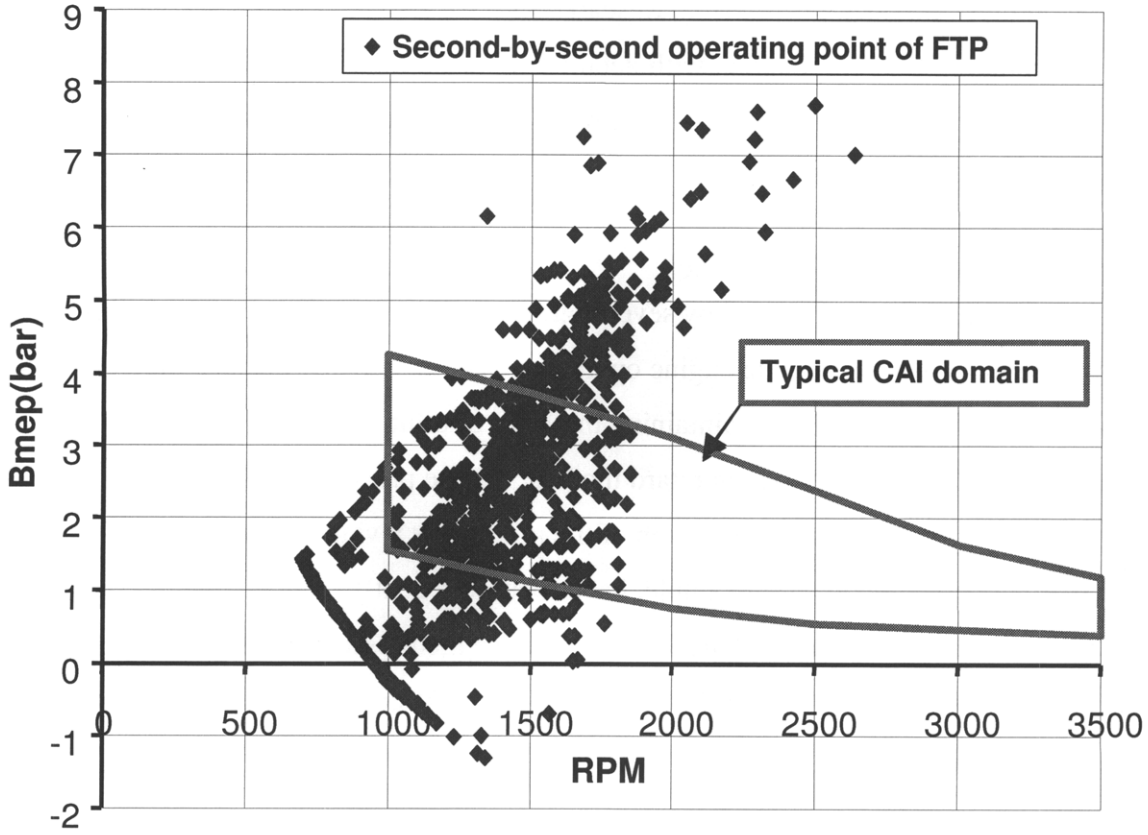


**Figure 1.2.** Second-by-second operating points on the engine map for the FTP Urban Fuel Economy Drive Cycle with a typical CAI domain overlaid. [3,4]

The CAI operating regime comprises approximately 40% of the operating points showing that there is considerable room for expansion of the operating regime [3,4].

## 1.2 Project Focus

This project focuses on identifying and quantifying the factors that constrain the HLL of a gasoline CAI engine under turbocharged conditions. The thesis features experimental work on a single-cylinder research engine. Boost pressure, intake temperature, valve timing, and exhaust gas recirculation (EGR) will each be varied to explore their effects on the high-load knock limit and the high-load misfire limit. Phenomenological models incorporating the data will be presented.

## 1.3 Previous Research

Researchers have approached the high load limit issue from several directions. Groups have attempted different methods to extend the high load limit. Other research efforts have centered on understanding CAI knock phenomena. Researchers have also demonstrated considerable success in simulating CAI combustion with detailed chemical kinetics models as well as with empirical ignition delay models. Experimental work has been undertaken to detail the nature of the charge before ignition as well.

### 1.3.1 Attempts to Abate CAI Knock

Turbocharging has been proposed by several groups as a means of extending the high load limit of the engine. By boosting, the engine operates at a higher charge density which allows the work output to be increased while maintaining the level of dilution or even increasing it. The high dilution level is presumed to help retard the heat release process [5, 6].

Others view controlling the stratification of the mixture as a viable way to control the rate of pressure rise. Sjöberg and Dec, for example, have focused recently on using direct injection to develop a mild stratification in the charge so as to reduce the pressure rise rate at high load [7]. Urata et al., however, reported increased COV of IMEP, $NO_X$ emissions, and indicated specific fuel consumption (ISFC) with their direct injection strategy versus their port fuel injected strategy [8].

A few groups have used a combination of trapped residuals and exhaust gas recirculation to mitigate knock. The latter lowers the mixture temperature because it acts as a low temperature diluent. The level of trapped residuals depended on valve timing so the amount of trapped residuals could be changed on a cycle-by-cycle basis despite the slower timescale of varying the EGR level. Cairns and Blaxill studied combustion over a wide range of speeds and loads in a multi cylinder engine with EGR and residual trapping. They found that EGR delayed ignition, prolonged combustion, and extended the knock limit [9]. Sjöberg and Dec found that EGR, in concert with varied boost and fuel chemistry, could be effectively used to foster consistently a strong low-temperature heat release [10].

Researchers at Stanford University have pursued a strategy of "residual-effected" HCCI combustion in which burned gas is exhausted from the engine and then drawn back into the engine during the induction process. This allows the burned gas to cool some during its time

outside the cylinder and provides a way to reduce charge temperatures compared with a residual gas trapping strategy via negative valve overlap with some success [11-13].

A number of groups have viewed the CAI combustion process as an alternative to the diesel process with significantly less $NO_X$ emissions. They, therefore, simply tolerate the higher rates of pressure rise, the higher maximum cylinder pressures, and the engine noise that are associated with CAI engine knock [14, 15].

### 1.3.2 Efforts to Understand CAI Knock

A number of researchers have focused efforts directly on understanding the CAI knocking phenomenon. They first drew on the large volume of research on spark-ignition engine knock [16]. Especially pertinent was Draper's work of 1938 that related the audible knock to the in-cylinder pressure oscillations. He determined theoretically which vibrational "drum" modes described the oscillation frequency of the gas [17]. Eng noted in 2002 that while researchers had mainly focused on the rate of pressure rise as a metric to determine knock intensity, they are not proportional. He defined a ringing intensity $I$ based on the gas composition, maximum cylinder temperature, maximum cylinder pressure, and maximum rate of pressure rise, as in Equation 1.1.

$$I \approx \frac{1}{2\gamma} \frac{\left(\beta \frac{dP}{dt_{\max}}\right)^2}{P_{\max}} \sqrt{\gamma R T_{\max}} \tag{1.1}$$

Here, $I$ denotes ringing intensity. $dP/dt_{max}$ is the maximum pressure rise rate ($PRR_{max}$); $P_{max}$ is the maximum cylinder pressure. $\gamma$ is the ratio of specific heats; $T_{max}$ is the maximum cylinder temperature; $R$ is the universal gas constant, and $\beta$ relates the amplitude of the acoustic wave to the pressure rise rate [18]. The following year at Lund University, Vressner et al. showed that most of the oscillation energy comes from the first of the "drum" modes [19].

Andreae et al. studied the sound emanating from the engine to the in-cylinder pressure trace with the purpose of developing a useful limit for engine knock based on engine parameters. They noted that $PRR_{max}$ could be used as a good metric to determine the knock threshold. By plotting the audible wave power versus the $PRR_{max}$, they noticed a "knee" in the data at 5MPa/ms. They concluded this would be an appropriate knock limit for the practical purpose of defining an upper boundary to the engine operating range [20].

### 1.3.3 Combustion Simulation Efforts

Complementing experimental efforts on the subject, Aceves and collaborators developed a multi-zone detailed chemical kinetics model for CAI combustion and emissions. They noted that the effects of in-cylinder turbulence can be largely neglected during combustion allowing considerable modeling success with less effort than for diesel or SI combustion. The Aceves model predicted maximum pressure, burn duration, and indicated efficiency to within 10% but yielded much greater error for HC and CO emissions predictions [21]. Yelvington and Green built upon their progress to make a model that was computationally faster and that focused on determining the limits to the operating range. Their knock limit was based on the criterion that in a knocking cycle a burning parcel of gas expands faster than the speed of sound. Local high pressures can develop, causing the parcel to expand faster than its pressure can equilibrate to the pressure of the rest of the mixture. These result in resonant pressure waves that can become sonic if the local pressure rise rate becomes very fast. They proposed the following criterion to determine if a cycle will knock.

$$\beta = \frac{L_c(\gamma - 1)}{\gamma} \frac{\dot{q}}{p u_{sound}} \leq 1 \tag{1.2}$$

If $\beta$ is less than 1, knock is not predicted (not the same $\beta$ as in Eng's work). $L_c$ is the characteristic length scale of the charge inhomogeneities. $\gamma$ is the ratio of specific heats. $p$ is the gas pressure; $u_{sound}$ is the speed of sound for the mixture, and $\dot{q}$ is the rate of heat release of the parcel of gas. They compared their model to experimental results from Oakley et al. and found that they underpredicted the onset of knock. They note that their model is quite insensitive to variations in charge temperature and pressure but more sensitive to fuel type and charge composition. The most likely source of error was a conservative estimate of heat release rate [22, 23] Angelos et al. extended this work to simulate combustion during transients [24].

### 1.3.4 Combustion Phasing Modeling

Researchers have had success modeling the timing of auto-ignition reactions in rapid compression machines, knock in SI engines, and autoignition in CAI engines by using global reaction rate models. The basis for such a chemical kinetics model is briefly described. More depth can be found in *An Introduction to Combustion* by Turns and in an *Introduction to Physical Gas Dynamics* by Vincenti and Kruger [25, 26]. To start from collision theory for a

bimolecular reactions, the reaction rate for the reaction of Equation 1.3 would take the form of Equation 1.4.

$$A + B \rightarrow C + D \tag{1.3}$$

$$\frac{d[A]}{dt} = -k[A][B] \tag{1.4}$$

Here, $k$ is determined by the probability of a collision $Z_{AB}$, the energy required for a reaction to take place, which is the exponential term, and a steric factor $P$ taking into account the orientation of the molecules taking part in the collision, as in Equation 1.5.

$$k = Z_{AB} P \exp\left(\frac{-E_A}{RT}\right) \tag{1.5}$$

Here, $E_A$ is the activation energy. The probability of a collision is dependent on the particle speed $\overline{C}$ and the mean free path $\lambda$, as in Equation 1.6. Formulas for the particle speed and the mean free path are given in Equations 1.7 and 1.8.

$$Z_{AB} = \frac{\overline{C}}{\lambda} \tag{1.6}$$

$$\overline{C} = \left(\frac{8kT}{\pi m}\right)^{1/2} \tag{1.7}$$

$$\lambda = \frac{1}{\sqrt{2}\pi d^2 \, n/V} \tag{1.8}$$

In Equations 1.7 and 1.8, $k$ is the Boltzmann constant. $T$ is temperature. $m$ and $d$ are the mass and diameter of the particle. $n/V$ is the number density of the particles. Combining Equations 1.4 through 1.8, the reaction rate for a bimolecular collision can be taken to be Equation 1.9.

$$\frac{d[A]}{dt} \propto -[A][B]\frac{P}{\sqrt{T}}\exp\left(\frac{-E_A}{RT}\right) \tag{1.9}$$

This sort of equation has been used to fit global reaction rates to experimental data, but the equation's form must be modified for this use. Combustion reactions are not strictly bimolecular so if Equation 1.9 was to be used as the form of a global reaction rate, then exponents would be added to the concentration terms and the pressure term to fit this model to experimental data, as in Equation 1.10.

$$\frac{d[fuel]}{dt} = -a_1[fuel]^{a_2}[O_2]^{a_3}\frac{P^{a_4}}{\sqrt{T}}\exp\left(\frac{-E_A}{RT}\right) \tag{1.10}$$

From this basis, researchers fit experimental data by defining an ignition delay $\tau$, as the time from a reference point before combustion starts to the time when autoignition takes place as in Equation 1.11. However when applied to a rapid compression machine experiment, this formula was found to be only valid for narrow temperature ranges and pressures [27, 28].

$$\tau \propto a_1 P^{a_2} \exp\left(\frac{-E_A}{RT}\right) \tag{1.11}$$

Livengood and Wu showed in 1955 that the ignition delay for an auto-ignition reaction could be described by integrating this ignition delay from the starting time to the time of autoignition to describe the phenomenon, as in Equation 1.12.

$$\frac{[x_p]}{[x_p]_c} = \int_{t=0}^{t=t_c} \frac{1}{\tau} dt = 1.0 \tag{1.12}$$

In Equation 1.12, $[x_p]$ is the concentration of products, and $[x_p]_c$ is the critical concentration of products required for autoignition. When the concentration of products reaches this critical value, the integral evaluates to 1, and autoignition takes place. They successfully applied this technique to auto-ignition data from a rapid compression machine experiment, to spark-ignition knock, and to "motoring data" which was essentially CAI combustion [29].

The strategy for using the integral of Equation 1.12 is to find the constants in Equation 1.11 for a particular fuel using a rapid compression machine where the integral is not necessary since $P$ and $T$ are constant after the initial compression. Then, once the constants are known, the integral could be used to predict autoignition timing in a knocking spark-ignition engine or at least to give comparisons between operating conditions.

In 1978, as a part of a spark-ignition knock study, Douaud and Eyzat used this Livengood-Wu integral with their data set to solve for the three constants with a least squares technique from the spark-ignition data directly [30]. This method appeared to obviate the need for a rapid compression machine to estimate what the correlation constants should be.

More recently, the necessity of predicting combustion phasing in CAI operation has become widely acknowledged, and various research groups have begun attacking the problem from different angles. It became apparent that there was a paucity of ignition delay data for the fuels and operating conditions found in CAI combustion. He et al., among others, conducted a rapid compression machine experiment in 2005 to describe the ignition delay characteristics of iso-octane at relevant conditions and published the empirical formula as stated in Equation 1.13.

$$\tau_{ign} = 1.3\times10^{-4} P^{-1.05} \phi^{-0.77} \chi_{O_2}^{-1.41} \exp\left(\frac{33{,}700}{R_{(cal/mol/K)}T}\right) \tag{1.13}$$

Here, $\varphi$ is the equivalence ratio, and $\chi_{O2}$ is the oxygen mole fraction [31].

Shahbakhti, Lupul, and Kock in 2007 used a modified knock integral based on Livengood's and Wu's work to predict combustion phasing for a CAI engine. They fit a model to simulation results and to experimental data featuring varied EGR, varied intake temperature, varied equivalence ratio, two speeds, and three fuels. They designed their model to use IVC data to predict SOC timing, as in Equation 1.14.

$$\int_{\theta_{IVC}}^{\theta_{SOV}} \frac{\phi^x}{A\omega\exp\left(\frac{b\left(P_{IVC}v_c^{n_c}\right)^n}{T_{IVC}v_c^{n_c-1}}\right)} d\theta = 1.0 \tag{1.14}$$

$$\text{where } v_c(\theta) = \frac{V(\theta_{IVC})}{V(\theta)}, \quad A = C_1 EGR + C_2$$

Here, ω is engine speed, and $C_1$, $C_2$, $b$, $n$, $n_c$, and $x$ are constants to be fit to the data. This model features the advantage that it incorporates controllable engine parameters such as the EGR rate. However, the predicted trend for SOC with the modified knock integral method does not match the simulation result trend for SOC over the operating conditions explored, particularly at late combustion phasing [32].

Yates and Viljoen extended the logic of the Livengood-Wu knock integral for combustion phasing to two-stage ignition. They proposed simply adding two ignition delay integrals to describe combustion as in Equation 1.15.

$$\int_{t_0}^{t_1} \frac{1}{\tau_{h,i}} dt + \int_{t_1}^{t_2} \frac{1}{\tau_{h,CF}} dt = 1 \tag{1.15}$$

The low temperature heat release (LTHR) (termed cool flame in the paper) is described by the first integral and the high temperature heat release (HTHR) is the second. $\tau_{h,i}$ is the initial ignition delay, and $\tau_{h,CF}$ is the ignition delay starting at the LTHR. Although no experimental data is presented in this work, the simple formulation and associated logic fit the detailed chemical kinetics model well [33].

### 1.3.5 Energy Release Rate Modeling

In 1983, Najt and Foster studied CAI combustion in a cooperative fuels research (CFR) engine with EGR and three different fuels, and they proposed a simple equation to describe the average energy release rate during combustion. They considered combustion to happen in three distinct but overlapping steps listed in Equation 1.16: 1.) the conversion of alkanes to alkenes, 2.) the conversion of alkenes to carbon monoxide and water, and 3.) the conversion of CO to $CO_2$.

$$\begin{aligned} &\text{Fuel} + O_2 \rightarrow \text{alkene} + H_2O \quad (1) \\ &\text{Alkene} + O_2 \rightarrow CO + H_2O \quad (2) \\ &CO + O_2 \rightarrow CO_2 \quad (3) \end{aligned} \tag{1.16}$$

Najt and Foster noted that fuel and fuel radicals compete successfully against CO for OH since the second reaction in Equation 1.17 is much faster – possibly several orders of magnitude faster – than the first reaction.

$$\begin{aligned} &CO + OH \rightarrow CO_2 + H \\ &F + OH \rightarrow F + H_2O \end{aligned} \tag{1.17}$$

They concluded that the reaction rate is limited by $CO/H_2O/O_2$ kinetics rather than fuel consumption reactions and cite the semi-global reaction rate for $CO_2$ in Equation 1.18 from Dryer and Glassman as the basis for an overall reaction rate model [34].

$$\frac{d[CO_2]}{dt} = 10^{14.6} \exp\frac{-40{,}000}{RT}[CO]^{1.0}[O_2]^{0.25}[H_2O]^{0.50} \tag{1.18}$$

A CAI engine experiment by Sjöberg and Dec in 2003 further supports the claim of the different speeds of the reactions in Equation 1.17. They enleaned the mixture until the burn was consistently quenched. Large amounts of CO were produced, thus illustrating the slowness of the first reaction in Equation 1.17 [35]. Najt and Foster replaced the CO and $H_2O$ terms of Equation 1.18 with a fuel term assuming all of the CO and $H_2O$ participating in the reaction come from the fuel. The convert the species terms to moles and then replace the resulting volume term with the clearance volume $V_{CL}$. They defined a Delivery Ratio *DR* as the amount of inducted air per cycle divided by the possible amount of air to fit in the displaced volume at 311K and 1atm. They then

reform the equation in terms of delivery ratio and equivalence ratio. Finally, they find constants, $C$ and $E_{ave}$, based on a least-squares analysis from their experimental data, as in Equation 1.19.

$$AERR = C\frac{\phi^{1.5} DR^{1.75}}{V_{CL}^{1.75}} \exp\frac{-E_{ave}}{RT_{ave}} \tag{1.19}$$

*AERR* is the Average Energy Release Rate defined in fuel mass per unit time as the average burn rate from CA25 to CA75. The resulting fit describes the general trend of the experimental data of all three fuels tested [36]. It should be noted that this relationship does not account for thermal stratification effects so the resulting correlation should be interpreted as an empirical fit.

### 1.3.6 Charge Stratification

Early analysis of the behavior of CAI combustion concluded that the overall reaction rate was much slower than predicted by chemical kinetics models for a single zone of well mixed fuel, air, and diluent. It was evident that the charge was not well mixed, and that temperature and/or concentration variations in the charge were substantial enough for a staged combustion event to take place. Consequently, the simulation efforts of Aceves et al. and Yelvington and Green have had considerable success modeling combustion by dividing the charge into 10 zones with a predetermined temperature distribution. These zones burn in series according to their individual temperatures [21, 22].

*Temperature Gradients in the Bulk of the Charge*

Several groups have made progress characterizing the nature of charge stratification and its impact through experimental work. A particularly insightful study conducted by Rothamer et al. illustrated the distribution of residual gas and temperature at the end of compression in a very lean, low residuals scenario and in a lean, high trapped residuals scenario. The engine was constructed so that wide two-dimensional optical access was possible through the piston, and a planar laser induced fluorescence (PLIF) technique was used to gain information on the spatial distribution of residuals and temperature in the plane parallel to the piston. Images for residuals and for temperature taken at 154° BBC compression, 120° BBC compression, and 24° BTC compression are reprinted for their low residuals operation condition in Figure 1.3 and for the high residuals condition in Figure 1.4. In the low-residuals scenario in Figure 1.3, there are clear pockets of residuals at the 154° picture, as this is during the induction event. Temperature variations reflect the location of residual gas.

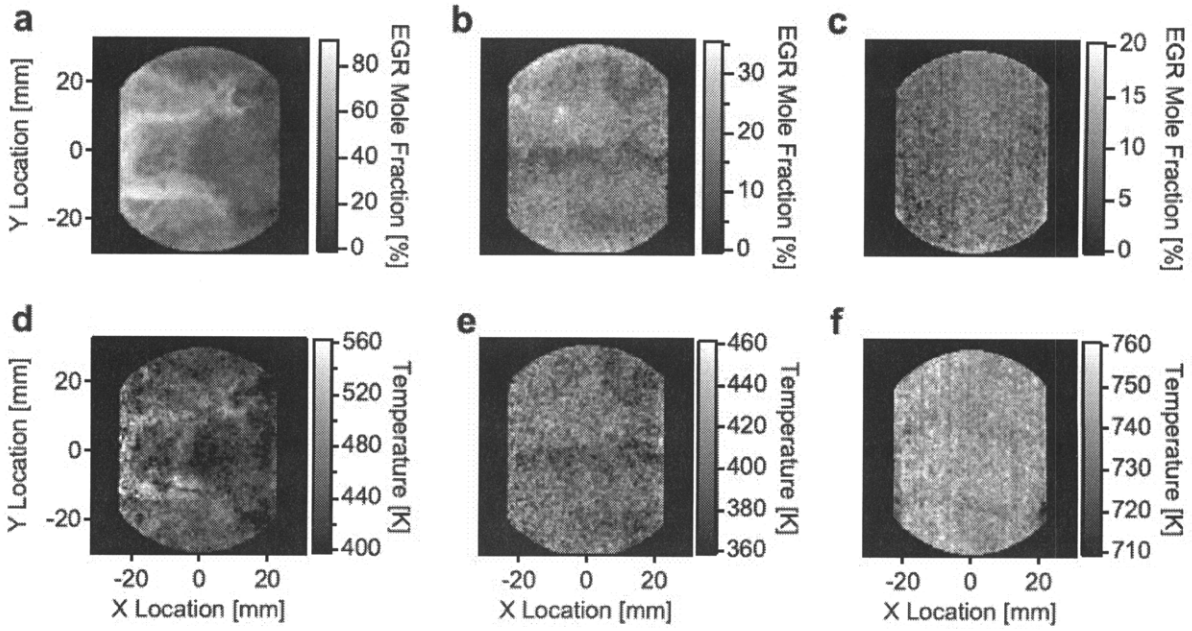


**Figure 1.3.** Distributions for Residual Gas Mole Fraction and Temperature. $\Phi = 0.29$. Residual fraction at 154°BBC (a), 120°BBC (b), and 24°BTC (c); temperature at 154°BBC (d), 120°BBC (e), and 24°BTC (f). Reprinted from Rothamer et al. [37].

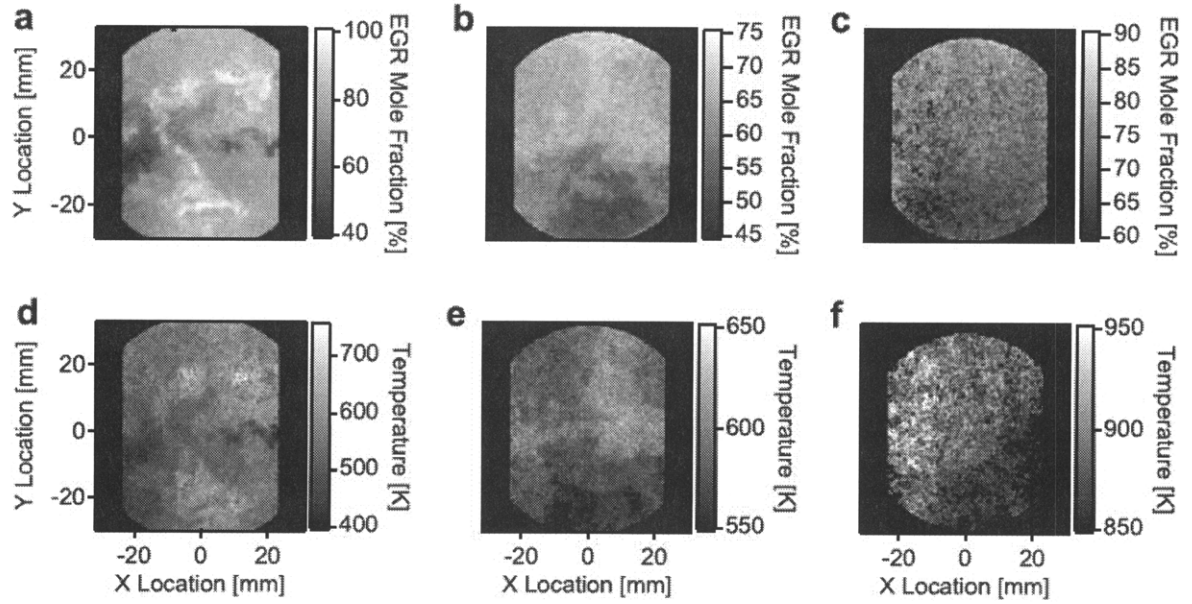


**Figure 1.4.** Distributions for Residual Gas Mole Fraction and Temperature. $\Phi = 0.82$. Residual fraction at 154°BBC (a), 120°BBC (b), and 24°BTC (c); temperature at 154°BBC (d), 120°BBC (e), and 24°BTC (f). Reprinted from Rothamer et al. [37].

However, by the end of compression, in (c) and (f), the charge is homogeneous to within the limits of visual inspection. Their data for high residuals operation paint a different picture. Picture (a) in Figure 1.4 shows that most of the charge is residual gas since this occurs before

IVO. Once the intake air has been inducted, a clear high residuals/hot zone is established in the upper half of the pictures in (b) and (e). By the end of compression, in (c) and (f), there are still zones of high and low residual and high and low temperature. The authors note that the temperature variations do not correlate to residual gas concentrations at the end of compression as their reprinted joint probability distribution function plots show in Figure 1.5 [37]. Adiabatic mixing is apparently an inappropriate assumption for the compression process.

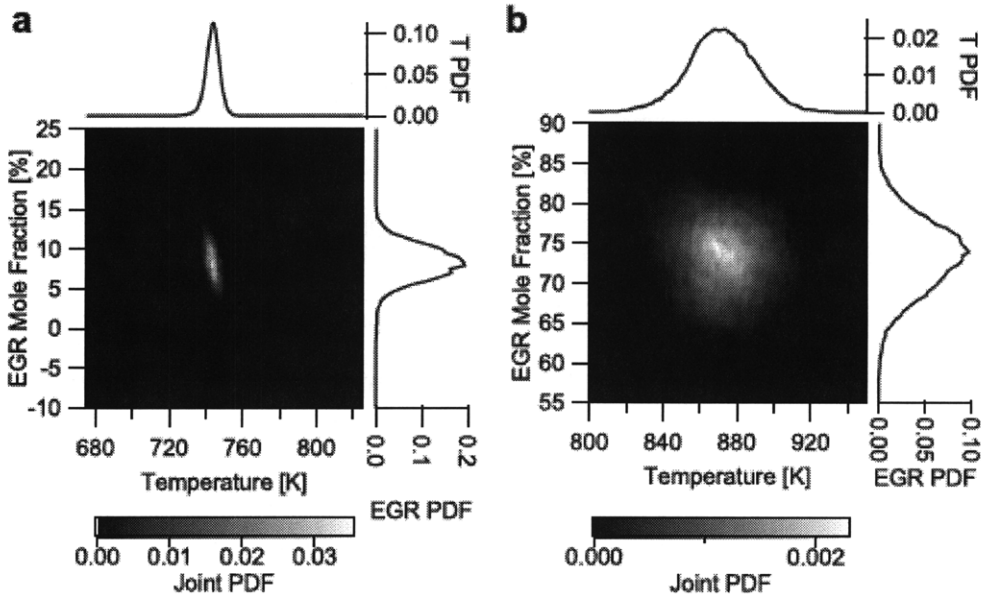


**Figure 1.5.** Joint Probability Distribution Functions. (a) $\Phi = 0.29$, low residual operation and for (b) $\Phi = 0.82$, high residual operation. Reprinted from Rothamer et al. [37].

In 2006, Lim et al. conducted a rapid compression machine experiment where they compared autoignition of a thermally stratified charge to a more homogenous charge for air-fuel mixtures using *n*-heptane and *iso*-octane. They used a series of thermocouples to measure the initial temperature distribution, and they used a chemiluminescence technique to optically track combustion both spatially and temporally. Their stratified charge exhibited a temperature deviation of 25K, and their homogeneous charge exhibited a deviation of 10K before compression. The average gas temperatures were held equal to one another. They observed the stratified charge ignite earlier and burn slower. The hot zone of the stratified charge was hotter than the warm zone of the homogeneous charge so ignited sooner, but the colder zone of the stratified charge featured more of a delay than the cooler zone of the homogeneous charge. The maximum rate of pressure rise was observed to decrease by 27% with this stratification. Comparable series of chemiluminescence images are reprinted in Figure 1.6 to illustrate the

difference burn characteristics [38]. Lim et al.'s experiment shows how even a modest temperature gradient can result in significantly different burn characteristics.

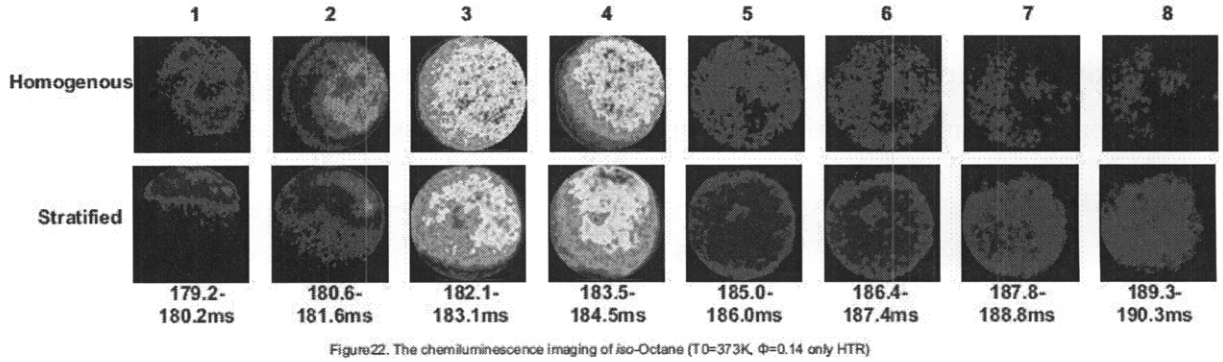


**Figure 1.6.** RCM Chemiluminescence Images from Lim et al. The upper series features a spatial temperature difference of 10K whereas the lower series features a difference of 25K [38].

Rothamer's work illustrated that for NVO operation, hot zones and zones of a high concentration of residuals will persist until the end of compression. Lim's work illustrated that if there is a strong temperature stratification, it will advance combustion but slow down the burn in an RCM. In 2006, Kakuho et al. combined both concepts in an engine experiment by establishing a strong temperature gradient and illustrating its effects on combustion. Separate air intake lines, each with an electric heater, fed the two intake ports, and the intake port temperatures were set to be equal in a base case, to yield a difference of 150K in a second case, and to yield the opposite temperature difference in a third case. Each condition featured the same average temperature. The engine featured low swirl motion. PLIF was used to assess the charge temperature during compression, and a high speed camera was employed to observe the progress of combustion. A key observation about their established temperature distribution was that the charge remained thermally stratified, retaining a $\Delta T$ of 50K at 10° BTC. Next, they observed that combustion of the stratified charge started earlier and burned for a longer time than for the homogeneous case, just as in Lim's RCM experiment. The photographs of combustion confirmed that the burn started in the hot zone of the stratified charge and propagated to the cold zone [39].

Dec et al. conducted a chemiluminescence study to characterize charge stratification as well. They concluded also that thermal charge stratification plays a significant role in combustion phasing and burn duration. They noted also that most of the charge burns in the bulk so stratification in the bulk was pivotal to burn duration [40].

*Wall Temperature Effects*

In 2001, Hultqvist et al. studied the velocity and thermal boundary layer with laser-doppler anemometry (LDA), LIF, and numerical modeling. They operated a high compression ratio engine with low residual trapping, burning natural gas. By observing spatially and temporally the depletion of fuel during combustion, they observed combustion slow as it neared the wall. They concluded that a thermal boundary layer existed with a thickness of 1-2mm during combustion [41]. This thickness is consistent with the thickness estimated in a one-dimensional heat transfer model reported by Borman and Nishiwaki [42].

Sjöberg et al. explored whether the wall temperature could be used to mitigate high heat release rates in an experimental engine study in 2004. They compared conditions where the wall temperature was set to 100°C and then to 50°C to vary convective heat transfer and therefore the temperature distribution in-cylinder. They also presented a third condition where the intake air swirl ratio was significantly increased as another means of increasing heat transfer to the walls. KIVA simulation results indicated that both reducing the wall temperature and increasing the swirl should increase the maximum gas temperature and also increase the mass of gas at low temperature, say below 900K. The effects on combustion are that the overall heat release rate and maximum pressure are diminished significantly. Combustion retards, and the efficiency drops. Although cold-wall operation may not be practical, this experiment demonstrated the dependence of thermal distribution on wall temperature [43].

A team of researchers at the University of Michigan studied wall temperature effects for CAI engines in a series of projects over the last few years. An especially noteworthy conclusion was that existing heat transfer correlations for spark-ignition or diesel combustion were inappropriate for CAI combustion. Chang et al. devised a new heat transfer correlation as in Equation 1.20 and 1.21 after a thorough experimental study. This was based on the often applied Woschnii correlation [44].

$$h_{new}(t) = \alpha_{scaling} \cdot L(t)^{-0.2} \cdot p(t)^{0.8} \cdot T(t)^{-0.73} \cdot v_{tuned}(t)^{0.8} \tag{1.20}$$

$$v_{tuned}(t) = C_1 \bar{S}_p + \frac{C_2}{6} \frac{V_d T_r}{p_r V_r} (p - p_{mot}) \tag{1.21}$$

$\alpha_{scaling}$ is a factor to be tuned to the system. $L(t)$ is a characteristic length scale, taken to be the chamber height. $p(t)$ is cylinder pressure. $T(t)$ is temperature, and $v_{tuned}$ is the average cylinder gas velocity. $\bar{S}_p$ is the mean piston speed. $V_d$ is the displaced volume. $T_r$, $p_r$, and $V_r$ are

temperature, pressure, and volume taken at a reference point. $P_{mot}$ is the pressure for a motoring trace. $C_1$ and $C_2$ are taken to be the same as in the Woschnii model.The modifications that Chang made are changing the temperature exponent from -0.55 to -0.73, basing $L$ on the chamber height, and dividing $C_2$ by 6 [45].

The Michigan team studied the wall temperature heat transfer effects on transients. The general premise is that a condition that the time scale for the wall temperature to adjust to a change in engine load or speed is much longer than for cyclic parameters such as fuel rate or valve timing. Therefore, engine control must take into account wall temperatures from previous conditions [46].

*Fuel Distribution Effects*

In 2000, Richter et al. used a PLIF imagining system with an acetone tracer to visualize the OH distribution just after the beginning of combustion. They endeavored to show a well-mixed case and a less-well mixed case by going to special effort to mix fuel and air in a mixing tank in the intake. Interestingly, their two cases both showed a highly heterogeneous charge where neither the location nor the size of the OH zones were repeatable. This engine was run with port-fuel injection with low residual gas trapping in both cases [47].

Herold and collaborators conducted a thorough study in 2007 to explore the effects on combustion of fuel unmixedness in the absence of thermal and residual gas unmixedness. They devised a well-mixed case where iso-octane was vaporized and mixed well upstream of the intake port. They also devised a means to inject fuel in the port but only after equilibrating its temperature with that of the incoming air so as to ensure temperature uniformity. Injection timing was varied to change the distribution of fuel in-cylinder. They recirculated exhaust gas and operated lean in this experiment. PLIF data was acquired to show that injection timing effectively varied the distribution of fuel and that the well-mixed case provided a homogeneous charge. Combustion performance and emissions data acquired in a metal engine with the same injection apparatuses yielded almost no difference in phasing, burn duration, or rate of pressure rise between the different injection cases. This showed that fuel stratification does not play a factor in burn rate and cannot be used as a means of control. Emissions data showed that $NO_X$ emissions increase with the degree of unmixedness; local hot zones were more plentiful where there are rich pockets of fuel [48].

## 1.4 A Summary of CAI Combustion Theory

A concise summary of CAI combustion theory will be presented here so that the reader can gain some sense of what to expect in the data presented later in the work and why certain decisions are consistently made here.

### 1.4.1 Bulk Characteristics of the Charge

To start with mixture preparation, the charge is composed of air, fuel, and exhaust from a previous cycle. The equivalence ratio is chosen to be 1 with only the amount of air sufficient to burn the fuel. The charge is diluted as much as possible with exhaust rather than air because the availability of oxygen increases the reaction rates, and mitigating rate of pressure rise is a key challenge. Second, the premise is assumed that a three-way catalyst requires this equivalence ratio in the exhaust. The ratio of specific heats is also lower for $CO_2$ and $H_2O$ than for $O_2$ thus retarding the burn rate, but this effect is expected to be minor.

Several factors control the exhaust fraction and temperature. The fractions of air versus exhaust are dictated by valve timing and throttles in the exhaust and EGR loop. The EVC and EVO timings drive the amount of trapped residuals. The pressure difference between intake and exhaust as well as the flow restriction in the EGR loop drive the amount of EGR. The EGR temperature is assumed to be at the same temperature as the intake air. The trapped residual temperature is assumed to be a function of exhaust temperature of the previous cycle and IVO timing. The exhaust energy can be approximated in terms of fuel energy, work, heat loss which is a function of combustion phasing, as in Equation 1.22.

$$m_f LHV = W - Q + U_{exhaust} \tag{1.22}$$

$m_f$ is fuel mass. $LHV$ is the lower heating value of the fuel. $W$ is the work done to the piston. $Q_{HL}$ is the heat loss, and $U_{exhaust}$ is the exhaust energy. Next, fuel mass is written in terms of residual fraction and equivalence ratio. $c_v$ is approximated as equal for exhaust and for air. A factor for EGR will be added in later.

$$n_{tot} \cdot (1 - x_{res}) \cdot M_{air} \cdot \phi \cdot \left(F/A\right)_{ST} \cdot LHV \approx W - Q_{HL} + n_{tot} \cdot c_p \cdot T_{exh} \tag{1.23}$$

$(F/A)_{ST}$ is the stoichiometric fuel-air ratio. $n_{tot}$ is the total number of moles. The equation is rearranged to solve for exhaust temperature as in Equation 1.24.

$$T_{exh} \approx (1 - x_{res}) \cdot \phi \cdot \frac{M_{air} \cdot \left(F/A\right)_{ST} \cdot LHV}{c_p} + \frac{Q_{HL} - W}{c_p \cdot n_{tot}} \tag{1.24}$$

The work term can be written in terms of efficiency, fuel mass, and the fuel heating value. These terms are incorporated, and the work term appears as (1-$\eta$) in the exhaust temperature equation.

$$T_{exh} \approx (1 - x_{res}) \cdot \phi \cdot \frac{M_{air} \cdot \left(F/A\right)_{ST} \cdot LHV(1-\eta)}{c_p} + \frac{Q_{HL}}{c_p \cdot n_{tot}} \tag{1.25}$$

Some charge parameters are listed Table 1.1 so that a comparison of magnitudes can be done for the terms and incorporated into 1.26

**Table 1.1.** Charge Parameters

| |
|---|
| $(F/A)_{ST} = 0.0688$ |
| $c_p = 30$ J/(mol K) |
| $M_{air} = 0.0288$ kg/mol |
| $LHV = 44*10^6$ J/kg |
| $\eta_i \approx 0.35$ |

$$T_{exh} \approx 1890 \cdot (1 - x_{res}) \cdot \phi \cdot + \frac{Q_{HL}}{c_p \cdot n_{tot}} \tag{1.26}$$

The temperature at IVC, $T_{IVC}$, although a weak function of heat loss, can be written in terms of intake temperature at IVO temperature, as in Equation 1.27.

$$T_{IVC} \approx (1 - x_{res}) \cdot T_{in} + x_{res} \cdot T_{IVO} \tag{1.27}$$

IVO temperature is approximated as exhaust temperature next.

$$T_{IVO} \approx T_{exh} \tag{1.28}$$

Equation 1.26 is incorporated into 1.27and 1.28 for an approximation for $T_{IVC}$ in Equation 1.29.

$$T_{IVC} \approx (1 - x_{res}) \cdot (T_{in} + 1890 \cdot x_{res} \cdot \phi) + x_{res} \cdot \frac{Q_{HL}}{c_p \cdot n_{tot}} \tag{1.29}$$

If the intake temperature is set to 400K (127°C) and if the residual fraction is 50%, then $T_{in}$ will be approximately 42% of the residual fraction term next to it. The terms are about the same size. The heat loss term matters but is hard to determine simply. If we were to assume it to be zero, the behavior of $T_{IVC}$ would be as in Figure 1.7. Accounting for EGR modifies Equation 1.29 such that it is convenient to put it in terms of total burned gas fraction $x_b$ and EGR fraction $x_{EGR}$ where burned gas fraction is composed of EGR and residual gas.

$$x_b = x_{res} + x_{EGR} \tag{1.30}$$

The modified formula for $T_{IVC}$ is shown in 1.32, and $T_{IVC}$ is plotted for four settings of EGR in Figure 1.8. EGR has a strong effect on temperature.

$$T_{IVC} \approx (1 - x_b) \cdot [T_{in} + 1890 \cdot (x_b - x_{EGR}) \cdot \phi] + x_{EGR} T_{in} + (x_b - x_{EGR}) \cdot \frac{Q_{HL}}{c_p \cdot n_{tot}} \tag{1.32}$$

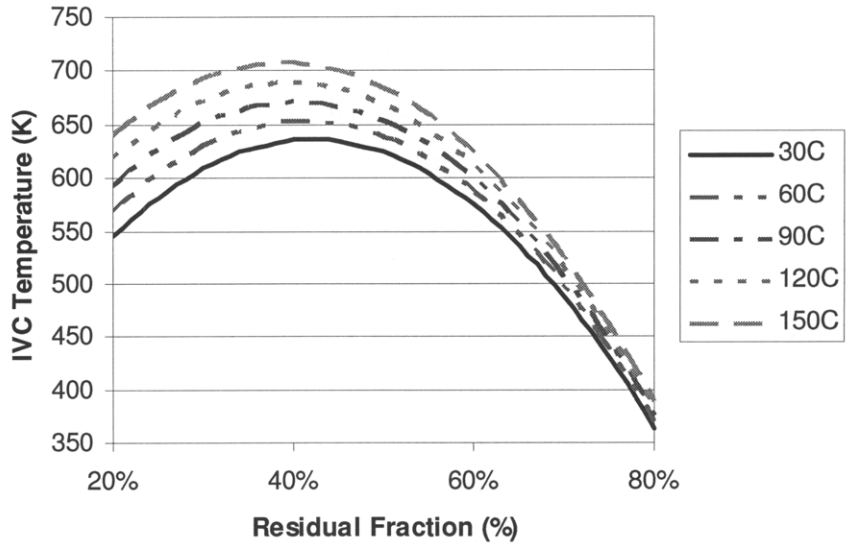


**Figure 1.7.** Theoretical IVC Temperature as a Function of Residual Fraction for Five Intake Temperatures. Equivalence ratio is held constant. Heat loss is assumed to be zero.

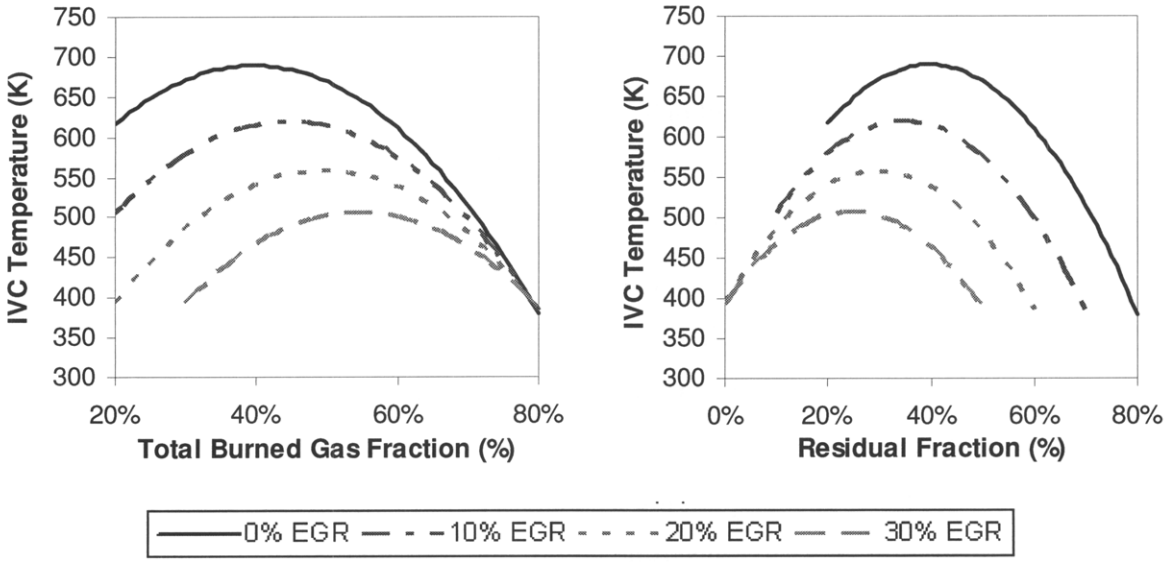


**Figure 1.8.** Theoretical IVC Temperature Plotted Versus Total Burned Gas Fraction and Residual Fraction for Four EGR Settings. Heat loss is neglected. $T_{in}$ = 120°C. $\Phi$ = 1.0.

During compression, the charge is first heated by the wall and then transfers heat to the wall as the bulk temperature exceeds the wall temperature. The volume change is non-linear such that the charge spends a disproportionate amount of time in the small volume near TDC so an isentropic compression estimate over-estimates the bulk temperature at the end of compression.

### 1.4.2 Charge Stratification and Combustion

From the spectroscopy work done by other research groups, several claims can be made about the charge before combustion. In the center of the chamber, there are temperature gradients and concentration gradients of residual gas, but these two gradients do not correlation because heat transfer during compression has warmed the air and any EGR. There is also a thermal boundary layer perhaps 1.5mm thick on the piston, head, and wall because these surfaces are significantly colder than the average gas temperature at the end of compression. Gradients in fuel and oxygen concentration form as well.

Near the end of compression, low temperature reactions begin to take place, and concentrations of radicals begin to build. The charge can be thought of as discretized into parcels of gas. The parcel of gas that is hottest with sufficient oxygen and the suitable radicals undergoes high temperature heat release first. A steeper gradient in temperature will result in an earlier burn of the first parcel since the hottest parcel will be hotter than the hottest parcel in a more thermally homogeneous charge. This has been shown in more than one spectroscopy study as well as described in modeling work. To the author's knowledge, no study has shown effects of diluent versus oxygen concentration stratification under equal thermal distributions. The distribution of fuel apparently plays a very minor role.

The first parcel's burn causes it to heat and expand thus causing a global pressure rise and catalyzing reactions in the rest of the charge. The volume heats via compression, and the next hottest parcels of gas with radicals and sufficient oxygen release heat and expand. Parcels burn in the order of descending temperature. The rate of parcels burning increases as the temperature of the parcels approaches the mode temperature of the parcels, as depicted in Figure 1.9. The zones with the mode temperature, at a reference time before ignition, are the zones that burn at the point of maximum pressure rise rate. The burn rate depends on charge temperature stratification because the ignition delay of a given parcel of gas will be longer if this parcel starts at a comparatively lower temperature than the first parcel to ignite. If the burn is temperature-stratification limited, it will slow down near the end of the burn as fewer and fewer parcels are brought to their ignition temperature. At some point during the burn, the pressure will rise faster in the volume that is burning than the chamber volume can equilibrate. Pressure waves will result. Strong pressure waves may dominate the deceleration-by-temperature-stratification effect.

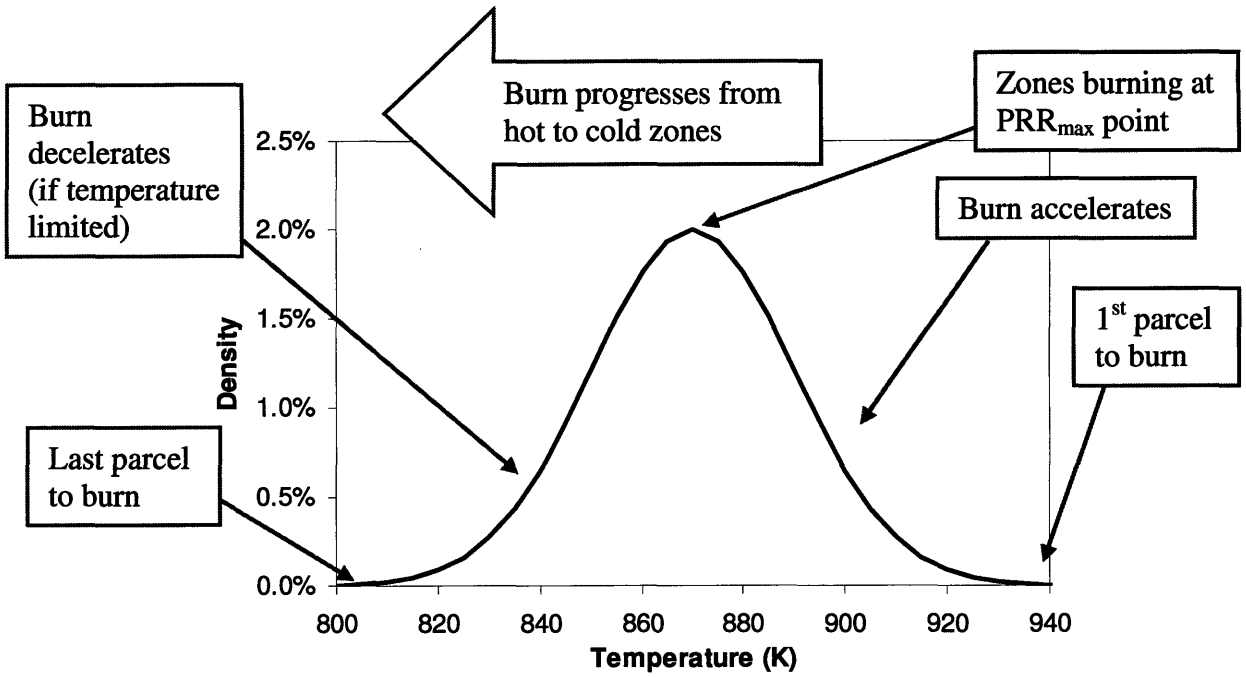


**Figure 1.9.** Fictitious (Gaussian) charge temperature distribution for a time shortly before ignition.

A fuel molecule's or radical's accessibility to oxygen affects the burn rate as well. For equal temperature distributions, the burn will progress faster if there is excess oxygen in the mixture than if there is instead inert diluent such as nitrogen or carbon dioxide. This effect implies that EGR will result in a slower burn than dilution by excess air.

Accessibility to oxygen also means that simply higher concentrations of air and fuel will accelerate the burn. Boosting the engine or increasing the compression ratio results in higher concentrations during the burn. Combustion phasing also dictates concentration. If the burn is initiated after top center, the cylinder volume will be slightly larger during the burn than if the burn took place at TDC. As the burn is retarded more, the cylinder volume increases at a higher rate as determined by the slider-crank equation. As the volume increases, the concentrations, as well as the temperature, fall correspondingly. The effect on phasing is expected to be minor but not insignificant.

# Chapter 2 Experimental Apparatus

The theme of the experimental apparatus was for a test engine to be similar to a passenger vehicle engine yet flexible enough for ease of experimentation, maintenance, and modification. The principal capabilities required of it were as follows:

- Varying the residual gas fraction on a cycle-by-cycle basis via valve timing
- Mimicking turbocharged and supercharged operation while independently varying the intake air temperature
- Yielding data that could serve as useful metrics for load and for knocking intensity
- Yielding data to reflect the operating condition of the engine
- Varying the amount of exhaust gas recirculation (EGR)

Pictured in Figure 2.1, a single-cylinder test engine system located in the Sloan Automotive Laboratory at MIT was used for all experiments.

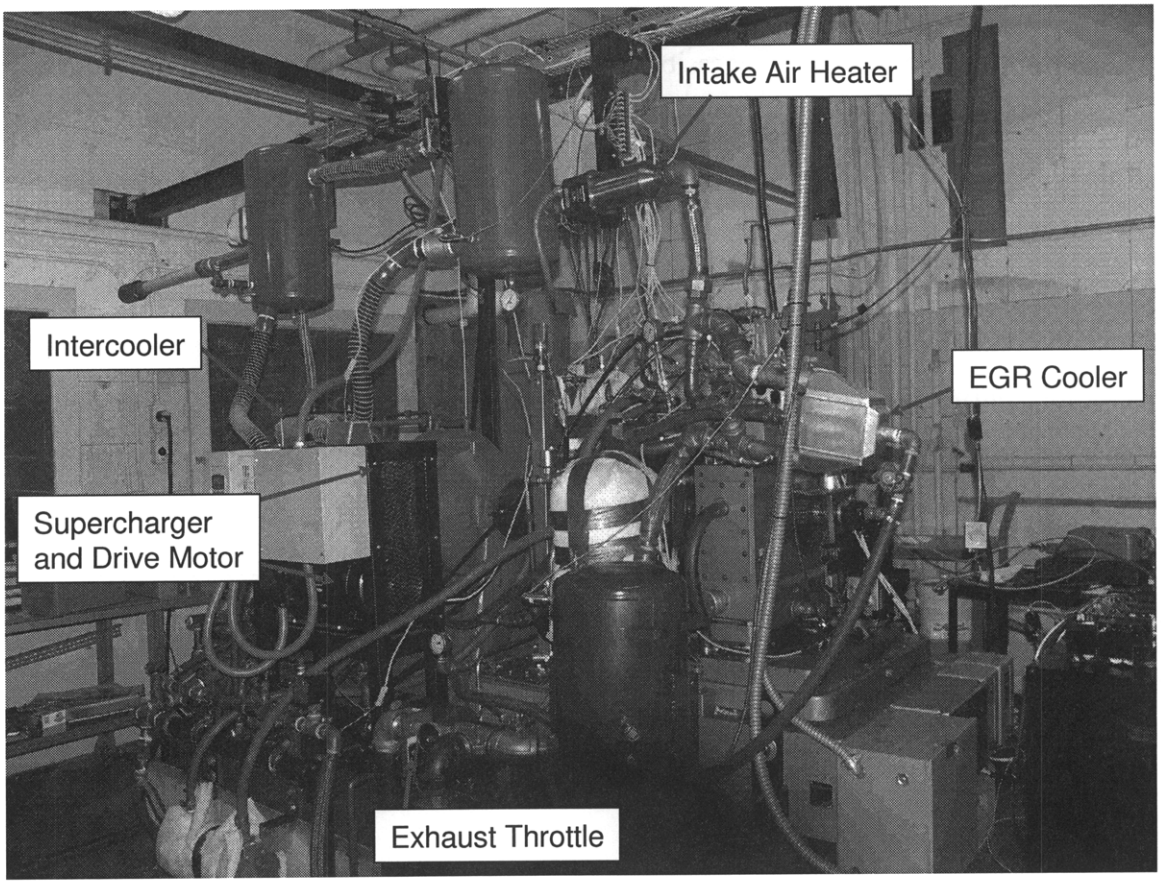


**Figure 2.1.** Single-Cylinder Experimental Engine System.

## 2.1 Test Engine

A single-cylinder Ricardo Hydra served as the CAI test engine with specifications shown in Table 2.1 and pictured in Figure 2.2.

**Table 2.1.** Test Engine Specifications

| | |
|---|---|
| Bore | 80.26mm |
| Stroke | 88.9mm |
| Connecting Rod Length | 158mm |
| Displaced Volume | 450cm$^3$ |
| Clearance Volume | 49.45cm$^3$ |
| Compression Ratio | 10.1 |

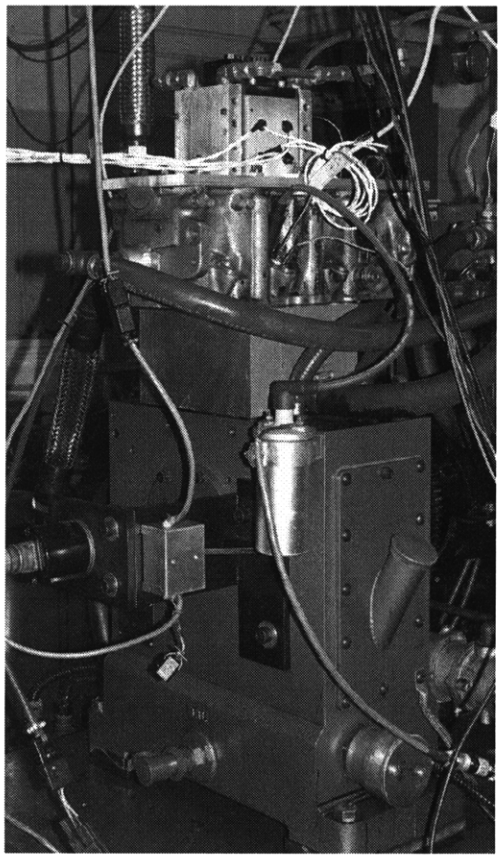

**Figure 2.2.** CAI Test Engine. A Ricardo Hydra with an Audi TDI head served as the test engine.

A Volkswagen TDI head with two valves per cylinder was installed on a custom-made cylinder block which was mounted on the Ricardo crankcase. The combustion chamber geometry featured a flat piston and a flat head with a spark plug installed in the fuel injector hole of the head. This head, shown in Figure 2.3, was chosen because it was built to withstand high, diesel-level cylinder pressures and because the valves were compatible with the electromagnetic valve actuation (EVA) device. The combustion chamber size and the compression ratio were typical for a passenger car engine, although the pancake combustion chamber geometry is not reflective of state of the art engines. It allowed easy adaptation of the EVA system and simplicity. A port fuel injection (PFI) system was added to allow typical PFI SI operation. The engine was coupled to a Dynamatic dynamometer, type DR model 2U, rated for 75hp and 3400rpm.

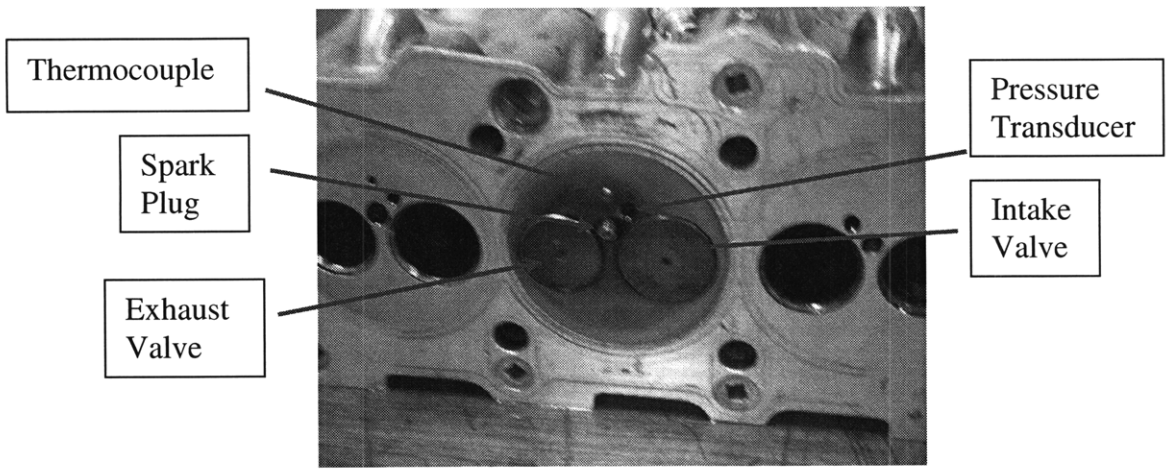


**Figure 2.3.** The Volkswagen TDI head.

### 2.1.1 Electromagnetic Valve Actuation (EVA) System

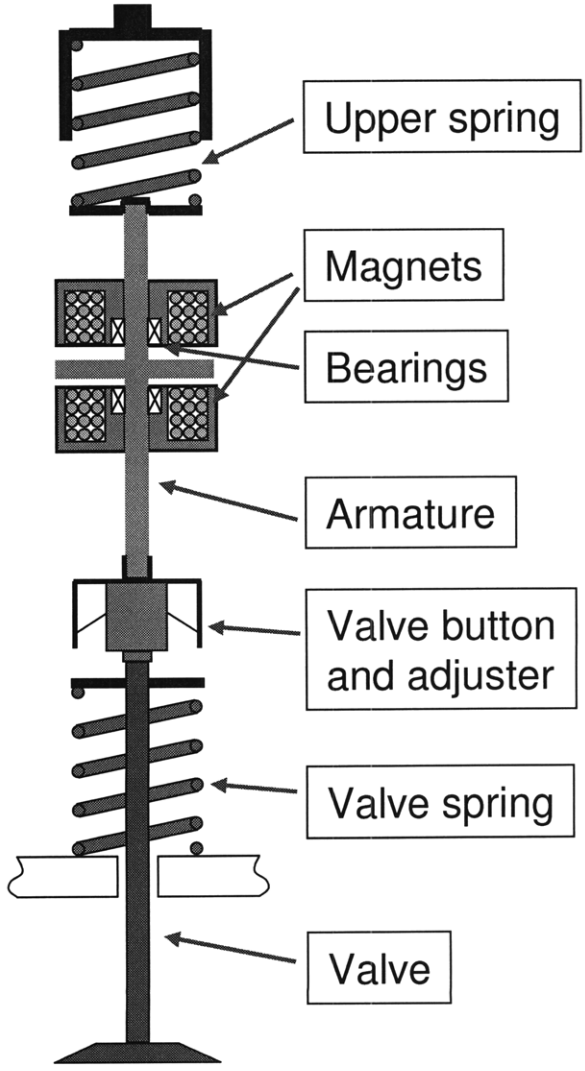


The electromagnetic valve actuation (EVA) system was originally designed and built by Aura Systems Inc. in 1995 for Chrysler Corp. In 2001, the system was donated to MIT. The device consists of electromagnets above and below an armature. The magnets pull the armature up and down, respectively, as diagrammed in Figure 2.4. The armature pushes down on the Volkswagen stock button and valve assembly in the head. Each magnet is only strong enough to pull the armature when it is halfway between the magnets or closer to itself. A spring is mounted above the upper magnet to return the armature to center from the top position, and the stock valve spring is used to return the armature to center from the bottom position.

**Figure 2.4.** Diagram of the EVA system

The order of operation for opening a valve is as follows:

1. The armature is at rest against the upper magnet
2. The top magnet is turned off
3. The top spring pushes the armature to the center position
4. The lower magnet is energized and pulls the armature against itself to a resting position
5. The magnet current is reduced to a lower level since the magnetic field is much stronger near the magnet than far away from it

To perfect the EVA system operation, the device was mounted on an engine head section with the valves exposed below for initial tests. An eddy-current position sensor (Kaman 6C) was mounted under the valve so that the timing and speed of valve movements could be studied. Figure 2.5 shows the bench-level apparatus and a close-up photograph on the mounted position sensor.

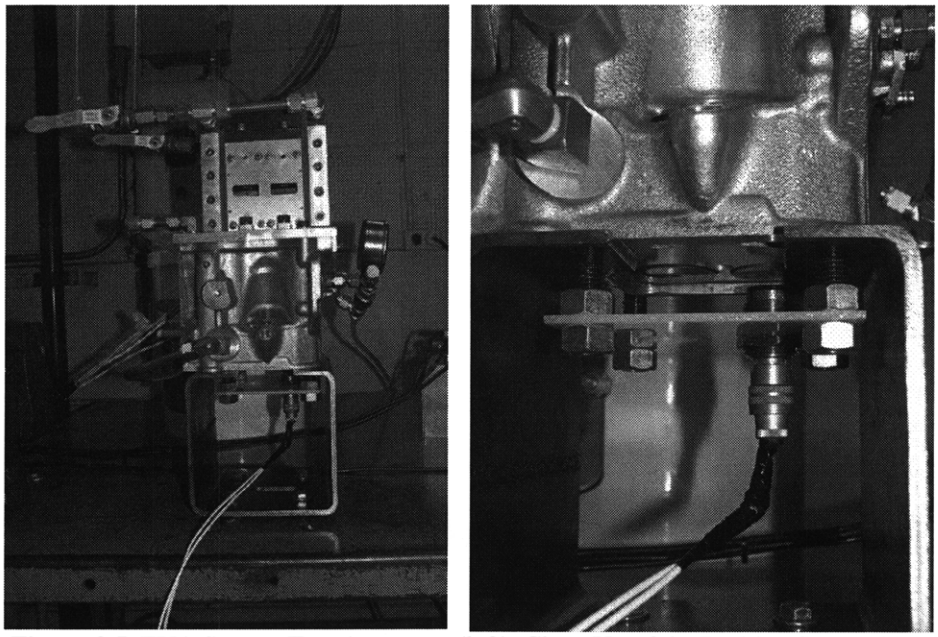

**Figure 2.5.** EVA System Test Apparatus (left), Close-Up of the Position Sensor (right)

Data collected using this apparatus are featured in Figure 2.6 and Figure 2.7. As shown in Figure 2.6, the voltage command starts at a high value when the armature is far from the magnet. Once the armature is touching the magnet, the command voltage is dropped to a lower value to hold it there. The current allowed to a magnet was 6.89 times the signal voltage so the maximum current draw was about 24A, and the voltage driving the magnets was held at 50V.

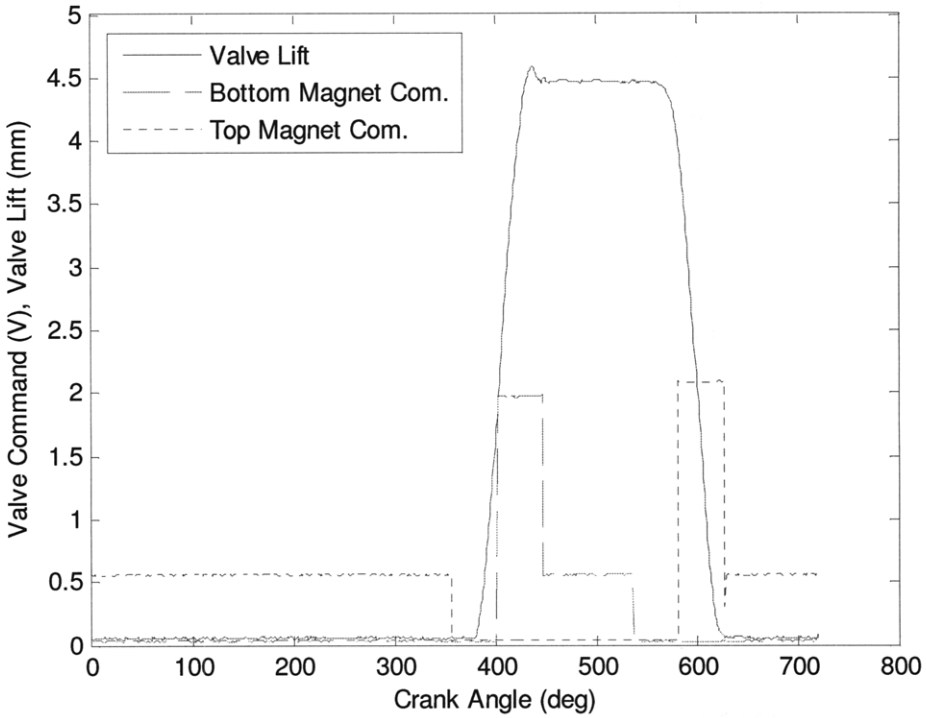


**Figure 2.6.** Bench-level position data from the EVA test apparatus. The valve position is plotted along with the command signals for the top and bottom magnets. The average of 300 cycles of intake valve operation are plotted at the equivalent of 1515rpm.

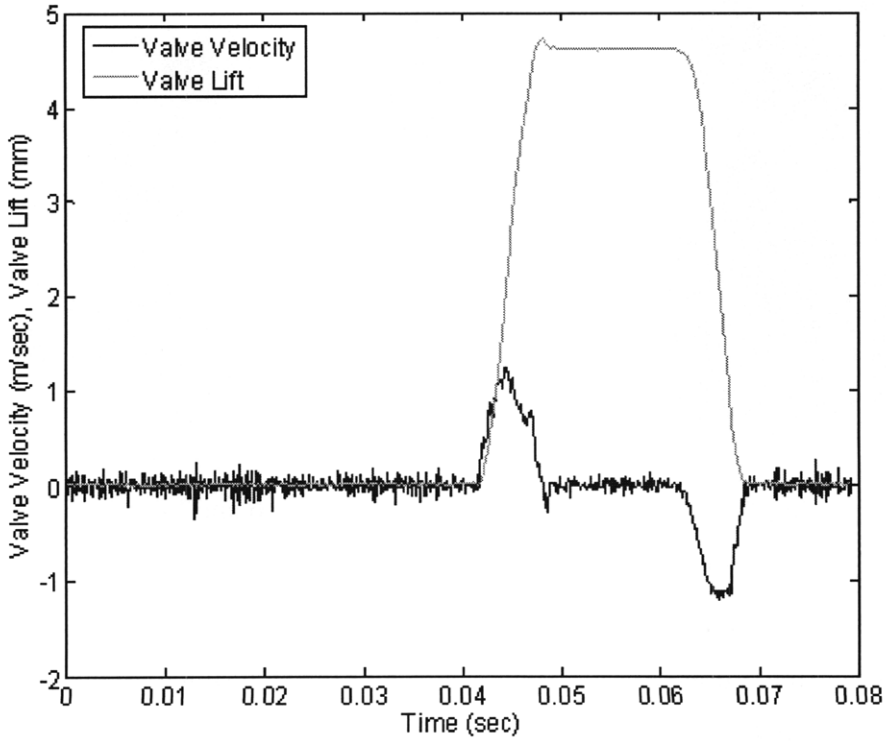


**Figure 2.7.** The valve position and valve velocity are plotted versus time for 300 cycles of intake valve operation at the equivalent of 1515rpm.

From the plot in Figure 2.6, it was possible to estimate when the valve would start and finish moving with respect to the valve command. This unfortunately could be only used as a rough calibration for engine operation since gas exchange processes would retard or hasten the valve movements depending on the operating conditions. Figure 2.7 shows the valve velocity as well as the position. Here, it is evident that the valve moves at a maximum speed of about 1.2 m/s.

Once mounted on the engine, position sensor data was not available so another way to measure the valve timing was necessary. An accelerometer, a Bosch knock sensor, was mounted on the side of the EVA system to observe the vibrations resulting from the armature landing on a magnet. While crude, this method was effective at sensing the finishing time of the valve movements. The valve durations were estimated from the bench level position data.

### 2.1.2 Air Intake and Exhaust Systems

The experimental engine system was designed so that the intake air temperature and pressure could be varied independently and so that the exhaust pressure could be increased. In particular, the system needed to be capable of assessing affects of turbocharging. As diagrammed in Figure 2.8, an electric motor was used to drive an Eaton supercharger to boost the intake pressure.

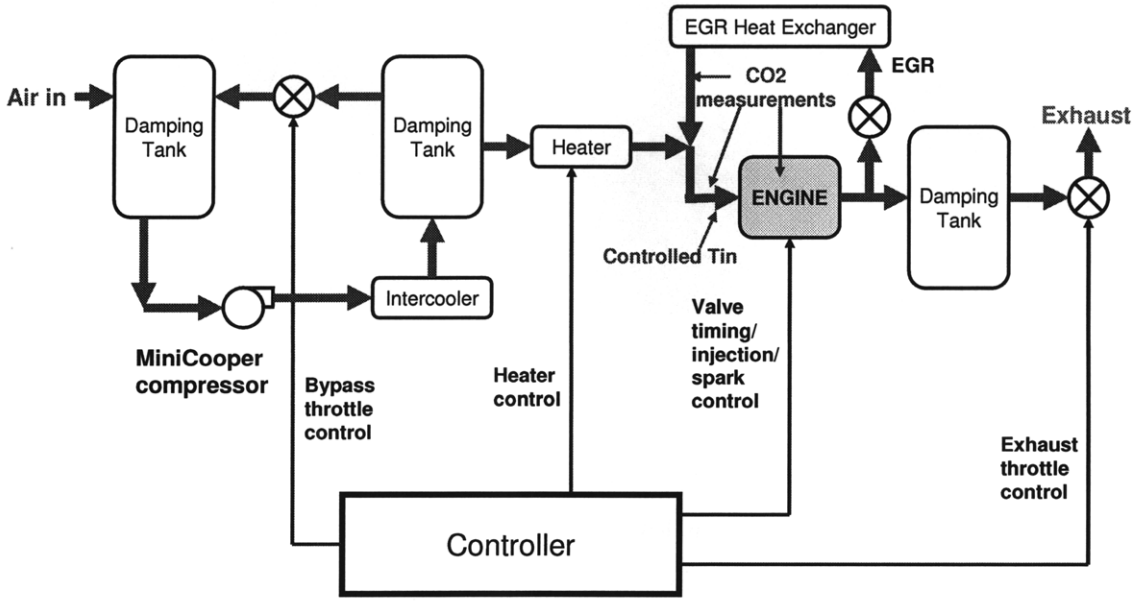


**Figure 2.8.** Diagram of the air intake and exhaust systems.

This supercharger was designed for a four-cylinder engine so delivered far more air than was necessary. Most of this air was recirculated, and an electric throttle valve was used to restrict recirculation and therefore force air into the engine. An intercooler was installed downstream of

the supercharger to allow low-temperature, boosted intake air. A volumetric flow sensor was installed at the furthest point upstream of the system. Two damping tanks were installed to ensure smooth flow through the flow sensor and to reduce any pulsation effects of the compressor on the cylinder pressure during the induction process. A photograph of the intake is shown in Figure 2.9.

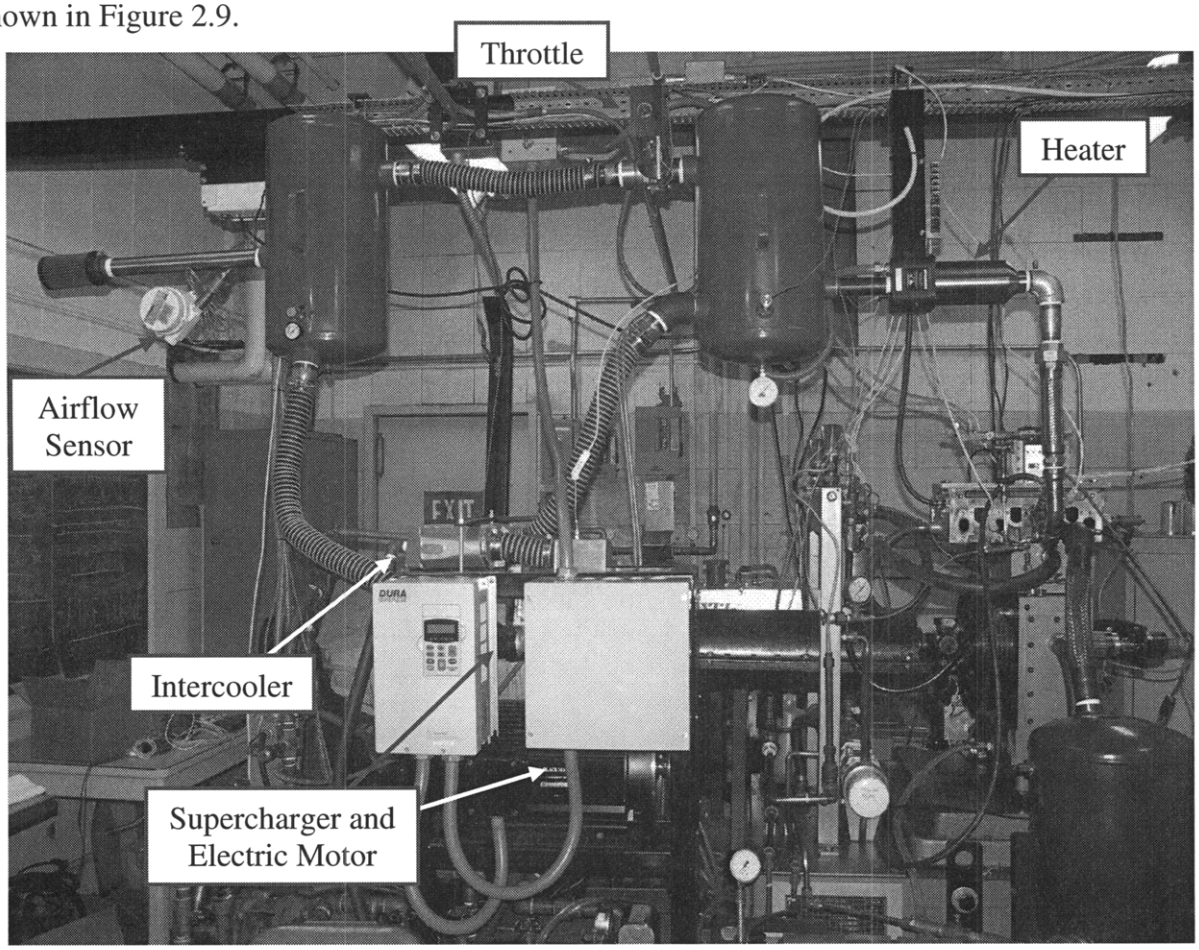


**Figure 2.9.** The Intake Air System.

A 6kW electric heater from Osram-Sylvania was installed between the second damping tank and the engine to heat the intake air. Heating the intake air was necessary to achieve auto-ignition since the compression ratio was low at 10.1:1. Changing the degree of heating was far easier than changing the compression ratio so this configuration allowed for more flexibility. Typical intake air temperatures ranged from 35˚C to 120˚C.

The exhaust pressure was increased via an electrically controlled throttle. The exhaust pressure was increased to match the intake pressure to simulated ideal turbocharged operation. This system was used instead of a turbocharger because the ideal turbocharger characteristics

were not known and because acquiring a turbocharger sized for a single-cylinder engine was not feasible.

An EGR loop, as pictured in Figure 2.1, was installed to flow cooled exhaust gas to the intake. A gate valve on the loop and the exhaust throttle valve were used to control the flow. For all EGR data, the exhaust pressure was set to be 30mbar above the intake pressure to drive the EGR flow. A Horiba Automotive Emission Analyzer (MEXA-554JU) was used to sample gas from the intake to asses the fraction of the gas that was $CO_2$. The EGR flow rate was derived from this measurement.

## 2.2 Data Acquisition

The data acquisition system was designed to characterize the engine operating condition as well as to assess the degree of engine knocking. The system was also designed so that as many signals as possible were acquired by computer to minimize human error. The system comprised five subsystems: pressure measurements in the intake and exhaust lines, measurements for intake air flow, fuel flow, and oxygen fraction in the exhaust, in-cylinder pressure measurements, accelerometer measurements, and temperature measurements.

### 2.2.1 Intake and Exhaust Pressure Measurements

The gas pressure was measured in the intake and exhaust systems since a primary goal of the experiment was to assess turbocharging. The intake pressure was measured in the damping tank just upstream of the heater. The exhaust pressure was measured in the exhaust damping tank. Average values were used from each measurement as wave dynamics in the lines make determining the pressure more difficult. They also make deriving meaning from an accurate measurement far more difficult. An Omega PX 209-060A5V transducer was used for each application with a ceramic filter piece to dampen pressure spikes and keep the transducer clean of particulate matter in the exhaust.

### 2.2.2 In-Cylinder Pressure Measurements

The in-cylinder pressure measurements formed the basis for most of the combustion metrics. Indicated load, efficiency, burn duration, combustion phasing, and pressure and temperature during compression all depended on a fast pressure measurement in-cylinder.

A Kistler 6125A piezoelectric pressure transducer was mounted in the head of the engine, as noted in Figure 2.3. A Kistler 5010 charge amplifier was used to amplify the signal. Since the

transducer yielded a differential measurement, the data acquisition script calibrated the in-cylinder pressure against the intake pressure at BDC on a cycle-by-cycle basis.

### 2.2.3 Air Flow, Fuel Flow, and Equivalence Ratio

As noted in Figure 2.8 and pictured in Figure 2.9, the air volume flow was measured via a flow meter. The device was a Kurz 505 Series Flow meter. While the instrument was recently calibrated and accurate, the intake system with its many connections suffered small leaks. A wide-band Bosch $O_2$ sensor and Etas Lambda meter measured and calculated the air-fuel ratio from the exhaust chemistry. The fuel mass flow rate was estimated in two ways. First, the injector was calibrated with a volumetric measurement. Also, during many of the data acquisition runs, the mass flow of the fuel was measured via a pale-on-scale strategy. A flask of fuel was placed on a balance, and the change in mass of the fuel flask was recorded thus yielding the rate of depletion of fuel. An Ohaus Scout Pro balance was used. Minor differences emerged between the injector calibration and the mass measurement strategy, and the final estimation was a calibration based on the mass measurement. The air mass flow was estimated based on the fuel flow and the air-fuel ratio estimate since leaks led the flow meter measurement to be inaccurate at high boost pressures.

These measurements were necessary for developing several key metrics. First, knowing the mass fuel was required for calculating the efficiency of the engine. Also, estimating the residual gas fraction and the temperature and pressure during compression required knowing the number of moles in the charge which required knowing the air and fuel flows.

UTG-91 gasoline was used for all tests. It was chosen to typify pump fuel found in the United States. The specifications for this fuel are detailed in Appendix A1.

### 2.2.4 Accelerometer Measurements

As previously noted, an accelerometer was mounted on the side of the EVA system to sense the vibrations of the structure resulting from the landing of the armature on a magnet. From this signal, the timing of the end of the valve movement could be precisely determined. A sample accelerometer signal is shown in Figure 2.10. Incidentally, the accelerometer also manages to observe vibrations in the structure resulting from engine knock.

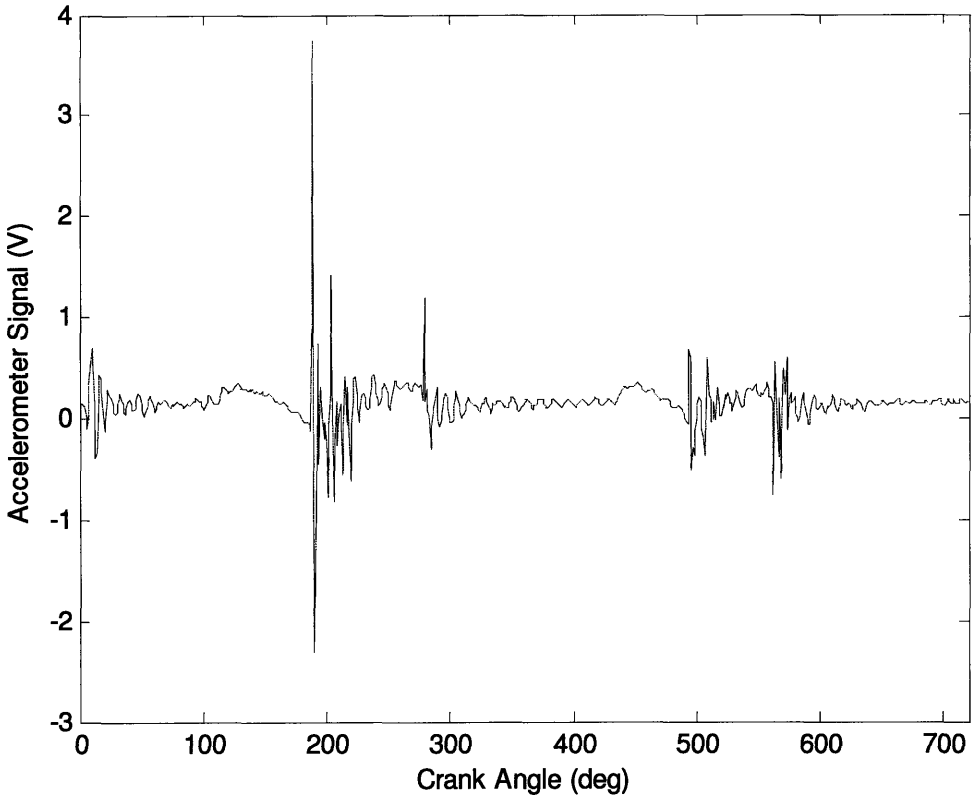


**Figure 2.10.** A Typical Accelerometer Signal vs. Crank Angle. Strong vibrations at 188°, 278°, 493°, and 561° indicate valve landing for EVO, EVC, IVO, and IVC respectively. The vibrations near 0° indicate engine knock.

### 2.2.5 Temperature Measurements

Various temperature measurements were made about the apparatus to help the operator keep components from over-heating, to keep the operating conditions consistent from one test to the next, and to use temperature as independent or dependent variable. The engine oil temperature, fuel filter temperature, and engine coolant temperature were all taken to keep operating conditions consistent. The intake air temperature, measured at the opening of the intake port, was used as an independent variable. The exhaust temperature, measured at the exit of the exhaust port, and the head temperature, measured at the surface of the head, were both used as dependent variables. The former was used to estimate residual gas fraction as will be discussed later. The head temperature measurement gave a sense for how wall temperature was varying at various operating conditions. The location of the head thermocouple is noted in Figure 2.3. The dynamometer coolant temperature was measured as a check to make sure it was not overheating. K-type thermocouples were used in all measurements.

### 2.2.6 Data Acquisition Hardware and Software

A desktop computer with an Intel Pentium IV processor and Windows XP operating system severed as the data acquisition computer. A National Instruments PCI-6023E data acquisition card was used to acquire pressure data, accelerometer data, and valve timing command data. The card featured 8 differential inputs, 12 bit resolution, and 200kS/s maximum sampling rate. An NI USB-9211A was used to acquire coolant temperature, intake temperature, head temperature, and exhaust temperature. At 12S/s, the device was adequate for showing slowly changing temperature measurement trends. The balance for fuel mass measurements communicated data to the computer via a USB port and virtual serial port connection.

National Instruments Labview was used to monitor the operating parameters of the experiment and to record data. The script calculated metrics, such as NIMEP, valve timing, and average $\lambda$, on a cycle-by-cycle basis to help the operator properly set the apparatus at a given test condition.

### 2.2.7 Residual Fraction Estimation

Estimating accurately the amount of trapped residual gas is essential to quantifying the contents of the cylinder and therefore to estimating the bulk temperature in-cylinder. The method proposed to estimate the number of moles of trapped residuals was to use the Ideal Gas Law to find the number of moles at EVC by estimating the pressure and temperature in-cylinder at this point as in Equation 2.1.

$$n_{trapped} = \frac{P_{EVC}V_{EVC}}{RT_{EVC}} \approx \frac{P_{EXH}V_{EVC}}{RT_{EXH}} \tag{2.1}$$

Here, the volume at EVC can be found via the slider-crank equation, and $P_{EXH}$ was measured with the exhaust pressure transducer. $T_{EVC}$ is estimated to be the average exhaust temperature. Next, the total number of moles is found in Equation 2.2.

$$n_{tot} = n_{fuel} + n_{air} + n_{trapped} \tag{2.2}$$

The recompressed gas is assumed to become the residual gas. The residual gas fraction is the residual gas divided by the total number of moles.

$$x_{residual} = \frac{n_{trapped}}{n_{tot}} \tag{2.3}$$

In-cylinder $CO_2$ measurements were conducted to assess the accuracy of these methods for estimating residual fraction. An NDIR spectroscopy system (NDIR500 from Cambustion) was used with the sample probe mounted in the place of the cylinder head thermocouple pictured in Figure 2.3. This absorption spectroscopy technique had been used effectively to estimate residual fraction by other groups in this manner in the past [49, 50]. A second sample probe was mounted in the exhaust as a check on the in-cylinder measurement. Typical $CO_2$ fraction traces for in-cylinder and for exhaust measurements are presented in Figure 2.11.

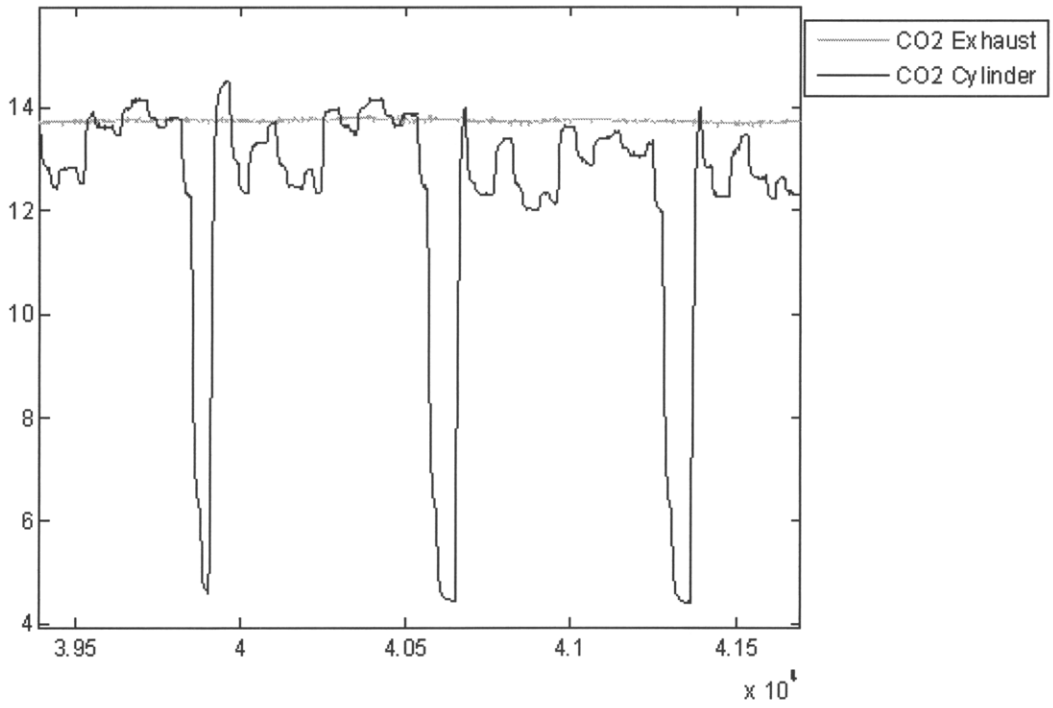


**Figure 2.11.** $CO_2$ Traces for In-Cylinder and Exhaust Measurements.

The instrument's response time was approximately 8ms which corresponds to 72 CAD at 1500rpm. This means that one point during compression and one point during expansion should be expected. The low point of the in-cylinder measurement is the point during the compression stroke. From stoichiometry, the residual fraction can be found from this gas fraction measurement point alone. The accumulation of oil, soot, or other non-gaseous substance in the NDIR sample chamber can cause error or a fault. These foreign substances act to absorb light broadly and so add noise to the signal. Although calibration and signal processing built into the instrument software address this issue in part, even a short period of in-cylinder sampling can add significant error to the calibration via contamination. Misfires appeared especially taxing

thus emphasizing the need for a robust engine start routine. In one test session, the $CO_2$ calibration gas (13% $CO_2$, 87% $N_2$) was measured in sample mode before testing and after testing. After testing for 3 hours involving one engine start, the reading went from 13.1% just after calibration to 12.57% after testing. Considering the possibility in signal drift, we concluded the most accurate way to estimate residual fraction using this equipment was to use the $CO_2$ value during compression divided by the $CO_2$ value during expansion. This way, any variation in the in-cylinder sensor is normalized out. This is also the way advocated by Cambustion in the equipment manual.

The in-cylinder $CO_2$ measurements confirmed that the exhaust state method of estimating residual fraction was accurate. Figure 2.12 features residual fraction vs. EVC timing for an NVO sweep where the intake and exhaust pressure was 1.1bar and the intake temperature was 120°C.

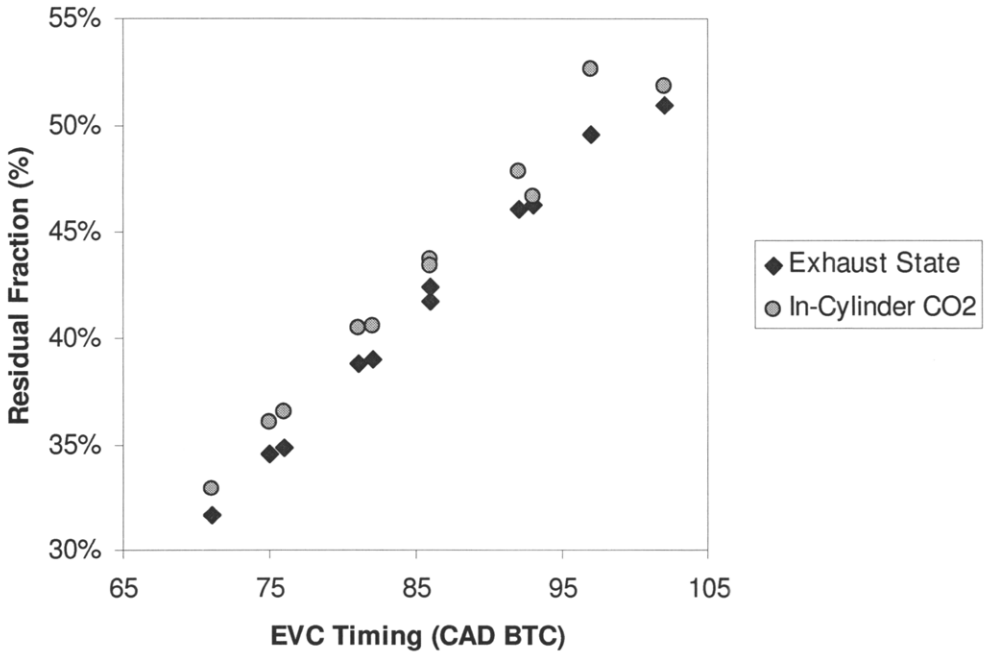


**Figure 2.12.** Residual Fraction vs. EVC Timing, $P_{in}$ = 1.1bar. The exhaust gas state method estimates residual fraction approximately 1-2% lower than the in-cylinder $CO_2$ measurement method.

The exhaust state method estimates consistently estimates residual fraction to be 1-2% higher than the in-cylinder $CO_2$ measurement. Figure 2.13 shows a similar plot except that these data feature intake and exhaust pressure at 1.3bar. The agreement here was better than in the 1.1bar data. Figure 2.14 features an EVO Timing sweep at 1.1bar intake pressure. The data show good agreement at 30° BBC.

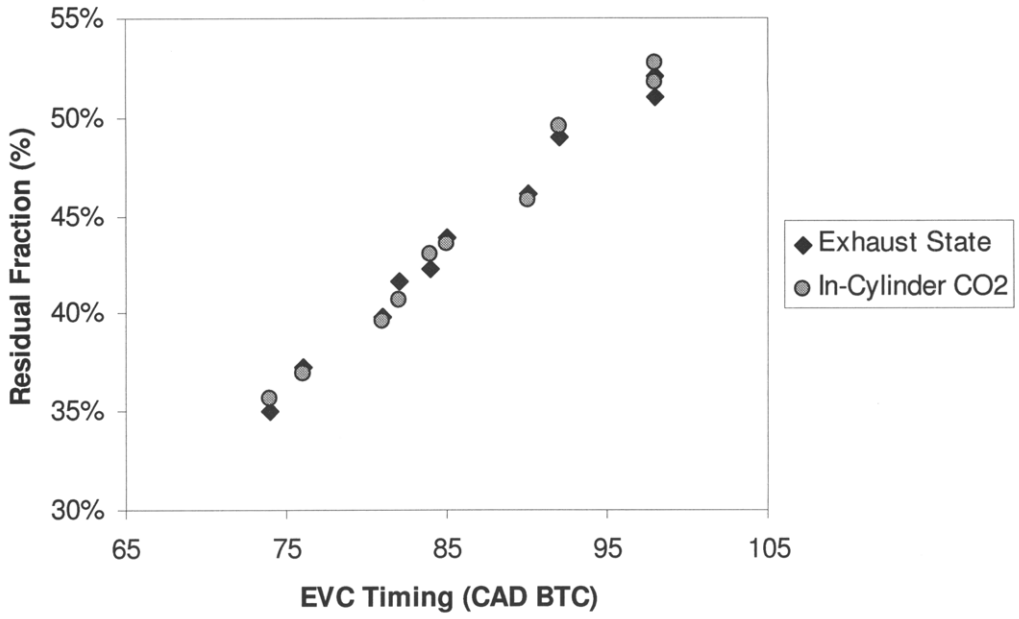


**Figure 2.13.** Residual Fraction vs. EVC Timing. Pin = 1.3bar. The exhaust state estimate method matches the in-cylinder measurement well.

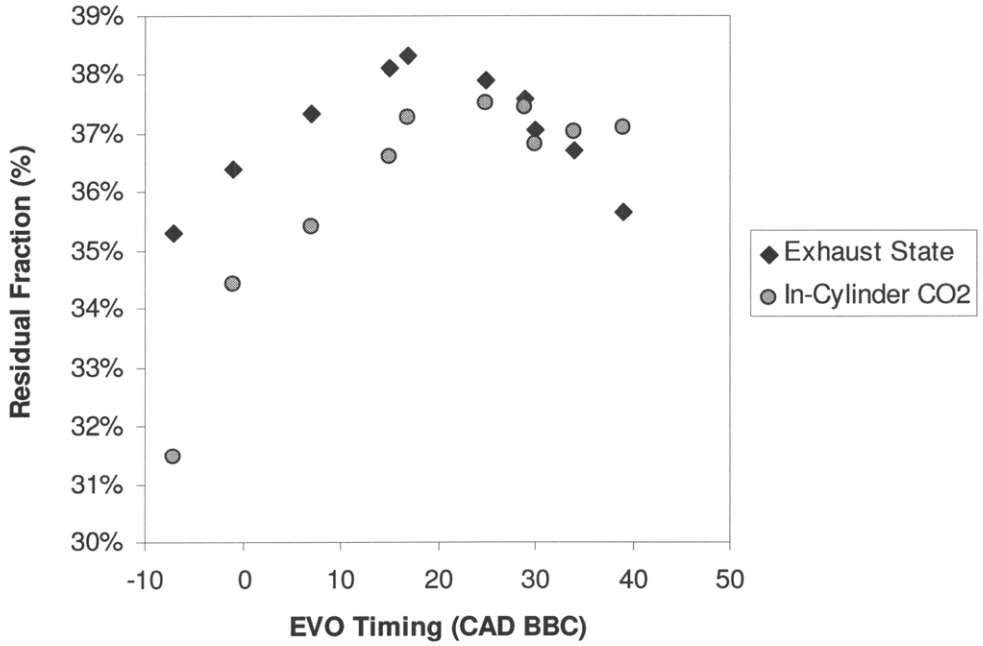


**Figure 2.14.** Residual Fraction vs. EVO Timing. Pin = 1.1bar. The exhaust state estimate features good agreement at 30° BBC but over-estimates the residual fraction at very late EVO Timing.

The exhaust state method estimates residual fraction to be increasingly higher than the $CO_2$ measurement method at EVO timing is retarded. This is potentially because EVO timing affects the temperature of the trapped residual and therefore increases the error between exhaust temperature and EVC temperature. All of the data where EVO timing is held constant features an

EVO timing of 30° BBC so the bulk of the data should yield accurate residual fraction data. The residual fraction estimate is less reliable for the EVO sweep data.

The $CO_2$ measurements confirmed that this exhaust state method can be used effectively to estimate the quantity of trapped residuals. The in-cylinder gas measurements required great care and considerable effort so they were only used for verification purposes rather than as the primary method for all of the data.

# Chapter 3 Effects of Intake Temperature, Boost, and Valve Timing

Three primary ways to control combustion are to vary the intake temperature, to vary the level of boost taken to mean changing intake and exhaust pressure together, and varying the valve timing. This chapter will explore the effects of these control parameters on maximum rate of pressure rise, load, efficiency, combustion phasing, and the misfire limit. Particular focus will be given to how the operating region, constrained by maximum rate of pressure rise, shifts with boost.

## 3.1 Sample Combustion Data

Before presenting results, sample combustion data is shown to familiarize the reader with the data to be presented. Figure 3.1 shows an example pressure trace of a single cycle.

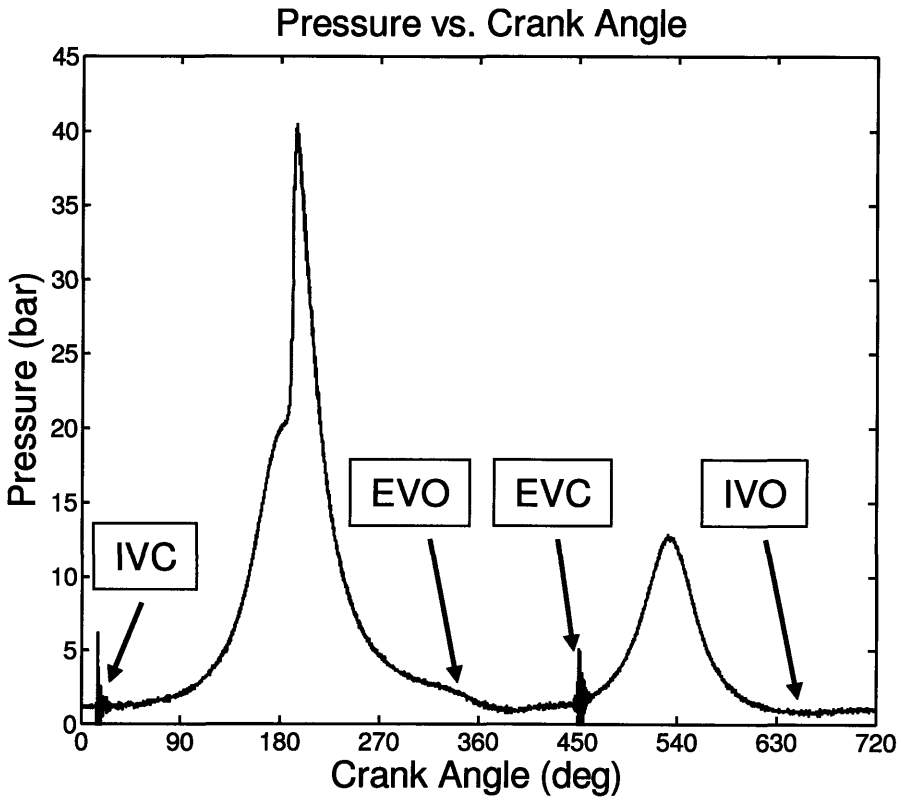


**Figure 3.1.** A Sample Pressure Trace of One Cycle.

As time advances from BDC (0°), the intake valve finishes closing at 20° ABC. The pressure rises due to compression until shortly after TDC when ignition occurs. The pressure rises very sharply until it peaks above 40bar. The jaggedness of the traces shortly after combustion

indicates pressure oscillations in-cylinder akin to the phenomenon of spark-ignition knock. Combustion is very short, taking perhaps only 15° from start to finish. At just before BDC, the exhaust valve opens, and the exhaust pressure equilibrates to the exhaust line pressure. The exhaust valve closes at approximately 85° BTC, and the residual gas is trapped in-cylinder and recompressed. Trapping hot residual gas from one cycle to the next is the principle characteristic of the negative valve overlap strategy. It is re-expanded until the intake valve begins to open at approximately 85° ATC. This is deliberately symmetric to the EVC timing about TDC so that as much as possible of the work done compressing the residual gas is extracted during the re-expansion stroke. If the pressure in-cylinder is not at the intake pressure, they equilibrate, and the intake process begins. The apparent pressure oscillations at IVC and EVC are noise. The transducer is recording vibrations in the head caused by the valves striking the head when they close.

Another perspective of the pressure history is shown in Figure 3.2 where the natural logarithm of the pressure is plotted against the natural logarithm of volume.

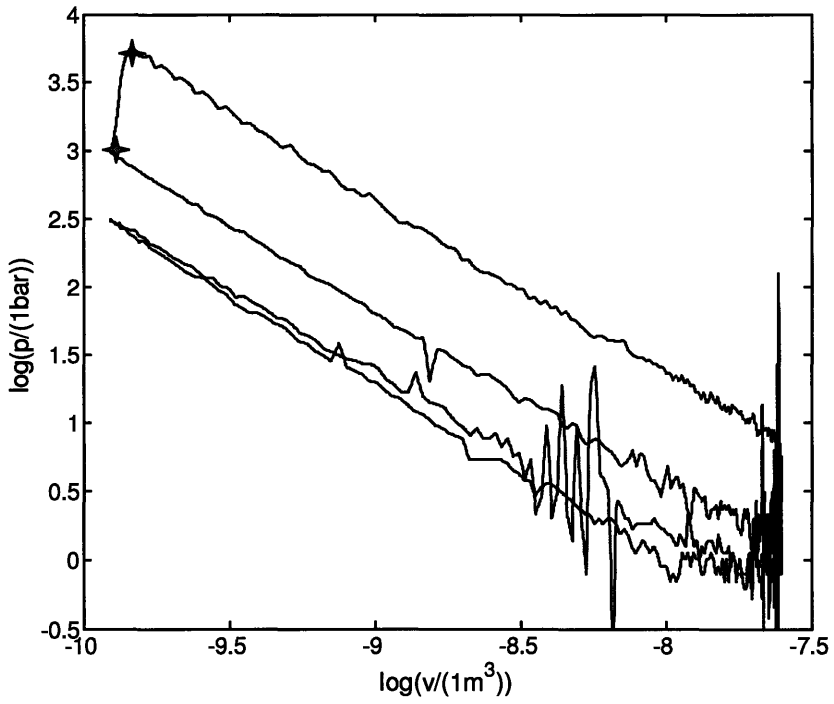


**Figure 3.2.** Log(P) vs. Log(V) Plot of an Example Cycle. Combustion start and finish are marked by stars.

The beginning and end of combustion are denoted with stars. Ignoring noise in the signal from valve strikes and electrical noise from the signal ground, one can clearly see the nearly straight

lines during compression and expansion as well as during the recompression and re-expansion processes. The speed of combustion is also clearer here, as it happens in nearly a constant volume.

## 3.2 Intake Temperature and Intake Pressure Effects

The reaction rate of fuel and air is strongly dependent on the temperature of the gas so a natural parameter to study is the temperature of the intake air. The following data show the effect of varying the intake air temperature and the level of boost. Exhaust pressure is held equal to the intake pressure. Valve timing was set such that a considerable amount of residual gas would be trapped but not so much that the residual temperature would be cold from lack of fuel. The valve timing is listed in Table 3.1 and depicted in Figure 3.3.

**Table 3.1.** Intake Temperature Study Valve Timing

| Valve Operation | Timing |
|---|---|
| IVC | 18° ABC |
| EVO | 30° BBC |
| EVC | 83° BTC |
| IVO | 83° ATC |

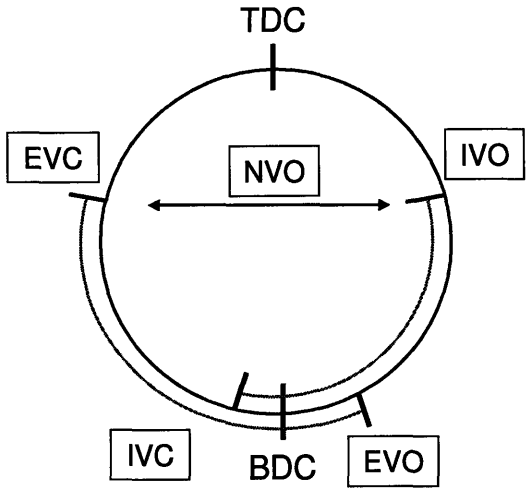


**Figure 3.3.** Diagram of Intake Temperature Study Valve Timing

The first effect to note is that increasing the intake temperature results in a linear increase of the bulk charge temperature at 15° BTC as shown in Figure 3.4. Five levels of boost ranging from 1.0bar to 1.4bar are plotted for an intake temperature range of 40°C to 120°C. 40°C was the lowest temperature the equipment would produce. The exhaust was throttled so that the exhaust pressure was held equal to the intake pressure. The 1.1bar and 1.0bar data feature limited temperature ranges because misfire occurred when the temperature was reduced sufficiently. The misfire limits are circled. Note that an increase in intake temperature results in a significantly lower increase in average charge temperature. For example at 1.2bar, an intake temperature increase of 70°C results in an increase of charge temperature of 40°C. This is because the charge

is composed of approximately 40% trapped residual which is not directly affected by intake air temperature. An increase in boost pressure also resulted in an increase in charge temperature. This is because heat transfer to and from the walls increased and because the residual gas fraction increased. The effect on residual gas fraction is shown in Figure 3.5, and since the residual gas was hot, this caused an increase in charge temperature.

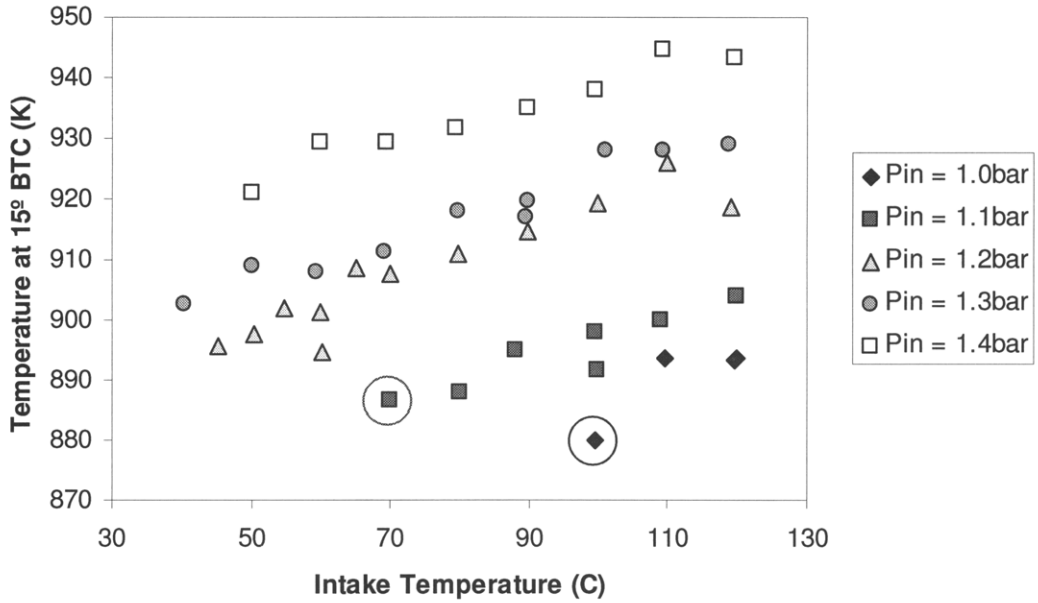


**Figure 3.4.** Average Charge Temperature at 15º BTC vs. Intake Temperature for Five Boost Pressures. Valve timing was fixed as depicted in Figure 3.3. Two points at the misfire limit are circled.

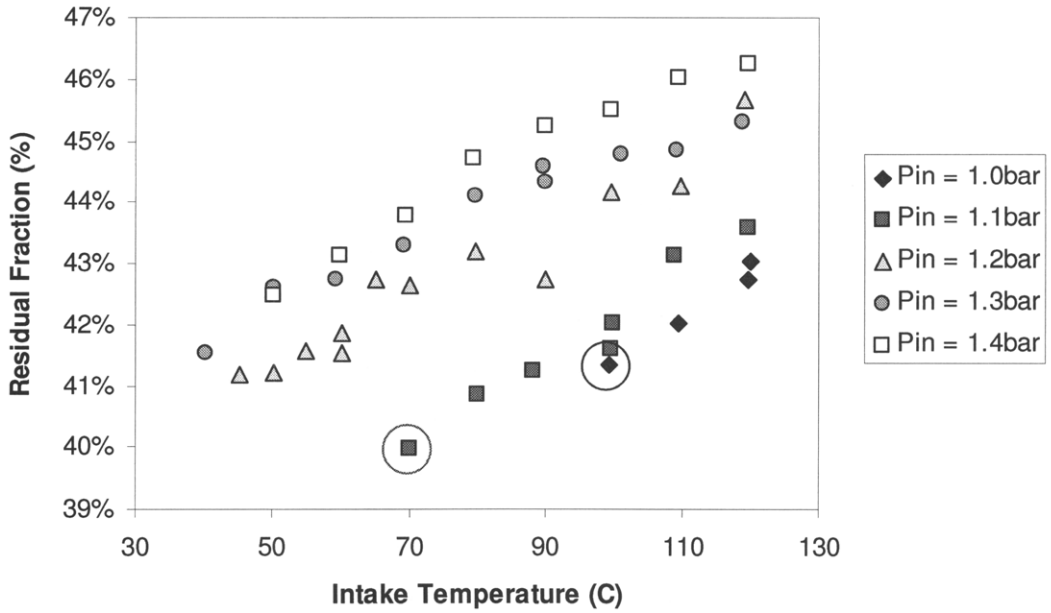


**Figure 3.5.** Residual Fraction vs. Intake Temperature for Five Boost Pressures. Valve timing was fixed as depicted in Figure 3.3. Two points at the misfire limit are circled.

The effect of boost on residual fraction appears to be simply a characteristic of the flow dynamics of the engine. A short amount of time was available for the exhaust process, and the valve lift was small at 4.7mm. The exhaust process was likely constrained by this. Residual fraction decreased as intake temperature was decreased, as shown in Figure 3.5. As the density of the air increased with decreased temperature, it accounted for proportionally more of the charge mass.

Combustion phasing, as indicated by the crank angle of 10% mass fraction burned (CA10), is plotted against intake temperature in Figure 3.6. Combustion is shown to occur earlier at higher intake temperature and later at lower temperature. The hottest part of the charge achieves a temperature favorable for fast reaction rates earlier in the cycle at higher intake temperatures. Note that at $P_{in}$ = 1.0bar and $P_{in}$ = 1.1bar, as temperature is reduced the rate of retard increases as the misfire limit is approached.

Combustion phases earlier with increased boost pressure. This could be because charge temperature increases with boost as was shown in Figure 3.4. It could also be because the density of fuel and oxygen molecules increases with pressure. Equations 1.4 and 1.5 show that reaction rate is a function of concentration, of pressure directly, and of temperature. Boost increases all of these factors.

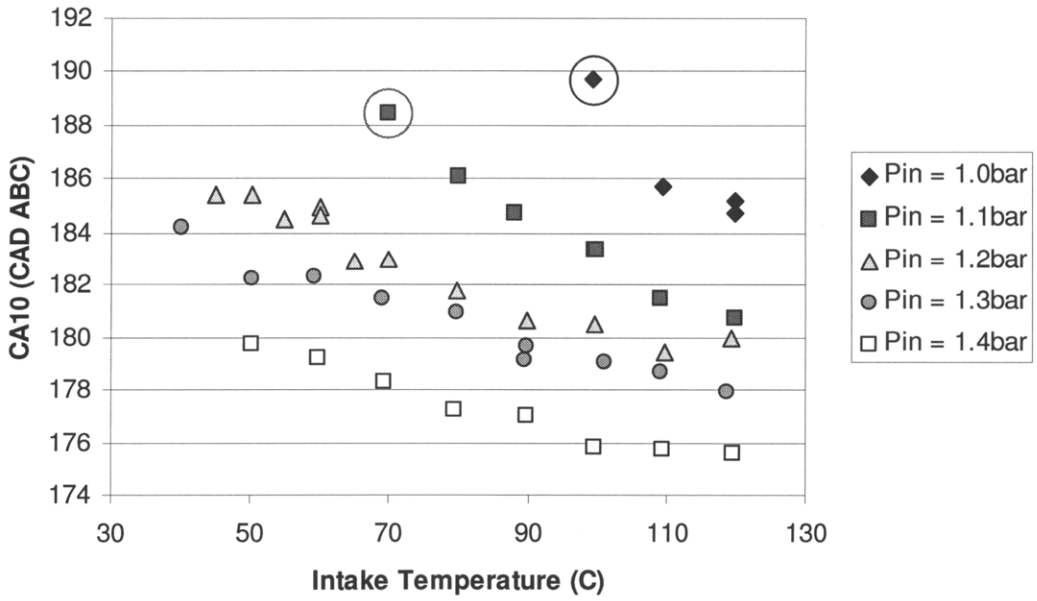


**Figure 3.6.** CA10 vs. Intake Temperature for Five Boost Pressures. Valve timing was fixed as depicted in Figure 3.3. Two points at the misfire limit are circled.

Decreasing intake air temperature increases indicated efficiency, as shown in Figure 3.7. A decrease in intake temperature of 70°C at Pin = 1.4bar results in an increase of 2.5%, indicating a clear advantage of operation with cool intake air.

The effect of boost pressure on efficiency is less clear than temperature. At 110°C intake temperature, efficiency is highest at 1.0bar, then 1.3bar, then 1.2bar, then 1.1bar, and finally at 1.4bar. Combustion phasing, residual fraction, and burn duration all affect the indicated efficiency.

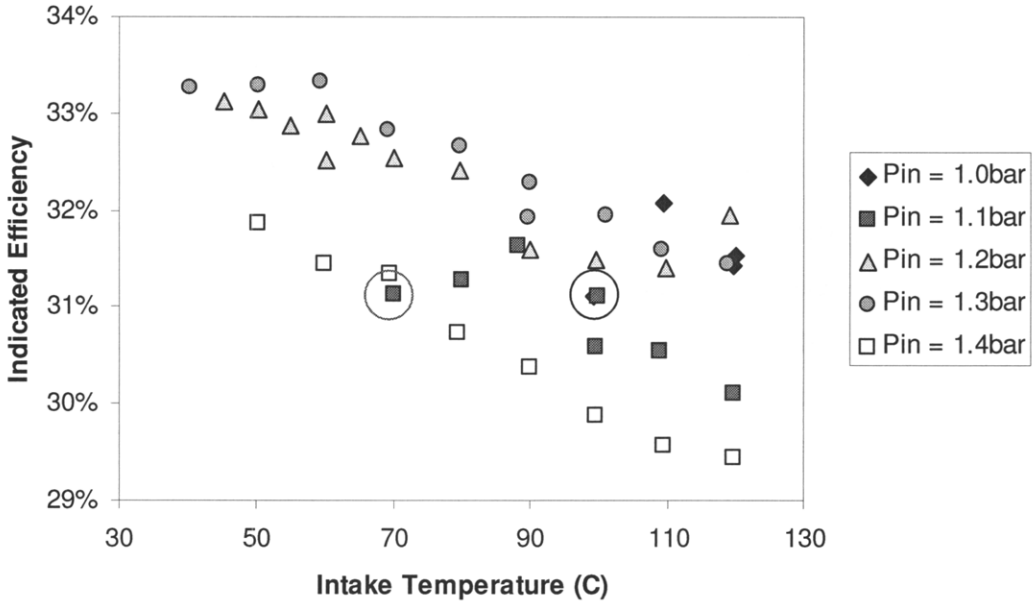


**Figure 3.7.** Indicated Efficiency vs. Intake Temperature for Five Boost Pressures. Valve timing was fixed as depicted in Figure 3.3. Two points at the misfire limit are circled.

The effects of intake pressure and boost on maximum pressure rise rate are shown in Figure 3.8. First, as boost is increased, the rate of pressure rise increases. Next, as intake temperature is decreased, the rate of pressure rise reduces. This effect is strongest at low boost and diminishes as boost increases to the point that no decrease in rate of pressure rise is observed at $P_{in}$ = 1.4bar.

What causes the pressure dependence of the intake temperature effect is not clear. Temperature has a strong, indirect effect via combustion phasing. As previously shown in Figure 3.6, reducing intake temperature causes combustion phasing to retard regardless of intake pressure. However, the resulting volume in which combustion occurs varies non-linearly with combustion phasing. A good comparison is the 1.1bar curve from 120°C to 70°C and the 1.4bar curve over the same pressure range. At 1.1bar, CA10 varies from 180.8° to 188.4° across this intake temperature range. Across this crank angle range, the cylinder volume expands by 5%.

For a theoretical motored pressure trace, this leads to a corresponding 6% decrease in pressure and a 2% decrease in temperature. The rate of expansion increases as timing phases later as well. At 1.4bar, CA10 occurs at 175.6° so a corresponding 7° delay would cause the volume to increase by only 0.05% since it reaches its minimum between these two points. This delay would not cause pressure or temperature to drop via isentropic expansion. In reality, at 1.4bar, the decrease in intake temperature by 50°C results in a delay of only 2.7°, not 7°, and so allows isentropic compression to increase pressure and temperature thus slightly counteracting any bulk temperature cooling effects.

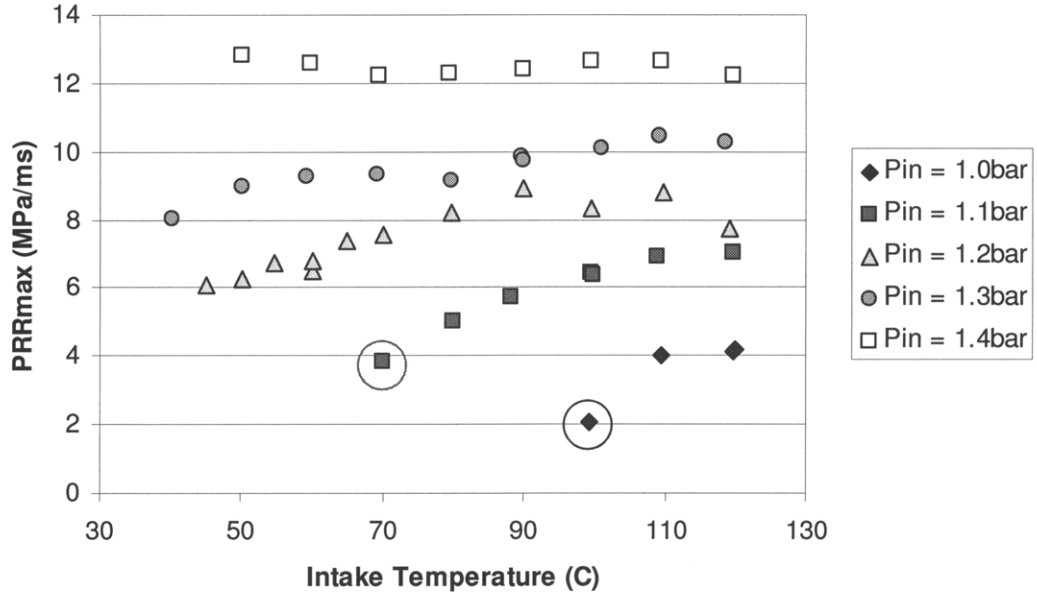


**Figure 3.8.** Maximum Pressure Rise Rate vs. Intake Temperature for Five Boost Pressures. Valve timing was fixed as depicted in Figure 3.3. Two points at the misfire limit are circled.

Another possible explanation for the pressure dependence of temperature effects is that the temperature stratification varies with level of boost. Maximum rate of pressure rise can be understood to be related to the duration of the burn, or rather, related to how soon a parcel of gas late in the burn reacts after a parcel early in the burn reacts. Of the three factors that affect the local reaction rate, concentration, temperature, and pressure, temperature is the most stratified and pressure is the most spatially uniform so variations in burn rate ought to be related to temperature variations and with a lesser likelihood to concentration gradients.

The charge is approximately 60% air and 40% trapped residual where the residual gas is approximately 600°C and the intake air is approximately 70°C when they begin to mix at IVO. During the intake and compression processes the gases mix and exchange heat; however, there

remains a temperature stratification among the fuel and air molecules at the beginning of combustion due to imperfect mixing. As the fraction of residual gas increases, which it does with increased boost, the charge may become more thermally uniform. The residual fraction does not increase very much however, perhaps 4% from 1.0bar to 1.4bar.

It is also possible that mixing is enhanced with increased boost. Boost results in a higher charge density so the Reynolds number should increase roughly proportionally with intake pressure. It also follows that the dissipation of turbulent kinetic energy would be lower as charge density increases as in Equation 3.1 so turbulence would be more intense at higher levels of boost.

$$\varepsilon = 2\frac{\mu}{\rho}\left\langle s_{ij} s_{ij} \right\rangle \tag{3.1}$$

Here, $\varepsilon$ is the dissipation; $\mu$ is the viscosity. $\rho$ is the density, and $s_{ij}$ is the fluctuating rate of strain [51]. A higher degree of mixing would result in a more thermally uniform charge and so would cause a parcel of gas that burns late to burn only slightly later than an early burning parcel and thus shorten the burn duration.

The combustion chamber walls encourage a thermal boundary layer as another significant temperature stratification. One-dimensional modeling work indicates that the boundary layers on the head and piston should be on the order of 1mm, which is significant since the height of the clearance volume is 10mm. During the majority of the compression process, the wall is hotter than the average charge temperature. Near the end of compression, the charge temperature exceeds the wall temperature [42]. The temperature field near the wall is therefore a strong function of average wall temperature which is driven by heat transfer. More fuel is burned as boost is increased thus increasing heat dissipation. Also, in-cylinder pressure waves increase heat transfer. For example, Woschnii and Fieger observed twice the heat transfer in the end-gas zone of a knocking SI engine as under normal operation [44]. Figure 3.9 shows the head temperature plotted against intake temperature for five boost pressures. The head temperature is measured by an 1/8" diameter thermocouple mounted flush with the surface of the head. The plot shows how head temperature drops slightly with intake temperature and increases substantially with boost pressure. It is reasonable then to assume that the thermal boundary layer changes with boost.

While it can be insightful to speculate about variations in the thermal distribution of the charge, this experiment features no method of showing or measuring them. Analysis of such

effects will be kept to speculation in this work with the hopes that future studies will address the topic.

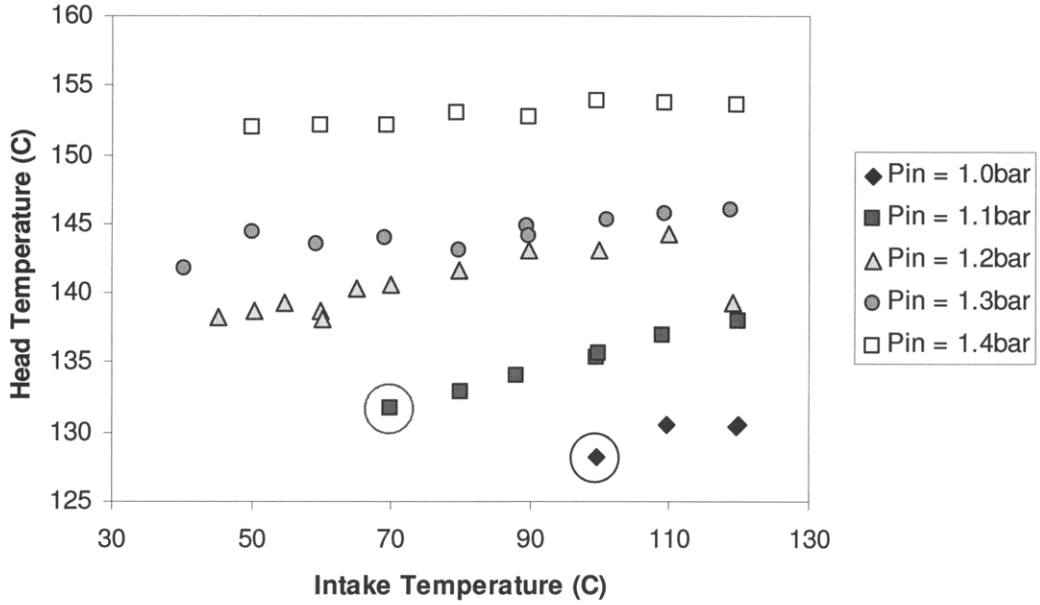


**Figure 3.9.** Head Temperature vs. Intake Temperature for Five Boost Pressures. Valve timing was fixed as depicted in Figure 3.3. Two points at the misfire limit are circled.

NIMEP is plotted against PRRmax in Figure 3.10 to illustrate the effects of intake temperature and boost.

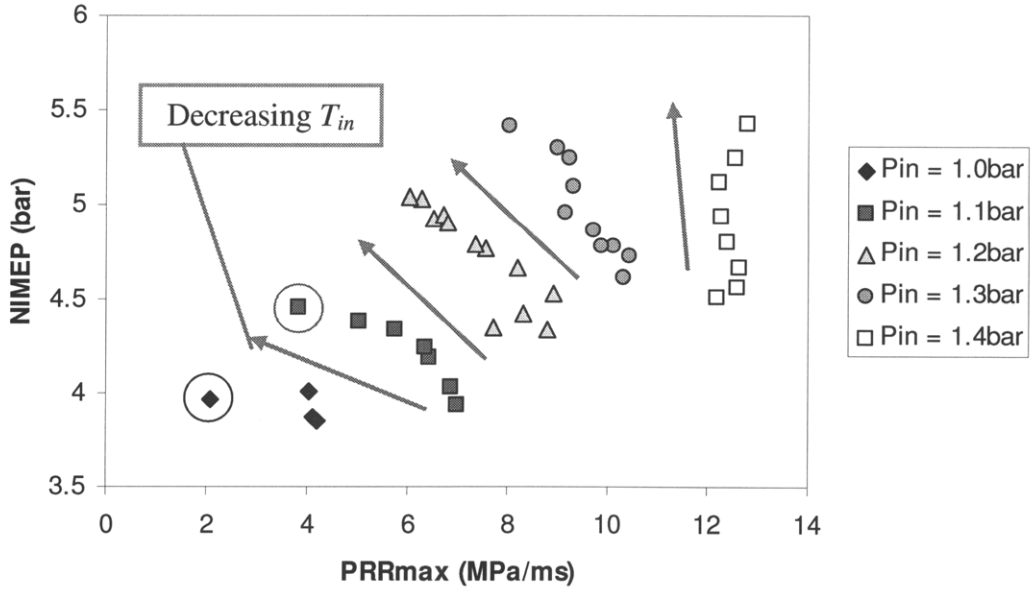


**Figure 3.10.** NIMEP vs. $PRR_{max}$ for Five Boost Pressures. Valve timing was fixed as depicted in Figure 3.3. Two points at the misfire limit are circled.

As intake temperature is decreased, load increases and the pressure rise rate decreases showing that low intake temperature is favorable for abating knock. Misfire limits the maximum load at low boost. The optimal condition to maximize IMEP appears to be boosting and heating the intake only enough to avoid misfire.

## 3.3 Valve Timing Effects

The valve timings were varied in three different ways to affect combustion. First, the negative valve overlap (NVO) defined as advancing EVC timing and retarding IVO timing symmetric about TDC was varied to change the amount of trapped residual gas. Next, the IVC timing was varied to vary the pressure at the end of compression. Third, the EVO timing was varied, which appeared to vary both residual fraction and residual temperature. While there is a wide variety of ways to vary the valve timing, these were selected because they are simple and because it was anticipated that their effects would be simply understood.

### 3.3.1 Negative Valve Overlap (NVO) Effects

Data were acquired for negative valve overlap sweeps for three intake temperatures and four boost pressures per intake temperature. The intake temperature was set to 60°C, 90°C, and 120°C, and the pressure was incremented by 0.1bar starting at the lowest pressure that would run stably per intake temperature. The valve timing was set as noted in Table 3.2 and as depicted in Figure 3.11.

**Table 3.2.** NVO Sweep Valve Timings

| Valve Operation | Timing |
|---|---|
| IVC | 20° ABC |
| EVO | 30° BBC |
| EVC | 70° to 108° BTC |
| IVO | 70° to 108° ATC |

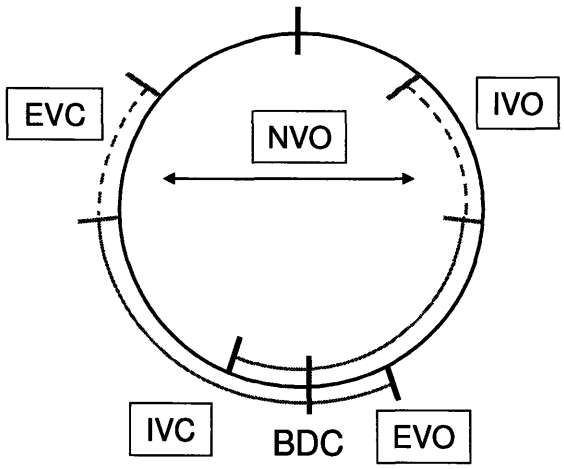


**Figure 3.11.** Diagram of valve timings for the NVO Sweeps

The EVC retard was limited by severe engine knock, and EVC advance was limited by a hardware constraint that limited the minimum valve duration time. Under particular conditions, both advance and retard were limited by misfire.

The primary effect of varying the degree of negative valve overlap was varying residual fraction, and this effect is shown in Figure 3.12 in which all of the NVO data is presented together. For all sweeps, the residual fraction ranges from approximately 30% at an EVC timing of 70° BTC to approximately 55% at 108° BTC. This shows that NVO is an effective means of varying the amount of trapped residual gas and therefore the residual gas fraction. It is also clear that while boost does result in small changes in residual fraction, as shown clearly in Figure 3.5, varying EVC timing has a considerably larger effect.

The first consequence of varying the trapped residual is that the amount of air inducted varies inversely. Because the equivalence ratio is held stoichiometric, the amount of fuel varies with the amount of air. Fuel mass per cycle is plotted against EVC timing with the intake temperature set to 120°C in Figure 3.13. Fueling decreases as EVC timing is advanced, and fueling increases as boost pressure is increased. As EVC timing is advanced, more residual gas is trapped thus less air and fuel are inducted.

A secondary effect of varying the valve timing is that by changing the fuel rate, the exhaust temperature changes which leads to variations in the temperature of the residual gas. Figure 3.14 features the temperature of the trapped charge at IVO versus the residual gas fraction with the intake temperature set to 120°C. Misfire limit points are circled. As residual gas is increased by advancing EVC timing, the temperature of the residual gas drops because the less fuel is burned and the exhaust is cooled. More fuel is burned at higher boost pressures so the temperature of the residual gas increases with boost.

This trade off is the reason for misfire limits both at high residual gas levels as well as at low residual gas levels. The curve at $P_{in}$ = 1.0bar features both of these misfire limits. At high levels of residual the charge temperature at the end of compression is low because the residual gas temperature is low, and at low levels of residual gas, the fraction of residual is too low to effectively heat the fuel and air to autoignition temperature.

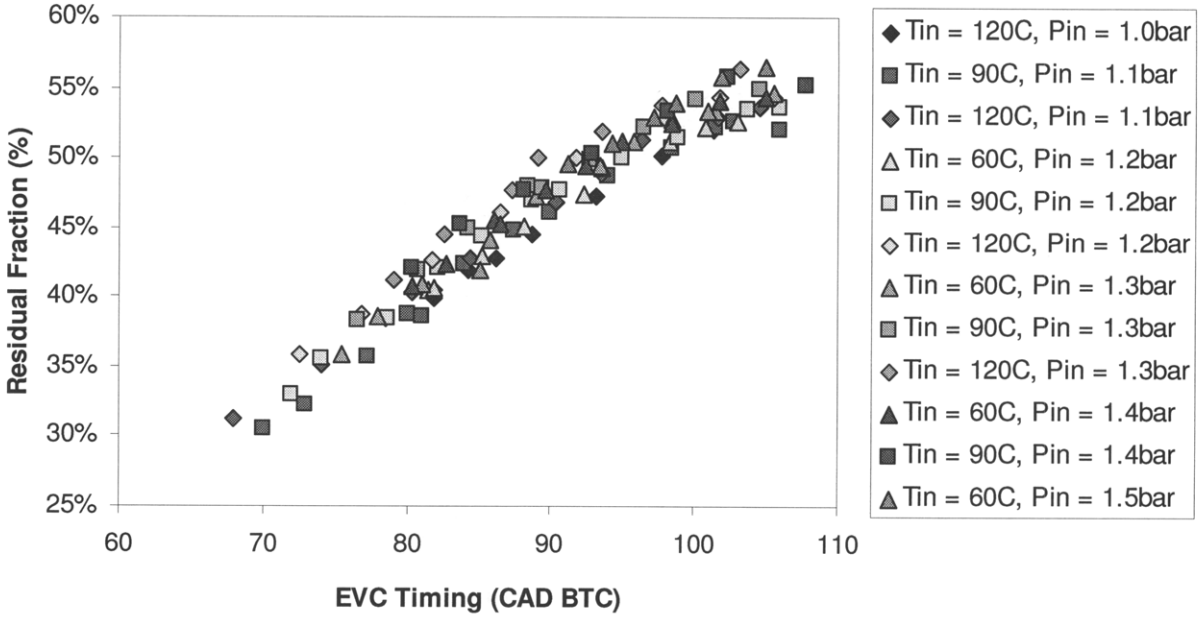


**Figure 3.12.** Residual Gas Fraction vs. EVC Timing. $T_{in}$ = 60°C, 90°C, 120°C; $P_{in}$ = 1.0bar – 1.5bar.

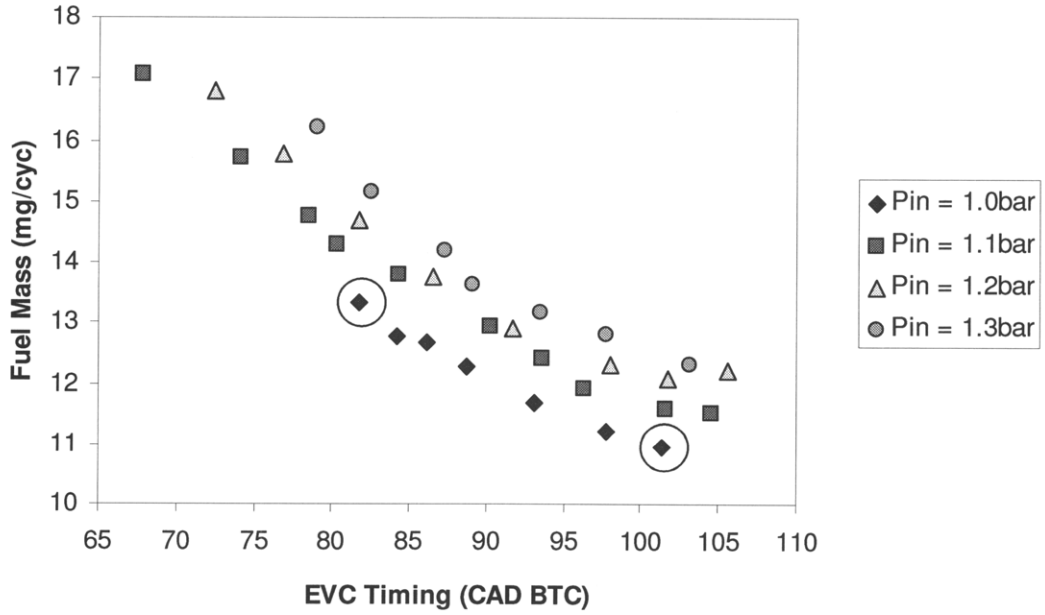


**Figure 3.13.** Fuel Mass per Cycle vs. EVC Timing. $T_{in}$ = 120°C. Misfire limits are circled.

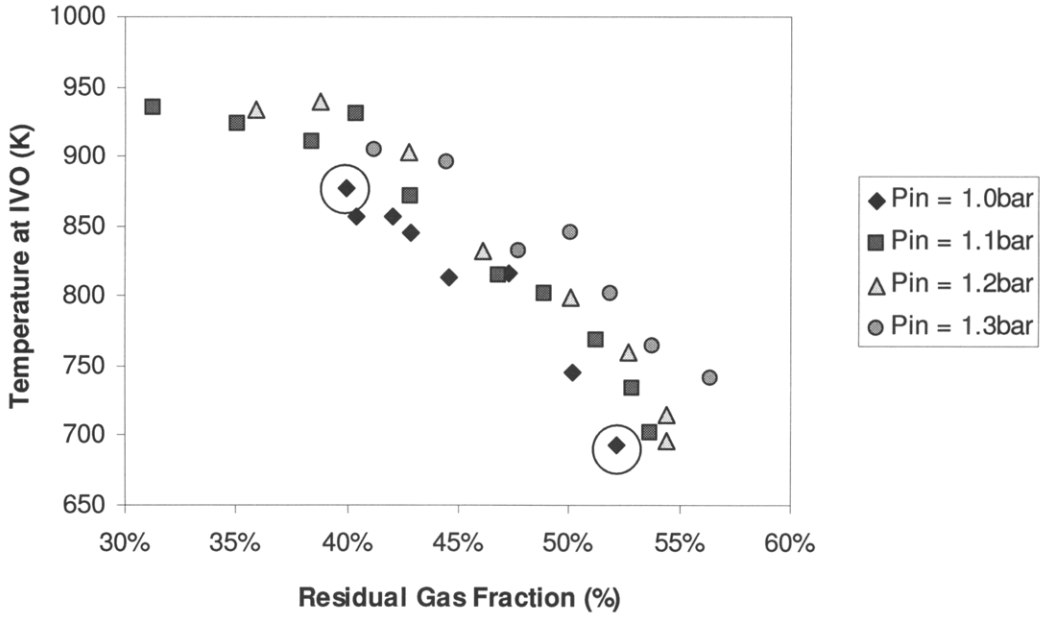


**Figure 3.14.** Temperature at IVO vs. Residual Gas Fraction. $T_{in}$ = 120°C. Misfire limits are circled.

Figure 3.15 shows the temperature at the end of compression, 15° BTC, plotted against residual gas fraction for 120°C intake air temperature data. The temperature features a maximum at mid-range residual fractions and decreases at low and high residual fraction for $P_{in}$ = 1.0bar, 1.1bar, and 1.2bar, illustrating the competing effects of residual gas temperature and residual gas fraction. This is not observed at $P_{in}$ = 1.3bar because this curve, along with $P_{in}$ = 1.1bar and 1.2bar were limited by severe engine knock. Data was not generated for residual fractions lower than those presented. Boost is shown again to increase charge temperature.

Figure 3.16 and Figure 3.17 also feature temperature at 15° BTC versus residual fraction but show curves for $T_{in}$ = 90°C and $T_{in}$ = 60°C, respectively. First, note that the charge temperature ranges spanned by the conditions presented are roughly the same for each of the three intake temperatures. Next, the charge temperature curves at $T_{in}$ = 60°C and 90°C also feature the behavior where they peak at mid-range residual fraction and dip at high or low levels of residuals unless limited by misfire or knock.

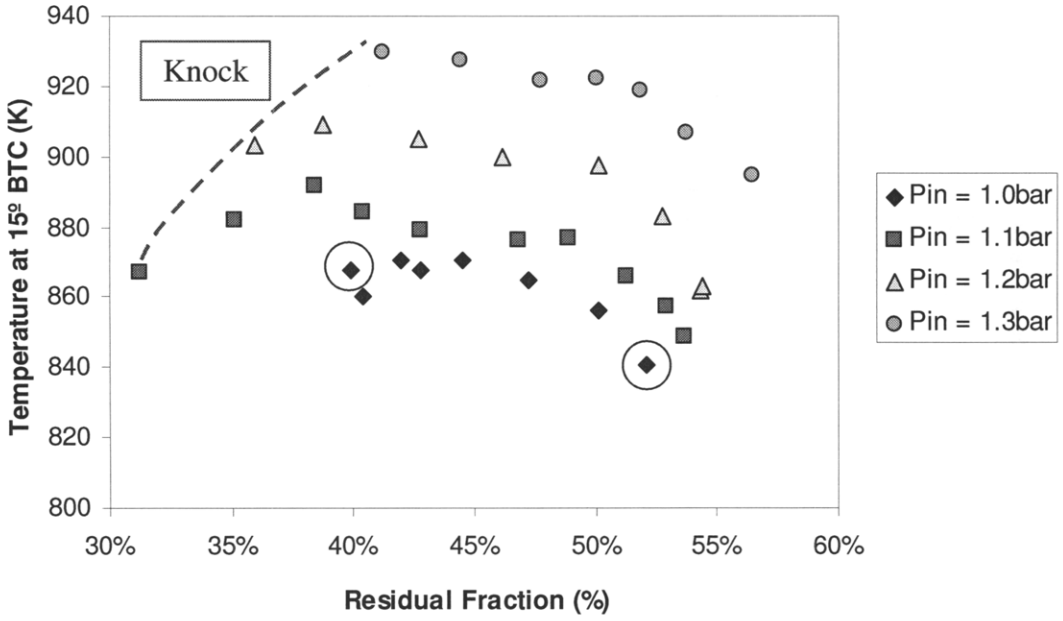


**Figure 3.15.** Temperature at 15° BTC vs. Residual Fraction. $T_{in}$ = 120°C. Misfire limits are circled.

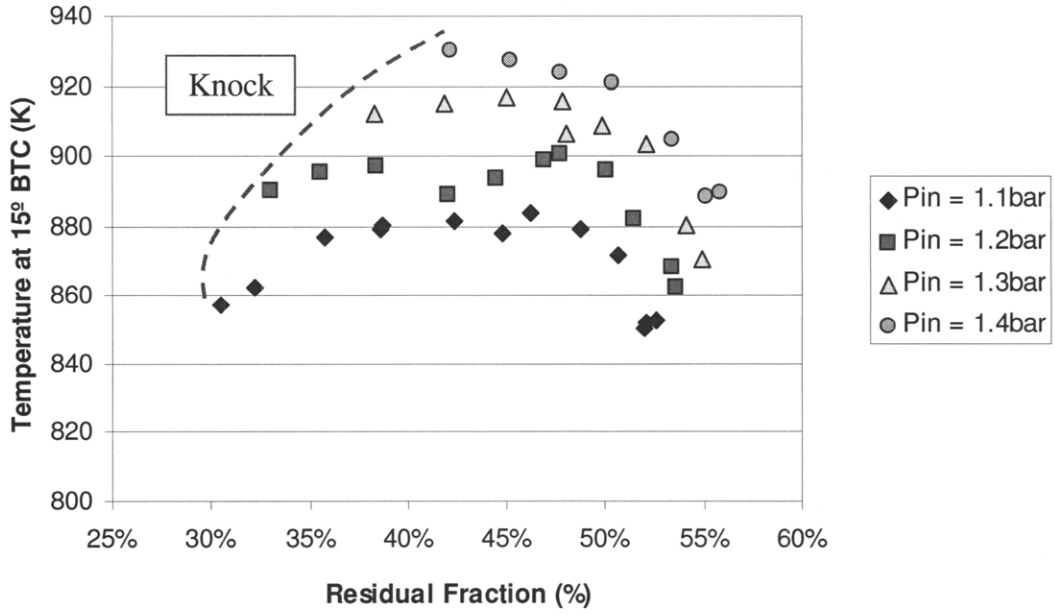


**Figure 3.16.** Temperature at 15° BTC vs. Residual Fraction. $T_{in}$ = 90°C.

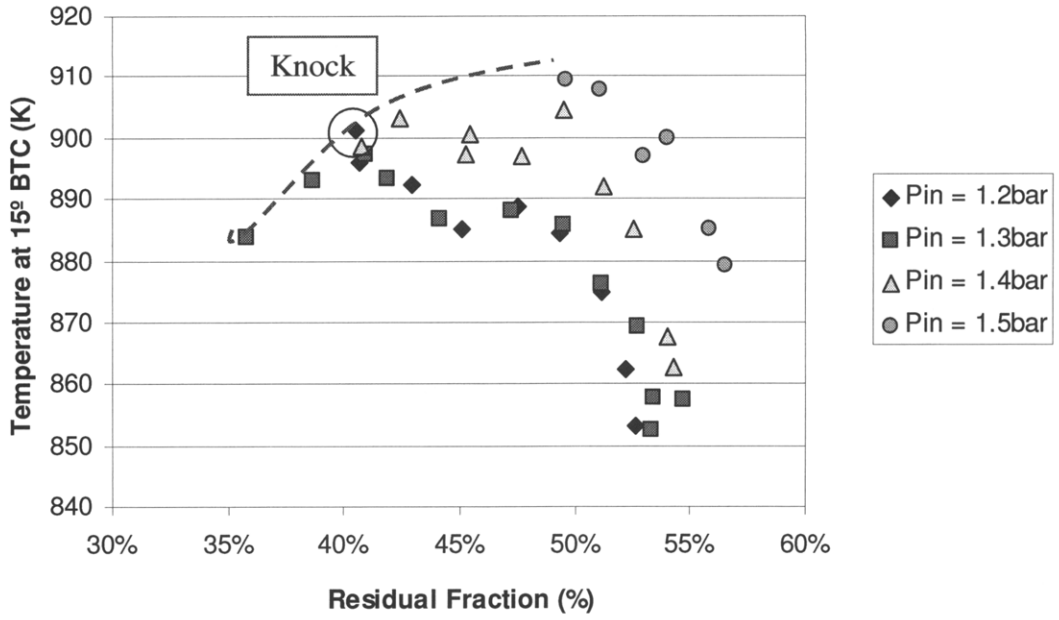


**Figure 3.17.** Temperature at 15º BTC vs. Residual Fraction. $T_{in}$ = 60ºC. Misfire limits are circled.

Given how NVO and boost pressure affect the state and composition of the charge, these properties can now be used to explore how the load, maximum rate of pressure rise, and efficiency change within the operating regime. Figure 3.18 features NIMEP and $PRR_{max}$ shown in a contour map on a space of oxygen mole fraction and intake pressure. Oxygen mole fraction is shown instead of residual gas fraction because oxygen concentration determines the reactivity of the mixture more than the degree of dilution and because fuel is proportional to oxygen concentration since the equivalence ratio is stoichiometric. Oxygen mole fraction varies with residual fraction simply as in Equation 3.2. The equation is written as an approximation because the mole fraction of fuel is neglected.

$$x_{O_2} \approx \frac{1 - x_{residual}}{0.2} \tag{3.2}$$

Figure 3.18 shows that both NIMEP and $PRR_{max}$ increase as intake pressure is increased and as oxygen mole fraction is increased. NIMEP ranges from 3.5bar to 5.0bar, and $PRR_{max}$ ranges from less than 2MPa/ms to 11MPa/ms. Comparing one to the other, $PRR_{max}$ increases more with pressure than NIMEP does and less with oxygen concentration than NIMEP does. The high load limit, defined as the highest NIMEP at a given $PRR_{max}$, is achieved at high oxygen concentration and at low pressure. This conclusion implies it is better to operate the engine with low or no boost and low trapped residuals than at high boost with high trapped residuals. This is because

boosting causes charge temperatures to increase. This exacerbates knock but does not increase load. It is observed that the contours of $PRR_{max}$ are steeper than those of NIMEP. A significant consequence of this observation is that the high load limit always occurs at the misfire limit.

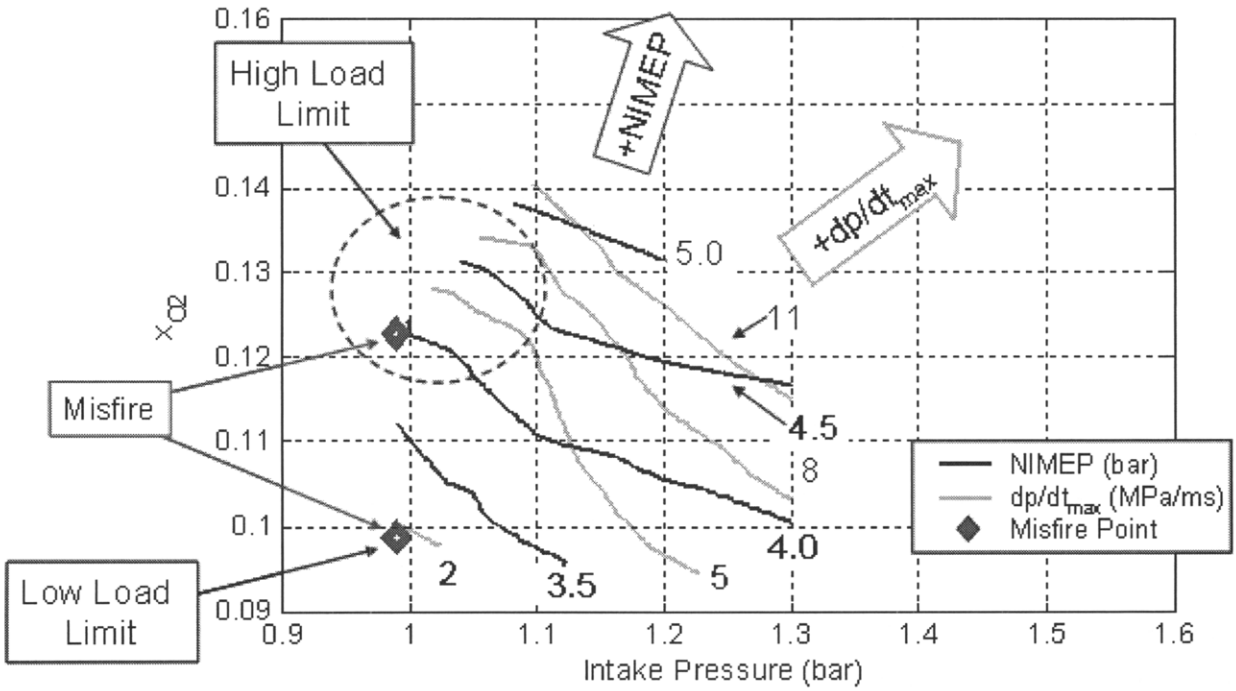


**Figure 3.18.** NIMEP and $PRR_{max}$ Contoured on Oxygen Mole Fraction and Intake Pressure; $T_{in}$ = 120°C. Misfire points are marked as diamonds.

The misfire limit encompasses two behaviors. The red diamonds represent points in a particular sweep just before the engine misfired. The point at (1.0bar, 0.12) forms a high-load limit. Here, the engine is set to a particular intake temperature and boost, and the amount of trapped residual gas is reduced via decreased NVO such that at some point, the charge is too cold to initiate combustion. The temperature is the limiting factor since the pressure is constant and the oxygen and fuel are increasing. This is termed a "high load limit" since fuel and therefore NIMEP are increasing through the sweep. Note how the oxygen fraction limit increases substantially with only a very modest increase in boost pressure. Boost is therefore an effective means of avoiding misfire.

The low load limit is formed on the left by a minimum pressure and on the bottom of the plot by a minimum oxygen fraction. If the fuel rate is reduced sufficiently, the temperature of the trapped residuals drops to be too cold to initiate combustion, as illustrated in Figure 3.14. This is the case for the red diamond at (1.0bar, 0.1).

The contour map in Figure 3.18, which shows data taken at $T_{in}$ = 120°C, is reprinted with similar maps showing data taken at $T_{in}$ = 90°C and $T_{in}$ = 60°C in Figure 3.19. The operating range shifts to higher boost pressures to compensate for decreased intake temperatures. The high load limit occurs at high oxygen concentration and low boost at the misfire limit in each contour map. Comparison of one contour map to the other indicate that the highest load for a given $PRR_{max}$ occurs at the lowest intake temperature, consistent with the intake temperature sweep data shown in Figure 3.10. This is because at low intake temperature, the reaction rates are slower, mitigating pressure rise rate but the charge density is higher allowing more fuel and air.

The contour plots of CA10, presented in Figure 3.20, show that combustion phasing is strongly affected by intake air temperature and boost pressure but not significantly by oxygen fraction. The effect of intake temperature on phasing, noted in Section 3.2 and in Figure 3.6, is to advance combustion with increased heating. The first charge to self-ignite reaches suitable temperatures for fast reactions sooner in the engine cycle. Increasing boost pressure, as noted earlier, directly increases reaction rates, increases concentrations of air and fuel, and causes an increase in temperature. All three factors result in earlier combustion.

What is less intuitive is the weak dependence of phasing on oxygen fraction, except near the high-load misfire limit. In the map of $T_{in}$ = 120°C data, for example, there appears to be almost no dependence on oxygen fraction. Figure 3.15, Figure 3.16, and Figure 3.17 show that, especially at high intake air temperature, there is weak dependence of charge temperature on EVC timing. The amount of residual fraction and the temperature of the residual gas do seem to compensate for one another to keep the compression temperature relatively constant, and this effect results in keeping combustion from phasing significantly with the degree of trapped residual. At high and low residual fraction levels, Figure 3.15 does show that the compression temperature drops off its plateau, and so combustion phases later allowing misfire to eventually occur.

Indicated efficiency, shown in the contour maps in Figure 3.21, appears to be a strong function of intake air temperature but less affected by oxygen concentration and boost. The average efficiency on the maps are approximately 34% at $T_{in}$ = 60°C, 32% at $T_{in}$ = 90°C, and 29% at 120°C. On the 90°C and 120°C, variations across the map are limited to 1-2%. On the 60°C contour map, the efficiency ranges from 32% to 40% in one spot. Efficiency is, in part, a function of combustion phasing, and this accounts for the local maximum in each map.

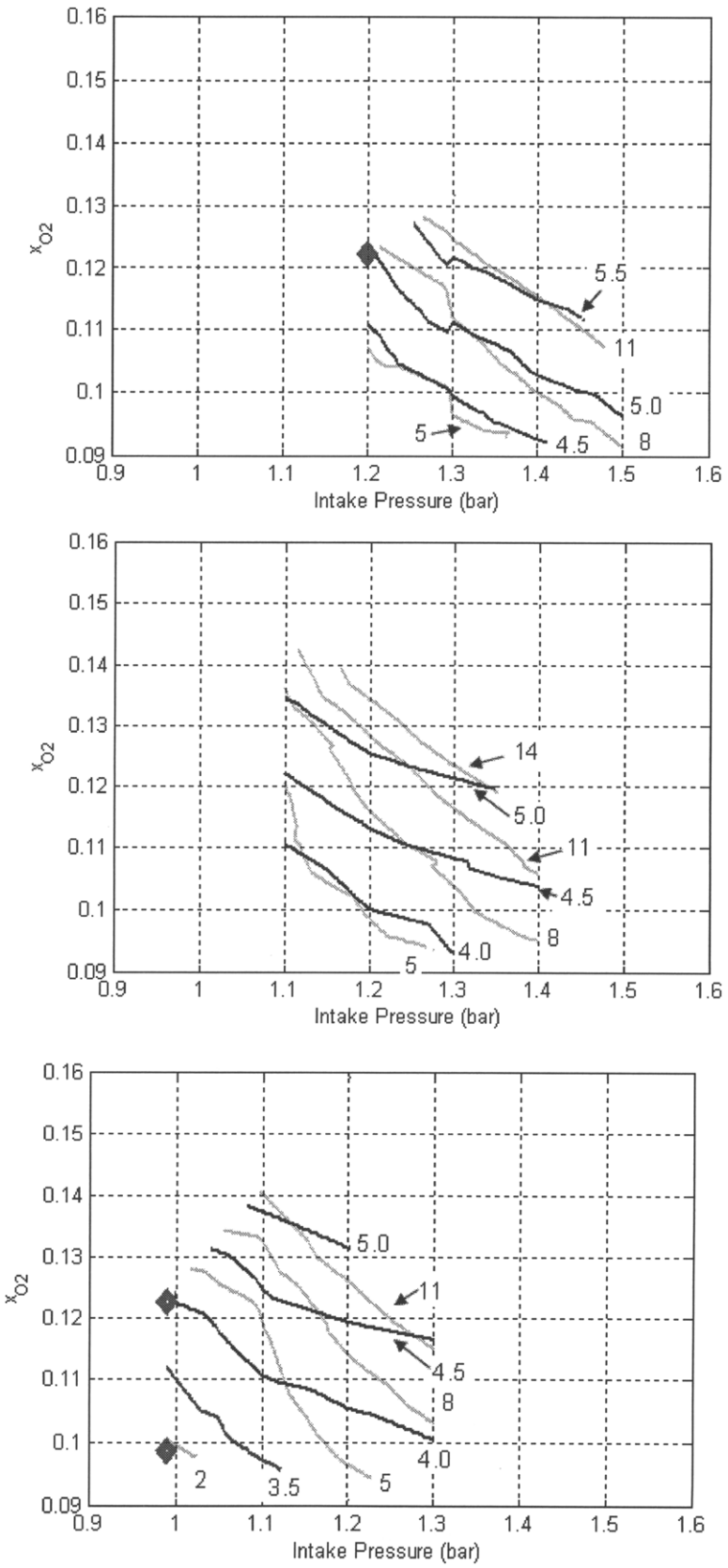


**Figure 3.19.** NIMEP and PRRmax Contoured on Oxygen Mole Fraction and Intake Pressure; $T_{in}$ = 60ºC (top), $T_{in}$ = 90ºC (middle), $T_{in}$ = 120ºC (bottom). Misfire points are marked in as diamonds.

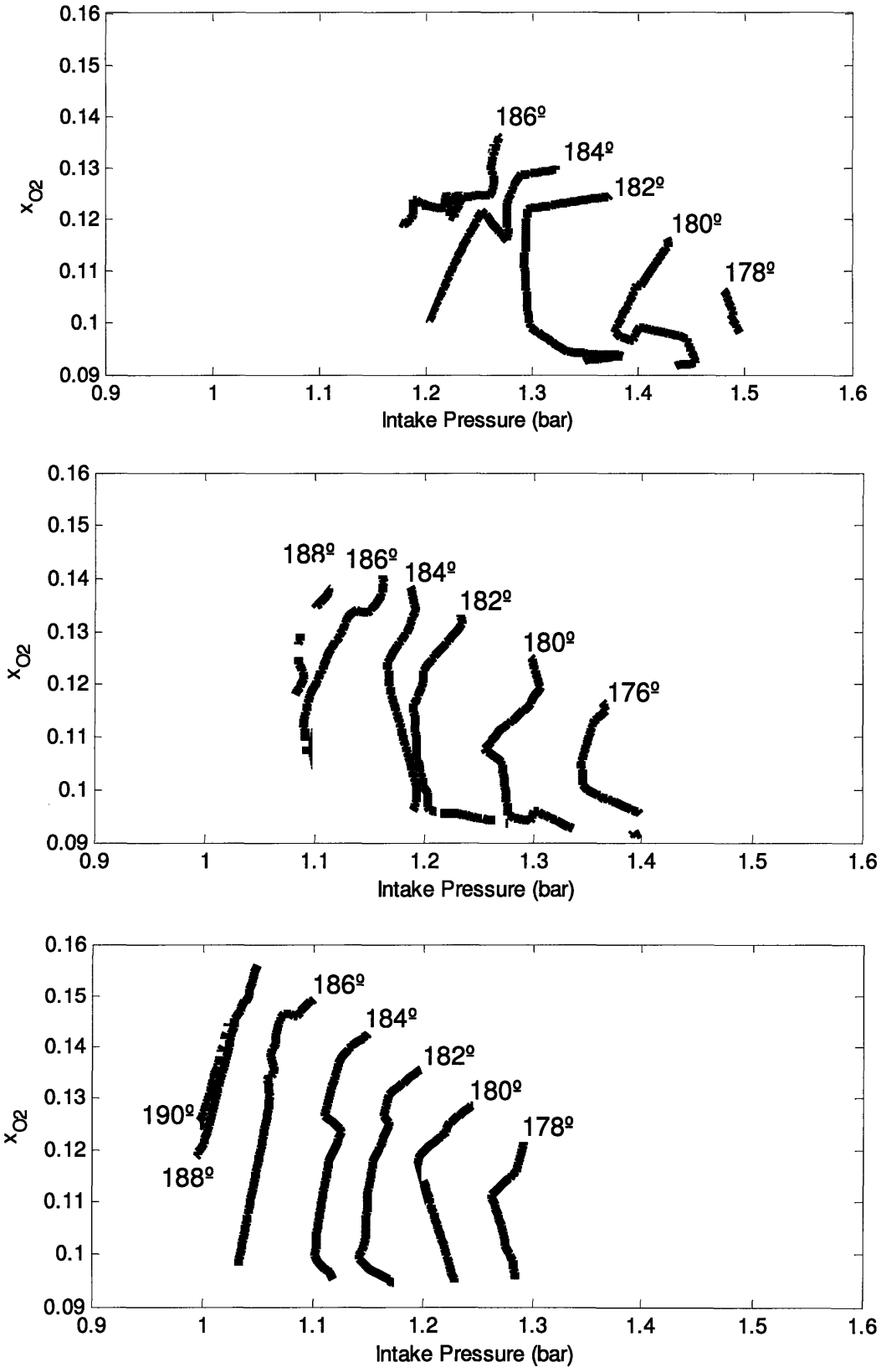


**Figure 3.20.** CA10 Contoured on Oxygen Mole Fraction and Intake Pressure; $T_{in}$ = 60°C (top), $T_{in}$ = 90°C (middle), $T_{in}$ = 120°C (bottom)

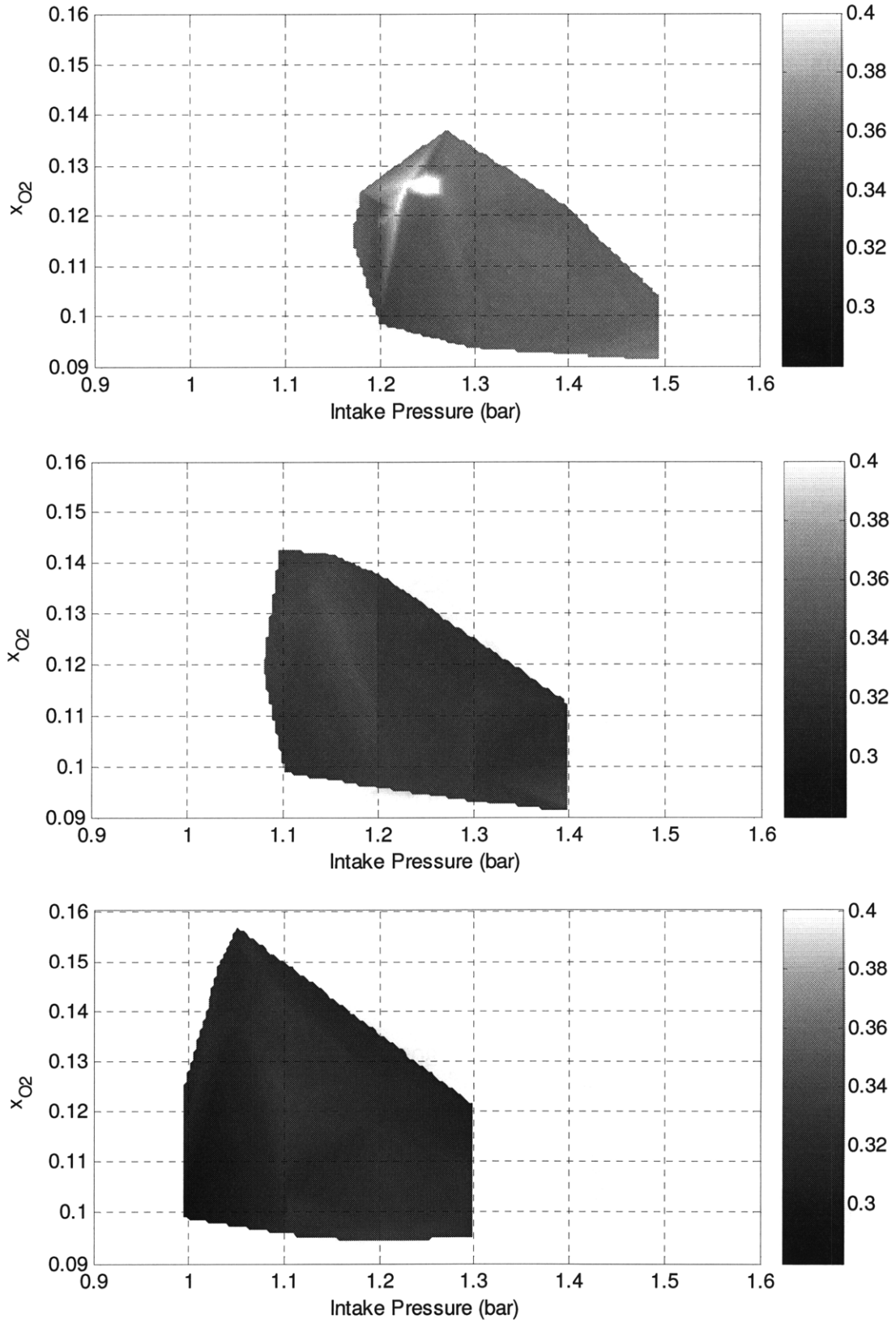


**Figure 3.21.** Indicated Efficiency Contoured on Oxygen Mole Fraction and Intake Pressure; $T_{in}$ = 60°C (top), $T_{in}$ = 90°C (middle), $T_{in}$ = 120°C (bottom).

### 3.3.2 High-Load Misfire Limit with NVO and Without EGR

In Section 3.2 and Section 3.3.1, the effects of NVO, intake temperature, and boost pressure were explored, and high load misfire limits were observed under various conditions. This section will introduce new data varying these parameters but focused to describe the high-load misfire boundary.

Two high-load misfire limits were observed: one associated with decreased trapped residuals and the other with decreased intake temperature. The load increases as the amount of trapped residuals is decreased, and this also reduces the charge temperature, which can lead to misfire. Figure 3.13, reproduced here in Figure 3.22, shows fuel mass per cycle versus EVC timing for NVO sweeps at four boost pressures. $P_{out}$ is held equal to $P_{in}$ as before. Intake temperature is set to 120°C. For the $P_{in}$ = 1.0bar sweep, as the residual fraction is decreased with retarded EVC timing, the fuel mass increases until misfire. Pressure is almost constant. Equivalence ratio is constant. Oxygen fraction is increasing, so the misfire is caused only by a temperature decrease due to lower trapped residual gas fraction.

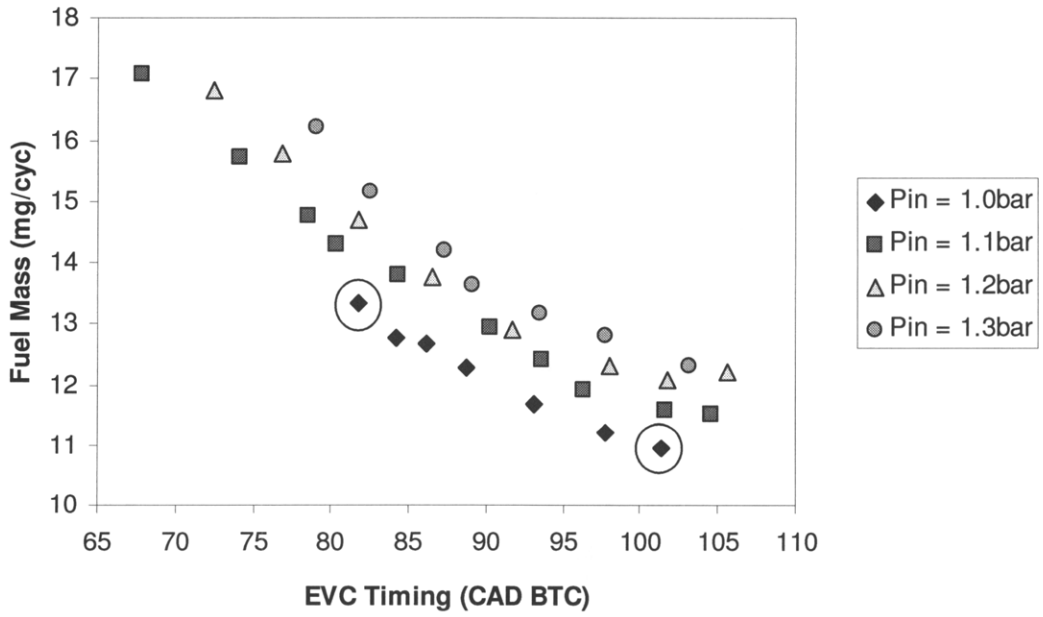


**Figure 3.22.** Fuel Mass vs. EVC Timing. $T_{in}$ = 120°C. Misfire points are circled. (Reproduced from Figure 3.13.)

The second observed high load limit occurs when intake temperature is reduced until charge temperature is insufficient for ignition. At the same time, charge density is increased which causes load to increase. Figure 3.23 shows NIMEP vs. intake temperature for five intake temperature sweeps, and misfire is observed at the two lowest pressures.

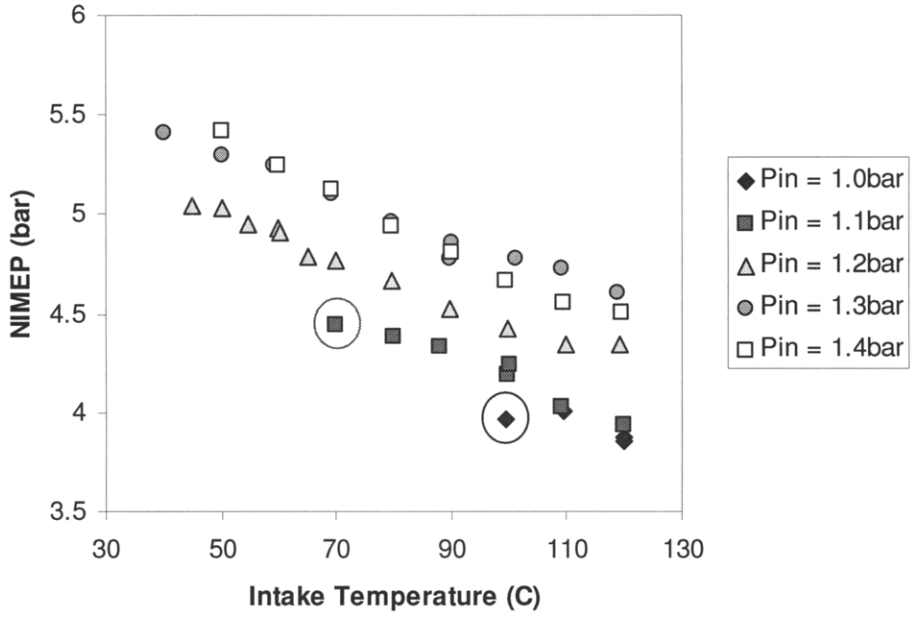


**Figure 3.23.** NIMEP vs. Intake Temperature for Five Intake Pressures. Misfire points are circled.

Data was acquired to explore the boundary of stable operation at the high load limit. The intake pressure and temperature were set with a valve timing that yielded stable combustion. The EVC timing was then retarded until trapped residuals provided insufficient thermal energy to sustain combustion. Figure 3.24 shows the conditions for the data points of the set.

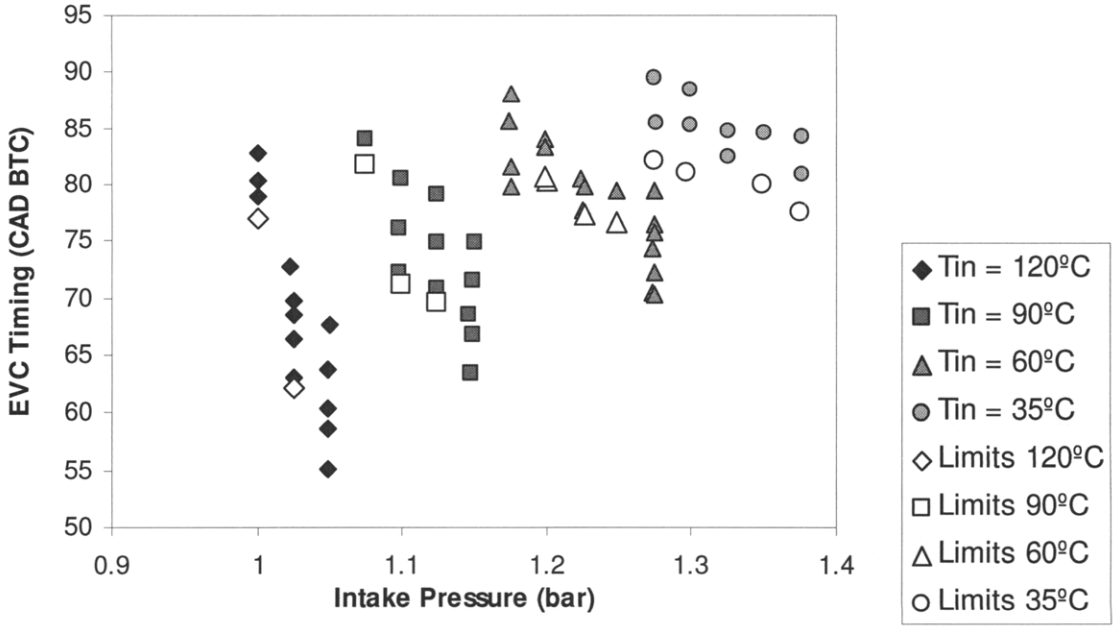


**Figure 3.24.** EVC Timing vs. Intake Pressure for Four Intake Temperatures. Misfire points are marked in open symbols.

EVC timing is plotted against intake pressure, and intake temperature is shown by colored symbols. Note the sensitivity to intake pressure, which is incremented by 25mbar. Open symbols indicate conditions where misfire occurred when EVC was retarded past this point. For each temperature, when boost is increased past a certain threshold, misfire did not occur at all. Misfire was defined as when the engine died. Figure 3.4 shows that compression temperature rises significantly with boost, and Figure 3.5 shows that residual fraction also increases with boost. This added thermal energy caused combustion to occur robustly even when EVC timing is highly retarded. Another phenomenon was that under low residuals and high boost, the engine might produce a very low NIMEP in a cycle but restart robustly on the next cycle.

Figure 3.25 features burned gas fraction versus pressure at 15° BTC. For a given intake pressure and temperature, as burned gas fraction is reduced, the engine eventually misfires. As pressure is reduced from a stable point, the engine also misfires.

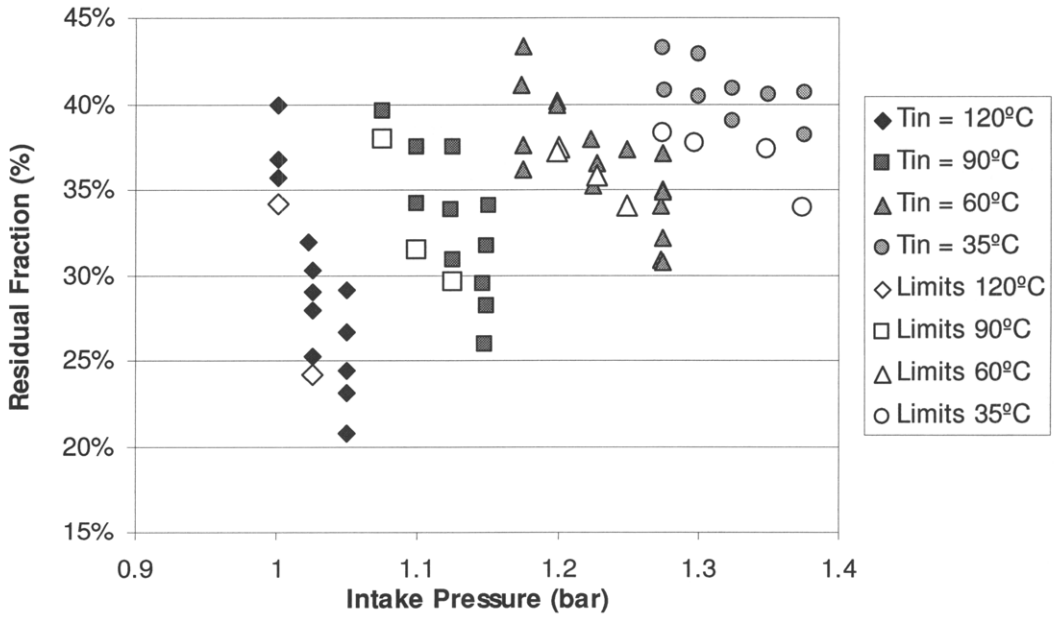


**Figure 3.25.** Residual Fraction vs. Pressure at 15° BTC. Misfire points marked in open symbols.

Another feature is that the sensitivity to residual fraction increases as intake temperature decreases. At 120ºC, residual fraction drops from 34% to 24% when intake pressure is increased from 13.6bar to 14.4bar. However, when $T_{in}$ = 35ºC, residual fraction is reduced from 38% to only 34% when pressure at 15° BTC is increased by 1.7bar. This is attributed to the effect that boosting the engine causes the temperature of the residual gas to increase.

Trade-offs between intake temperature and residual fraction might imply that the charge temperature takes into account both effects and serves as a critical factor determining misfire. As shown in Figure 3.26, the temperature at 15° BTC is plotted against the pressure at 15° BTC. Bulk temperature does not form a clear threshold with pressure. It cannot be used as a good metric for ignition delay, at least for this data set. The reason why this might be is because ignition depends on the temperature of the hottest parcel of gas in the charge, not the average temperature of the gas. If the hottest and the average were to correlate, then the thermal stratification of the charge would have to be consistent across the data set. This is unlikely since the thermal stratification depends on the difference in temperature between the intake air and the trapped residual and on the fraction of intake air versus the residual fraction. Increasing intake pressure may also have the effect of increasing the Reynolds number and therefore increasing mixing. Another reason why temperature is a difficult metric to use is because of its strong pressure dependence. A modest pressure increase causes a significant temperature increase via increased heat transfer between the charge and the walls. The correlation in Figure 3.26 implies a degree of causation. The issue of the accuracy of the temperature estimate is also relevant. The temperature at 15 ° BTC variation across this data set is only 10%, and variations for a fixed pressure are much smaller.

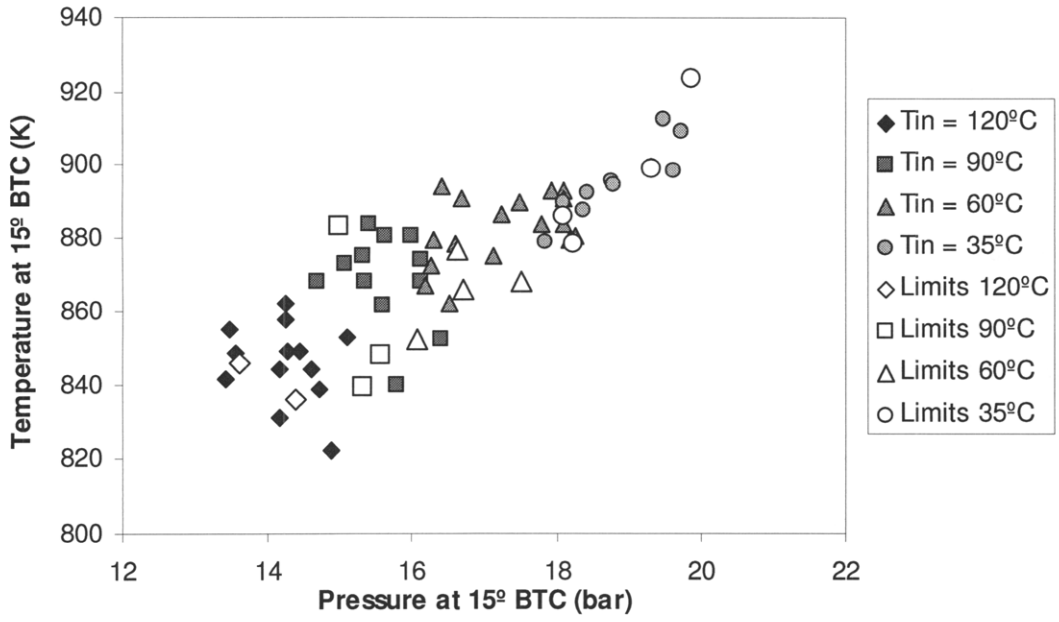


**Figure 3.26.** Temperature at 15° BTC vs. Pressure at 15° BTC. Misfire Points are marked as open symbols.

Combustion phasing, CA10, depends strongly on when the first parcel of gas burns, and whether or not combustion occurs at all depends on the first parcel of gas as well. It is intuitive that there is a relationship between CA10 and the misfire limit. CA10 and pressure at the end of compression for the misfire limit are shown in Figure 3.27.

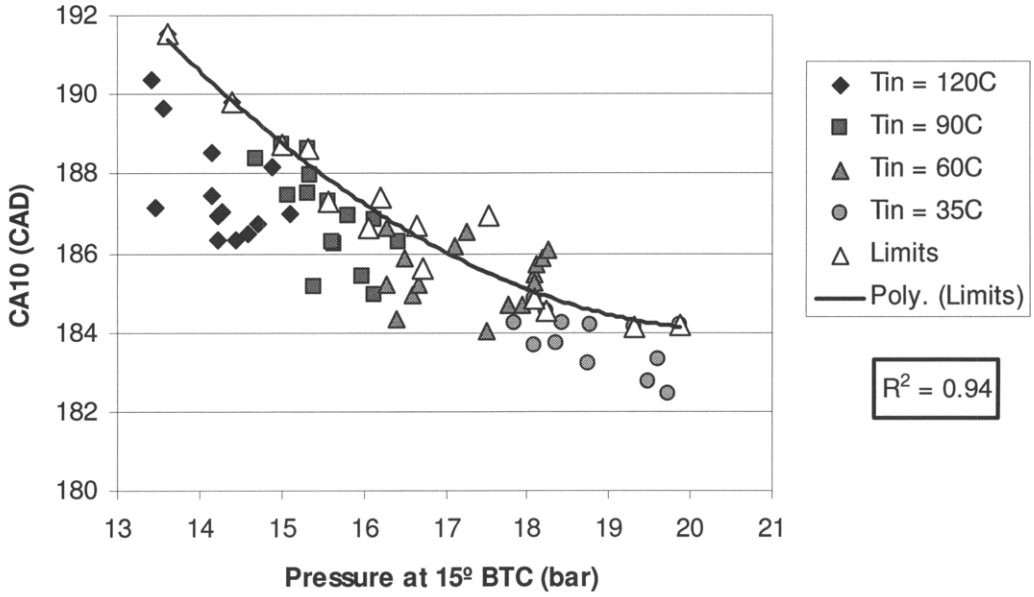


**Figure 3.27.** CA10 vs. Pressure at 15° BTC. Misfire points are marked in open triangles.

A clear trend emerges where the misfire limit occurs at the latest phasing for a given pressure. A quadratic fit relates CA10 to pressure at 15° BTC with an $R^2$ of 94% so this indicates that they depend on the same phenomena. At the misfire curve, on the left side of Figure 3.27, the pressure is low; the intake temperature is high, and the residual fraction is high. On the right side of the misfire curve, the pressure is high; the intake temperature is low, and the residual fraction is low. Ignition delay has been described as a function of pressure and temperature, and they trade off to determine the combustion phasing just before misfire. The Livengood-Wu knock integral is reprinted here to illustrate how delay depends on both pressure and temperature. Showing CA10 vs. pressure tells only part of the story, but the understanding of the system is limited since the temperature history of the hottest parcel of gas in the charge is not known.

$$\tau \propto a_1 P^{a_2} \exp\left(\frac{-E_A}{RT}\right) \tag{1.11}$$

$$\frac{[x_p]}{[x_p]_c} = \int_{t=0}^{t=t_c} \frac{1}{\tau} dt = 1.0 \tag{1.12}$$

The misfire criterion based on CA10 is revealed to be quite robust for the NVO data without EGR, as shown in Figure 3.28. CA10 is plotted against pressure at the end of compression.

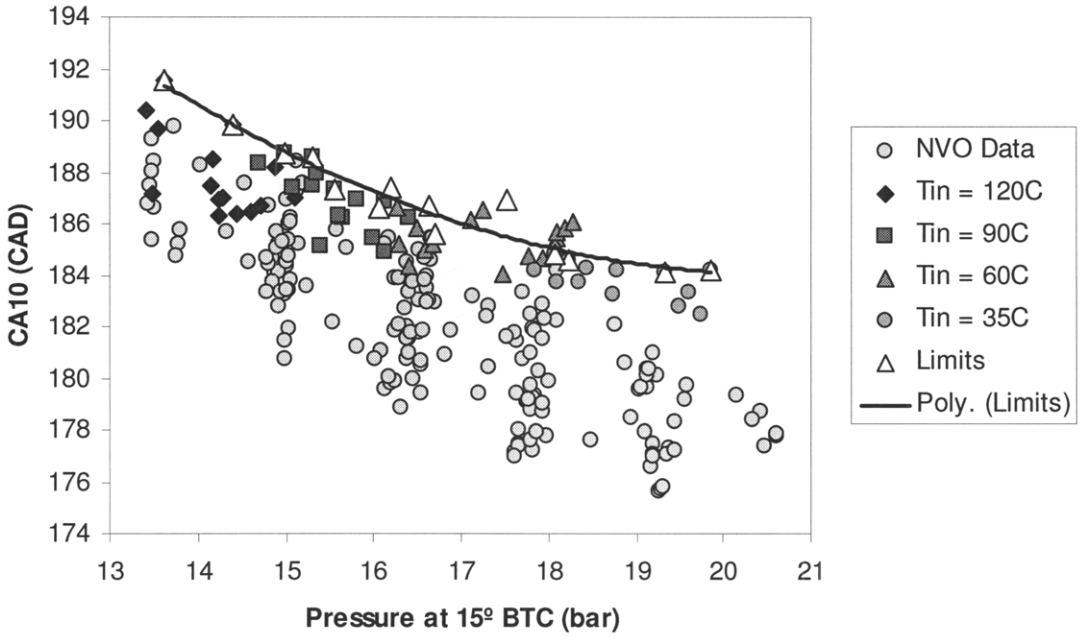


**Figure 3.28.** CA10 vs. Pressure at 15 BTC for Misfire Data: Limit Points, Four Intake Temperatures near the Limit, and NVO Data, IVO, and EVC data from 3.3.1, 3.3.4, and 3.3.5.

The data from this study is shown. The data presented also includes the data from Sections 3.3.1, 3.3.4, and 3.3.5 including full NVO sweeps at three intake temperatures and four pressures, intake temperature sweeps, IVO sweeps, and EVC sweeps. The misfire curve is not passed by any of the data from the previous set.

Ideally, a formula can be developed to predict misfire. Relationships between various parameters will be explored here to understand the misfire behavior of the engine. Empirical formulas will be presented to show engine behavior; however, they may not be accurate enough to be predictive.

To start, a strong correlation was observed between CA10 and $P_{15BTC}$. A non-linear optimization technique was used to develop a correlation between them. For the misfire limit, the relationship was as stated in Equation 3.3, and the correlation is shown in Figure 3.29.

$$\tau_{ig} = 33.3 \cdot P_{15BTC}^{-0.93} \tag{3.3}$$

Here, CA10 is written as an ignition delay after 165° ABC divided by engine speed to put the metric into milliseconds, as in Equation 3.4.

$$\tau_{ig} = \frac{CA10 - 165}{(engine\_speed)}[ms] \tag{3.4}$$

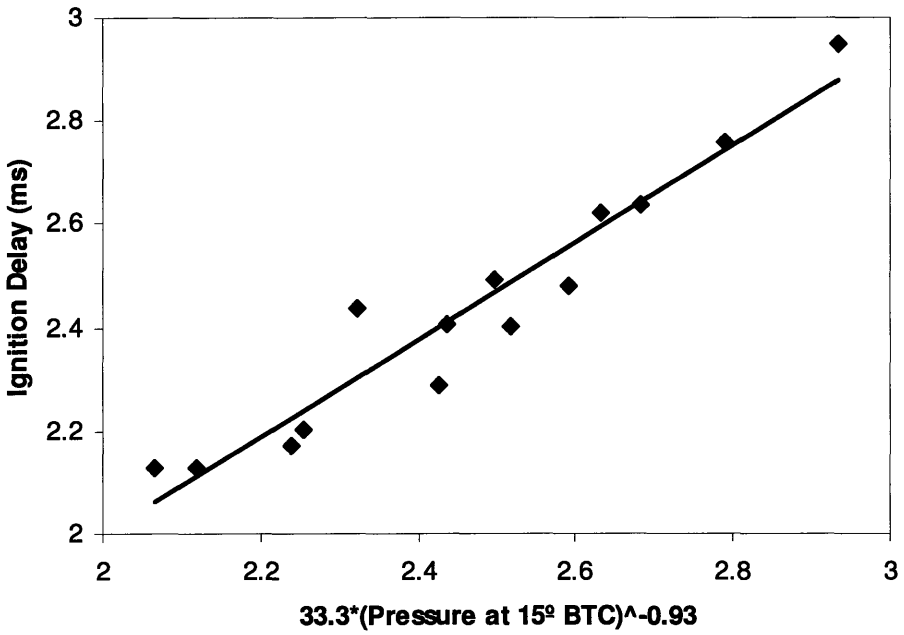


**Figure 3.29.** $\tau_{ig}$ vs. $33.3*P_{15BTC}^{-0.93}$, which is the correlation in Equation 3.3. $R^2 = 93\%$.

A threshold parameter $\beta$ is defined as a metric to indicate whether misfire will occur or not. The left side of Equation 3.3 is divided by the right so that this new function, stated in Equation 3.5, equals 1 at the misfire limit.

$$\beta_\tau = 0.03 \cdot \tau_{ig} \cdot P_{15BTC}^{0.93} \tag{3.5}$$

If $\beta$ is larger than one, then misfire is likely, and if $\beta$ is less then one, stable combustion is expected. $\beta_\tau$ was then calculated for the misfire points, the points of this data set near the misfire limit, and the earlier data set of NVO sweeps, and these are all shown in Figure 3.30. This plot shows that $\beta_\tau$ serves as an effective threshold parameter.

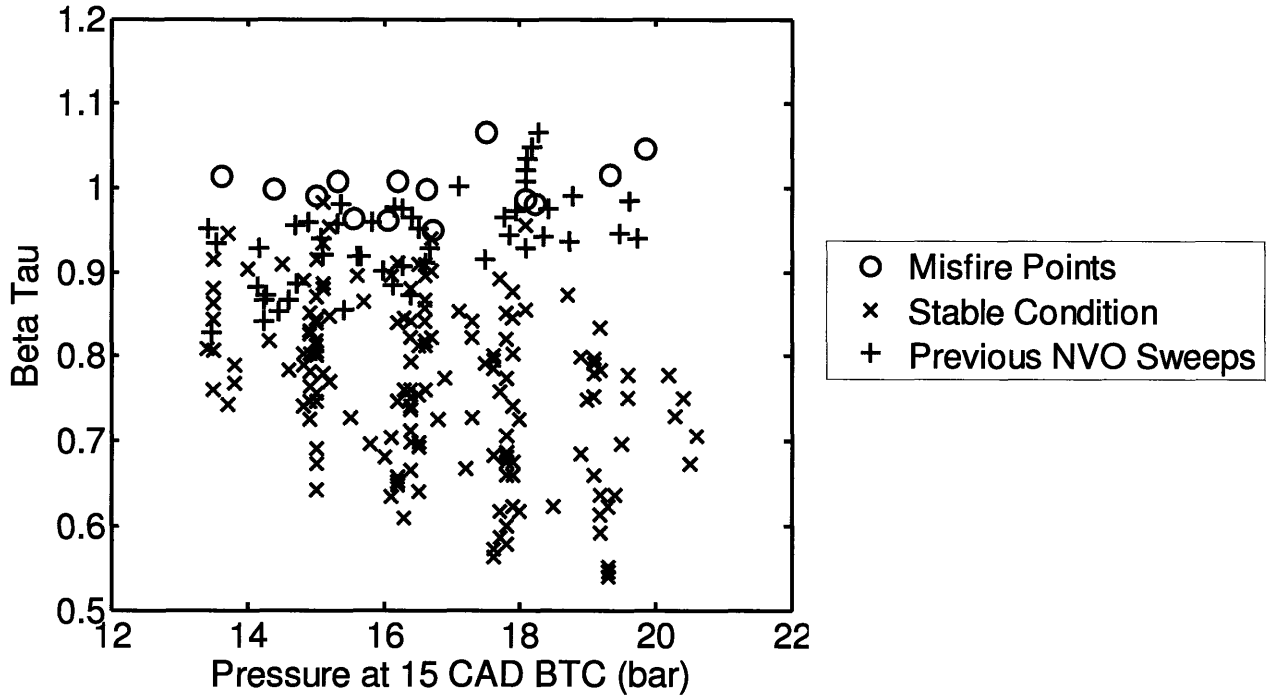


**Figure 3.30.** Threshold Correlation Based on CA10 and $P_{15BTC}$.

Ideally, the misfire limit could be determined by parameters that describe the charge during compression rather than combustion phasing. A correlation is explored where a function of residual fraction, $T_{15BTC}$, and $P_{15BTC}$ form a function that evaluates to 1 at the misfire limit in the form of Equation 3.6 as a new $\beta_{T15}$.

$$\beta_{T15} = a \cdot x_{res} \cdot P_{15BTC}^{b} \cdot \exp\left(c/T_{15BTC}\right) \tag{3.6}$$

The correlation is optimized to find a, b, and c as in the method previously described to minimize the error between $\beta_{T15}$ and 1 for the misfire points. The resulting correlation is stated in Equation 3.7, and the results are plotted in Figure 3.31.

$$\beta_{T15} = 0.16 \cdot x_{res} \cdot P_{15BTC}^{0.079} \cdot \exp\left(2317/T_{15BTC}\right) \tag{3.7}$$

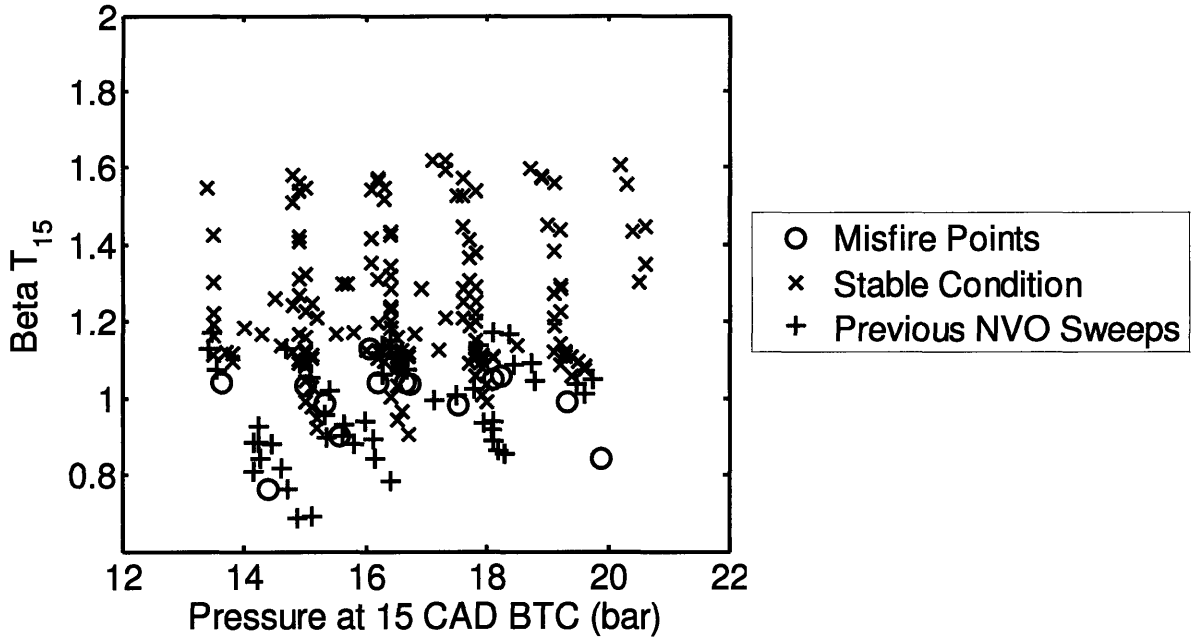


**Figure 3.31.** Beta Parameter vs. Pressure at 15° BTC. Here, Beta is based on $T_{15BTC}$, $P_{15BTC}$, and $x_{res}$.

The correlation shows that there is promise; however, it is considerably worse than the correlation that incorporates phasing. Misfire, like combustion phasing, depends on charge stratification, and this is not well represented by bulk temperature so the quality of the threshold is inherently limited. Combustion phasing incorporates this effect, which is why the previous correlation is significantly better.

To account for thermal stratification effects, bulk temperature is replaced with the intake temperature. $P_{15BTC}$ is replaced with $P_{in}$ so that the misfire limit can be overlaid on the $x_{O2}$ vs. $P_{in}$ maps shown in the previous section. A correlation relating $P_{in}$ to $x_{O2}$ and $T_{in}$ for the misfire points was found, stated in Equation 3.8.

$$P_{in} = 3840 \cdot {x_{O2}}^{0.35} {T_{in}}^{-1.26} \tag{3.8}$$

This correlation yielded an $R^2$ of 96.2%. Again, the correlation was reformed such that a $\beta$, called $\beta_{Pin}$ here, was set to the left side divided by the right side, as shown in Equation 3.9.

$$\beta = 2.60 \cdot 10^{-4} \cdot P_{in} \cdot {x_{O2}}^{-0.35} {T_{in}}^{1.26} \tag{3.9}$$

The resulting plot showing the misfire points, the near misfire points, and the points from the other NVO sweeps is shown in Figure 3.32. The threshold shown by this correlation indicates a clear but not perfect boundary for the points near the misfire versus the misfire points.

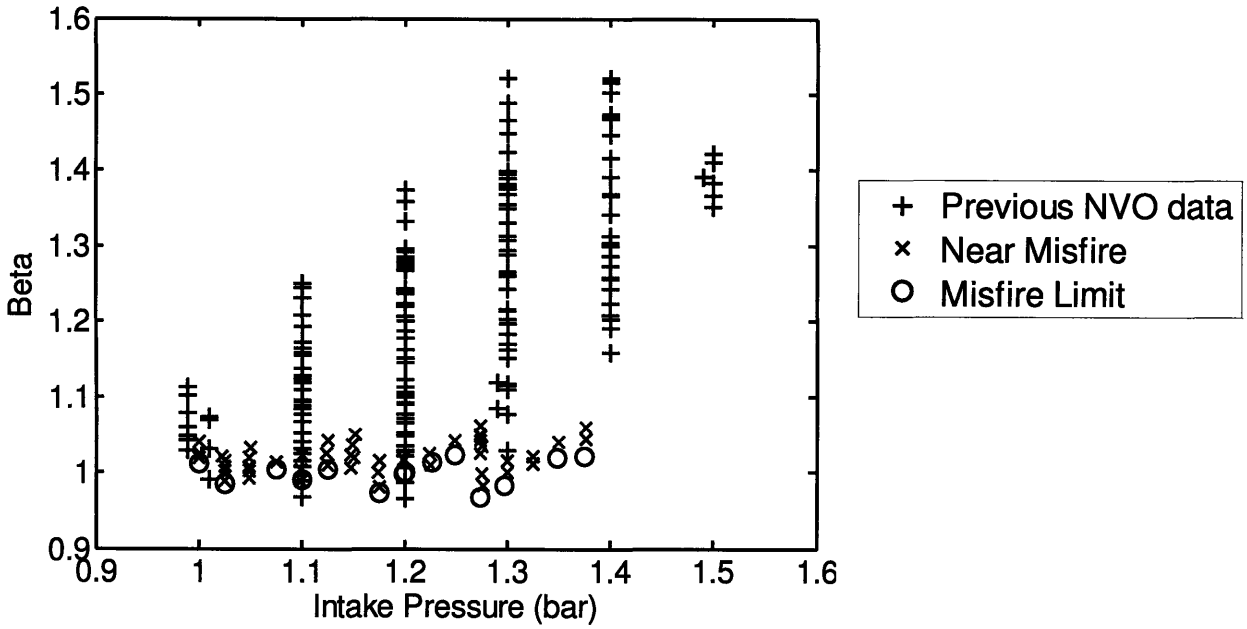


**Figure 3.32.** Correlation Result Based on $P_{in}$, $T_{in}$, and $x_{O2}$ vs. $P_{in}$. Misfire points are shown in circles; points taken in this data set are shown in x marks, and + marks denote points from the previous NVO sweeps.

This correlation is used to illustrate the high-load portion of the misfire limit on maps of oxygen fraction and intake pressure in Figure 3.33. Three maps are shown, as in Figure 3.19, featuring $T_{in}$ = 60°C, 90°C, and 120°C. The misfire curves appear to be located in approximately the right place. The slope appears to fit the 90°C data the best; however, the true dependence on $x_{O2}$ and $P_{in}$ appear to have a more complex trend then the curves do. It should be noted that the misfire curves do not accurately predict misfire at low load and do not attempt to do so. These maps show clearly that the high load limit, constrained by $PRR_{max}$, occurs at the misfire limit.

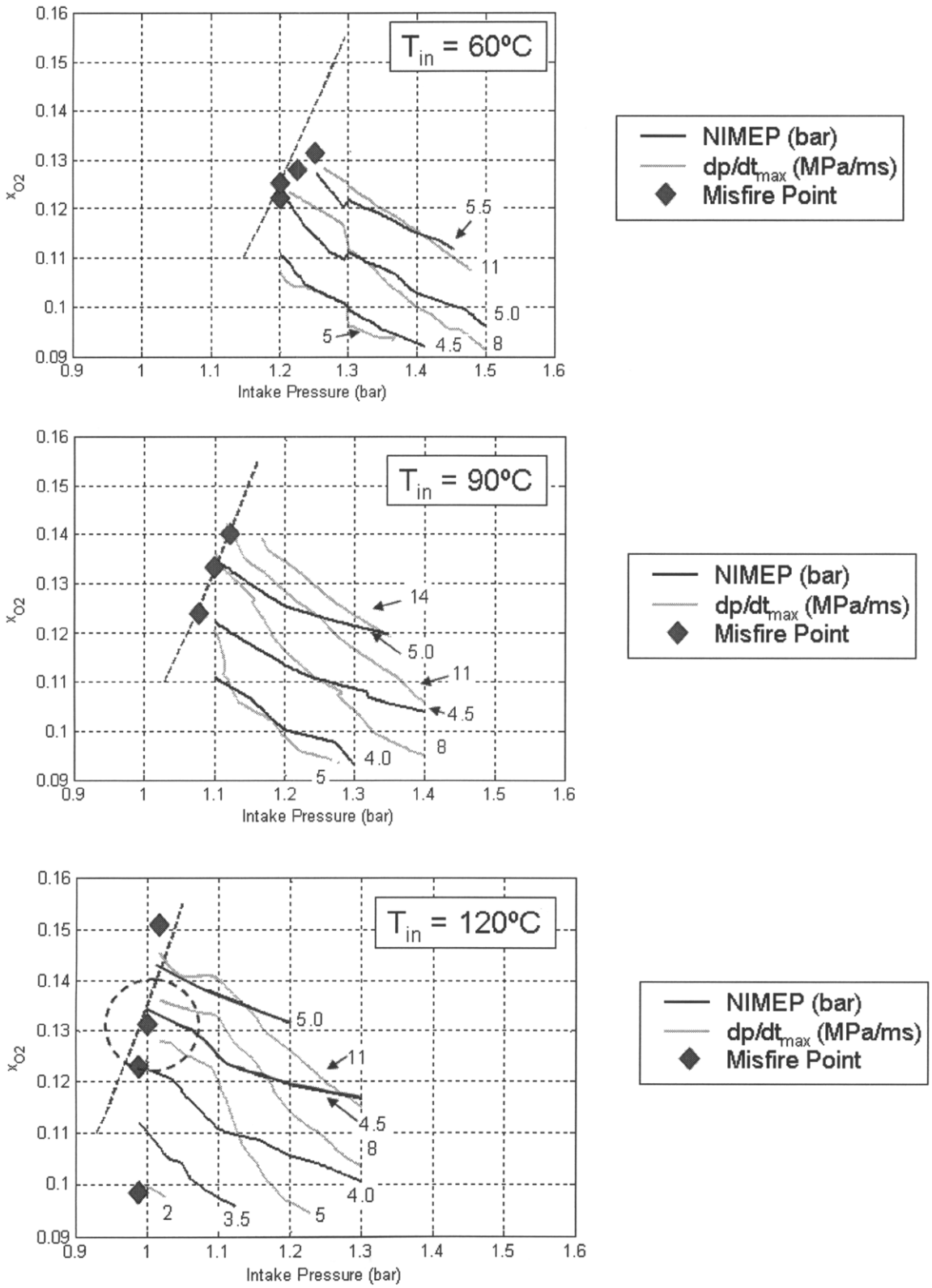


**Figure 3.33.** NIMEP and $PRR_{max}$ Contoured on Oxygen Mole Fraction and Intake Pressure; $T_{in}$ = 60°C (top), $T_{in}$ = 90°C (middle), $T_{in}$ = 120°C (bottom). Misfire points are marked as diamonds. The correlation for misfire, stated in Equation 3.16, is overlaid.

### 3.3.3 Mechanisms for Misfire, NVO High Load Limit

The high-load misfire phenomenon is addressed in this section by exploring cycle-by-cycle behavior and five-cycle averages. This section does not pursue an exhaustive study of the misfire occurrence. The engine's instrumentation is not designed to study cycle-by-cycle behavior. The electromagnetic valve system operates with some cycle-by-cycle variability, which cannot be ruled out as a contributing factor for misfire as will be shown. In this section, two examples of misfire will be explored to illustrate basic themes only. The two points are circled on the plot of misfire points and near-misfire points from Figure 3.25 reprinted in Figure 3.34. The first point features $T_{in}$ = 120°C, $P_{in}$ = 1.0bar, and $x_{res}$ = 27%. The second point is located at a higher boost condition where $T_{in}$ = 35°C, $P_{in}$ = 1.3bar, and $x_{res}$ = 36%.

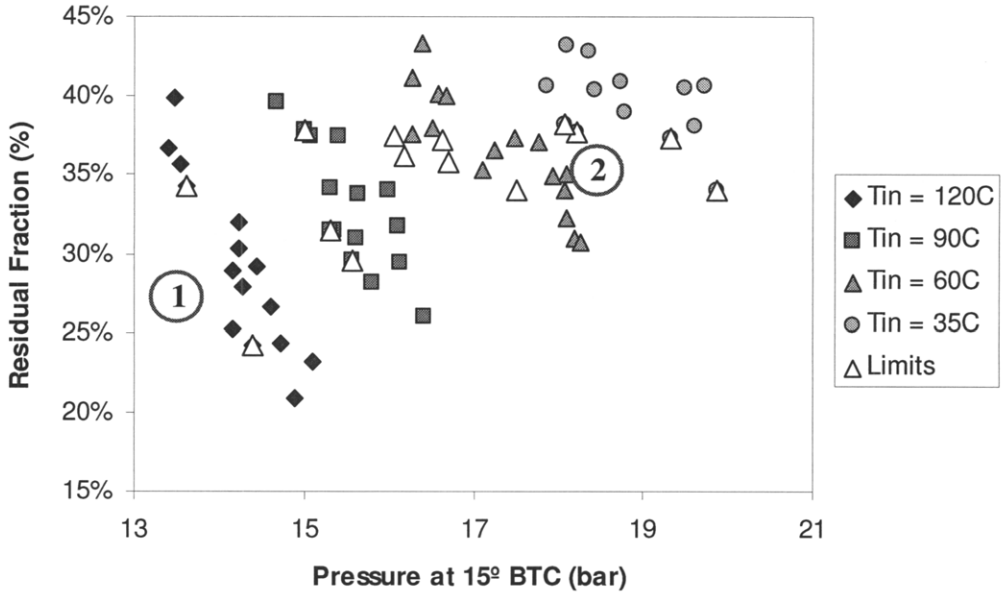


**Figure 3.34.** Residual Fraction vs. Pressure at 15° BTC for Misfire Points and Near-Misfire Points. The two misfire cases are circled.

The first observation for Case #1 is that combustion phases earlier just before misfire. Figure 3.35 and Figure 3.36 show two different parts of the pressure trace for 5 consecutive cycles where the fifth cycle is the one in which the engine dies. Figure 3.35 shows the combustion event, and Figure 3.36 shows the peak of the recompression event. Note that the recompression peak for cycle 4, say, follows the combustion peak shown for cycle 4 and leads into cycle 5. Cycle 1 features a late combustion event. Then combustion phases 6° earlier and retains this phasing for three cycles until the engine dies. The recompression event shows that peak recompression pressure starts somewhat low then increases for two cycles before dropping low

again. The misfire cycle features a much higher peak, possibly because the exhaust valve open timing shifted in the absence of combustion, but this is after the engine has died.

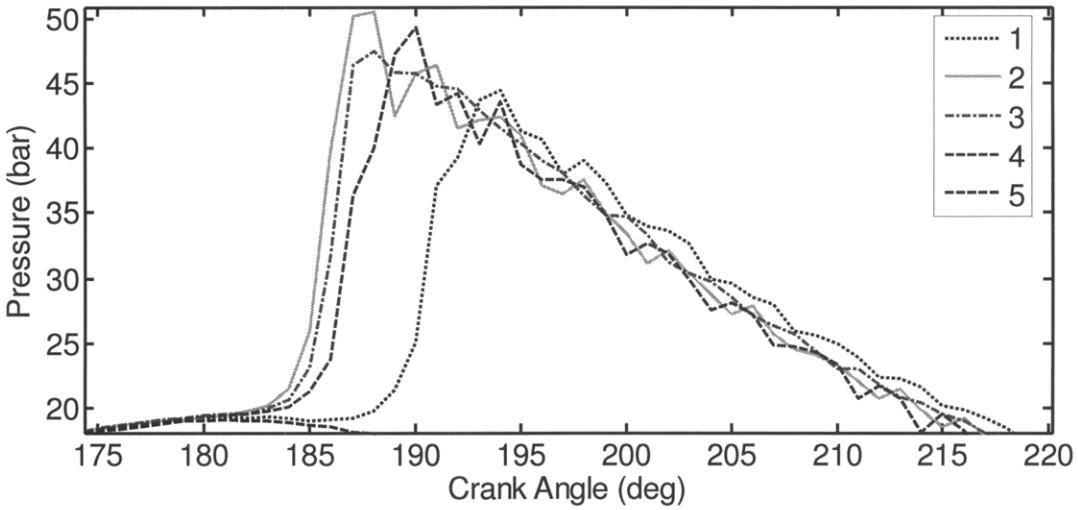


**Figure 3.35.** Case #1: Pressure Traces for Five Individual Cycles where the Fifth One Misfires. The traces feature the combustion event.

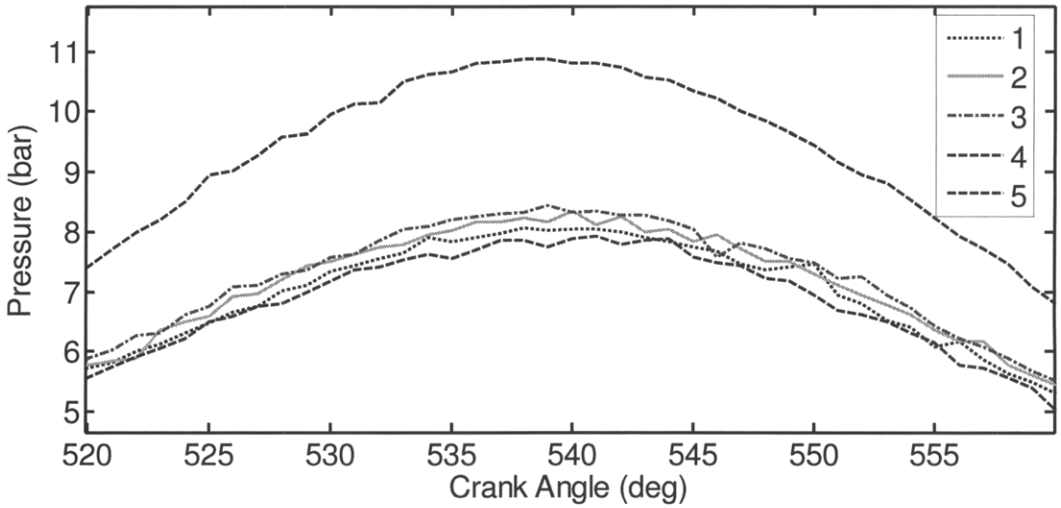


**Figure 3.36.** Case #1: Pressure Traces for Five Individual Cycles where the Fifth One Misfires. The traces feature the recompression event. Cycles 1 through 5 correspond to the same cycles in Figure 3.35.

The peaks of the cycle 1 and cycle 4 recompression processes are of similar magnitude, but combustion in cycle 4 is phased much earlier than in cycle 1. The earlier phasing of cycle 4 implies that the exhaust from cycle 4 is colder than from cycle 1. For the recompression peaks to be similar, fewer moles of gas are trapped in cycle 1, but they are hotter than in cycle 4. Since the trapped residual is colder in cycle 4, the hottest parcel of gas in the next cycle does not reach ignition temperature.

Figure 3.37 and Figure 3.38 show the cycle-by-cycle and 5-cycle averages of NIMEP, airflow, λ, and CA50. NIMEP and airflow are shown as the percent deviation from their respective stable average values. λ is shown as the percent deviation multiplied by 5 for clarity. CA50 is shown as the deviation in CAD from the stable average value. These are noted in Equations 3.16, 3.17, and 3.18.

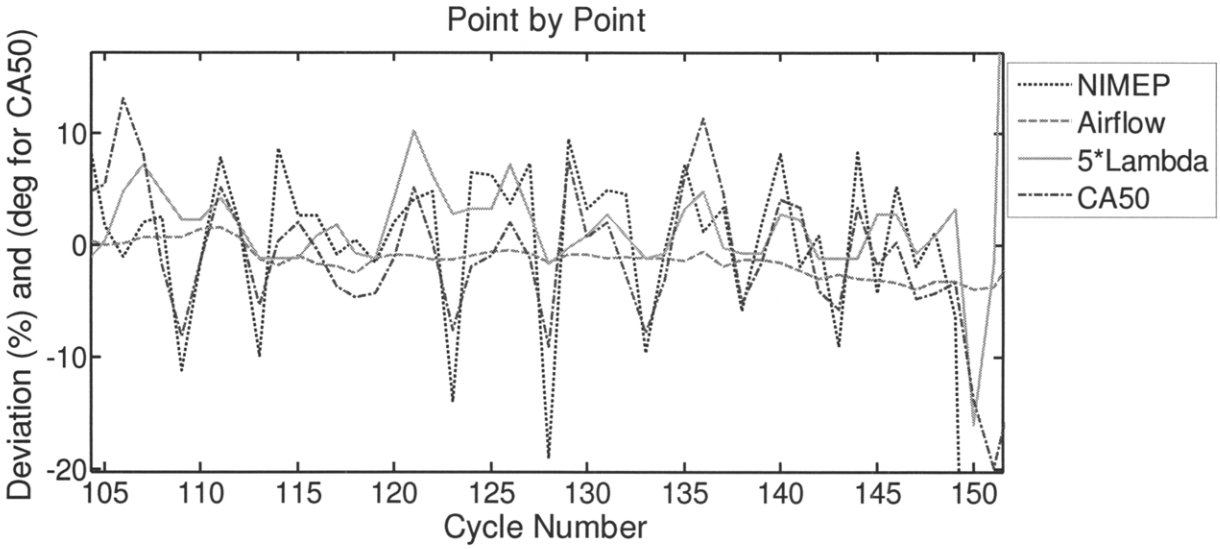


**Figure 3.37.** Case #1. Cycle-by-Cycle Data Leading up to the Misfire. NIMEP, Airflow, λ, and CA50 recorded. For NIMEP and Airflow, the percent deviation from the stable value is plotted. For λ, 5*the percent deviation is plotted. For CA50, the number of CAD deviation from the stable value is plotted.

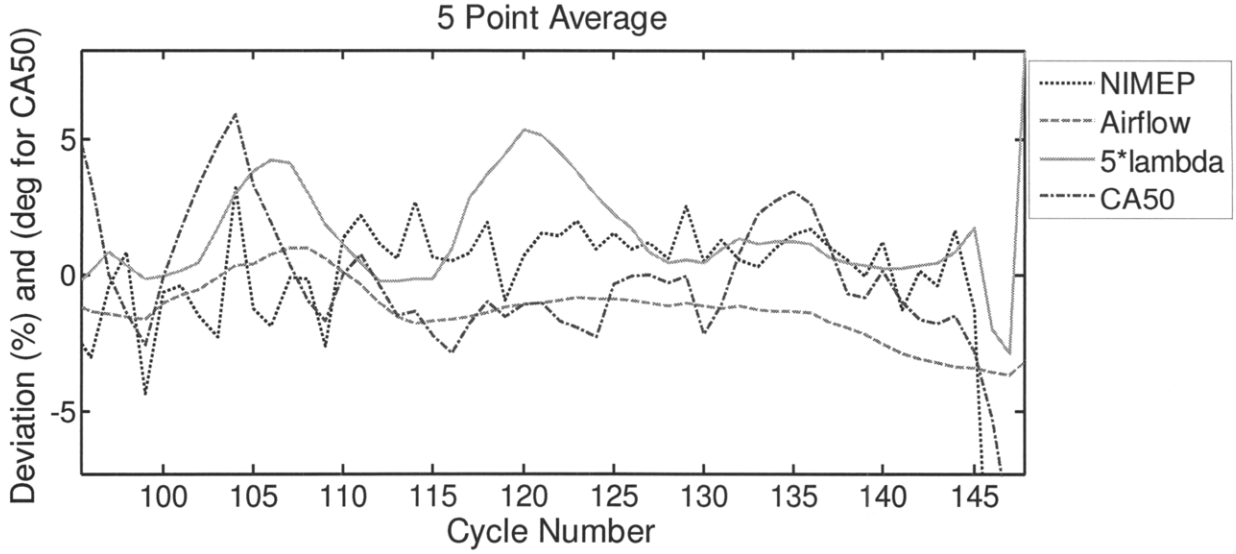


**Figure 3.38.** Case #1. Five-Point Averages of Cycle-by-Cycle Data Leading up to the Misfire. NIMEP, Airflow, λ, and CA50 recorded. For NIMEP and Airflow, the percent deviation from the stable value is plotted. For λ, 5*the percent deviation is plotted. For CA50, the number of CAD deviation from the stable value is plotted.

$$\text{Percent Deviation of NIMEP} = \frac{NIMEP_i - \frac{\sum_{i=1}^{100} NIMEP_i}{100}}{\frac{\sum_{i=1}^{100} NIMEP_i}{100}} \cdot 100\% \tag{3.16}$$

$$\text{Percent Deviation of } \lambda = 5 \times \frac{\lambda_i - \frac{\sum_{i=1}^{100} \lambda_i}{100}}{\frac{\sum_{i=1}^{100} \lambda_i}{100}} \cdot 100\% \tag{3.17}$$

$$\text{Deviation of CA50} = CA50_i - \frac{\sum_{i=1}^{100} CA50_i}{100} \tag{3.18}$$

A first observation from the cycle-by-cycle data is that CA50 and NIMEP move together. This is likely an efficiency effect where retarding combustion increases efficiency.

The plotted parameters vary considerably on a cycle-by-cycle basis, but the five-cycle average plot shows that there are trends on the time scale of 10-20 cycles. Airflow drops below average at cycle 110 and then drops again at cycle 137 to where it is almost 5% lower than average. The air-fuel ratio peaks at cycle 107 and at cycle 120 before staying at a somewhat constant value that is higher than average. The fuel injection rate can be assumed to stay constant so if the air-fuel ratio and the airflow do not vary together, it implies that there is significant variation in the fuel pooling rate. The assumption is that some amount of fuel pools in the intake port so for a given cycle, some of the fuel comes from the injection and some of the fuel comes from the pool. Some of the injected fuel is stored in the pool. This pooling phenomenon has been shown to vary on a time scale of tens to hundreds of cycles, which is consistent with the timescale of these variations. Scaringe and Cheng observed a short time scale, tens of cycles, for pool depletion when injection was turned off. They attributed this depletion time scale to the pool location near the valve [52]. The engine misfires just after the air flow drops the second time at 137 cycles implying that this effect, in concert with air flow variations, is instrumental in causing the misfire. Variation in pool size might be caused by variations in turbulence in the

intake or variations in the temperature of the gas in the intake. Residual gas may move into the intake port during the intake process and affect evaporation.

Variations in residual fraction may also be relevant, but no evidence suggests this as a stand-alone cause for misfire. A strong variation in residual fraction is observable at cycle 107. Here, combustion phases later, likely causing the trapped residual gas to be hotter. The airflow and air-fuel ratio both increase implying more air is entering the engine and therefore less residual is being trapped. While this is observable, the engine does not misfire, implying that the engine can withstand variations in residual fraction.

A final observation from Case #1 is the relationship between combustion phasing and EVO timing. Increased pressure in the cylinder at EVO retards the opening process. The electromagnetic valve system was weak to the point that the command timing had to be advanced to hold the same valve movement timing if pressure during the expansion stroke were increased. For a particular command setting, it is evident from Figure 3.39 that EVO timing followed CA90 timing very closely.

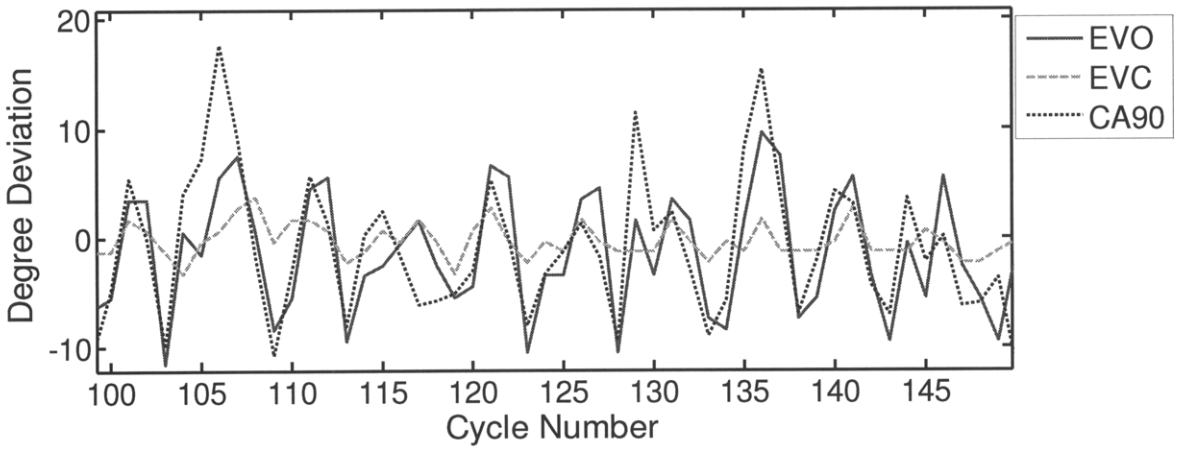


**Figure 3.39.** Cycle-by-Cycle Data for EVO, EVC, and CA90. Deviation from the stable average is plotted in CAD.

From Figure 3.54 in Section 3.3.5, it was also clear that residual fraction varied with EVO timing. Cycle-by-cycle variability may play a factor in misfire phenomena in this engine. However, it should be reiterated that longer time-scale phenomena appeared more responsible for misfire in this case.

Case #2 was taken where $T_{in}$ = 35°C, $P_{in}$ = 1.3bar, and $x_{res}$ = 36%. The average combustion phasing before misfire was 187° ABC. The pressure traces leading up to misfire are shown in Figure 3.40 and Figure 3.41 where the combustion event and the recompression event are presented, respectively.

Cycle 1 features phasing at approximately 187°, the stable average, then combustion phases later for cycle 2, then earlier, and then later again, and phases significantly earlier to 183° for cycle 5. The next cycle is the misfire. As in Case #1, the misfire is preceded by a very early cycle. The recompression event for cycle 4 features an especially high pressure peak implying that an above-average amount of energy is trapped for cycle 5. Cycle 5 consequently burns very early. This leads to a low compression event which does not provide enough energy for the combustion event to occur in cycle 6.

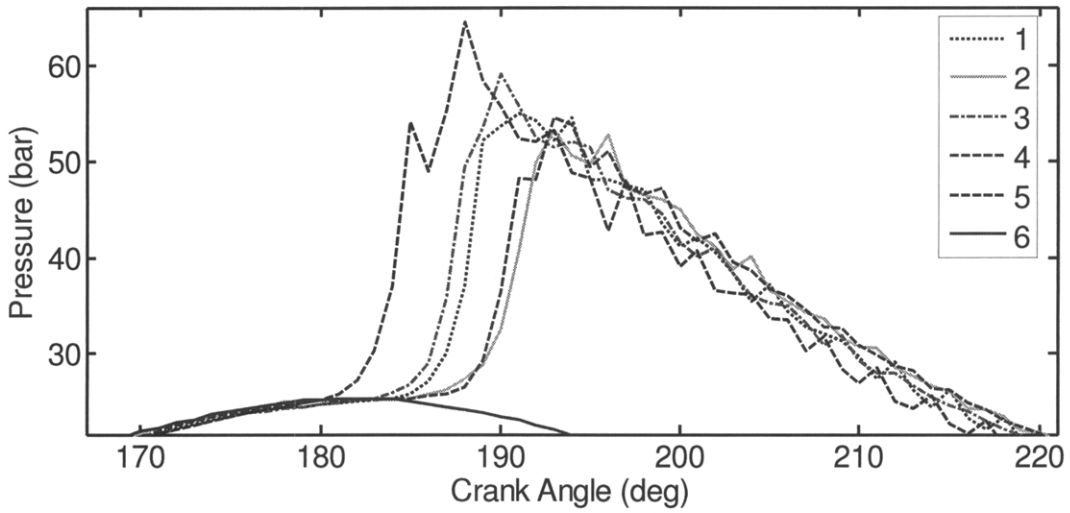


**Figure 3.40.** Case #2: Pressure Traces for Six Individual Cycles where the Sixth One Misfires. The traces feature the combustion event.

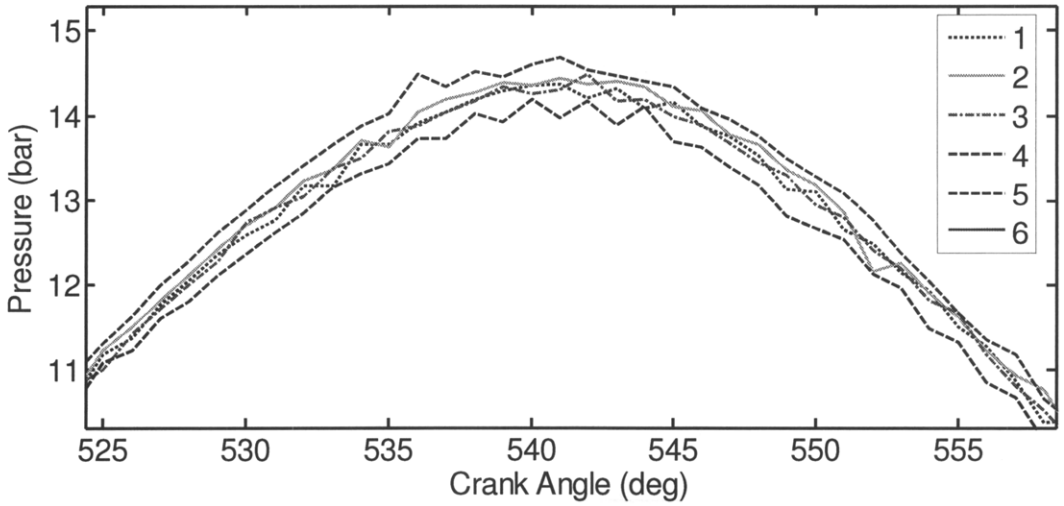


**Figure 3.41.** Case #2: Pressure Traces for Six Individual Cycles where the Sixth One Misfires. The traces feature the recompression event. Cycles 1 through 5 correspond to the same cycles in Figure 3.40.

Just as in Case #1, the several cycles before misfire are characterized by variations in combustion phasing and recompression pressure. Strategies to extend the misfire limit might consider controlling these symptoms.

NIMEP, airflow, $\lambda$, and CA50 are plotted on a cycle-by-cycle basis and 5-cycle average basis in Figure 3.42 and Figure 3.43. NIMEP and airflow are plotted as the percent deviation from the stable average value. $\lambda$ is the same but multiplied by 5 for clarity. CA50 is plotted as the deviation from the stable average in CAD.

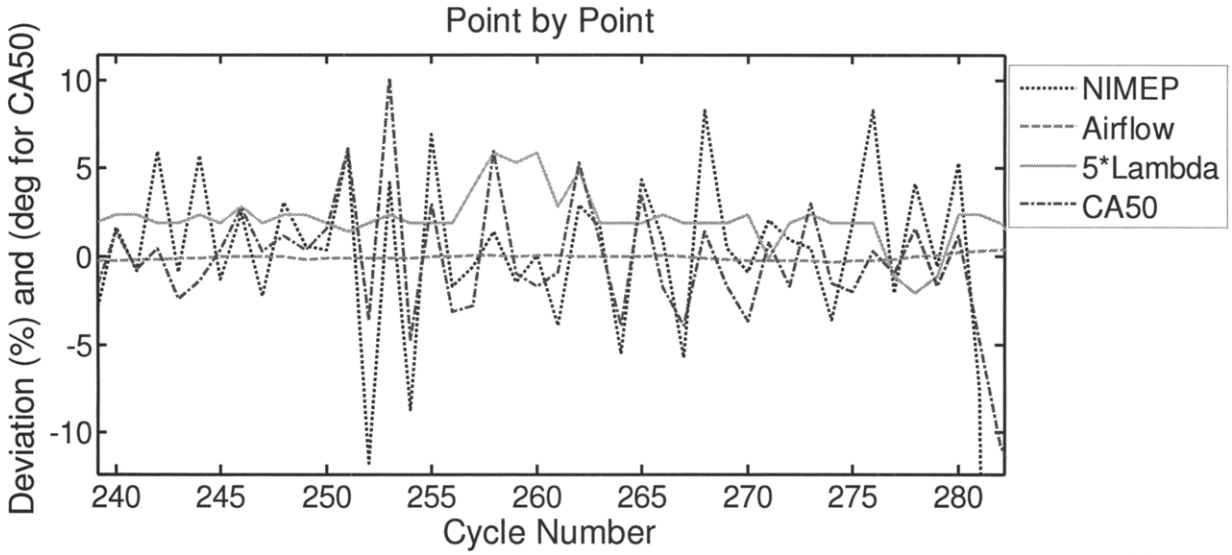


**Figure 3.42.** Case #2. Cycle-by-Cycle Data Leading up to the Misfire. NIMEP, Airflow, $\lambda$, and CA50 recorded. For NIMEP and Airflow, the percent deviation from the stable value is plotted. For $\lambda$, 5*the percent deviation is plotted. For CA50, the number of CAD deviation from the stable value is plotted.

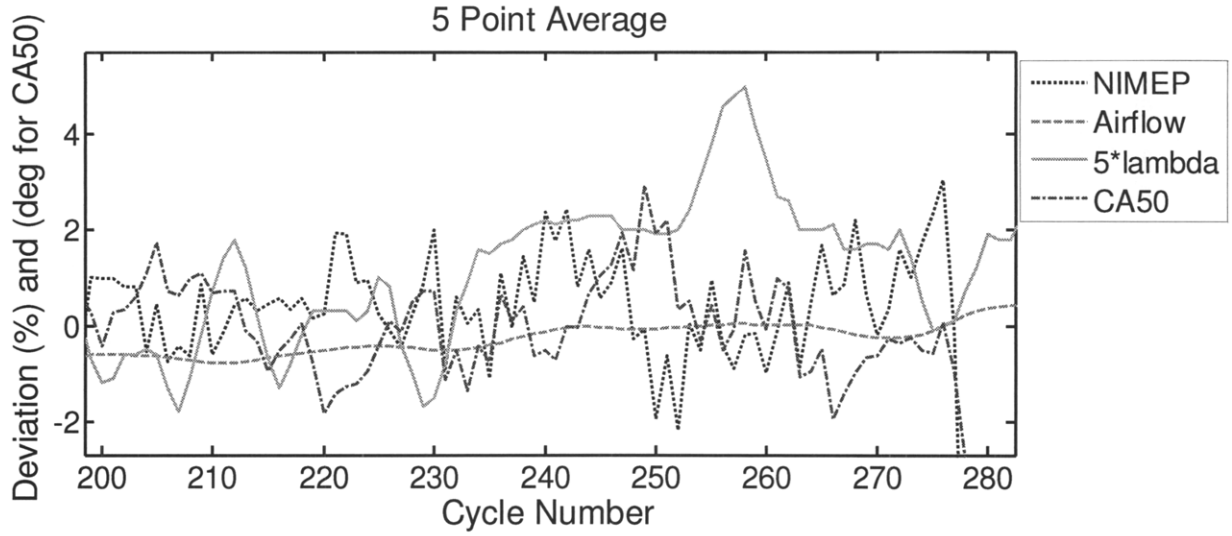


**Figure 3.43.** Case #2. Five-Point Averages of Cycle-by-Cycle Data Leading up to the Misfire. NIMEP, Airflow, $\lambda$, and CA50 recorded. For NIMEP and Airflow, the percent deviation from the stable value is plotted. For $\lambda$, 5*the percent deviation is plotted. For CA50, the number of CAD deviation from the stable value is plotted.

CA50, NIMEP and airflow show no significant variations just before misfire in the cycle-by-cycle plot. The air-fuel ratio, however, peaks briefly at cycle 257 and then dips at cycle 276 just before the engine dies. The 5-cycle average shows a more telling story with air-fuel ratio. $\lambda$ indicates a shift to lean operation at cycle 232, and then consistently lean operation continues. The engine air-fuel ratio peaks at an even more lean condition at cycle 257 before settling to the previous setting. $\lambda$ dips to stoichiometric just before the engine dies. The air-fuel ratio varies on a time scale of 10-20 cycles, and the air flow holds very steady. Injection rates are assumed constant implying that variations in fuel pooling are present, as in Case #1.

In summary, two factors are suggested to contribute to misfire. Variations in fuel pooling in the intake port vary on the time-scale of tens of cycles, and this leads to unstable conditions. Variations on a cycle-by-cycle basis in combustion phasing and consequently the amount and temperature of the trapped residuals contribute to misfire. Significantly variations in the latter are observed without misfire which leads to the conclusion that the factor of fuel pooling variations are necessary for misfire. An in-depth study is required to verify this suggestion and to understand in detail how variations in relevant parameters affect one another.

### 3.3.4 IVC Timing Effects

Besides varying the degree of trapped residuals via the EVC and IVO timings, varying IVC timing is another way to control combustion. In this study, the EVO timing, EVC timing, and IVO timing were set to trap a mid-range amount of residual gas, and the IVC timing was varied at four different boost pressures. Exhaust pressure was set to intake pressure for all data in this section. Intake temperature was set to 120°C. The valve timing settings are listed in Table 3.3 and diagrammed in Figure 3.44.

First, it should be observed that residual fraction does not change significantly by varying IVC timing, as shown in Figure 3.45. Residual fraction is largely determined by the exhaust valve behavior. By retarding the IVC timing, the piston pushes the charge back into the intake port after inducting air which means that the inducted charge actually contains some residual gas that had been pushed into the intake during the previous cycles. The two primary effects of retarding IVC timing are reducing the effective compression ratio and reducing the number of moles in-cylinder. Whereas the geometric compression ratio is defined in terms of the minimum and maximum volumes, as in Equation 3.5, the effective compression ratio is a function of the volume at IVC as in Equation 3.6.

$$CR_{Geometric} = \frac{V_{max} - V_{min}}{V_{min}} \tag{3.5}$$

$$CR_{Effective} = \frac{V_{IVC} - V_{min}}{V_{min}} \tag{3.6}$$

**Table 3.3.** IVC Sweep Valve Timings

| Valve Operation | Timing |
|---|---|
| IVC | 20° to 67° ABC |
| EVO | 30° BBC |
| EVC | 81° BTC |
| IVO | 81° ATC |

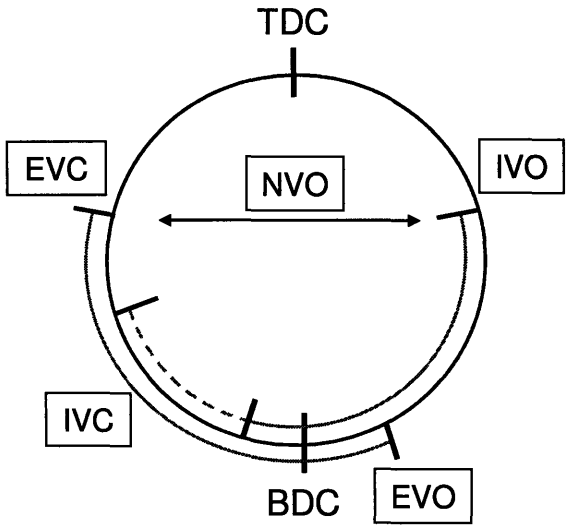


**Figure 3.44.** Diagram of Valve Timings for the IVC Sweeps

Reducing the effective compression ratio results in lower pressures at the end of the compression process, as shown in Figure 3.46. The pressure at 15° BTC drops with a slightly stronger-than-linear dependence on IVC retard. Eventually, pressure drops sufficiently that misfire occurs as shown for the $P_{in}$ = 1.1bar and 1.2bar cases.

Besides reducing the effective compression ratio, the number of inducted moles of air, fuel, and residual gas decreases as IVC timing is retarded. Figure 3.47 shows the decrease in fuel mass per cycle with IVC timing. The rate of decrease is stronger at higher boost likely because the residual fraction increases slightly at high boost.

The temperature at the end of compression behaves similarly to pressure; it drops with IVC retard as shown in Figure 3.48. Varying IVC timing by 25° results in a temperature decrease of 30°C at 15° BTC. The temperature reduction occurs in part because of decreased cylinder pressure but also because the residual gas temperature is colder since less fuel is burned per cycle.

Combustion phases later with retarded IVC timing as shown in Figure 3.49. Both temperature and pressure are lower so the charge does not reach a state adequate for fast

reactions until later in the cycle as IVC timing is retarded. This trend persists until the misfire limit is encountered.

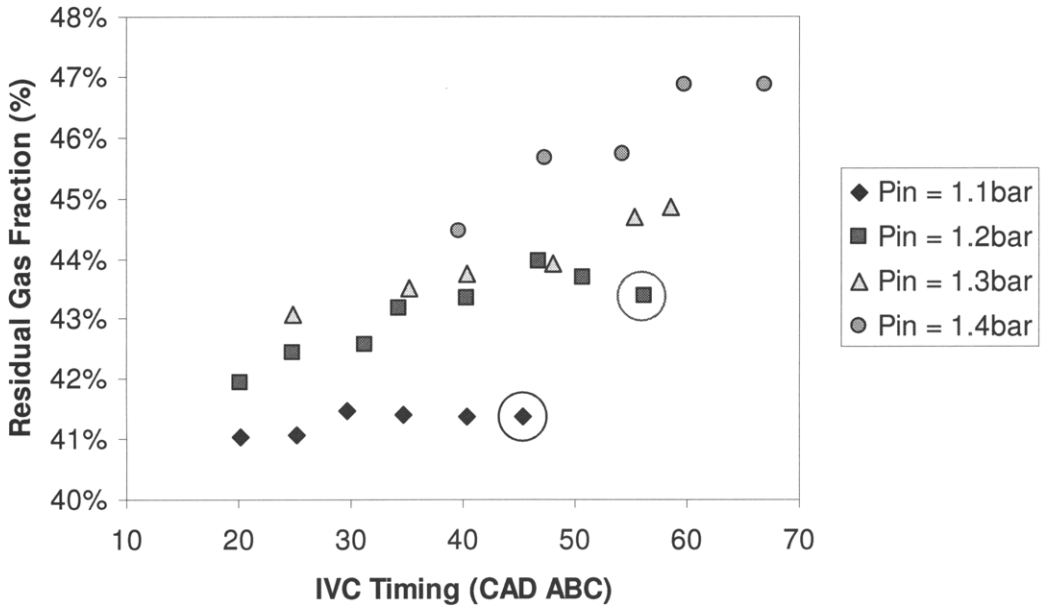


**Figure 3.45.** Residual Fraction vs. IVC Timing for Four Boost Pressures. Misfire limit points are circled.

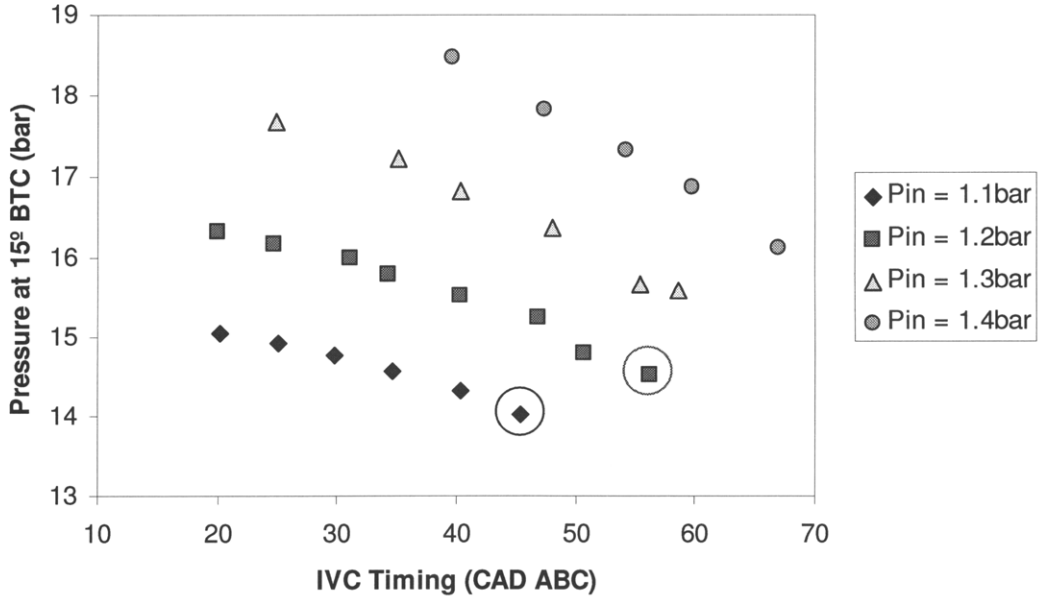


**Figure 3.46.** Pressure at 15° BTC vs. IVC Timing for Four Boost Pressures. Misfire limit points are circled.

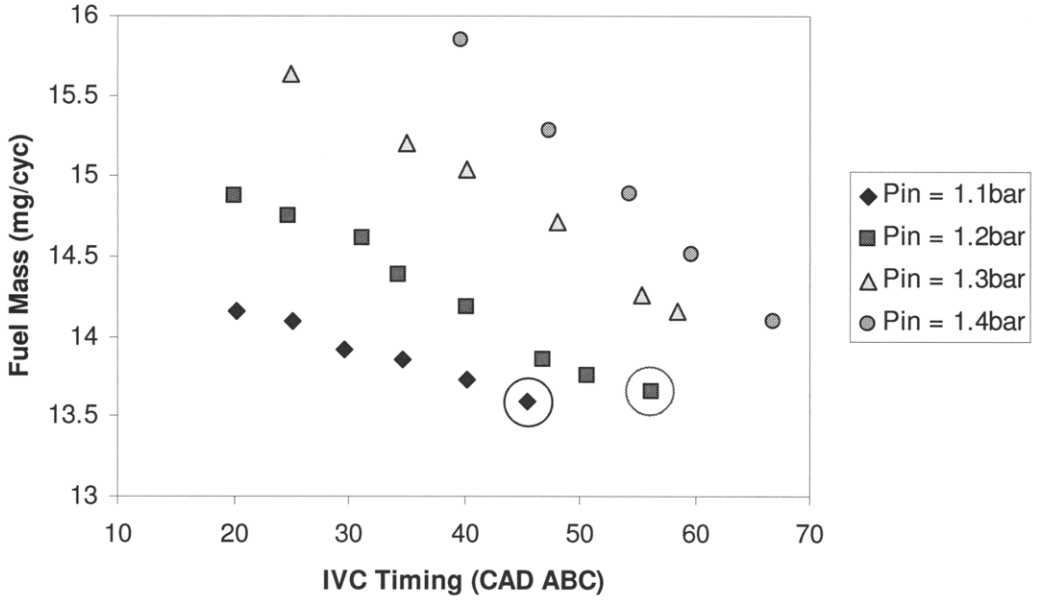


**Figure 3.47.** Fuel Mass vs. IVC Timing for Four Boost Pressures. Misfire limit points are circled.

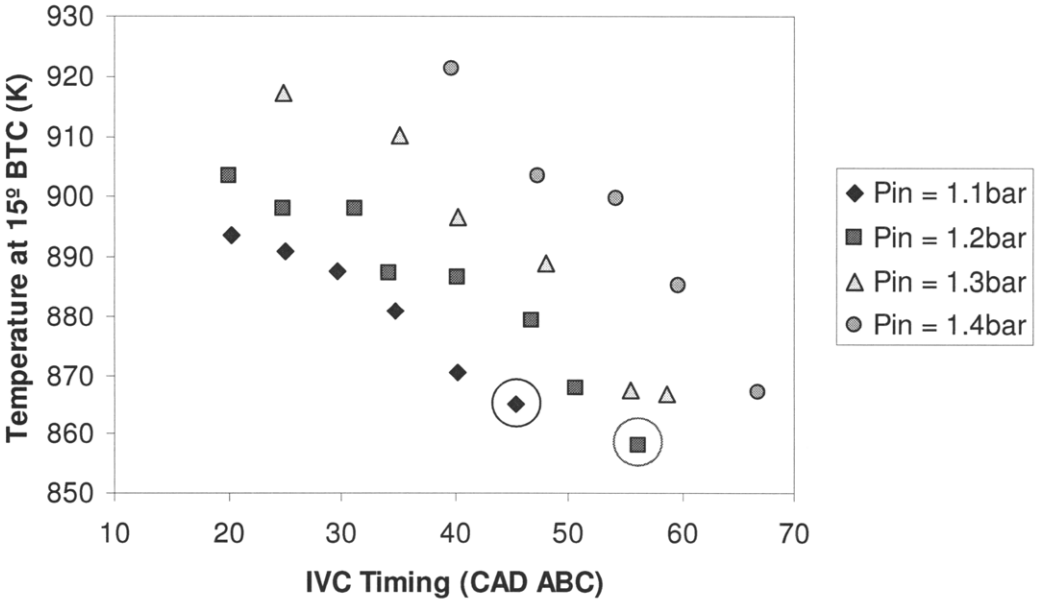


**Figure 3.48.** Temperature at 15° BTC vs. IVC Timing for Four Boost Pressures. Misfire limit points are circled.

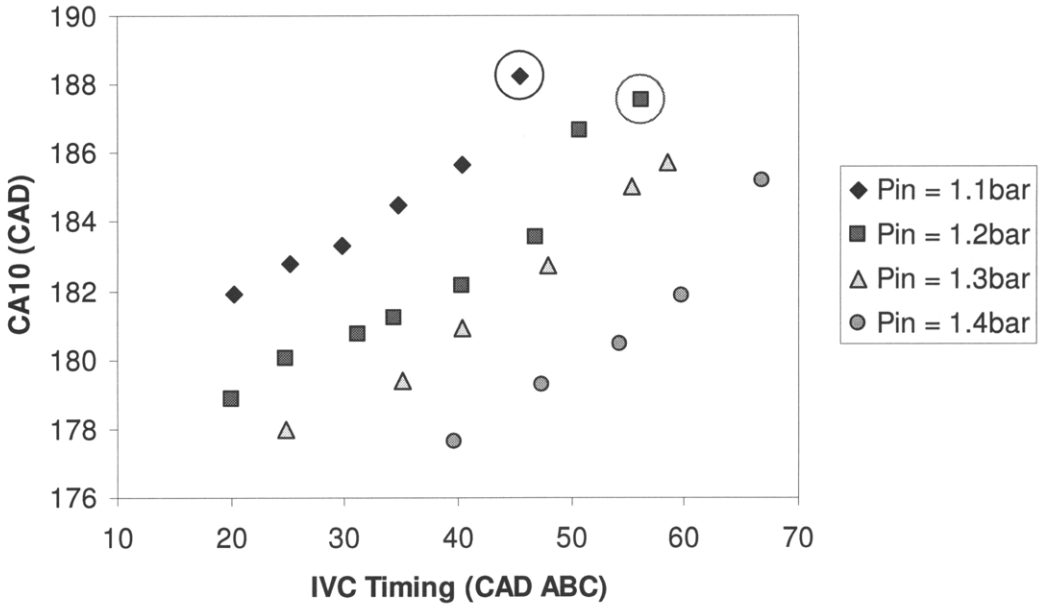


**Figure 3.49.** Combustion Phasing vs. IVC Timing for Four Boost Pressures. Misfire limit points are circled.

Just as combustion retards, maximum pressure rise rate drops with retarded IVC timing as shown in Figure 3.50. Dropping temperatures and fuel rates result is slower reaction rates overall.

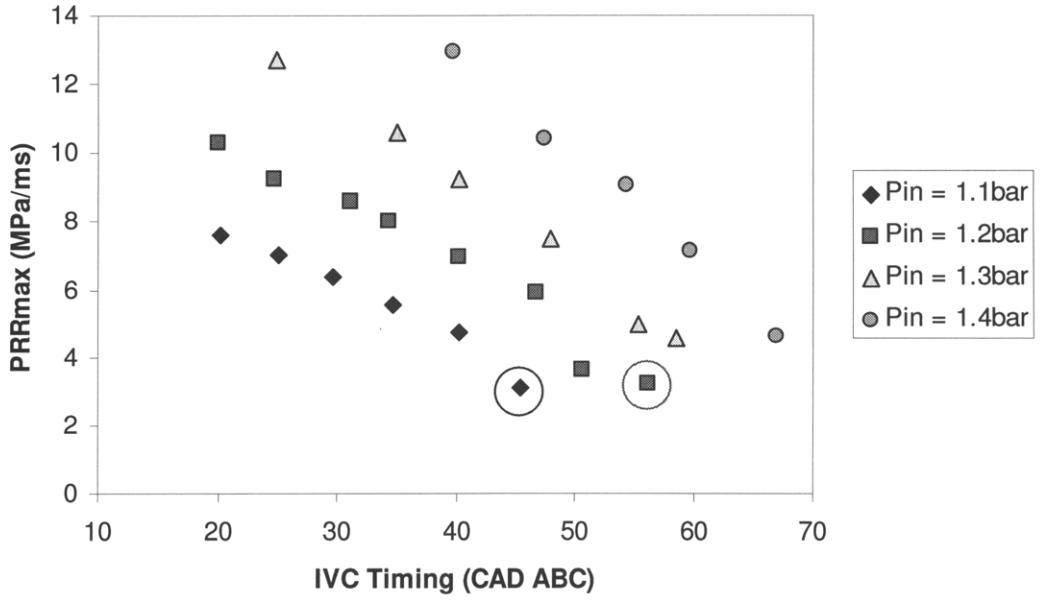


**Figure 3.50.** PRRmax vs. IVC Timing for Four Boost Pressures. Misfire limit points are circled.

Since fuel rate drops as temperature and pressure drop with IVC retard, the NIMEP and $PRR_{max}$ scale together with IVC timing as illustrated in Figure 3.51. IVC timing and boost both serve as means to vary the NIMEP, and it appears that a combination of the two allows for the highest increase of NIMEP for a given rate of pressure rise. A way to increase load constrained by $PRR_{max}$ appears to be to retard IVC timing while boosting the engine. Charge density can be increased while the pressure at the end of compression can be managed. NIMEP and $PRR_{max}$ are contoured on the effective compression ratio and intake pressure in Figure 3.52. This contour plot shows that a small increase in the high load limit can be achieved by moving to a low effective compression ratio and high boost.

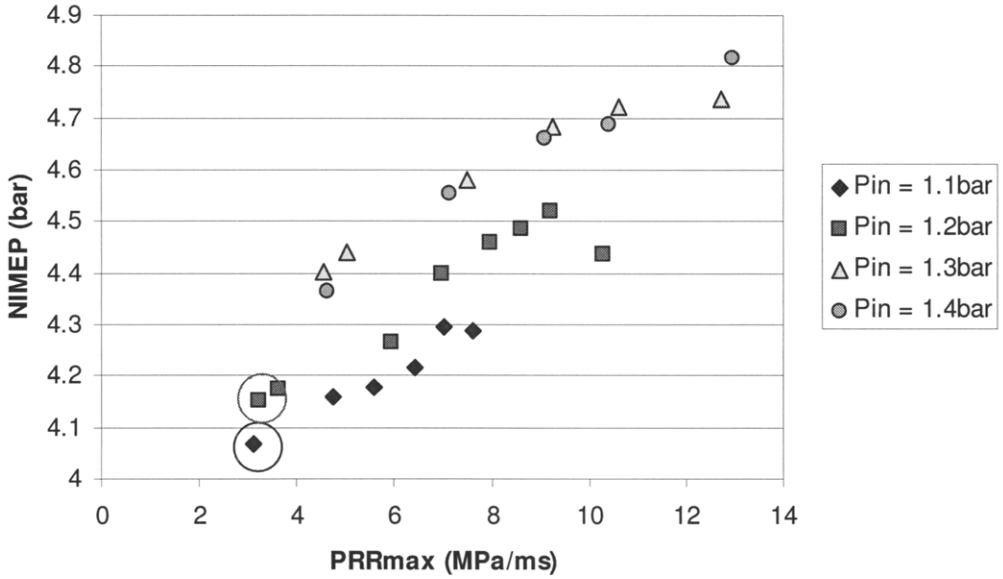


**Figure 3.51.** NIMEP vs. PRRmax for Four Boost Pressures. Misfire limit points are circled. Red dashed lines indicate constant IVC timing values.

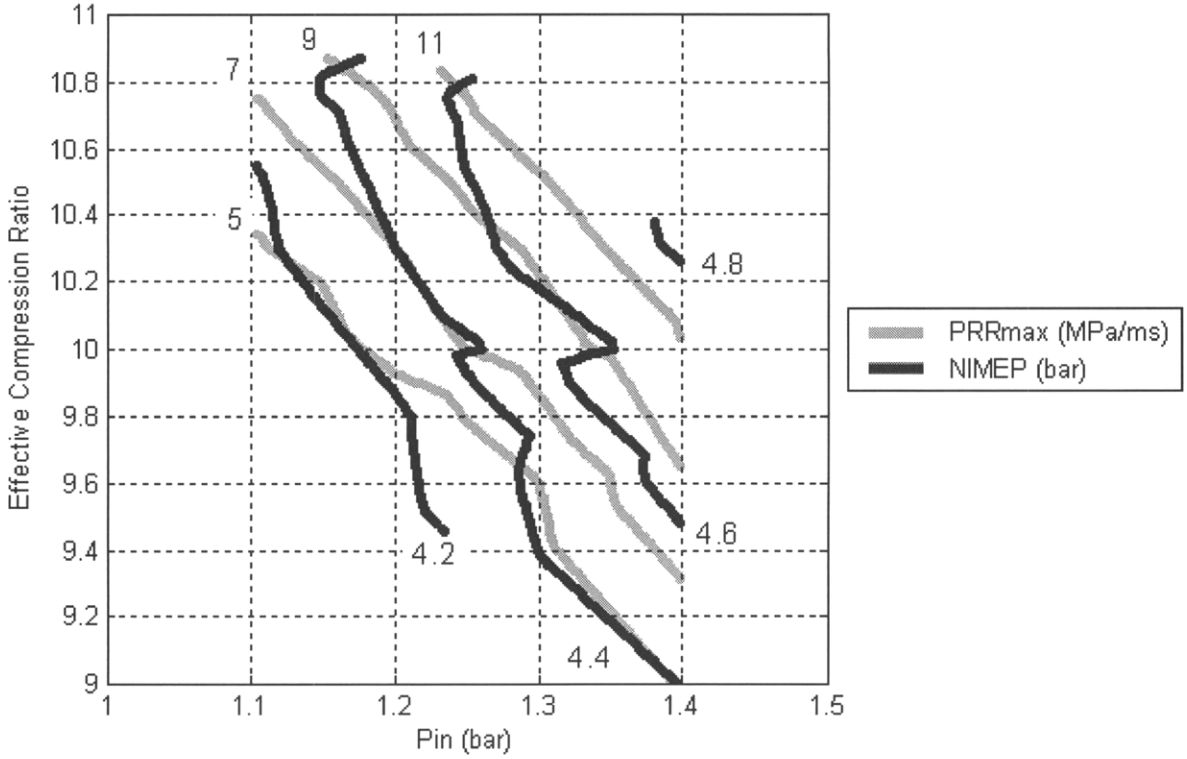


**Figure 3.52.** NIMEP and $PRR_{max}$ Contoured on Effective Compression Ratio and Intake Pressure. $T_{in}$ = 120ºC.

### 3.3.5 EVO Timing Effects

Another means of controlling combustion is by varying EVO timing. This study assessed the effect of varying EVO across five intake pressures. Exhaust pressure was held equal to the intake pressure. The intake temperature was set to 120°C. EVO timing was varied from 65° BBC to 10° ABC. The other valve timings were fixed such that a mid-range amount of residual gas was trapped as listed in Table 3.4 and diagrammed Figure 3.53.

**Table 3.4.** EVO Sweep Valve Timings

| Valve Operation | Timing |
|---|---|
| IVC | 20° ABC |
| EVO | -10° to 65° BBC |
| EVC | 81° BTC |
| IVO | 81° ATC |

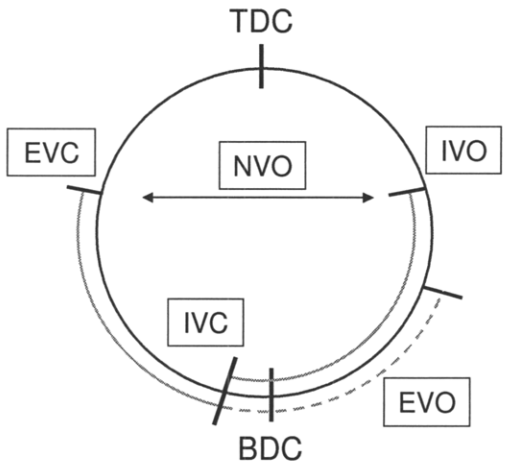


**Figure 3.53.** EVO Sweep Valve Timings

The effects of varying the EVO timing are not simple, but varying EVO timing significantly changes charge characteristics so the topic should not be neglected.

First, the effect of EVO timing on the residual gas fraction is illustrated in Figure 3.54.

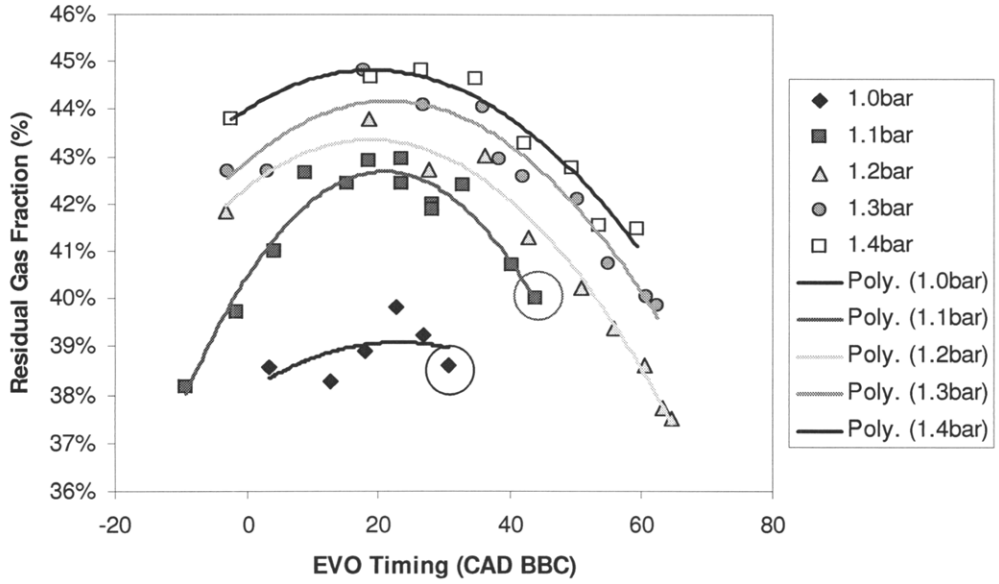


**Figure 3.54.** Residual Gas Fraction vs. EVO Timing. Pin = 1.0bar – 1.4bar; Tin = 120°C. Misfire limit points are circled.

Residual fraction increases with boost pressure as in the previous studies. Residual fraction shows a parabolic dependence on EVO timing. It peaks where EVO is approximately 20° BBC and diminishes as EVO is retarded or advanced from this timing.

The decrease in residual fraction as EVO timing is advanced can be explained simply by the fact that the exhaust duration is increasing so the engine becomes more effective at expelling burned gas. The number of moles of trapped residuals is plotted against EVO timing in Figure 3.55 and shows a consistent, slight decrease in trapped moles as EVO timing is advanced.

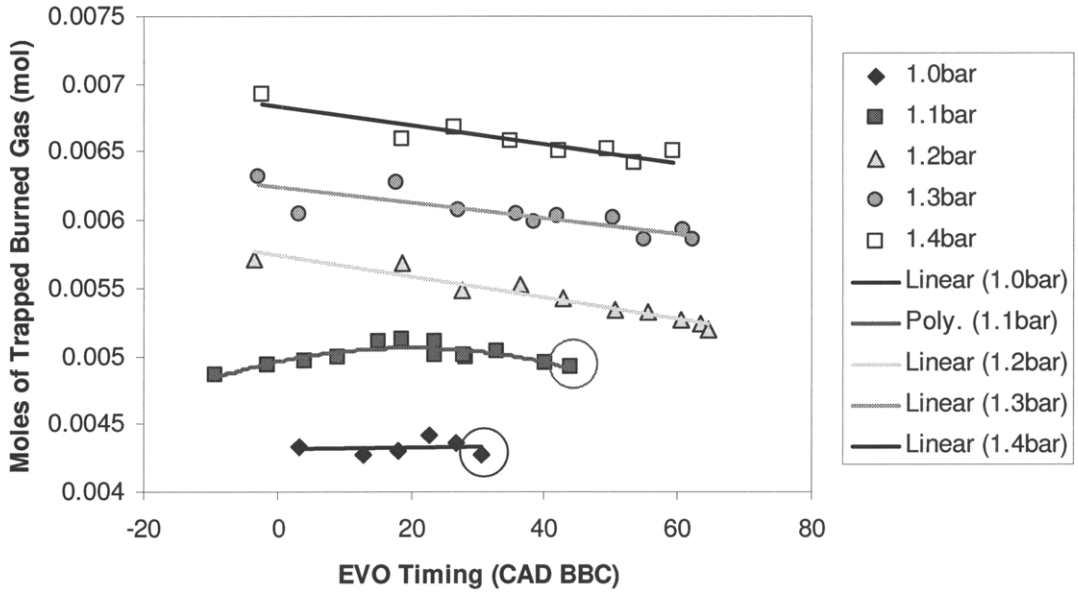


**Figure 3.55.** Moles of Trapped Burned Gas vs. EVO Timing for Five Intake and Exhaust Pressures. $T_{in}$ = 120°C. Misfire points are circled.

The explanation for why very retarded EVO timing reduces the trapped residual fraction requires inspection of the pressure trace. Figure 3.56 features the averaged in-cylinder pressure trace for six EVO timings where $P_{in}$ = 1.2bar and $T_{in}$ = 120°C. The crank angle is referenced here, and only here, so 0° is BDC exhaust for convenient reference for EVO timings. The close-up below shows the pressure remaining high longest for the latest EVO timing, -3° BBC, and retained shortest for the earliest EVO timing, 63° BBC. When EVO timing is late, at -3° BBC, the blowdown event of the exhaust process occurs while the cylinder volume is decreasing after TDC.

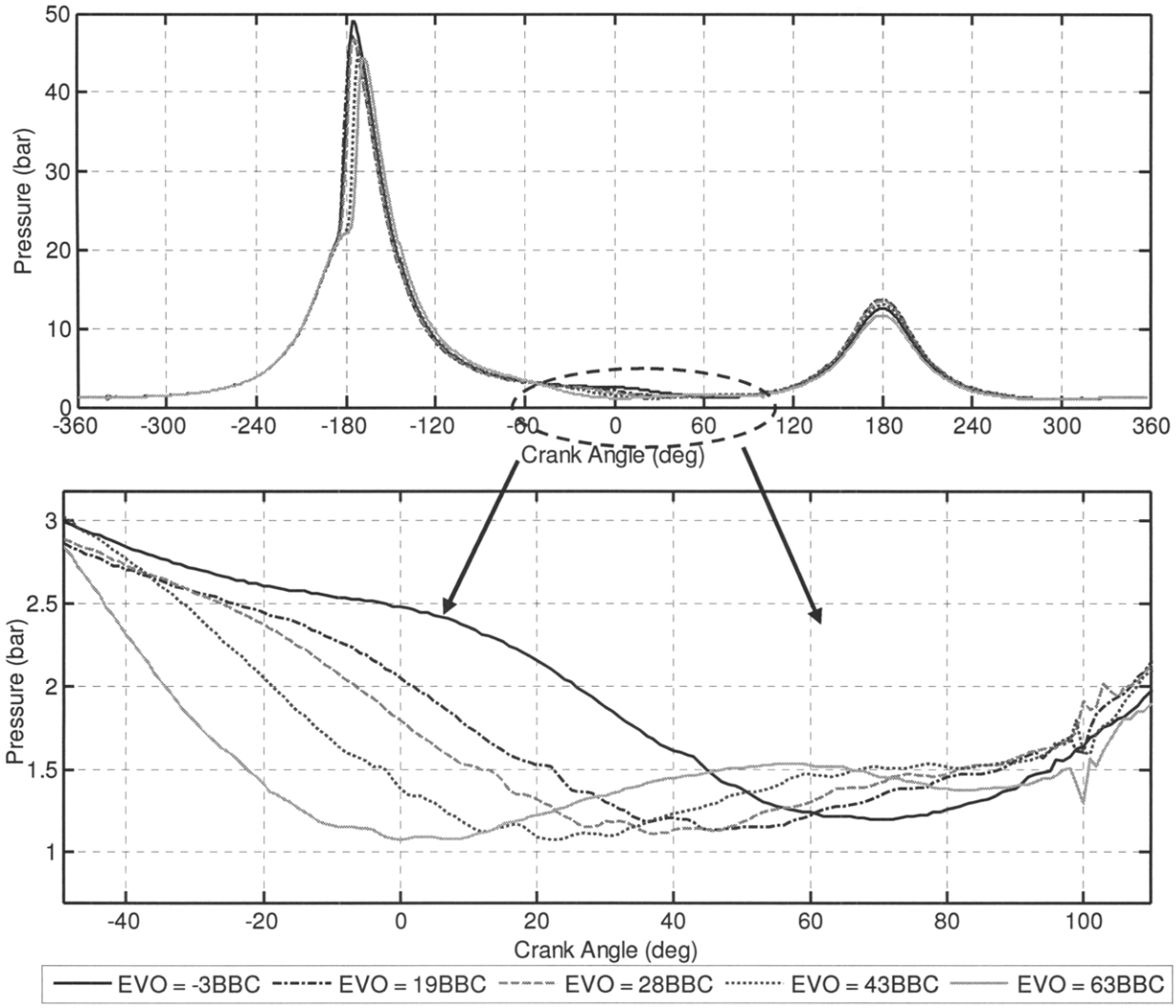


**Figure 3.56.** Averaged In-Cylinder Pressure Traces for 5 EVO Timings. Top: Full averaged cycle. Bottom: Focused on the exhaust event, circled in black in the top plot. $P_{in}$ = 1.2bar; $T_{in}$ = 120°C.

This acts to enhance the blowdown process and to force more exhaust out of the cylinder. The fuel mass per cycle varies inversely with residual fraction since the residual fraction displaces air and since the air-fuel ratio is held at stoichiometric. Varying EVO can therefore be used to vary the load. Fuel mass per cycle vs. EVO timing is shown in Figure 3.57.

It was shown in the discussion of NVO sweeps that varying the temperature of the charge can keep $PRR_{max}$ low as fueling is increased. EVO significantly affects the temperature of the trapped residuals as shown as $T_{IVO}$ in Figure 3.58. $T_{IVO}$ varies parabolically with EVO timing. Unlike in an NVO sweeps, $T_{IVO}$ moves with residual fraction and against fuel mass. In an NVO sweep, it was presumed that burning more fuel resulted in hotter exhaust which translated to

hotter residual gas. Here, while exhaust temperature may increase, this effect is dominated by other processes.

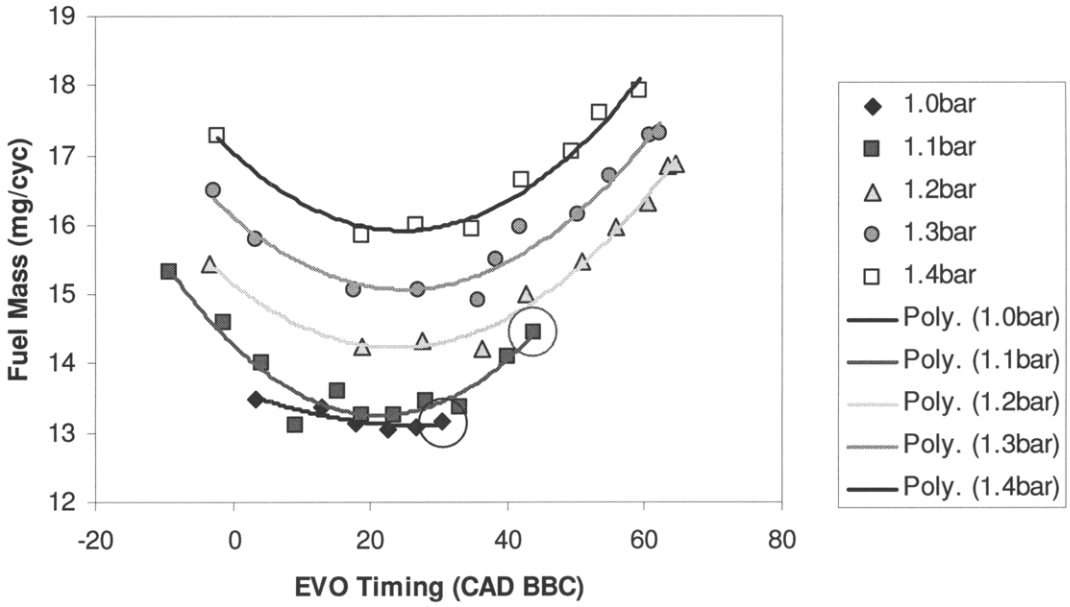


**Figure 3.57.** Fuel Mass per Cycle vs. EVO Timing. Pin = 1.0bar – 1.4bar; Tin = 120° C. Misfire limit points are circled.

Inspection of averaged pressure traces in Figure 3.56 suggests the timing of pressure waves in the exhaust account for this residual gas temperature behavior. The exhaust blowdown event generates a pressure rise in the exhaust line which causes a pressure wave to move back into the engine shortly after the blowdown. The blowdown event causes the cylinder pressure to drop from above 2.5bar to below 1.3bar. Following the yellow curve where EVO = 63° BBC, the pressure rises to more than 1.5bar and then drops to about 1.4bar before rising again just before the end of the EVC event (indicated by the vibrations in the pressure trace at 100° ABC). Note that the average exhaust pressure is 1.2bar, and the cylinder pressure drops to below this value. There appears to be a pressure wave traveling out of the cylinder then back into it and then out again. This wave behavior is evident in each of the curves however it phases later as EVO timing is phased later. The cylinder pressure and the number of moles in cylinder at EVC are prime drivers for IVO temperature. The pressure at EVC of each curve shown ranks from highest to lowest the same as the temperature at IVO does for each condition. The difference between pressures is significant, ranging from 1.4bar to 1.8bar, which is approximately a 25% difference. The IVO temperature varies by approximately 15%. This makes sense that the difference is

lower since the number of moles is acting against the trend in pressure and since heat transfer during recompression and re-expansion will reduce differences between cases.

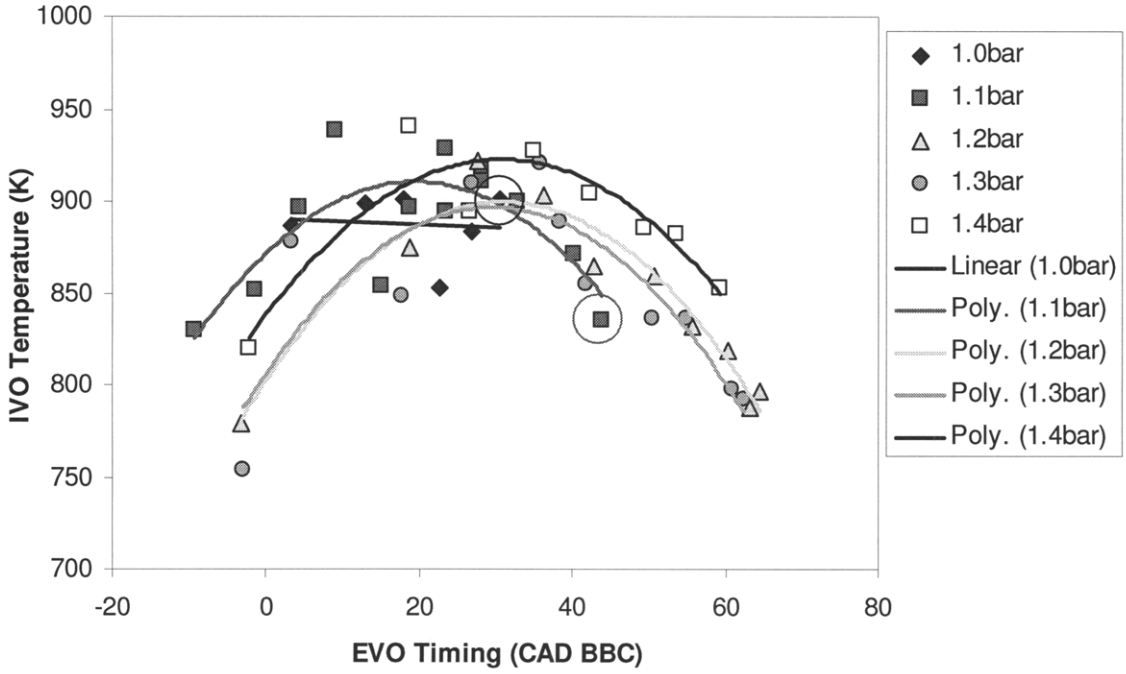


**Figure 3.58.** IVO Temperature vs. EVO Timing. $P_{in}$ = 1.0bar – 1.4bar; $T_{in}$ = 120° C. Misfire limit points are circled.

Given that the residual gas temperature drops as EVO timing is advanced and that the residual fraction also drops, it is understandable that the charge temperature would drop to the point of misfire which it does for the lowest two pressures tested as denoted by the circles. The temperature at the end of compression, shown in Figure 3.59, reflects changes in $T_{IVO}$ and also shows parabolic behavior. The IVO temperature of the residual gas reaches a maximum near the timing where the residual fraction reaches a maximum, and these factors act together to increase or decreases the charge temperature. It should be noted that resulting variations in temperature across a given sweep are stronger than for the NVO sweeps.

Temperature effects are further confirmed with the observation of combustion phasing denoted as CA10 in Figure 3.60. Combustion retards as EVO timing is advanced and also retards slightly as EVO timing is retarded past the maximum residual gas fraction point.

The maximum rate of pressure rise is plotted against the EVO timing in Figure 3.61. The rate of pressure rise does not show a strict correlation with fuel mass but instead holds flat where fuel mass increases at advanced EVO. The low charge temperature resulting from the pressure waves during the exhaust process prolong the burn duration even though fuel mass is increasing. Figure

3.62 shows NIMEP plotted against $PRR_{max}$ showing that there is opportunity to increase the high load limit by advancing EVO timing because of the residual gas cooling effects.

It should be noted that this behavior may be specific to this engine and to 1500rpm. Tuning effects will likely change from engine to engine and vary with engine speed. Nevertheless, the concept may be employed to manage charge temperature if the pressure wave behavior is well understood for a given speed and exhaust system configuration. This issue can alternatively be thought of as a liability. If EVO timing is fixed, pressure wave effects may vary with engine speed and cause the charge temperature to vary with engine speed. The operating range might be unnecessarily constrained as a result.

NIMEP and $PRR_{max}$ are contoured on EVO Timing and Intake Pressure in Figure 3.63. The map shows that load increase constrained by $PRR_{max}$ can be achieved by advancing EVO timing. This results in reducing residual gas temperature and therefore the temperature at the end of compression. This causes a reduction in $PRR_{max}$ while at the same time, fuel rate is increased.

A potential concern for advancing EVO timing is that efficiency will be reduced because pressurized burned gas will be exhausted before it can impart the maximum amount of work upon the piston. This effect if present at all is subordinate to other effects as indicated efficiency increases with EVO advance, as shown in Figure 3.64. The increase of efficiency may be caused by retarded phasing or by improved volumetric efficiency from variations of the exhaust pressure waves. Efficiency falls just before the misfire limit.

In this thesis, the EVO timing is set to 30° BBC, on one hand, to operate the engine away from the misfire limit and on the other hand, to allow the EVC timing to be advanced as much as possible. The latter motive is because the electromagnetic valve system requires a minimum valve duration for stable operation. In a production CAI engine, the EVO timing would be varied to optimize exhaust pressure wave effects to both avoid misfire and mitigate rate of pressure rise.

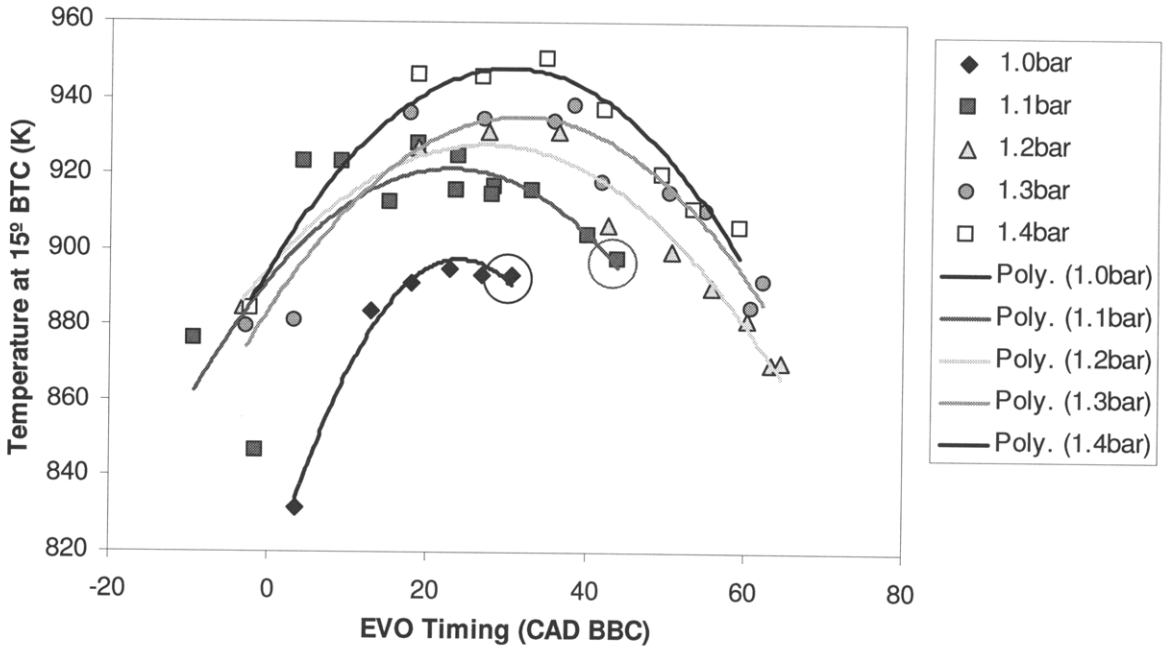


**Figure 3.59.** Temperature at 15° BTC vs. EVO Timing. $P_{in}$ = 1.0bar – 1.4bar; $T_{in}$ = 120° C. Misfire limit points are circled.

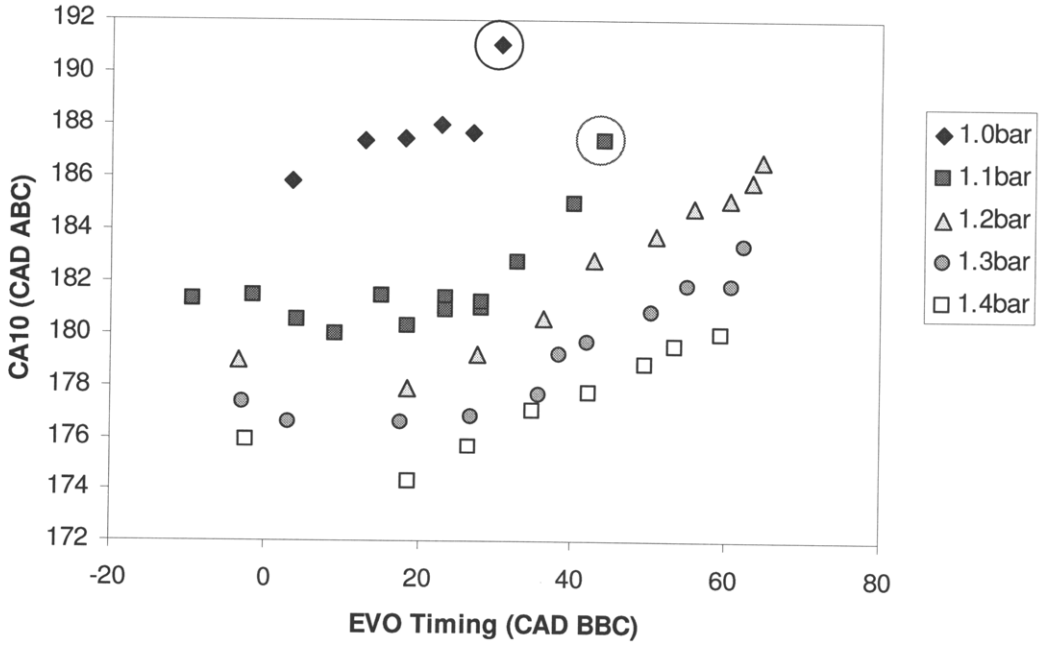


**Figure 3.60.** CA10 vs. EVO Timing. $P_{in}$ = 1.0bar – 1.4bar; $T_{in}$ = 120° C. Misfire limit points are circled.

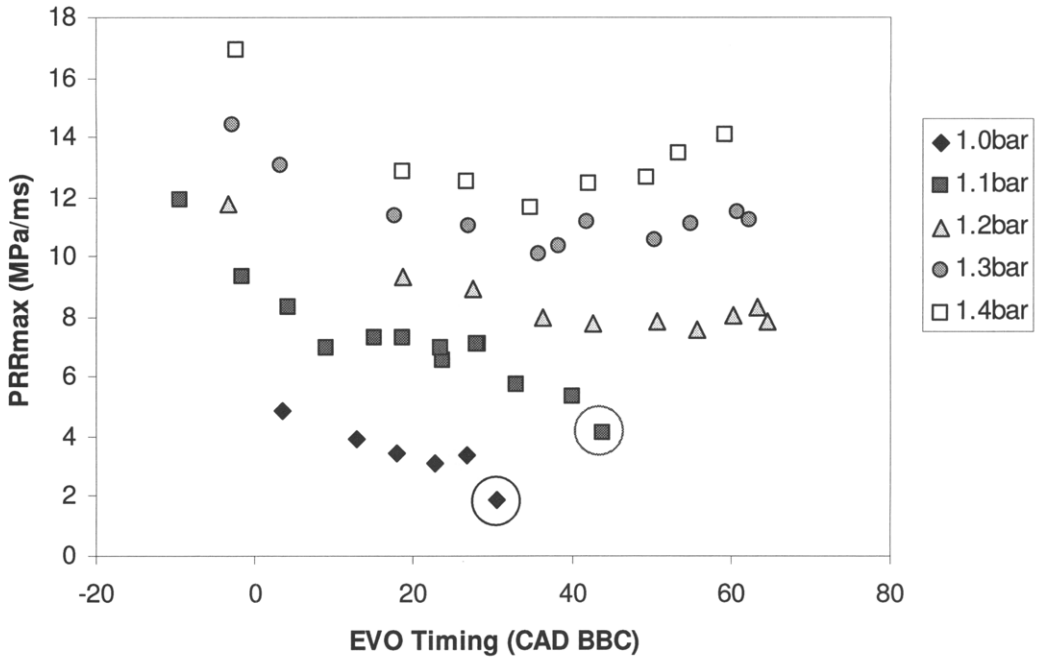


**Figure 3.61.** $PRR_{max}$ vs. EVO Timing. $P_{in}$ = 1.0bar – 1.4bar; $T_{in}$ = 120° C. Misfire limit points are circled.

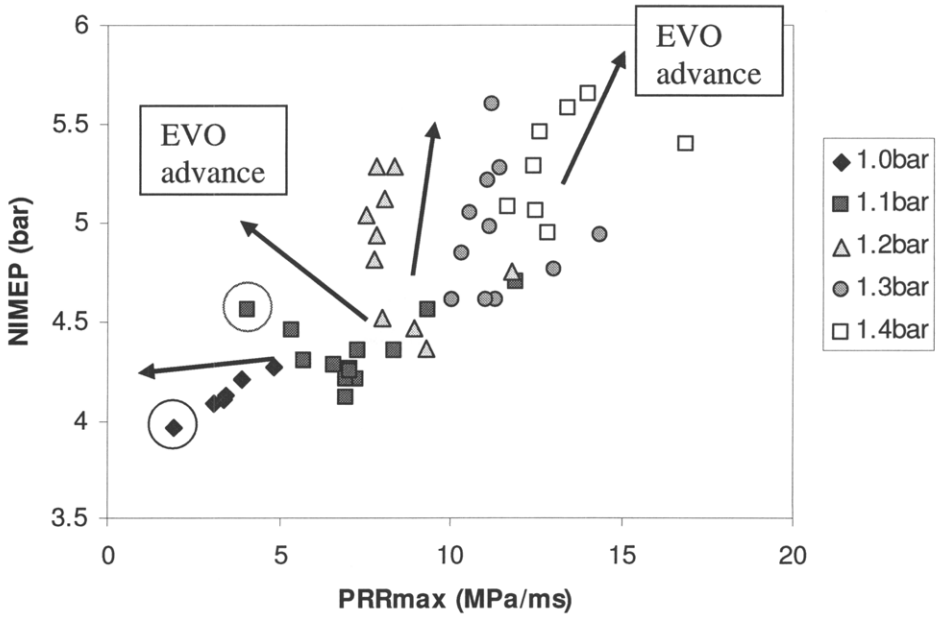


**Figure 3.62.** NIMEP vs. $PRR_{max}$. $P_{in}$ = 1.0bar – 1.4bar; $T_{in}$ = 120° C. Misfire limit points are circled. The arrows point in advancing EVO timing.

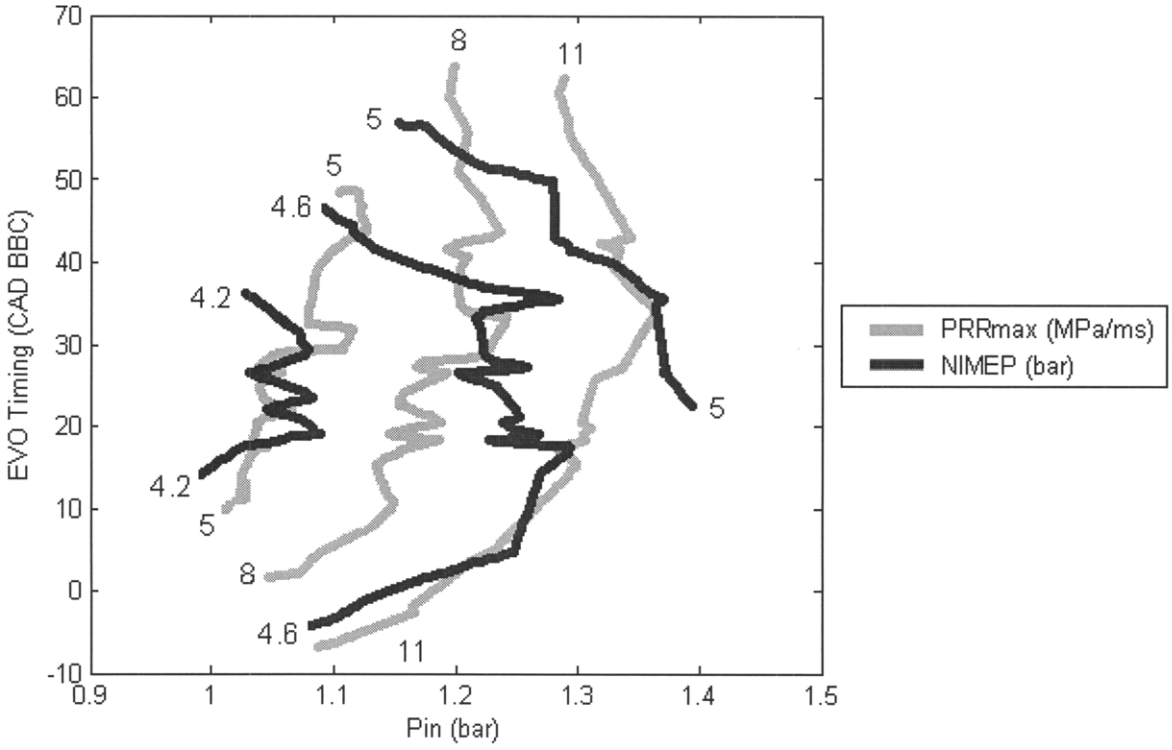


**Figure 3.63.** NIMEP and $PRR_{max}$ Contoured on EVO Timing and Intake Pressure; $T_{in}$ = 120ºC.

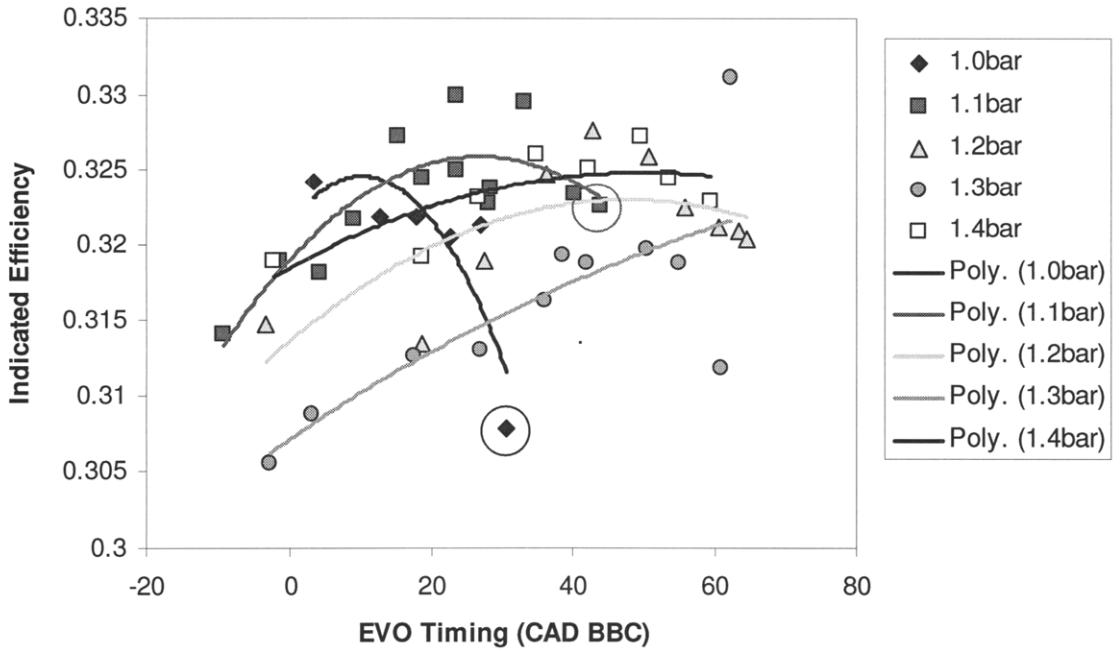


**Figure 3.64.** Indicated Efficiency vs. EVO Timing. $P_{in}$ = 1.0bar – 1.4bar; $T_{in}$ = 120º C. Misfire limit points are circled.

# Chapter 4 Trapped Residual Gas versus Recirculated Exhaust Gas

A central problem with a residual gas trapping strategy is that the residual gas may add more thermal energy to the charge than desired, especially under boosted conditions. An alternative is to use exhaust gas recirculation (EGR) where the EGR gas is cooled before introduction with the intake air. The hypothesis is that the bulk gas temperature can be reduced thus reducing the maximum rate of pressure rise for constant fueling.

This study presents data and analysis comparing the effects of EGR under varied NVO valve timing, boost pressure, and intake temperature. The valve timing settings are listed in Table 4.1 and diagrammed in Figure 4.1. The IVC timing and EVO timing were fixed, and the EVC timing was varied in 5° increments from 65° to 100° BTC. IVO timing was held symmetric about TDC to EVC. For a given intake temperature and boost setting, the EVC timing and the EGR were varied. The intake pressure was varied from 1.1bar to 1.7bar in 0.2bar increments with the intake temperature set to 120°C to show pressure effects. In the second part of the study, the intake pressure was set to 1.5bar, and the intake temperature set to 60°C, 90°C, and 120°C to show the effect of EGR and residual trapping versus intake air temperature on bulk charge temperature and on combustion.

**Table 4.1.** EGR Study Valve Timings

| Valve Operation | Timing |
|---|---|
| IVC | 30° ABC |
| EVO | 30° BBC |
| EVC | 65° to 100° BTC |
| IVO | 65° to100° ATC |

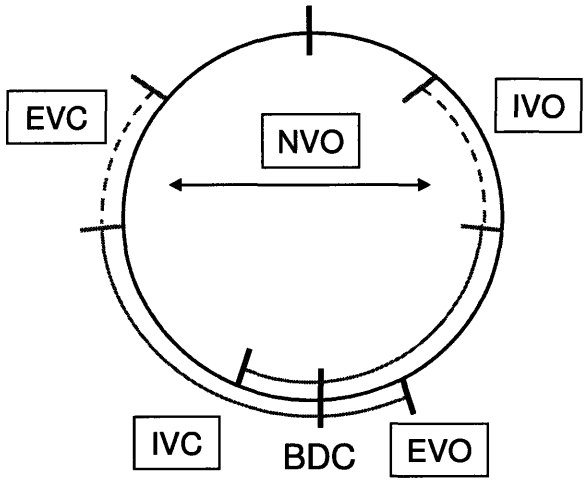


**Figure 4.1.** Diagram of Valve Timings for the EGR Study

To vary the flow of gas through the EGR loop into the intake, the exhaust pressure was set to be 30mbar higher than the intake temperature for all data in this study. Note also that the EGR gas and intake air mix upstream of the thermocouple measuring intake temperature so now the intake

temperature represents the temperature of this mixture of EGR gas and air rather than simply intake air.

EGR gas and trapped residual gas can be varied separately. The effect of EGR is assumed to be dilution without increased temperature so the residual gas, not the EGR gas, is more relevant to combustion since it adds thermal energy to the incoming charge. To discuss the effects of trapping residual gas versus recirculating it, the term residual-burned fraction is introduced to be the residual fraction divided by the EGR fraction as in Equation 4.1 where residual fraction and EGR fraction are defined in Equation 4.2 and 4.3, respectively.

$$x_{res-burned} = \frac{x_{res}}{x_{burned}} = \frac{x_{res}}{x_{EGR} + x_{res}} \tag{4.1}$$

$$x_{res} = \frac{n_{trapped}}{n_{trapped} + n_{fuel} + n_{air} + n_{EGR}} \tag{4.2}$$

$$x_{EGR} = \frac{n_{EGR}}{n_{trapped} + n_{fuel} + n_{air} + n_{EGR}} \tag{4.3}$$

$n_{EGR}$ is the number of moles per cycle recirculated from the EGR loop. The EGR fraction $x_{EGR}$ is the moles of gas in-cylinder from the EGR loop dived by the total number of moles.

## 4.1 Effects of EGR vs. Residuals

The effects of EGR are introduced by showing various metrics plotted on contour maps of $x_{res\text{-}burned}$ versus $x_{burn}$ with intake temperature set to 120°C and intake pressure set to 1.7bar. In this way, if $x_{res\text{-}burned}$ is 1 then there is no EGR, and all of the burned gas is residual gas. If it is 0, all of the burned gas has been recirculated versus trapped. The contour plots show the points at the misfire limit in diamonds.

Fuel mass per cycle is shown to vary only with burned gas fraction in Figure 4.2. This confirms the expectation that burned gas displaces air the same amount regardless of whether it was trapped or recirculated. At high EGR near 53% burned gas fraction, there also appears to be very slight dependence of fuel flow on $x_{res}/x_{burn}$, and this could be because the charge is cooler with more EGR so the intake air is cooled upon entering the cylinder causing charge density to increase.

Before exploring how the average charge temperature varies, the trapped residual temperature at IVO is shown in Figure 4.3.

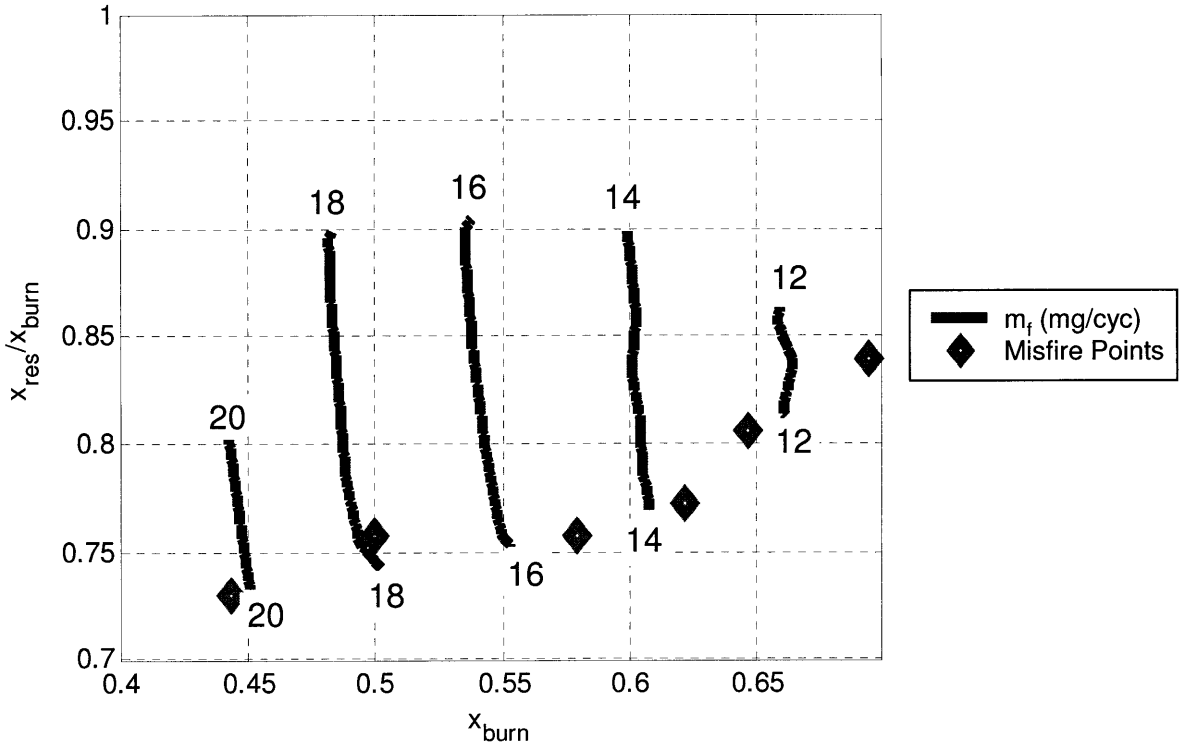


**Figure 4.2.** Fuel Mass per Cycle vs. $x_{res}/x_{burn}$ vs. $x_{burn}$. $T_{in}$ = 120°C; $P_{in}$ = 1.7bar.

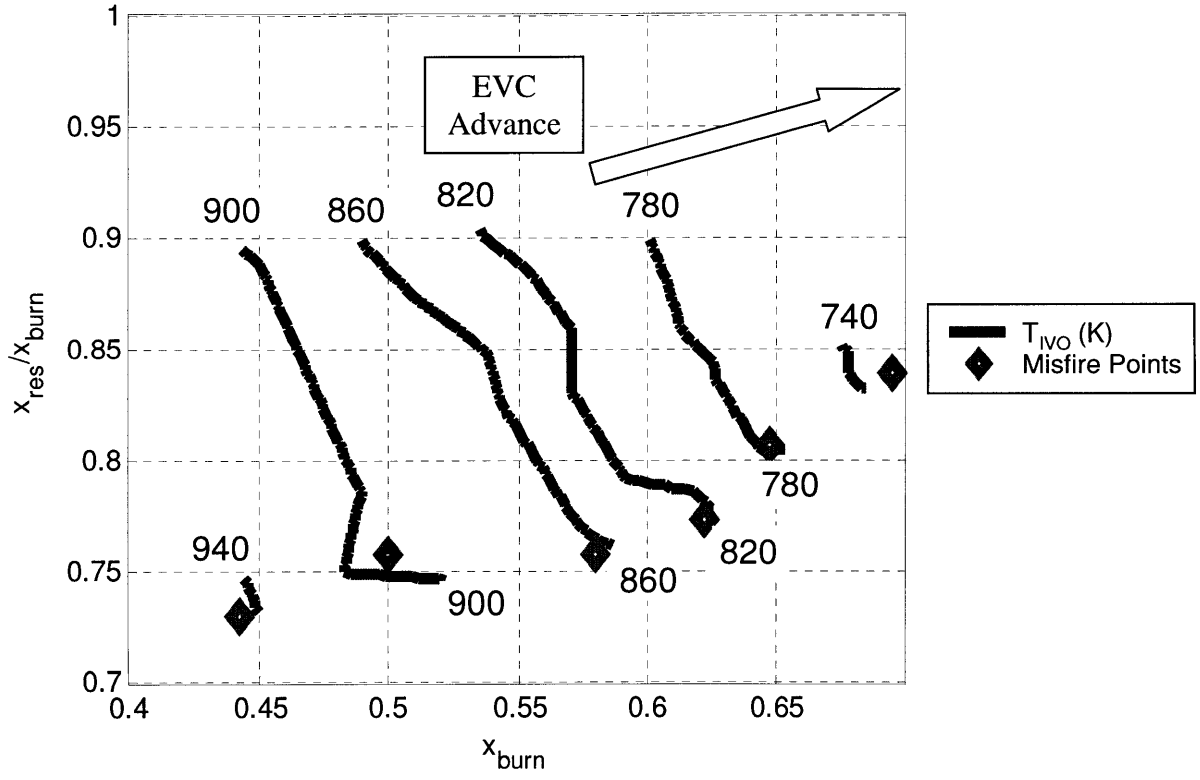


**Figure 4.3.** Temperature at IVO vs. $x_{res}/x_{burn}$ vs. $x_{burn}$. $T_{in}$ = 120°C; $P_{in}$ = 1.7bar.

$T_{IVO}$ decreases strongly with burned gas fraction and decreases less strongly with residual-burned fraction. As previously noted, trapped residual temperature drops with increased trapped residuals because less fuel is burned per cycle. Trapped residual temperature may decrease with residual fraction also because decreasing trapped residuals reduces heat transfer during the recompression process.

The bulk temperature at 15° BTC is determined by the trapped residual gas, which is hot, and by the intake air and EGR gas, which is considerably colder. At constant residual-burned fraction, varied burned gas fraction is simply an NVO sweep, and the temperature peaks at a mid-range value and drops as residual fraction is high and low, as shown in Figure 3.16, for example. The contour plot in Figure 4.4 shows temperature at 15° BTC peak as $x_{burn}$ is varied at constant $x_{res}/x_{burn}$, for example at 85%. As the residual-burned fraction is decreased, the temperature decreases, and this reflects the increasing fraction of gas that is cooled and reintroduced through the intake.

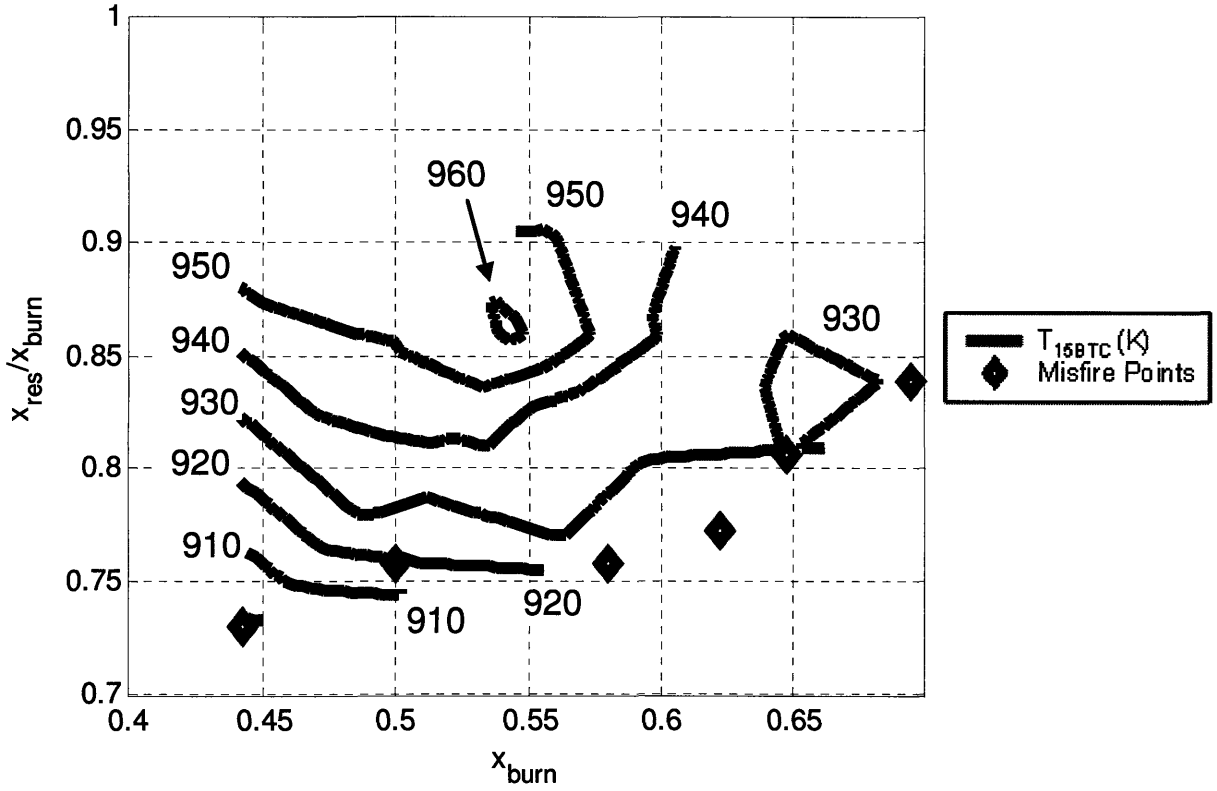


**Figure 4.4.** Temperature at 15° BTC vs. $x_{res}/x_{burn}$ vs. $x_{burn}$. $T_{in}$ = 120°C; $P_{in}$ = 1.7bar.

The effect of temperature can be clearly seen in the combustion phasing behavior, shown in Figure 4.5. For the range of residual-burned fraction plotted, CA10 retards from approximately

177° to 183° where the misfire limit is. When the charge is colder, combustion phases later. Also, moving along constant residual-burned fraction via varied valve timing causes the temperature to drop at high $x_{burn}$ fraction, which results in the misfire limit on the right side of the plot. This forms a low-load misfire limit. A high-load misfire limit is not encountered on the left side of the map because engine knock reached severe levels before the misfire limit was encountered.

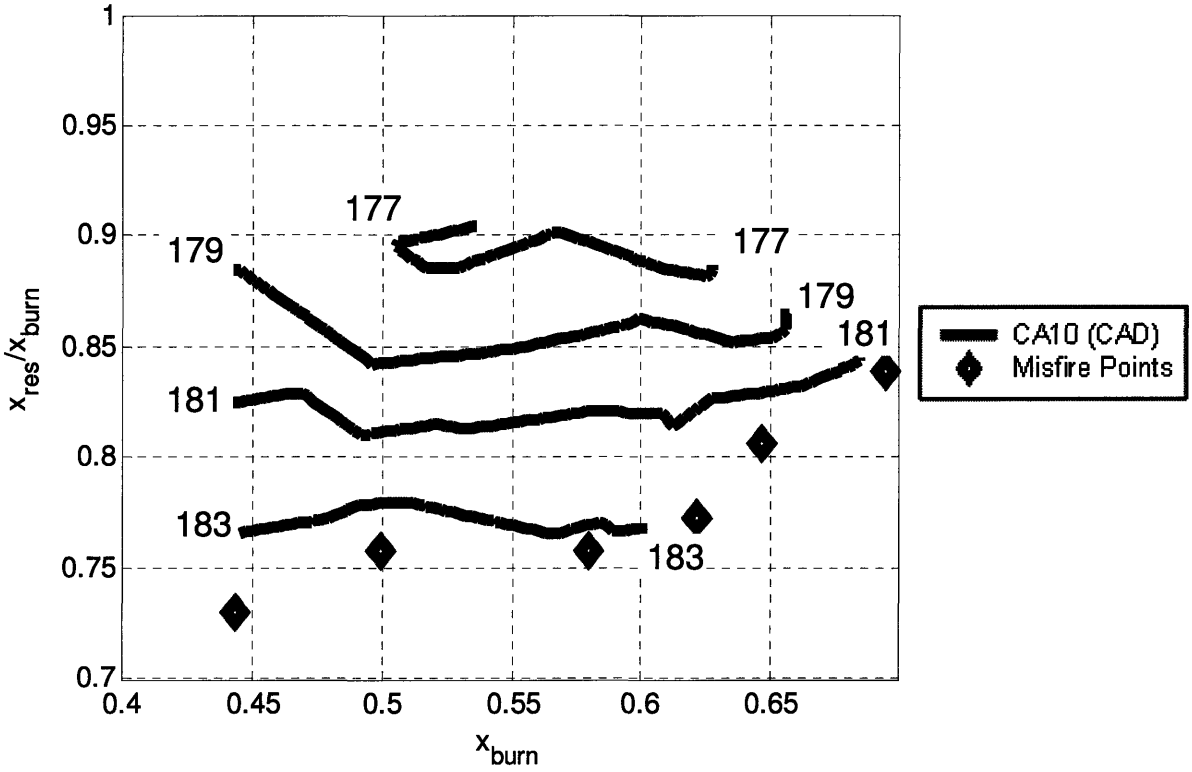


**Figure 4.5.** CA10 vs. $x_{res}/x_{burn}$ vs. $x_{burn}$. $T_{in}$ = 120°C; $P_{in}$ = 1.7bar.

The map of fuel mass in Figure 4.2 showed that fuel rate is constant where burned gas fraction is constant so the lowest $PRR_{max}$ for a given fuel rate occurs at the misfire limit, as circled. Here, EGR gas is flowed as high as possible to cool down the charge as much as possible just above the misfire limit. Under EGR operation, the high load limit will always occur at the misfire limit, and the high load limit will be maximized with the maximum rate of EGR.

Indicated efficiency is mapped in Figure 4.7 and features a relatively flat map. Efficiency is highest where residual-burned fraction is lowest. This could be because combustion is phased later and is more optimally positioned.

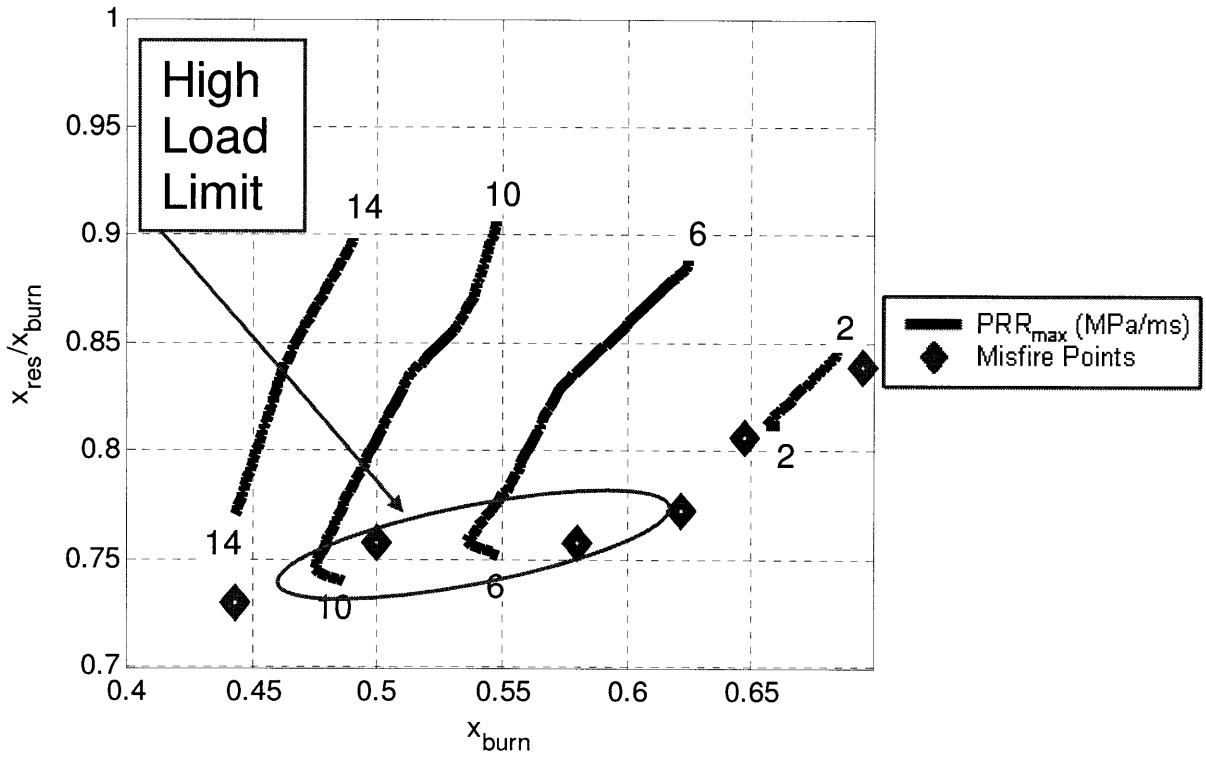


**Figure 4.6.** $PRR_{max}$ vs. $x_{res}/x_{burn}$ vs. $x_{burn}$. $T_{in}$ = 120°C; $P_{in}$ = 1.7bar.

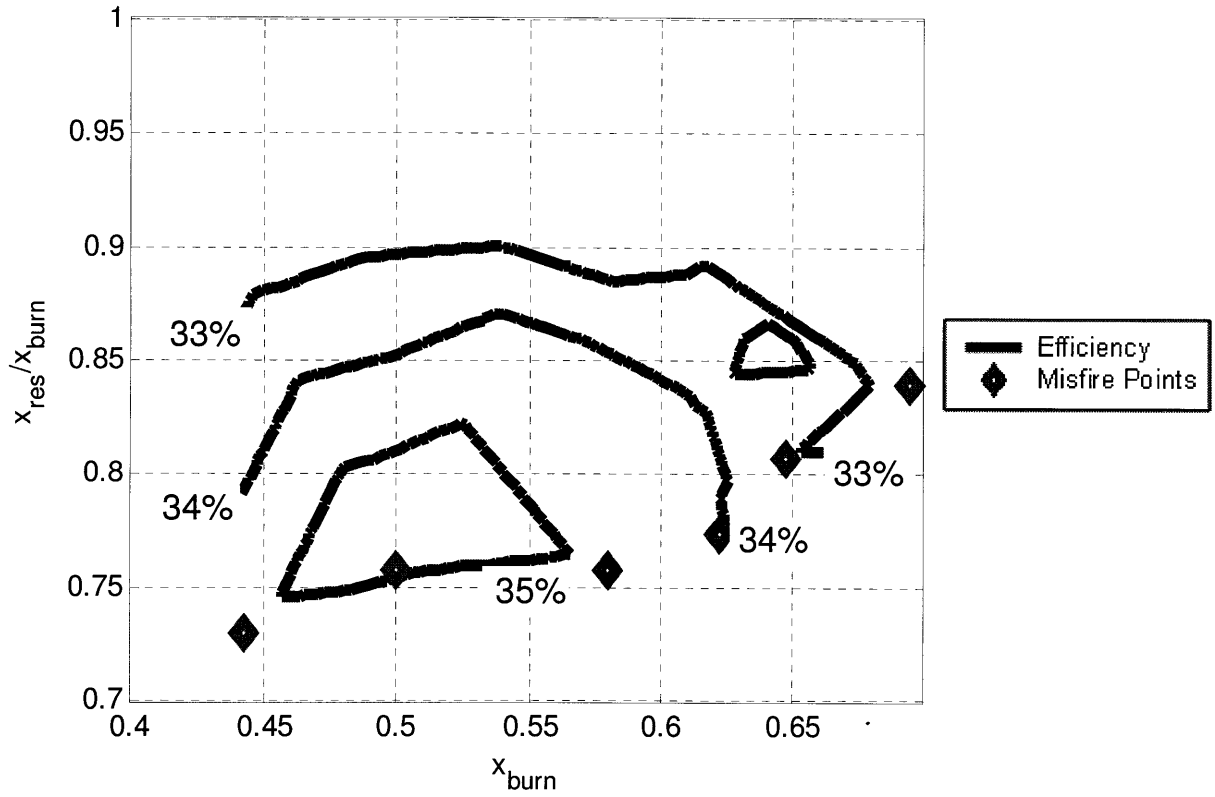


**Figure 4.7.** Indicated Efficiency vs. $x_{res}/x_{burn}$ vs. $x_{burn}$. $T_{in}$ = 120°C; $P_{in}$ = 1.7bar.

## 4.2 Boost Pressure and EGR

The contour maps presented in Section 4.1 feature $P_{in}$ = 1.7bar. Analogous maps were generated for $P_{in}$ = 1.1bar, 1.3bar, 1.5bar with $T_{in}$ = 120°C, and these maps show similar trends to those found at 1.7bar so are not shown. The trends of fuel mass, $T_{IVO}$, $T_{15BTC}$, CA10, $PRR_{max}$, and efficiency were the same for the lower boost pressure settings as for 1.7bar with minor variation.

The location of the misfire limit on the map was significantly affected by boost level. In Section 3.3.2, it was shown that increasing intake pressure allows the intake temperature or trapped residual fraction to be reduced without misfire. In this section, the concept is extended that boosting the engine allows a reduction in charge temperature via increased EGR. The misfire points for four boost pressure levels are plotted on a map of residual-burned fraction and total burned gas fraction in Figure 4.8.

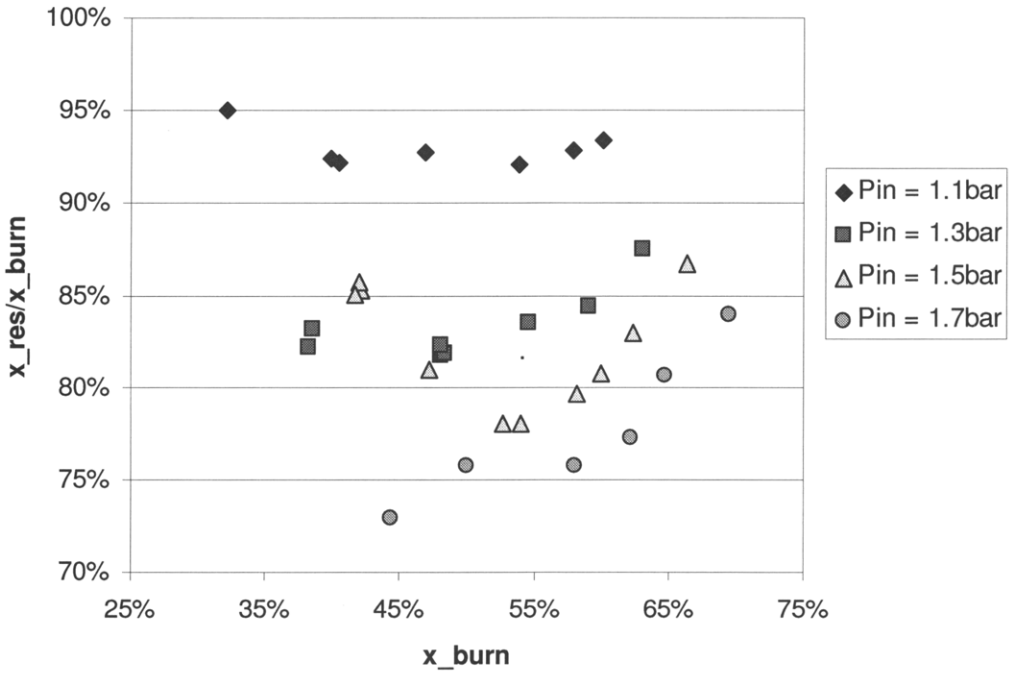


**Figure 4.8.** Misfire Points Plotted on $x_{res}/x_{burn}$ vs. $x_{burn}$ for Four Boost Pressures. $T_{in}$ = 120°C.

As the boost level is increased, misfire occurs at a lower $x_{res}/x_{burn}$. The engine will tolerate more EGR with increased boost. Boost is increased by 55% from 1.1bar to 1.7bar, and at 50% burned gas fraction, this allows the residual-burned fraction to reduce from 93% to 76%. It can also be seen that the shape of each curve changes with boost pressure. Observing the 1.1bar, 1.3bar, and 1.7bar curves shows that at low burned gas fraction, the misfire limit is extended more with boost than at high burned gas fraction. The 1.5bar curve features a different trend with repeatable

data. Where $x_{burn}$ is high, each curve follows roughly the same trend. Where $x_{burn}$ is low, the trends are not consistent between curves.

### 4.2.1 Load and Maximum Rate of Pressure Rise with Boost and EGR

There is clearly a trade-off between maximum rate of EGR and intake pressure at the misfire limit, but one condition is not necessarily better considering the goal of extending the high load limit. In Figure 4.9, fuel mass per cycle is plotted against total burned gas fraction for the misfire points for the four boost pressures under consideration. Fuel mass increases with boost, and fuel mass increases as the total burned gas fraction decreases.

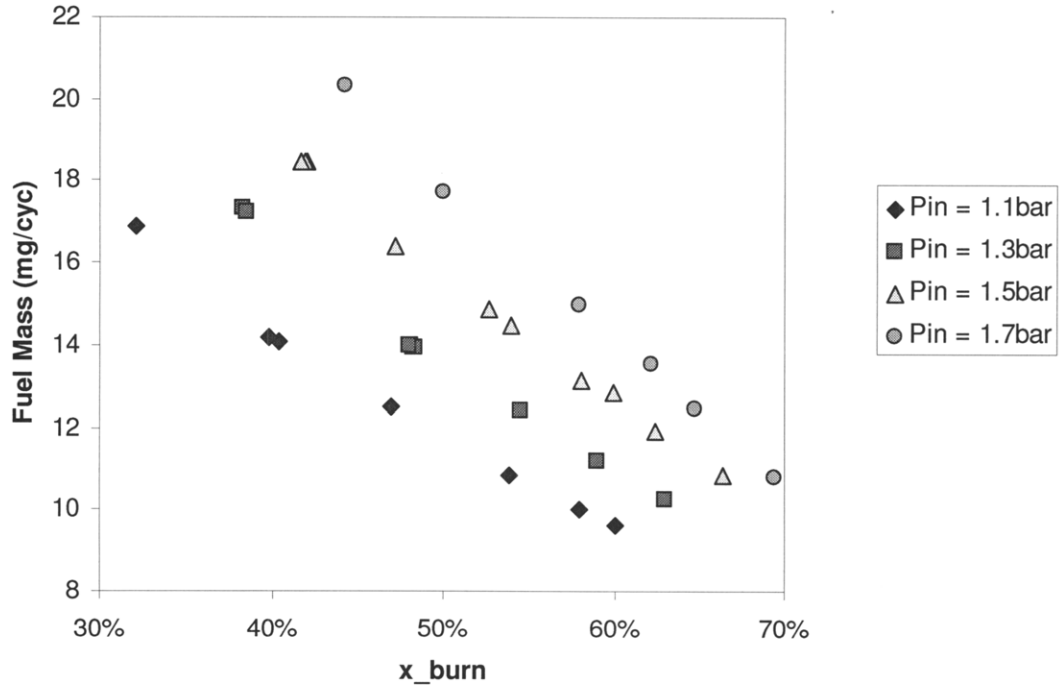


**Figure 4.9.** Fuel Mass per Cycle vs. Burned Gas Fraction for Misfire Points with EGR for Four Boost Pressures. $T_{in}$ = 120°C.

Maximum rate of pressure rise also increases with boost, as illustrated in Figure 4.10, so it is unclear whether or not boost helps increase load without increasing burn rate. Figure 4.11 shows maximum rate of pressure rise plotted against fuel mass. All four curves collapse to one curve showing there is neither benefit nor detriment to boosting. There does seem to be a small benefit to boosting at high fuel rate, but a typical $PRR_{max}$ limit is 5MPa/ms where the curves are quite close together. The decision of whether or not to boost the engine must therefore be decide by concerns other than the high-load limit.

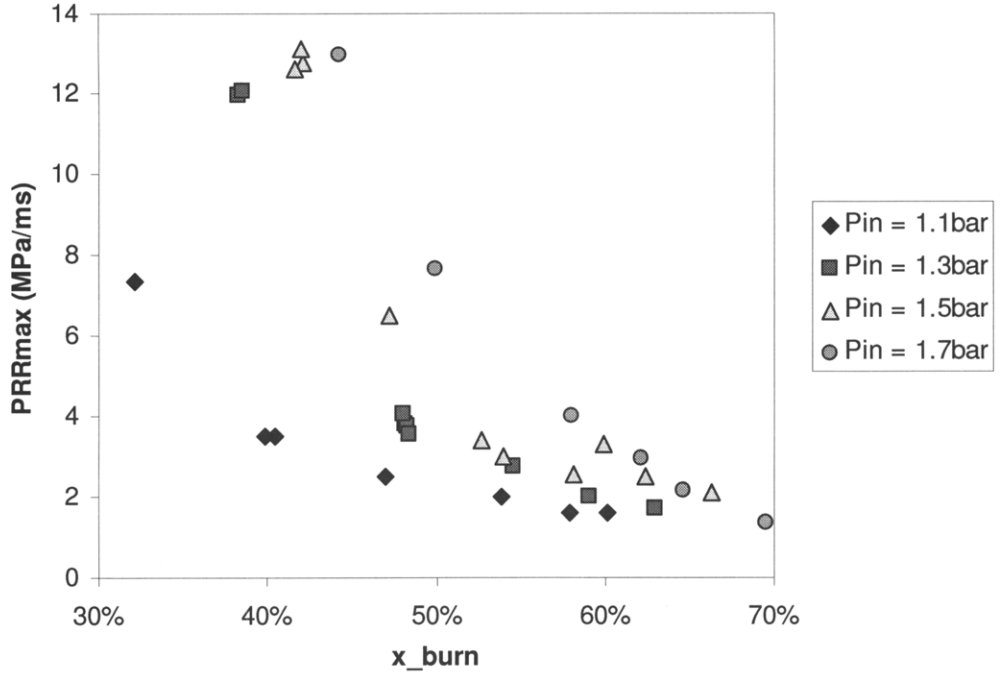


**Figure 4.10.** $PRR_{max}$ vs. $x_{burn}$ for the Misfire Points with EGR for Four Boost Pressures. $T_{in}$ = 120°C.

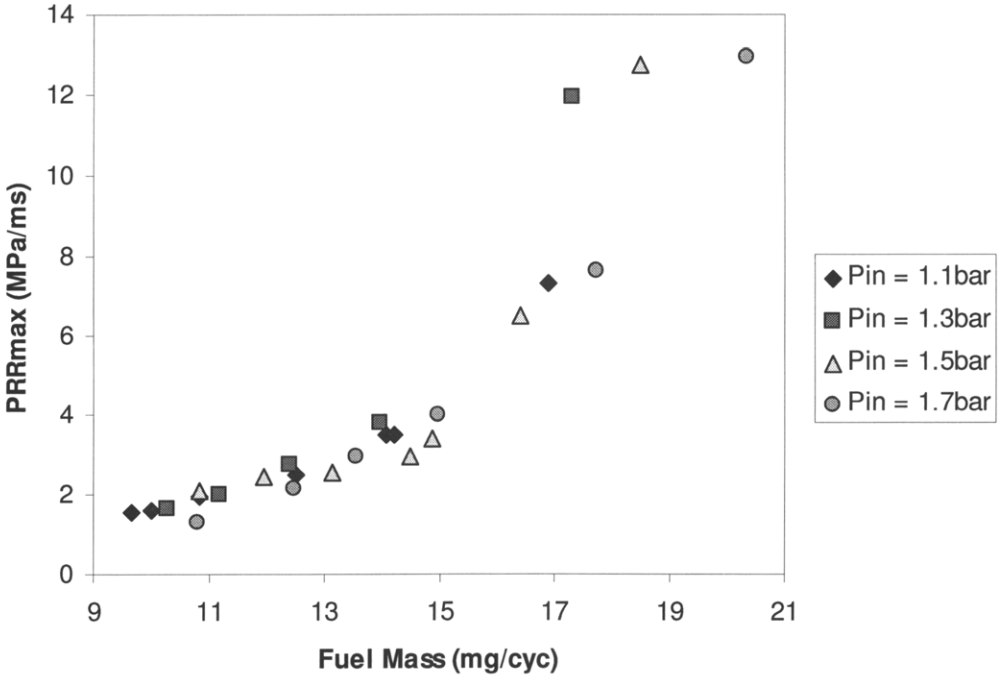


**Figure 4.11.** $PRR_{max}$ vs. Fuel Mass at the EGR Misfire Limit for Four Pressures. $T_{in}$ = 120°C.

The behavior of $PRR_{max}$ and fuel mass in Figure 4.11 shows clearly the trade-off between boost and EGR. Boost acts to increase charge density and thereby add fuel and to increase

temperature at the end of compression. EGR acts primarily to reduce charge temperature. At the misfire limit, the increase of charge temperature from increasing boost is cancelled out by an increased amount of EGR. The thermal energy may be assumed to be at some critical threshold characteristic of the misfire limit, implying that temperature effects dominate the effect of varied oxygen fraction. If the temperature effects of boost are cancelled out by EGR, then the only other effect is increased fuel. In this data set, $PRR_{max}$ has been shown to be dependent on fuel rate and temperature, as illustrated by Figure 4.6. If the temperature is held constant across conditions, particularly at a misfire temperature, then there should be no variation between $PRR_{max}$ values if the fuel mass is also held constant.

The other way to extend the high load limit than increasing fueling is to increase efficiency. Indicated efficiency is plotted against total burned gas fraction in Figure 4.12. The efficiency is shown to increase with boost, although the 1.5bar curve somewhat clouds the conclusion. Efficiency increases three percentage points from 1.1bar to 1.7bar so there is a modest load limit gain for boosted operation with EGR.

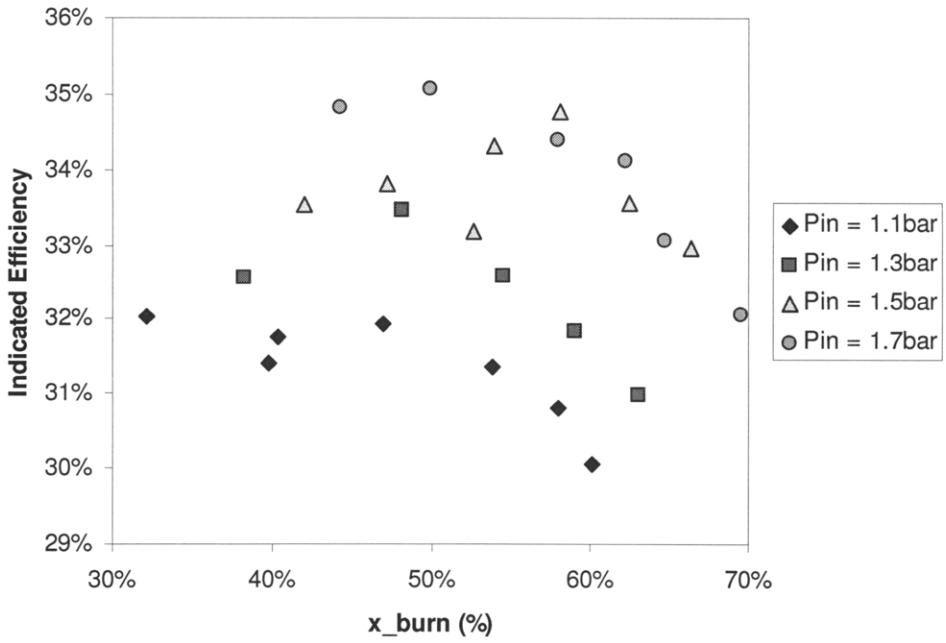


**Figure 4.12.** Indicated Efficiency vs. Burned Gas Fraction for Four Pressures. $T_{in}$ = 120°C.

This efficiency increase with boost is likely due to increased volumetric efficiency. The pressure difference between intake air and the cylinder pressure is a more significant positive impact that the pressure difference between the cylinder and the exhaust during the exhaust event. The

cylinder pressures are still considerably higher than the exhaust pressure. The variations of efficiency with EGR-burned fraction are due to combustion phasing. Figure 4.13 indicates a roughly linear dependence of efficiency on phasing up to 186° ABC.

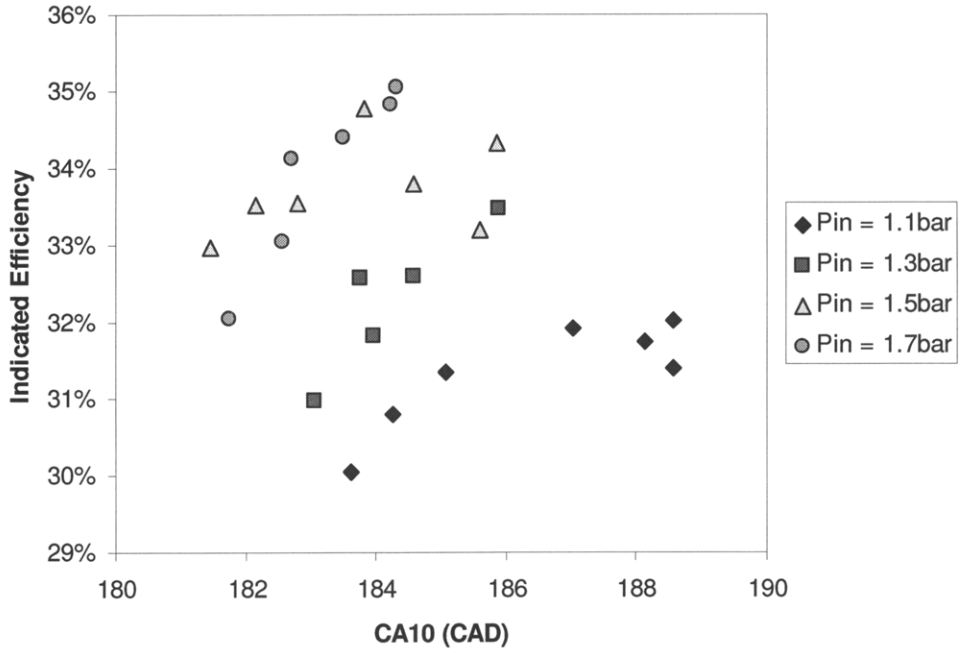


**Figure 4.13.** Indicated Efficiency vs. CA10 for the Misfire Points at Four Intake Pressures. $T_{in}$ = 120°C.

### 4.2.2 Temperature, Phasing, and Cyclic Variability Under Boost and EGR

The misfire limit occurs at a higher level of EGR with increased boost, and this implies that the boost is offsetting a drop in charge temperature at IVO. Temperature at 15° BTC, as shown in Figure 4.14, indicates that there is a noticeable temperature difference between the 1.1bar pressure curve condition and the 1.7bar pressure curve. Temperature increases with boost but not very much. The situation between 1.1bar and 1.7bar is less clear. At 1.1bar, the temperature peaks at a mid-range burned gas fraction and decreases at high and at low burned gas fraction. This reflects the temperature variation with residual fraction of the NVO sweep. This behavior is less clear for higher pressures because the burned gas fraction is composed of lower fraction of residual gas since the EGR rate is higher.

The temperature curves at the misfire limit do not demonstrate clear trends or the same trends for different pressures. There may be some error in the temperature estimate, or the misfire limit does not strongly depend on bulk temperature. Whether or not ignition occurs should depend on the hottest parcel of gas igniting, not the average parcel. Once the hottest parcel does ignite then the remainder of the charge should be compressed to the point of autoignition. Variations in EGR

rate, residual fraction, and boost level likely affect the thermal stratification characteristics. This would decouple variations in the average temperature from variations in the maximum temperature and compromise the bulk temperature as a metric for misfire.

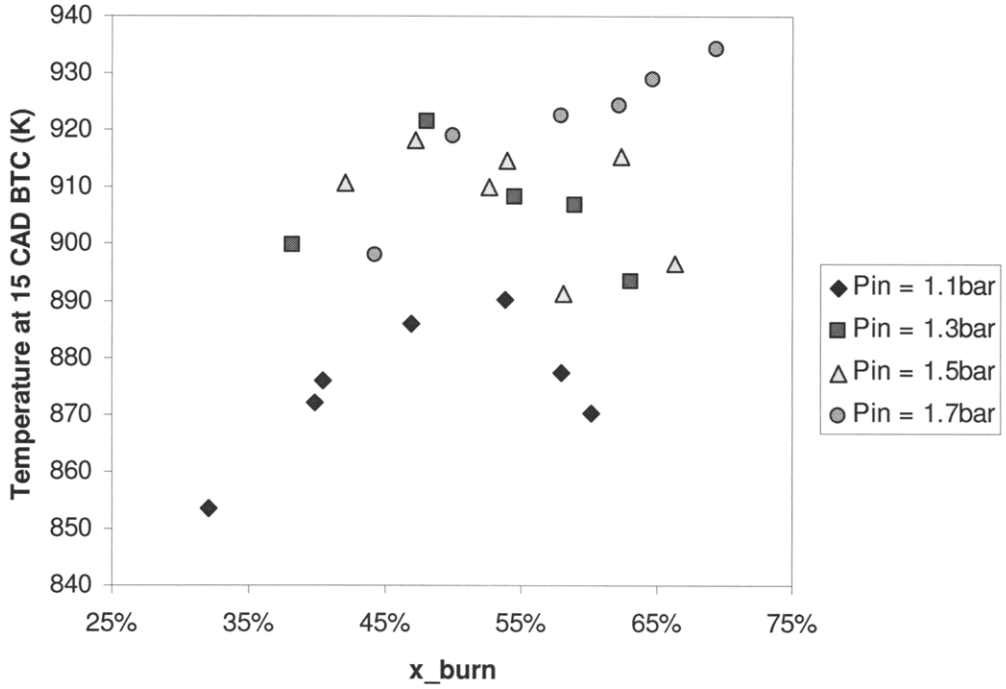


**Figure 4.14.** Temperature at 15° BTC vs. Total Burned Gas Fraction for the Misfire Points at Four Boost Pressures. $T_{in}$ = 120°C.

Combustion phasing is shown in Figure 4.15 against residual fraction for the EGR misfire points at the four pressures. It is plotted against residual fraction instead of burned gas fraction because there appear to be two regimes with a transition determined by residual fraction. When the residual fraction is higher than approximately 43%, denoted by the dashed line, combustion phasing retards linearly with decreased residual gas fraction. When residual fraction is lower than 43%, the trend changes, and it changes differently for each pressure curve. It is also observed that misfire occurs at a later CA10 for higher boost, consistent with the misfire data without EGR.

The dependence on residual fraction, rather than total burned gas fraction or compression temperature, indicates the influence of a stratification effect. At high residual fraction, the fuel rate is low so the residual gas is comparatively not hot. Also, the incoming oxygen and fuel have probable access to the hot residual gas since it occupies a majority of the cylinder volume. At low residual fraction, the residual gas is comparatively much hotter since the fuel rate is higher, especially at boosted operation. The incoming oxygen and fuel have considerably less probable

access to the hot residual gas because a substantial fraction of the cylinder volume is occupied by cooled EGR gas. The resulting comparison is that at low residual fraction, the heat transfer between oxygen and hot residuals features a higher temperature difference and a lower probability compared to the high residuals case. The interaction between residuals and fresh oxygen will depend on fluid motion increasingly as the residual fraction is reduced. Since the charge motion is turbulent, the low residuals case is far more susceptible to cycle-by-cycle variability than the high residuals case.

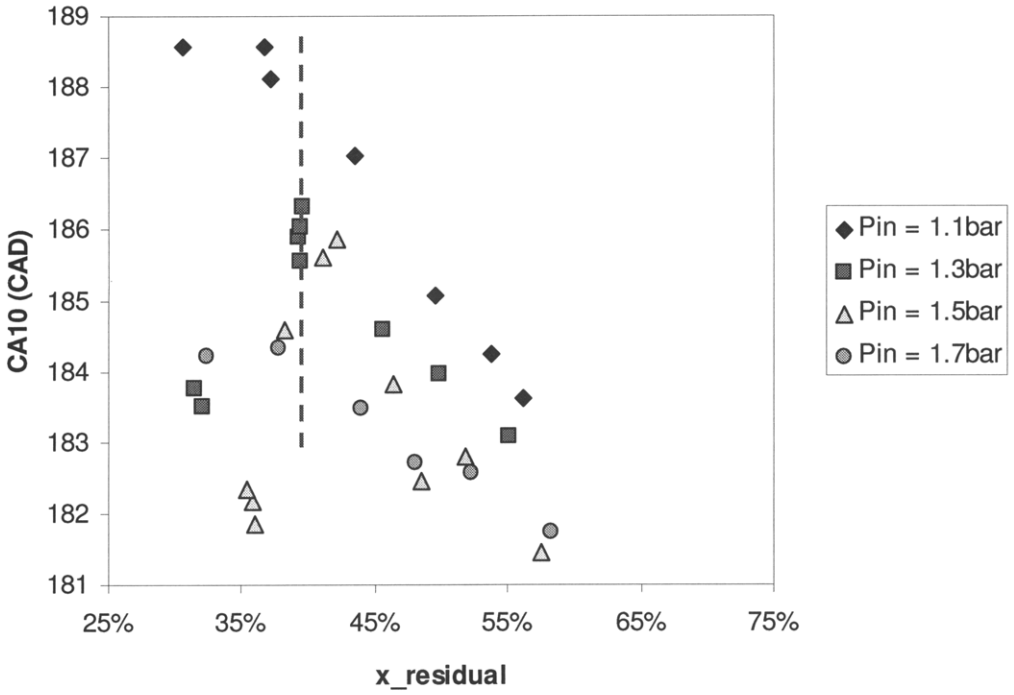


**Figure 4.15.** CA10 vs. Residual Gas Fraction for the Misfire Points at Four Boost Pressures.

The supposition that cyclic variability may account for different trends is supported by trends of coefficient of variation of the maximum rate of pressure rise (COV of $PRR_{max}$) as defined as in Equation 4.1. $\sigma_{PRRmax}$ is the standard deviation, and $\bar{x}_{PRR\,max}$ is the mean.

$$COVofPRR_{max} = \frac{\sigma_{PRR\,max}}{\bar{x}_{PRR\,max}} \cdot 100\% \tag{4.1}$$

COV of $PRR_{max}$ is mapped on contour plots of $x_{res}/x_{burn}$ vs. $x_{res}$ in Figure 4.16, Figure 4.17, Figure 4.18, and Figure 4.19 at $P_{in}$ = 1.1bar, 1.3bar, 1.5bar, and 1.7bar, respectively. Each plot shows low COV of $PRR_{max}$ where residual fraction is high and then high COV of $PRR_{max}$ where residual fraction is low. Dashed lines are overlaid to mark the transition between these two

regimes, and the transitions each appear to be at approximately 45% residual fraction, just as in the combustion phasing plot of Figure 4.15.

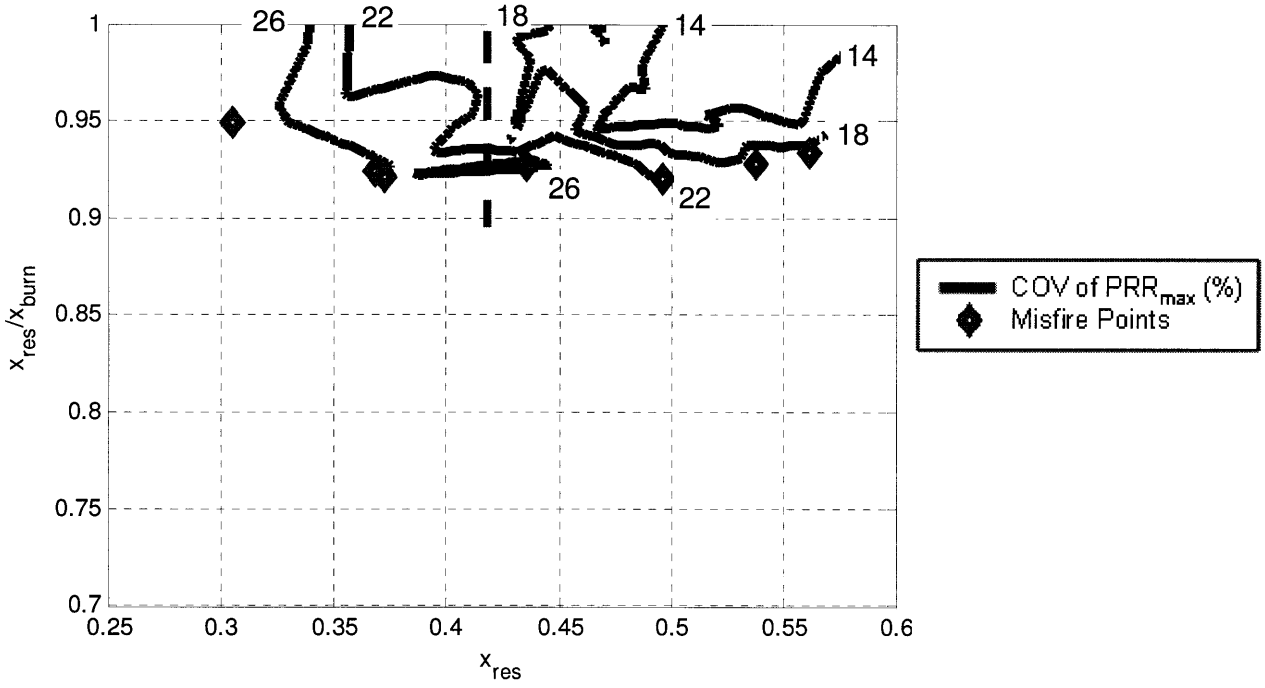


**Figure 4.16.** COV of $PRR_{max}$ Contoured on $x_{res}/x_{burn}$ vs. $x_{residual}$ for $T_{in}$ = 120°C, $P_{in}$ = 1.1bar.

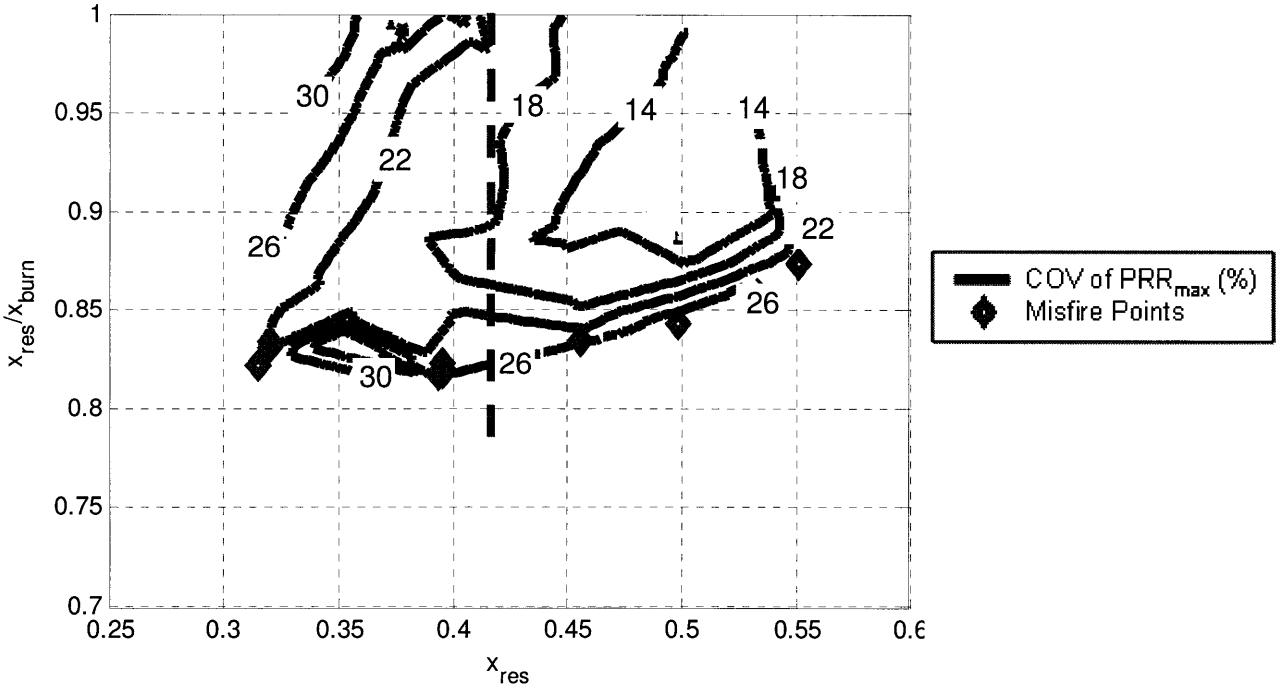


**Figure 4.17.** COV of $PRR_{max}$ Contoured on $x_{res}/x_{burn}$ vs. $x_{residual}$ for $T_{in}$ = 120°C, $P_{in}$ = 1.3bar.

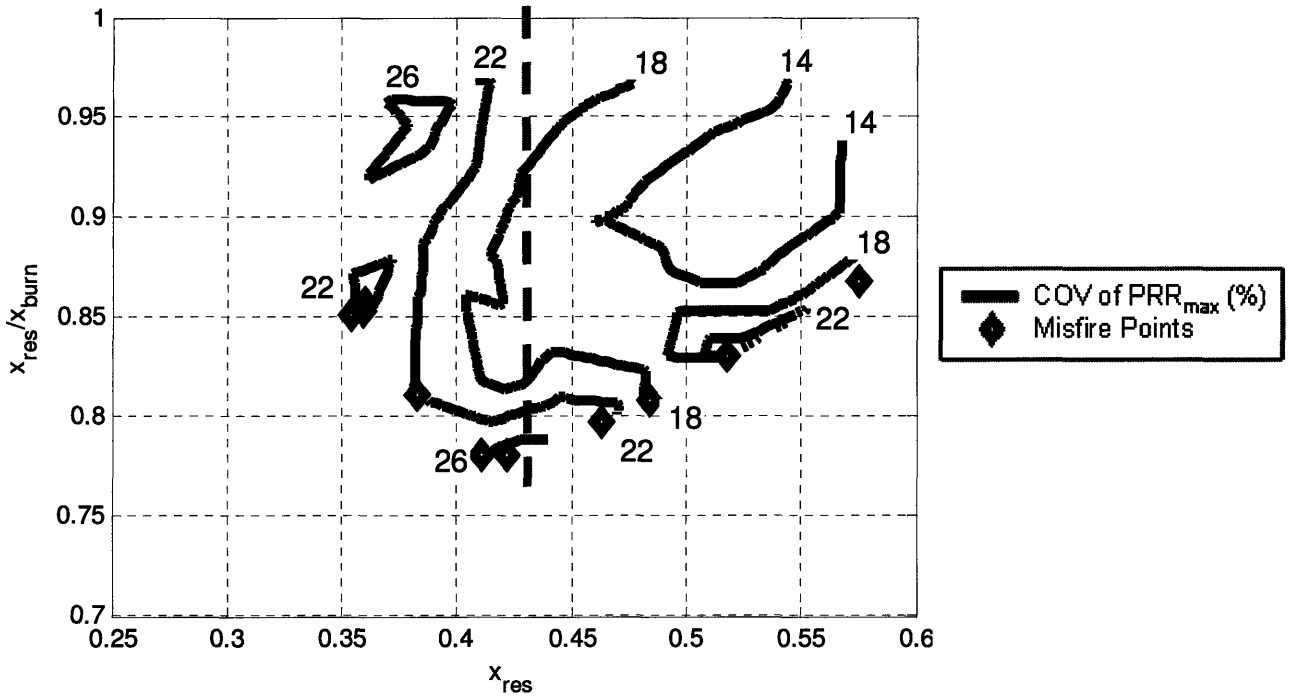


**Figure 4.18.** COV of $PRR_{max}$ (%) Contoured on $x_{res}/x_{burn}$ vs. $x_{residual}$ for $T_{in}$ = 120°C, $P_{in}$ = 1.5bar.

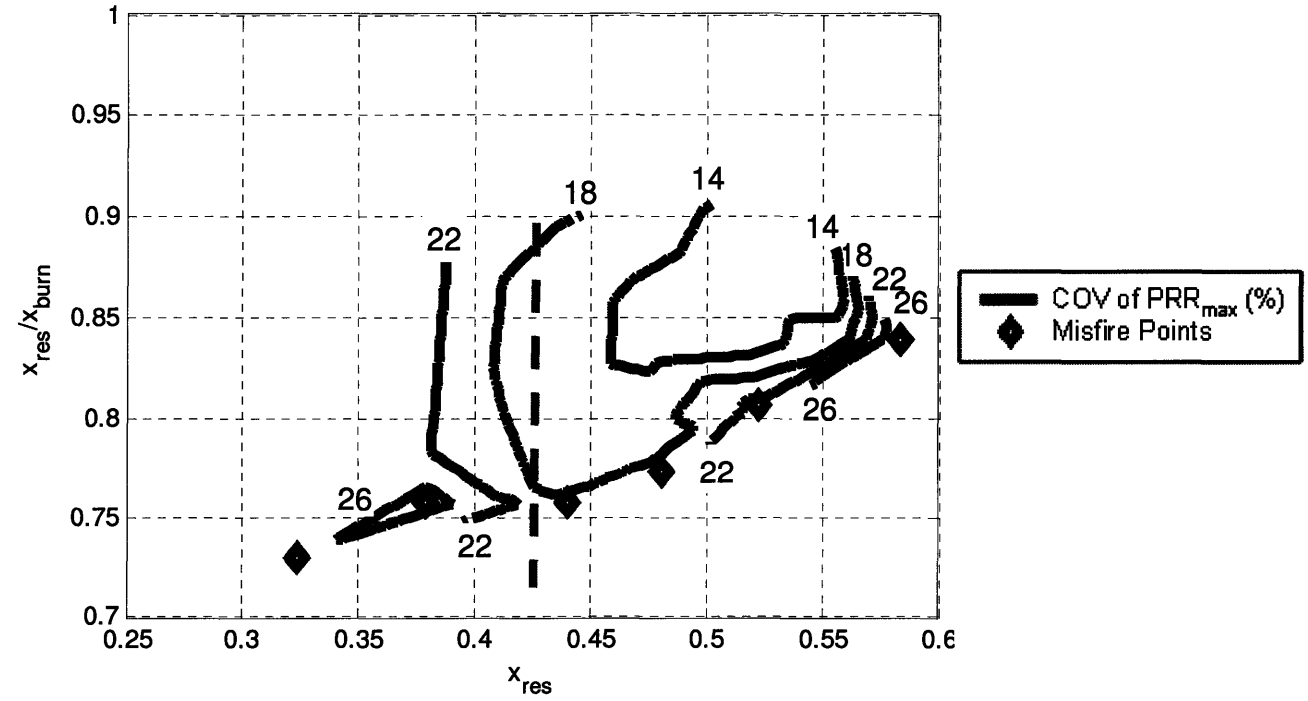


**Figure 4.19.** COV of $PRR_{max}$ Contoured on $x_{res}/x_{burn}$ vs. $x_{residual}$ for $T_{in}$ = 120°C, $P_{in}$ = 1.7bar.

The pivotal difference between these regimes is how COV of $PRR_{max}$ changes as $x_{res}/x_{burn}$ is increased at a fixed residual gas fraction. At high residual fraction, COV of $PRR_{max}$ is low across most of the operating regime and then sharply increases at the misfire limit. At low residual

fraction, COV of $PRR_{max}$ is higher throughout the operating regime and increases more gradually and more erratically both as residual fraction increases and as the misfire limit is approached. These two behaviors of COV of $PRR_{max}$ reflect the differences in thermal stratification established by low-temperature, high-fraction residuals and high-temperature, low-fraction residuals. Since COV of $PRR_{max}$ is not strictly higher at the misfire limit than at stable points in the low-residual fraction regime, it is unsuitable to serve as a metric for the misfire limit. Nevertheless, it still can yield insight into the behavior of combustion.

Another salient feature of these two regimes is that fueling is low at high residual fraction operation so the right side of the misfire limit forms a low-load limit. The fueling is high at low residual fraction operation so the left side of the misfire limit forms a high-load limit. The approach to the high load limit can be characterized by a significantly higher degree of cyclic variability than the approach to the low load limit.

## 4.3 Intake Temperature and EGR

In this part of study, the intake pressure is held to 1.5bar, and the intake temperature is set to 60°C, 90°C, and 120°C. EGR and NVO are varied as in Section 4.1 and 4.2. Exhaust pressure is set to 30mbar higher than intake pressure so as to drive EGR flow. The purpose of this study is to illustrate any difference between varying the charge temperature via the temperature of the air and EGR gas versus varying the fraction of trapped residuals versus EGR. Continuing on the conclusion that the high-load limit occurs at the misfire limit where EGR is as high as possible, the misfire points are shown first, mapped on $x_{res}/x_{burn}$ and $x_{burn}$ in Figure 4.20. The curves show that as intake temperature is increased, the engine will run stably at a lower $x_{res}/x_{burn}$ fraction. Less thermal energy is needed from the residual fraction for ignition when the intake temperature is higher.

Average temperature at 15° BTC is plotted against burned gas fraction for the misfire points in Figure 4.21. Misfire occurs at approximately the same temperature almost regardless of intake temperature and burned gas fraction. $x_{res}/x_{burn}$ clearly shows a trend against $x_{burn}$, while bulk temperature stays relatively constant, implying the misfire limit is more reliant on thermal stratification than the bulk temperature. It does matter then that thermal energy is added via trapped residual versus intake heating.

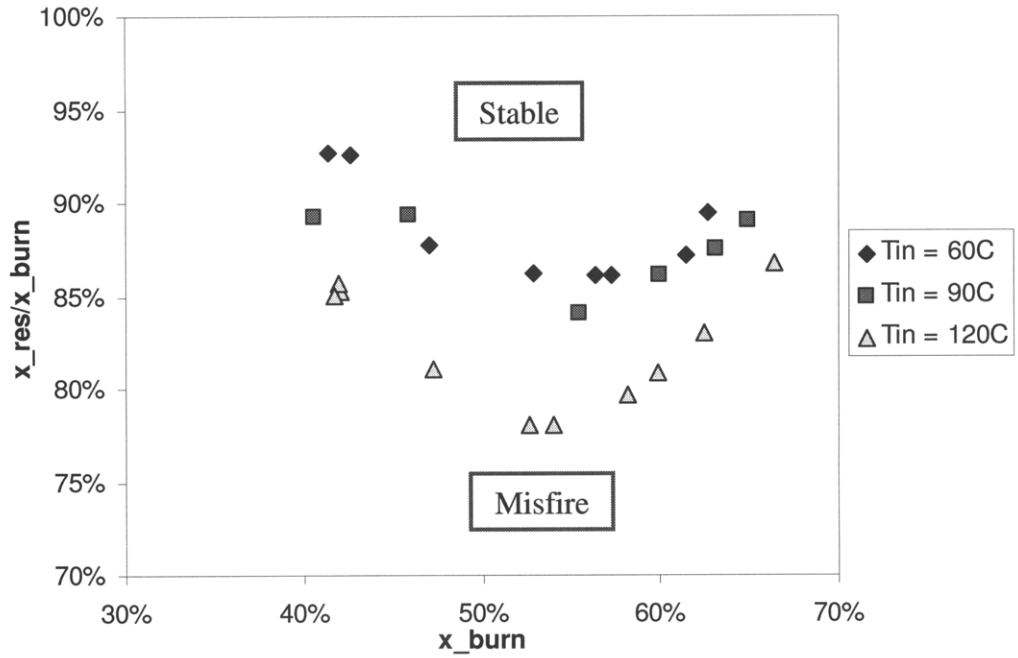


**Figure 4.20.** EGR Misfire Points Plotted on $x_{res}/x_{burn}$ vs. $x_{burn}$ for Three Intake Temperatures. $P_{in}$ = 1.5bar.

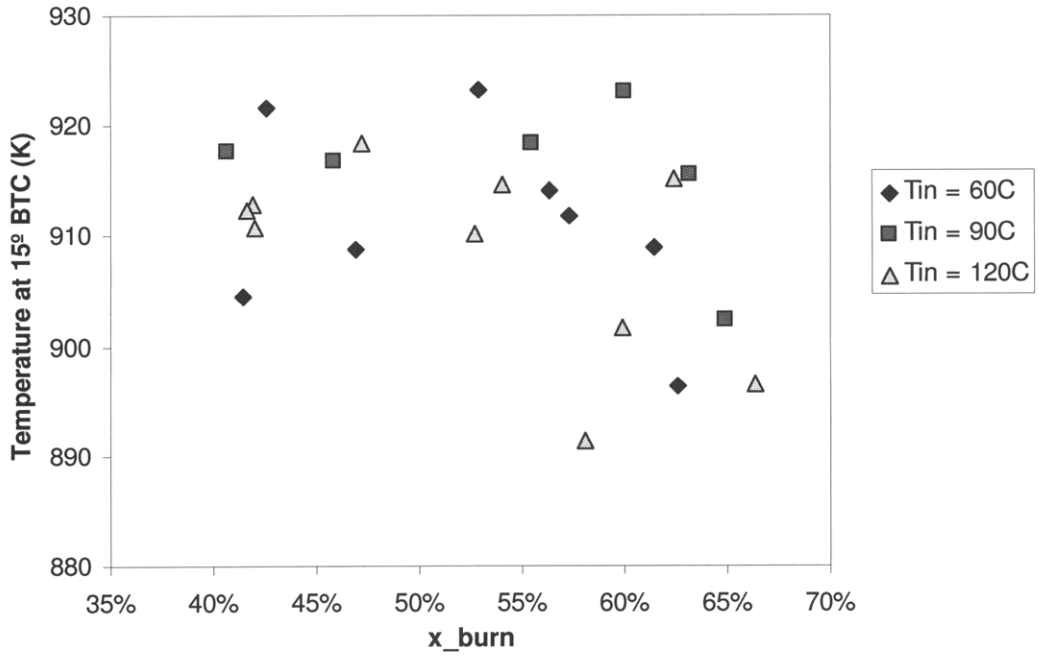


**Figure 4.21.** Temperature at 15° BTC vs. $x_{burn}$ for the EGR Misfire Limits for Three Intake Temperatures. $P_{in}$ = 1.5bar.

The maximum rate of pressure rise, mapped in Figure 4.22, Figure 4.23, and Figure 4.24, shows a changing dependence on residual-burned fraction and total burned fraction with intake

temperature. $PRR_{max}$ increases with a slope of roughly +1 in the $T_{in}$ = 60°C and $T_{in}$ = 90°C maps.

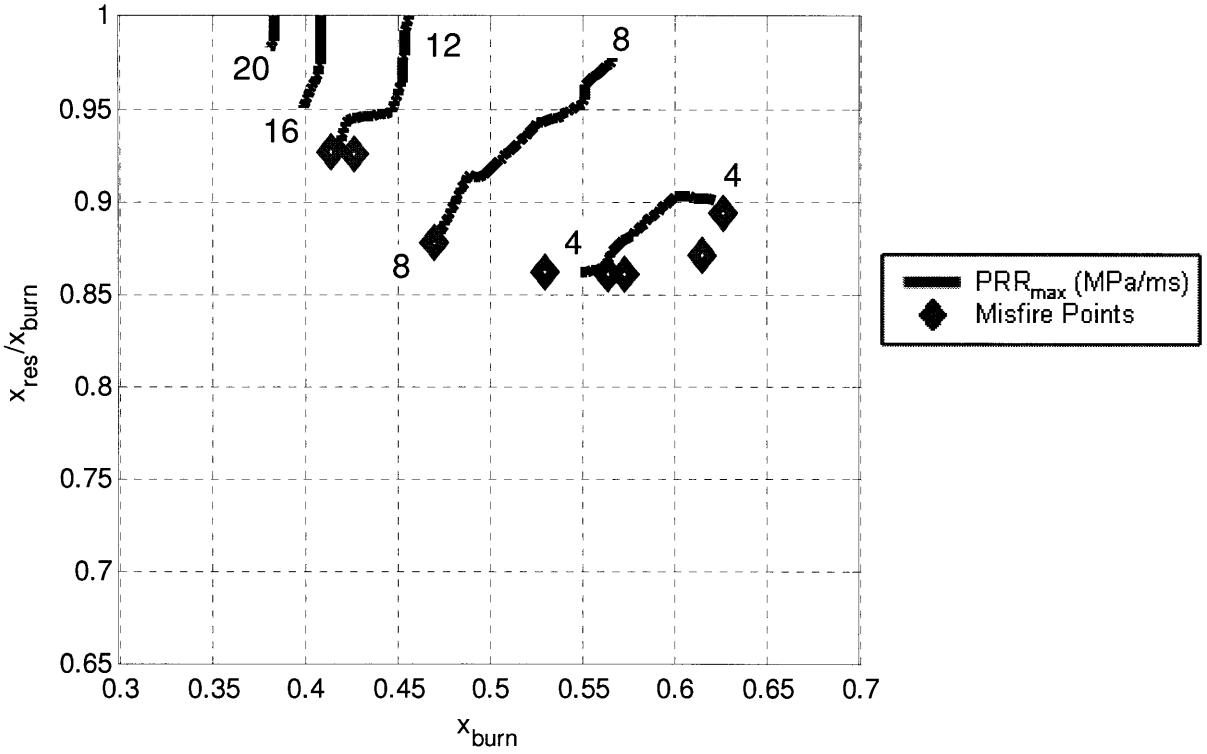


**Figure 4.22.** $PRR_{max}$ vs. $x_{res}/x_{burn}$ vs. $x_{burn}$. $T_{in}$ = 60°C; $P_{in}$ = 1.5bar.

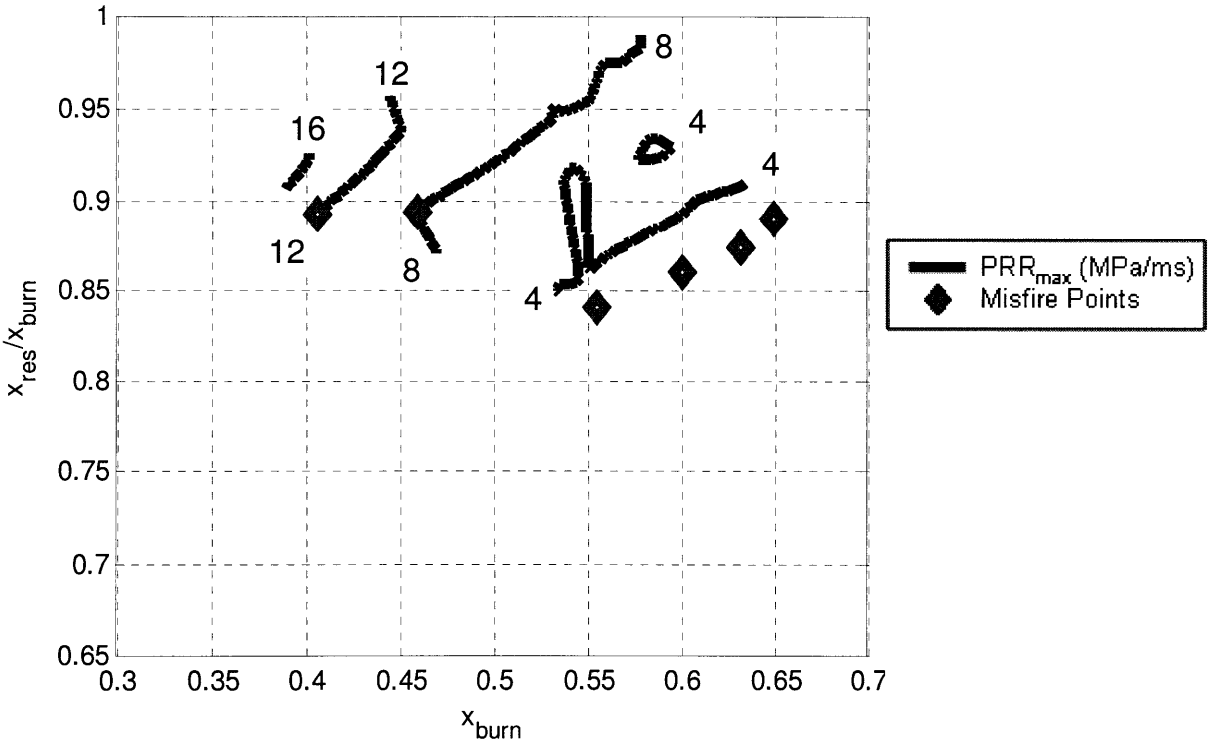


**Figure 4.23.** $PRR_{max}$ vs. $x_{res}/x_{burn}$ vs. $x_{burn}$. $T_{in}$ = 90°C; $P_{in}$ = 1.5bar.

As intake temperature increases to 120°C, $PRR_{max}$ depends less and less on the level of EGR. This is because, as intake temperature increases, the temperature of the EGR gas increases so it becomes less effective as a cool diluent. There becomes less of a difference between the EGR temperature and the trapped residual temperature. EGR, therefore, most effectively mitigates pressure rise rate if the intake air and EGR are kept cold.

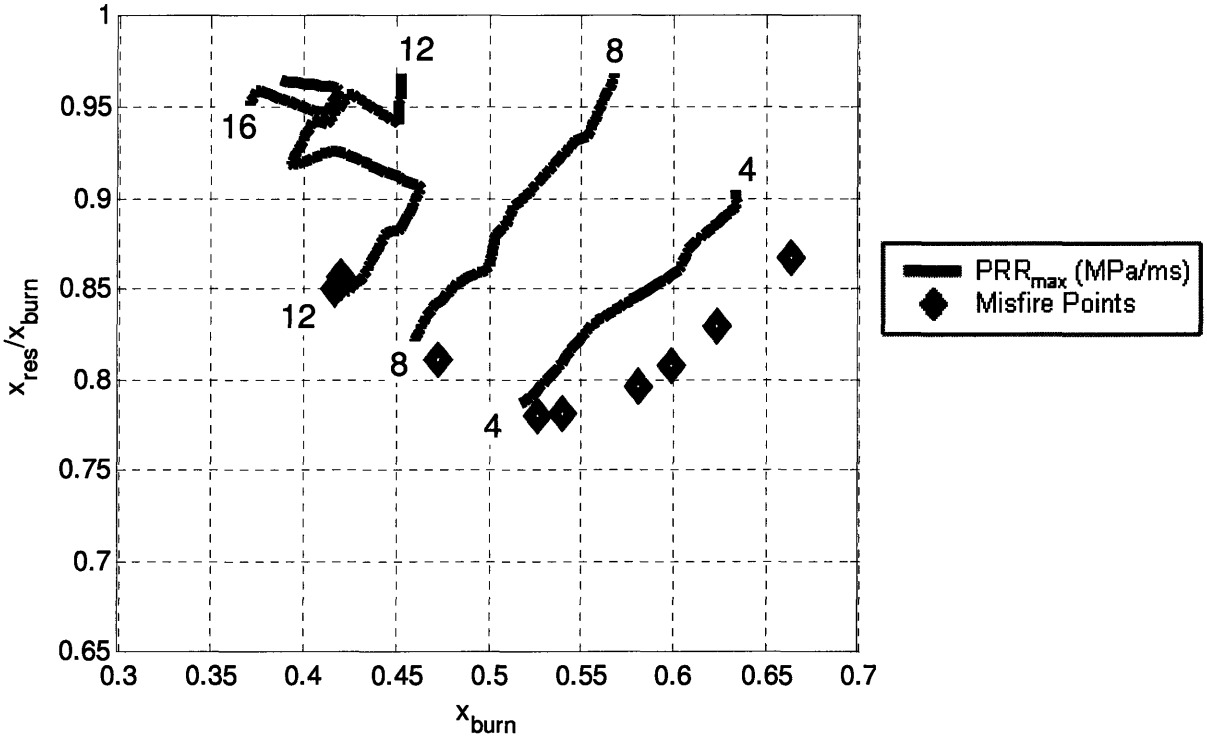


**Figure 4.24.** $PRR_{max}$ vs. $x_{res}/x_{burn}$ vs. $x_{burn}$. $T_{in}$ = 120°C; $P_{in}$ = 1.5bar.

## 4.4 A Misfire Limit Correlation with EGR

As in Chapter 3 for the data without EGR, correlations are proposed to describe the misfire limit with EGR. The first attempt to describe misfire with a function of oxygen fraction $x_{O2}$, pressure 15° BTC $P_{15BTC}$, and temperature 15° BTC $T_{15BTC}$ was not successful. The average temperature was not sufficient to describe the temperature effects on misfire. Figure 4.14 showed that temperature at 15° BTC was not a good metric for misfire limit across the four boost pressures studied. The next correlation attempts to capture the thermal stratification effects by residual fraction and intake temperature. $P_{in}$ replaces $P_{15BTC}$ so the correlation can be used with control parameters. The function describing misfire with EGR is stated such that oxygen fraction is a function of intake pressure, intake temperature, and residual fraction as in Equation 4.2.

$$x_{O_2} = 2.15 \cdot P_{in}^{-0.40} x_{res}^{-1.03} T_{in}^{-0.64} \tag{4.2}$$

This optimized correlation yields an $R^2$ of 96%, and the result is plotted in Figure 4.25.

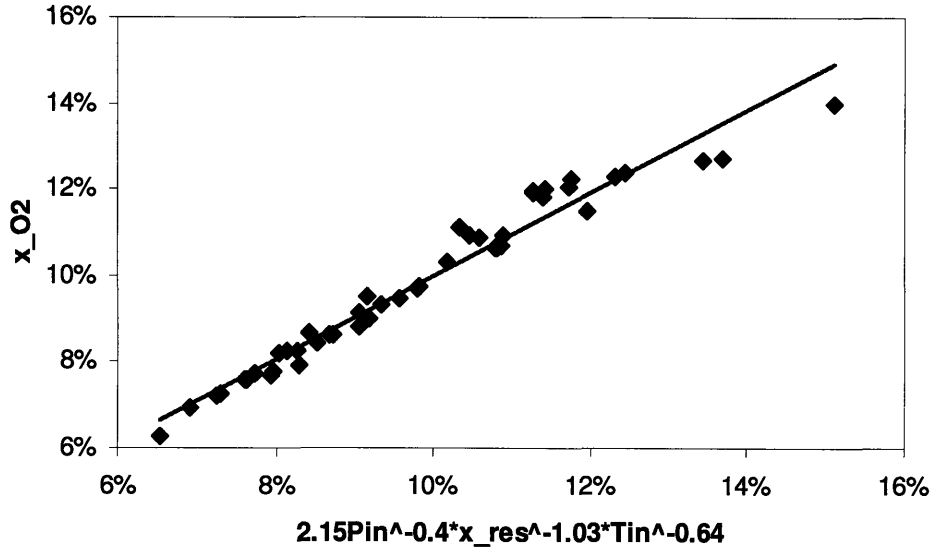


**Figure 4.25.** Correlation result for EGR misfire data of the form $x_{O_2} = 2.15 \cdot P_{in}^{-0.40} x_{res}^{-1.03} T_{in}^{-0.64}$.

The left side of the equation is divided by the right side to develop a threshold function, $\beta_{EGR}$, where $\beta_{EGR}$ is 1 at the misfire limit. This is stated in Equation 4.3.

$$\beta_{EGR} = 1 = 0.466 \cdot x_{O2} \cdot P_{in}^{0.40} \cdot x_{res}^{1.03} \cdot T_{in}^{0.64} \tag{4.3}$$

The correlation result is plotted in Figure 4.26 versus oxygen fraction. The correlation works well except for several points at high oxygen fraction.

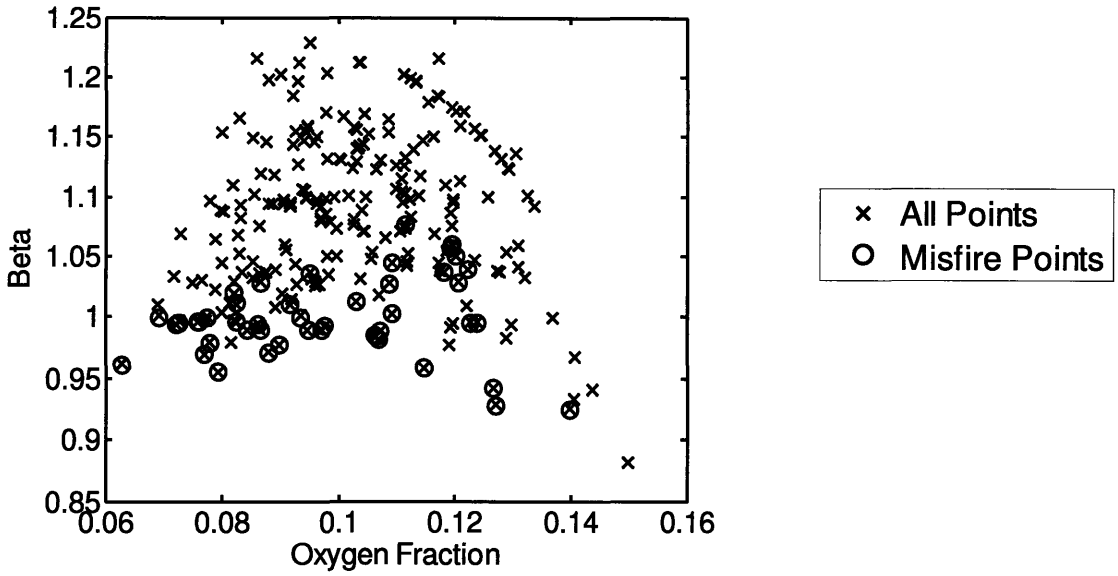


**Figure 4.26.** Correlation Result vs. Residual Gas Fraction. $x_{O2}$, $P_{15BTC}$, $x_{res}$, and $T_{in}$ are used for the correlation.

## 4.5 EGR Effects on the Range of Operation

The correlation stated in Equation 4.3 is now used to illustrate where the misfire limit is for constant levels of $x_{res}/x_{burn}$. Figure 4.27 features a contour map of the misfire limits at constant $x_{res}/x_{burn}$ mapped on oxygen fraction and intake pressure. Intake temperature for the data presented in this plot is 120°C. The acquired data lie at 1.1bar, 1.3bar, 1.5bar, and 1.7bar which allow misfire points to be shown for $x_{res}/x_{burn}$ levels of 95%, 85%, 80%, and 75%. The correlation results feature reasonable agreement with the data. There appears to be systematic error where pressure at the misfire limit is overestimated. The data's limit at high oxygen fraction at 85% $x_{res}/x_{burn}$ shows behavior where as pressure is increased, the allowable oxygen fraction decreases. This behavior is not captured by the correlation. In general though, the correlation illustrates how EGR advances the misfire limit to a higher pressure without shifting the optimal oxygen fraction for low-pressure operation. It also shows how the range of oxygen fraction allowable for stable operation narrows slightly as the EGR rate is increased and the pressure is increased.

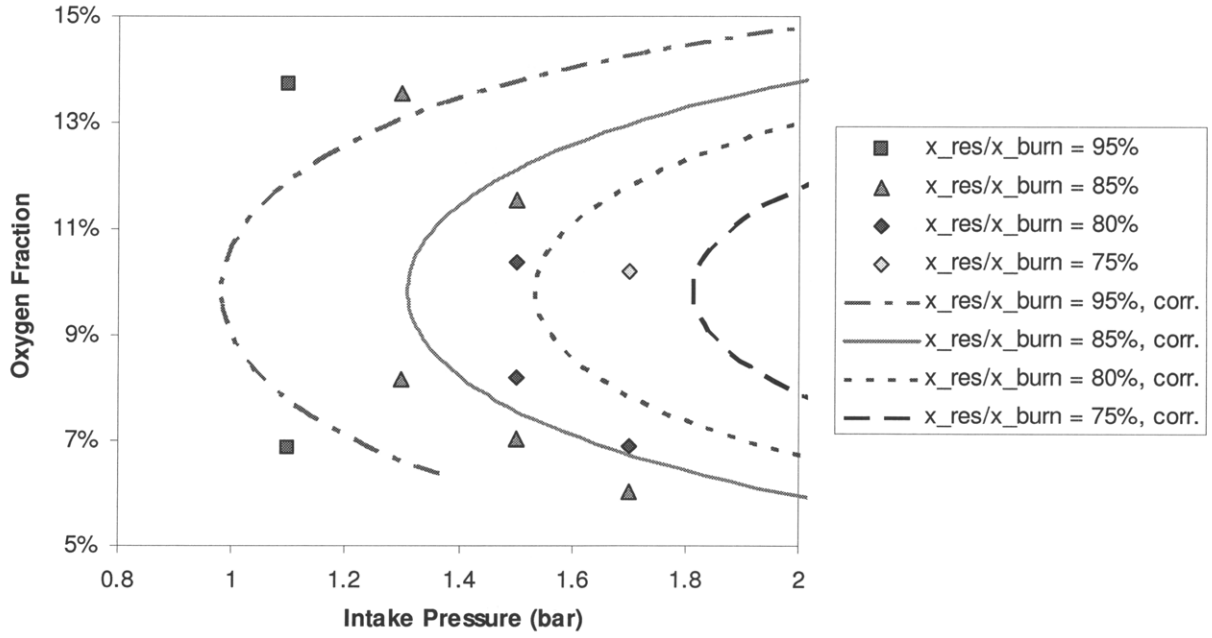


**Figure 4.27.** Misfire Contours Mapped on Oxygen Fraction and Intake Pressure. Each contour represents constant $x_{res}/x_{burn}$. The contours represent misfire limits for fixed $x_{res}/x_{burn}$ based on the correlation stated in Equation 4.3.

An analogous plot is presented for oxygen fraction and intake temperature in Figure 4.28. These data are located at $T_{in}$ = 60°C, 90°C, and 120°C with $P_{in}$ set to 1.5bar. These data allow contours for $x_{res}/x_{burn}$ at 90%, 85%, and 80% to be generated. The contours describe the variation

with intake temperature well. They seem to slightly overestimate oxygen fraction however. This may reflect the correlations failure to capture a trade off between temperature effects related to residual fraction and intake temperature.

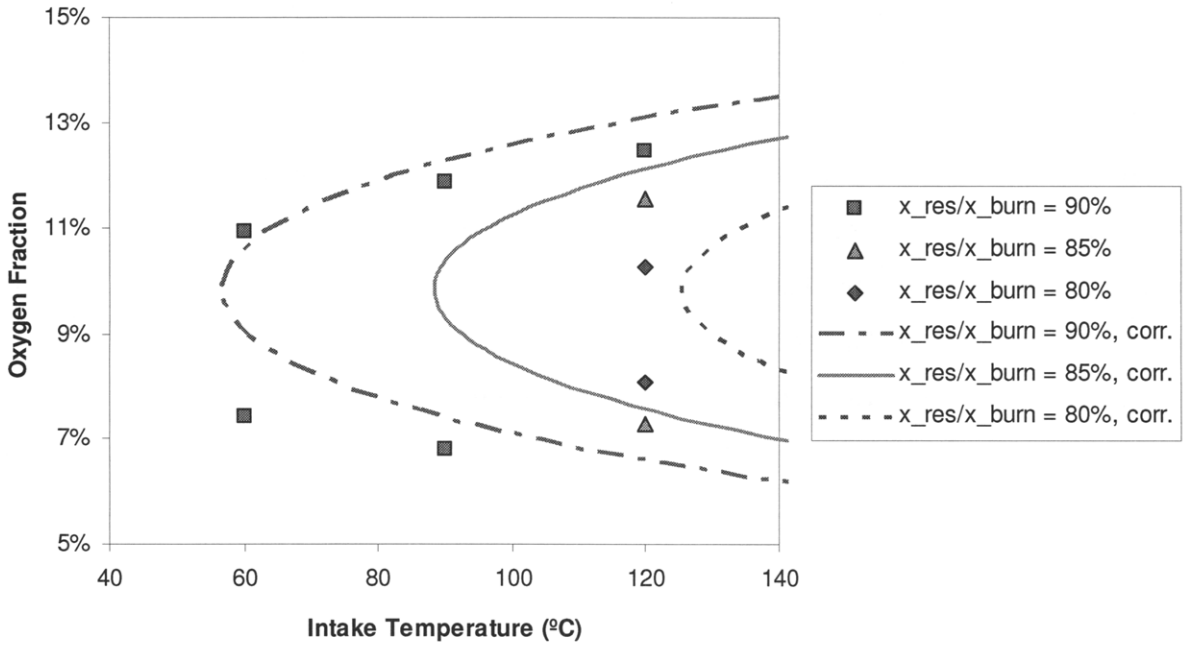


**Figure 4.28.** Misfire Contours Mapped on Oxygen Fraction and Intake Temperature. Each contour represents constant $x_{res}/x_{burn}$. The dashed lines are misfire limits based on the correlation stated in Equation 4.3.

The effects of boost and EGR on the misfire limit, on $PRR_{max}$, on fuel rate, and on efficiency have all been discussed. How load, the knock constraint, and misfire change together when EGR and boost are changed determines how the operating range shifts with EGR and boost. The effect of EGR on NIMEP, $PRR_{max}$, and misfire limit is shown step-by-step in the next three plots. NIMEP is contoured on $x_{O2}$ and $P_{in}$ for $x_{res}/x_{burn} = 95\%$ and for $x_{res}/x_{burn} = 85\%$ in Figure 4.29. The plot shows that the NIMEP contours retain the same slope when EGR is increased at the expense of trapped residuals. Also, the contours nearly line up; the fuel rate is independent of from where the burned gas arrives. There is a slight efficiency improvement with decreased trapped residuals since the 85% lines are shifted slightly to a lower $x_{O2}$ and $P_{in}$ level. This efficiency improvement stems from more optimal combustion phasing.

The maximum pressure rise rate and the misfire limit, derived from the correlation of Equation 4.3, are contoured on $x_{O2}$ and $P_{in}$ in Figure 4.30. The decrease of trapped residuals and replacement with EGR gas is shown to cause the $PRR_{max}$ to drop significantly.

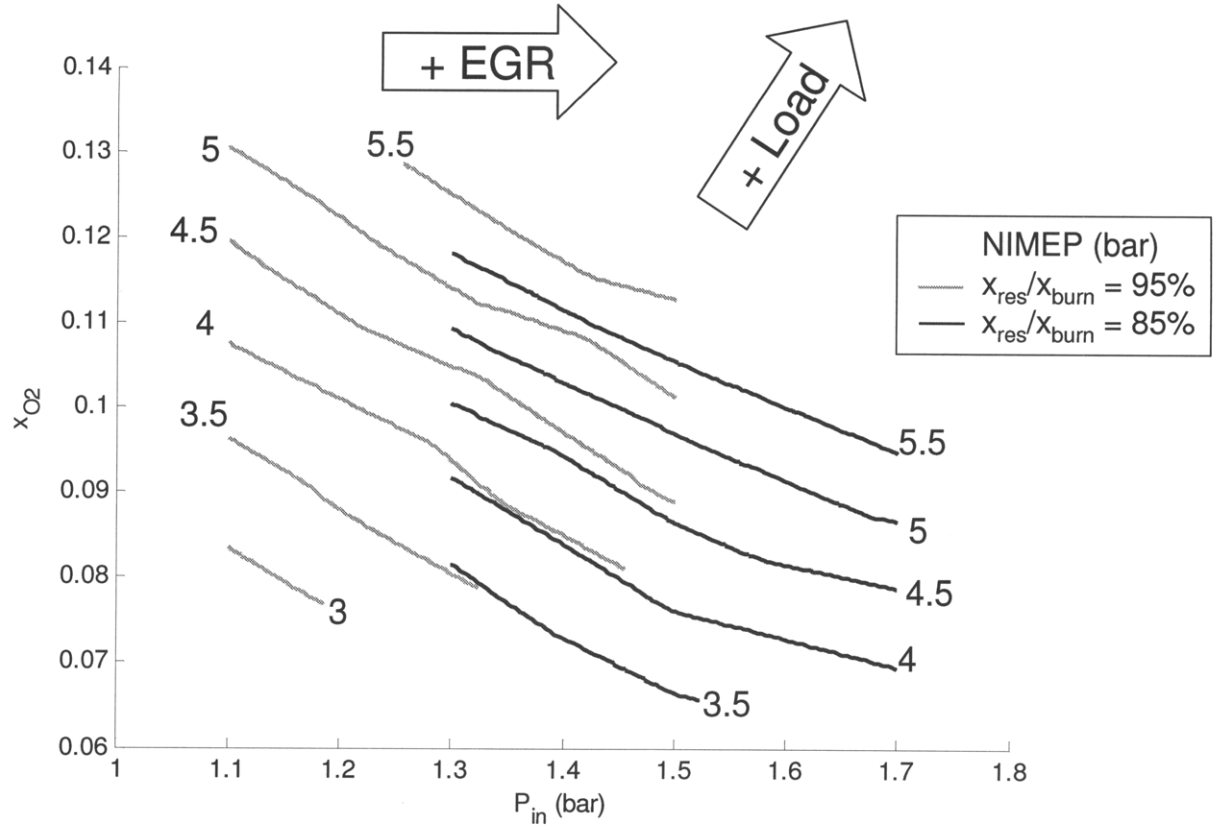


**Figure 4.29.** NIMEP Contoured on $x_{O2}$ and $P_{in}$ for $x_{res}/x_{burn}$ = 95% and $x_{res}/x_{burn}$ = 85%. $T_{in}$ = 120ºC.

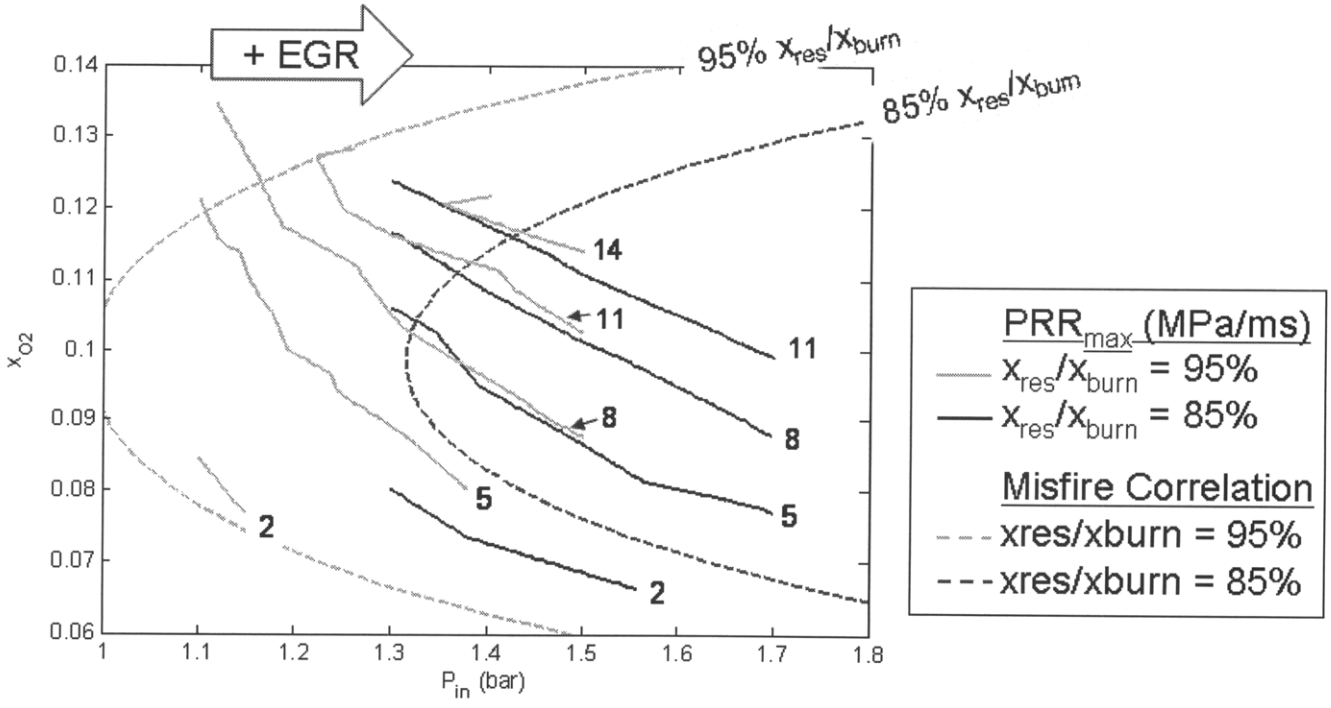


**Figure 4.30.** $PRR_{max}$ Contoured on $x_{O2}$ and $P_{in}$ for $x_{res}/x_{burn}$ = 95% and $x_{res}/x_{burn}$ = 85%. The misfire limit correlation from Equation 4.3 is overlaid for both conditions. $T_{in}$ = 120ºC.

The contour lines shift down and to the right. The misfire limit also shifts considerably when $x_{res}/x_{burn}$ is decreased from 95% to 85%. The misfire limit is where the maximum load occurs for a given maximum rate of pressure rise, as was concluded from Figure 4.2 and Figure 4.6. If 5MPa/ms is taken to be the upper limit of $PRR_{max}$, then it can be seen from Figure 4.30 that the maximum load point shifts from 12% $x_{O2}$, 1.1bar $P_{in}$ to 10.5% $x_{O2}$, 13.2bar $P_{in}$. Figure 4.31 shows NIMEP contours, the misfire limit, and the $PRR_{max}$ contour at 5MPa/ms are shown on $x_{O2}$ and $P_{in}$ for $x_{res}/x_{burn}$ = 95% and for $x_{res}/x_{burn}$ = 85%. By combining each of these features, the shift from one EGR to a higher EGR rate can be clearly shown. The NIMEP contours shift only slightly from efficiency effects. The $PRR_{max}$ contours and the misfire curves shift because charge temperature is reduced. The maximum load point shifts, but the value of the maximum load remains roughly the same.

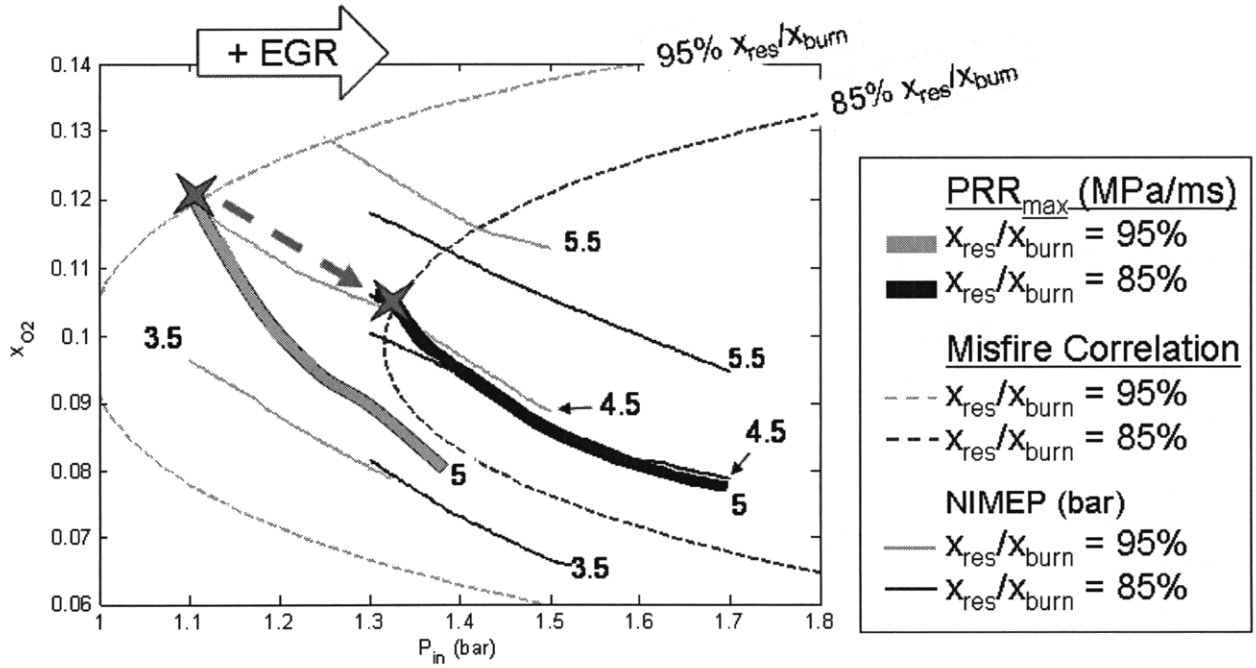


**Figure 4.31.** NIMEP Contoured on $x_{O2}$ and $P_{in}$ for $x_{res}/x_{burn}$ = 95% and $x_{res}/x_{burn}$ = 85%. The misfire limit correlation from Equation 4.3 is overlaid for both conditions. The contour for $PRR_{max}$ = 5MPa/ms is shown for both conditions as well. Stars mark the high load condition for each $x_{res}/x_{burn}$ level. $T_{in}$ = 120°C.

## 4.6 Misfire Mechanism Under EGR Operation

In this section, cycle-by-cycle data and 5-cycle averaged data will be inspected to gain insight on the misfire phenomenon under EGR operation. Just as in Section 3.3.3, the goal of this section is not to conduct an exhaustive exploration but simply to broach the topic of how the engine misfires to direct future study.

Case #3 is taken at $P_{in}$ = 1.5bar, $T_{in}$ = 60°C, $x_{burn}$ = 58%, and $x_{res}/x_{burn}$ = 86%. The location of this point is circled in the contour map of CA10 on $x_{res}/x_{burn}$ and $x_{burn}$ in Figure 4.32.

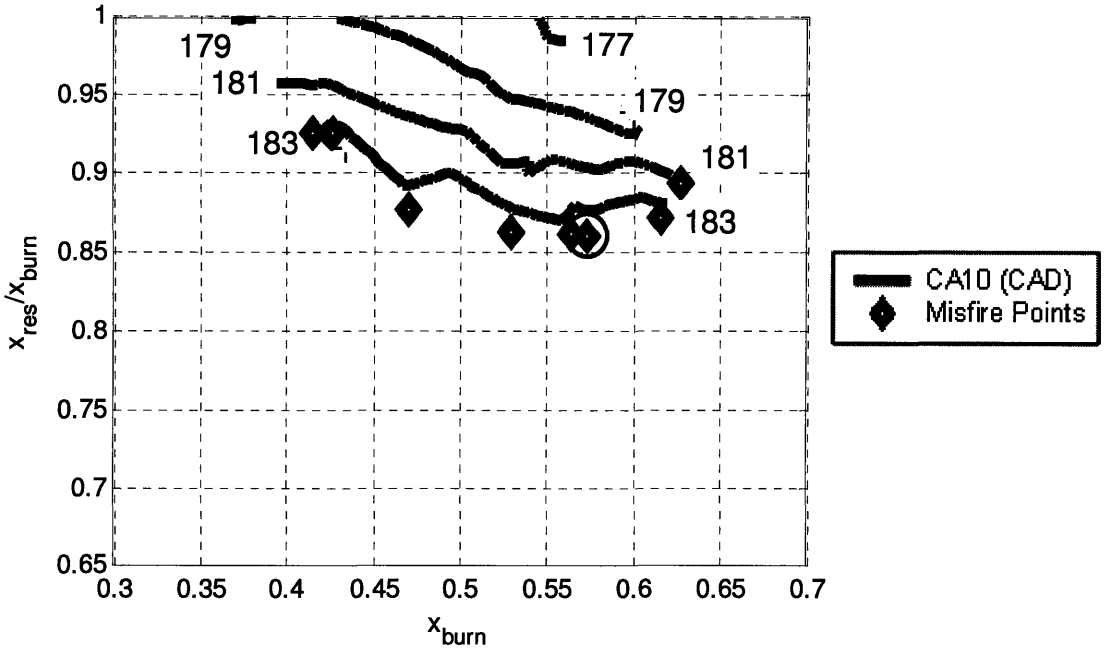


**Figure 4.32.** CA10 (CAD) vs. $x_{res}/x_{burn}$ vs. $x_{burn}$. $T_{in}$ = 60°C; $P_{in}$ = 1.5bar. Case #3 circled in black.

The four cycles leading to misfire and the misfire cycle are shown in parts of the pressure trace in Figure 4.33 and Figure 4.34. In the combustion event in Figure 4.33, it appears that combustion phasing starts at a mid-range phasing and then oscillates between early and late until it is too late for a full burn to take place. This plot is somewhat deceiving since all of the featured combustion events occur at late phasing. The recompression event shown in Figure 4.34 shows the corresponding oscillation of the maximum pressure of the recompression event indicating the link between the strong, early combustion event and the weaker recompression event of the same cycle which leads to a weak combustion event in the next cycle.

Figure 4.35 features cycle-by-cycle data for NIMEP, normalized air-fuel ratio $\lambda$, and CA50. They are plotted as the percent deviation of NIMEP, 5 times the percent deviation of $\lambda$, and the deviation in CAD from the stable average for CA50 as stated in Equations 3.16, 3.17, and 3.18, reprinted here.

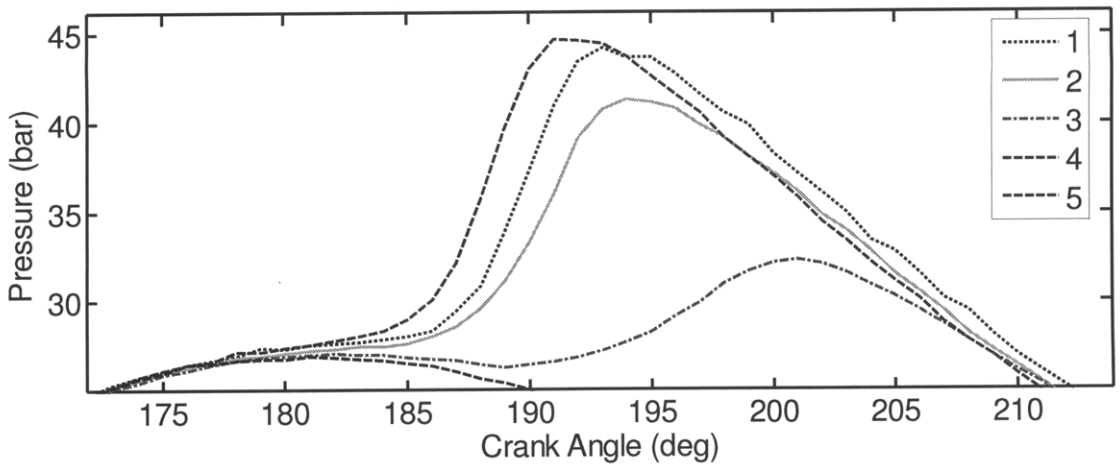


**Figure 4.33.** Case #3: Pressure Traces for Five Individual Cycles where the Fifth One Misfires. The traces feature the combustion event.

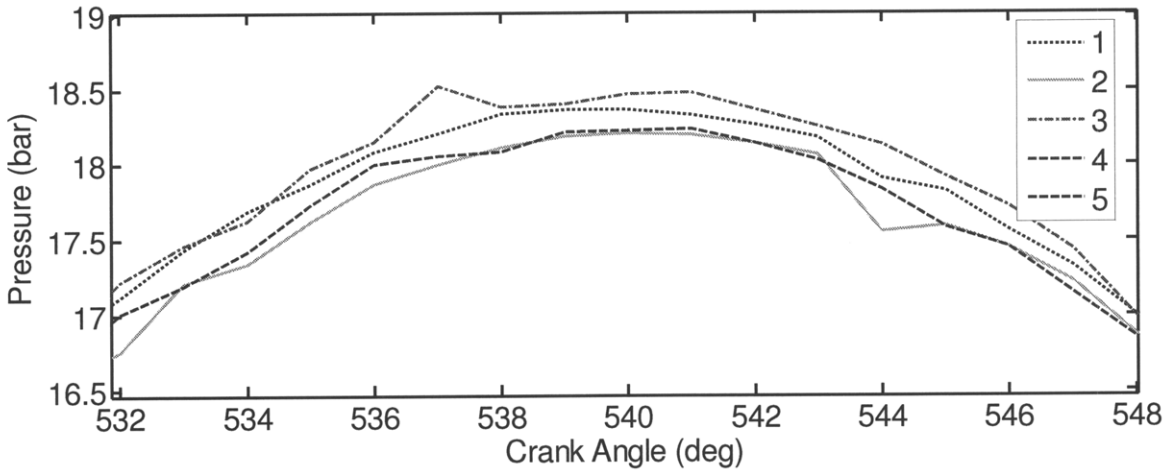


**Figure 4.34.** Case #3: Pressure Traces for Five Individual Cycles where the Fifth One Misfires. The traces feature the recompression event. Cycles 1 through 5 correspond to the same cycles Figure 4.33.

$$\text{Percent Deviation of NIMEP} = \frac{NIMEP_i - \dfrac{\sum_{i=1}^{100} NIMEP_i}{100}}{\dfrac{\sum_{i=1}^{100} NIMEP_i}{100}} \cdot 100\% \tag{3.16}$$

$$\text{Percent Deviation of } \lambda = 5 \times \frac{\lambda_i - \dfrac{\sum_{i=1}^{100} \lambda_i}{100}}{\dfrac{\sum_{i=1}^{100} \lambda_i}{100}} \cdot 100\% \tag{3.17}$$

$$\text{Deviation of CA50} = CA50_i - \frac{\sum_{i=1}^{100} CA50_i}{100} \tag{3.18}$$

The figure shows $\lambda$ drop significantly at cycle 132. NIMEP drops at the same time, and CA50 phases later at the same time. This suggests a lack of oxygen is causing combustion to phase later which leads to cycles at low efficiency. The engine recovers, and then a similar phenomenon happens again at cycle 144, but this time, $\lambda$ does not return to the average value, and the engine misfires.

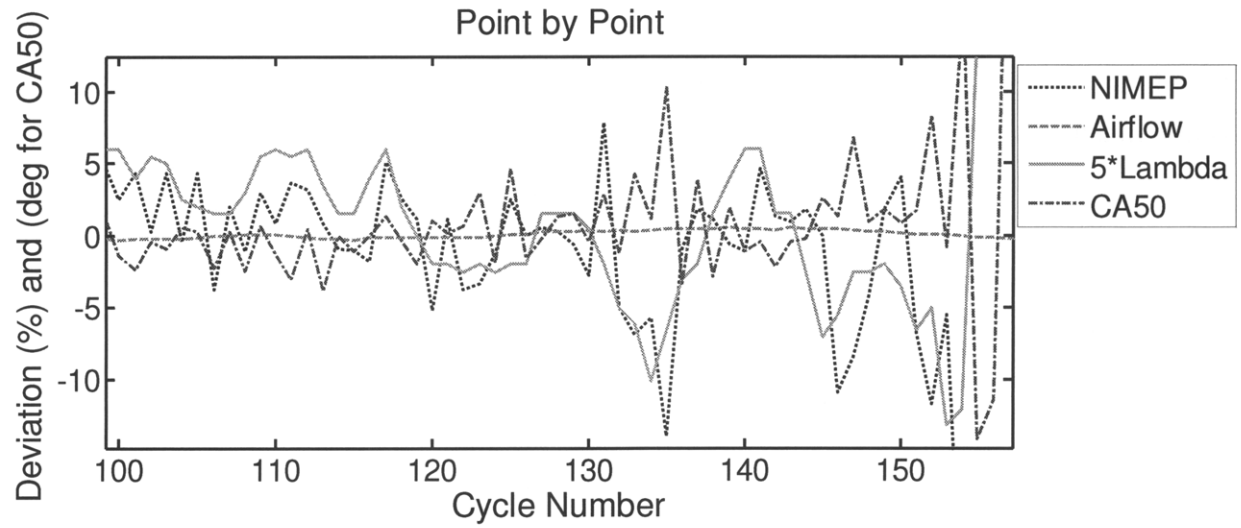


**Figure 4.35.** Case #3. Cycle-by-Cycle Data Leading up to the Misfire. NIMEP, λ, and CA50 recorded. For NIMEP, the percent deviation from the stable value is plotted. For λ, 5*the percent deviation is plotted. For CA50, the number of CAD deviation from the stable value is plotted.

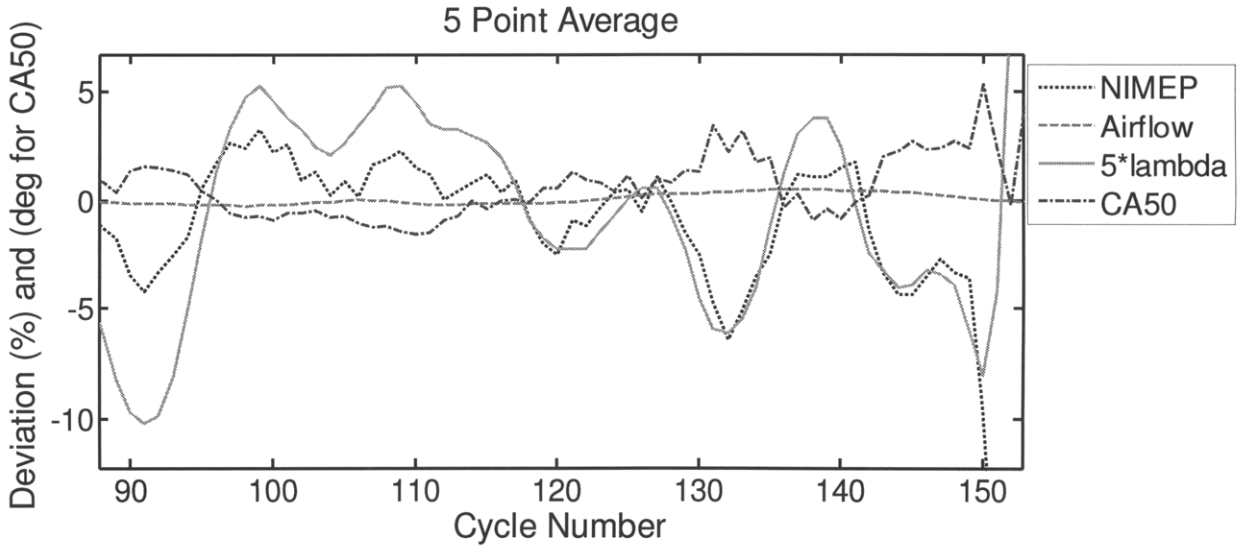


**Figure 4.36.** Case #3. Five-Point Averages of Cycle-by-Cycle Data Leading up to the Misfire. NIMEP, λ, and CA50 recorded. For NIMEP, the percent deviation from the stable value is plotted. For λ, 5*the percent deviation is plotted. For CA50, the number of CAD deviation from the stable value is plotted.

The 5-cycle averages plotted in Figure 4.36 show more clearly that $\lambda$ is varying quite a bit, and NIMEP and CA50 vary at the same time. The time scale for these variations appears to be approximately 10 cycles.

Misfire does seem to be related to these slow variations in $\lambda$. These variations in $\lambda$ were not observed in Cases #1 and #2 which did not use EGR. It is possible that the EGR loop generated flow dynamics that pulsed exhaust into the intake thus varying the air flow. If this were the case, then this phenomenon would be highly engine specific. A four or six cylinder engine would yield completely different EGR flow characteristics than the single-cylinder research engine used for this experiment. Nevertheless, the point that the EGR flow can affect $\lambda$ in an unsteady, periodic fashion illustrates an issue that would need to be addressed to extend the misfire limit.

# Chapter 5 A Phenomenological Model for the High Load Knock Limit

A good deal of data has been presented, and still more data, including lean operation data, has been presented in the doctoral thesis of R.J. Scaringe [53]. Here, these data will be used to develop a phenomenological model to describe the high-load knock limit. This model will be based on bulk parameters including oxygen fraction, equivalence ratio, pressure, and average temperature. It is understood from previous work that distributions in temperature and concentration play a roll in determining CAI knock. This experiment is not equipped to measure such distributions so the model aims will be limited to describing combustion with bulk parameters.

## 5.1 CAI Knock

A first step to developing the model is defining the limit. One proposal is to define it when knock starts to occur or when pressure waves are first observed in the pressure trace. Pressure data was acquired at 90kHz at a variety of operating conditions to observe the pressure wave phenomena in closer detail. Even at a modest rate of pressure rise, oscillations were observed indicating pressure waves. Figure 5.1 features an example pressure trace in which the average maximum rate of pressure rise over 300 cycles was 4.0MPa/ms. This cycle was typical of the set.

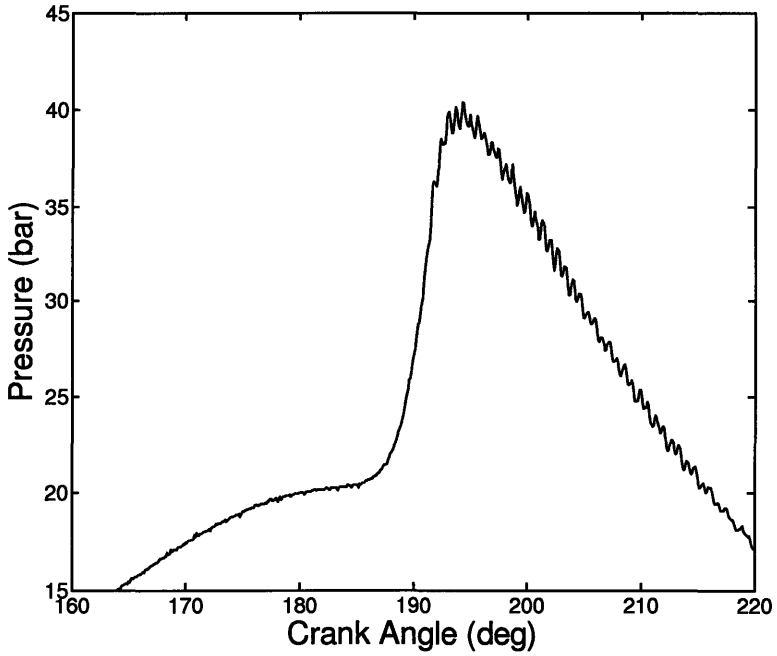


**Figure 5.1.** Pressure trace acquired at 90kHz sampling rate. Average PRRmax (for 300 cycles) = 4.0MPa/ms.

Pressure oscillations are evident, starting before pressure nears its peak and continuing at least 25° after the end of combustion. The data recorded for this thesis feature $PRR_{max}$ values ranging from just under 2 to 21MPa/ms so 4MPa/ms is low. It is also below Andreae et al.'s knock limit of 5MPa/ms [20]. Using the criterion of the onset of knock is therefore not feasible.

The two problems with knock are unacceptable levels of noise and accelerated wear on the mechanical components of the engine. The stricter criterion is noise so an arbitrary limit based on the emitted noise is appropriate. What that limit should be is really a question of product design and depends on how the engine is used and whether the rest of the product can be designed to separate the user from the noise source. This model will not define a threshold but instead will relate charge parameters to combustion parameters that relate to emitted noise.

As mentioned in Chapter 1, Eng developed a relationship between ringing intensity $I$, which was a measurement of the noise emitted from an experimental engine, and various combustion parameters, restated in Equation 1.1 [18].

$$I \approx \frac{1}{2\gamma} \frac{\left(\alpha \frac{dP}{dt_{max}}\right)^2}{P_{max}} \sqrt{\gamma R T_{max}} \tag{1.1}$$

$dP/dt_{max}$ is the maximum pressure rise rate ($PRR_{max}$); $P_{max}$ is the maximum cylinder pressure. $\gamma$ is the ratio of specific heats; $T_{max}$ is the maximum cylinder temperature; $R$ is the universal gas constant, and $\alpha$ is a correlation constant. Figure 5.2 features this ringing intensity plotted against $PRR_{max}$ for the NVO sweep data, IVC sweep data, EVO sweep data, and intake temperature sweep data. This plot shows that ringing intensity strongly correlates with $PRR_{max}$ and that the dependence is stronger than linear. $PRR_{max}$ can therefore be used as a good metric for emitted engine noise for CAI knock.

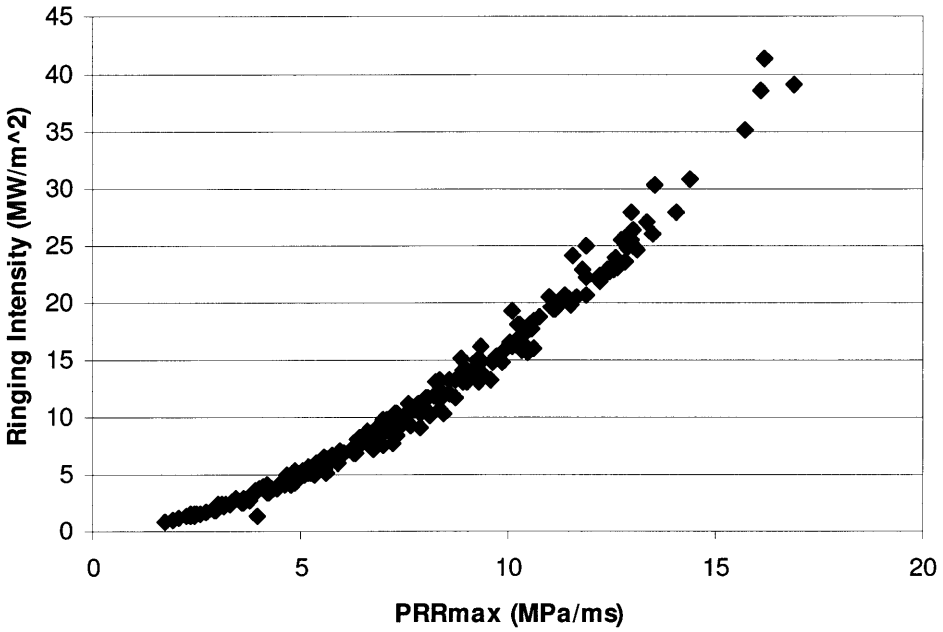


**Figure 5.2.** Ringing Intensity vs. $PRR_{max}$. The NVO, IVC, EVO, and $T_{in}$ sweeps are included.

## 5.2 Characteristic Burn Duration

Maximum rate of pressure rise is a suitable metric for the noise limit for the engine, but it yields no information about the engine load so another metric building on this is required to indicate both noise and load. The following analysis, drawing from the personal notes of Wai Cheng, show how a characteristic burn duration can be developed to account for rate of pressure rise and fuel rate together [54].

Considering a uniform charge, the chemical energy heat release acts to heat the gas and to do work on the piston, as in Equation 5.1.

$$V\dot{q} = mc_v \frac{dT}{dt} + p\frac{dV}{dt} \tag{5.1}$$

$V$ is the cylinder volume; $\dot{q}$ is the volumetric heat release. To simplify the analysis, the gas is assumed to have a uniform temperature $T$ and specific heat capacity $c_v$. Substituting the ideal gas law into Equation 5.1 for mass and temperature yields a relationship for the rate of pressure rise in Equation 5.2.

$$\dot{p} = (\gamma - 1)\dot{q} - \gamma\frac{p\dot{V}}{V} \approx (\gamma - 1)\dot{q} \tag{5.2}$$

Under conditions where the $PRR_{max}$ is high, the heat release term dominates the work extraction term on the right side of the equation so the right hand term can be neglected.

The total chemical energy of the fuel can be thought of as occurring at a particular time with a reaction duration $\tau$ in a volume $V(\Theta)$, which is a function of crank angle. In Equation 5.3, $\tau$ is defined as the time for the fuel mass $m_f$ to burn at an average heat release rate $\dot{q}(\theta)$ in this volume.

$$\tau \equiv \frac{LHV \cdot m_f}{\dot{q}(\theta)V(\theta)} \tag{5.3}$$

$LHV$ is the lower heating value of the fuel. Combining Equations 5.2 and 5.3 yields the pressure rise rate as a function of combustion phasing, fuel mass, and combustion duration.

$$\tau = (\gamma - 1)LHV \frac{m_f}{V(\theta)\dot{p}} \tag{5.4}$$

$V(\Theta)$ can taken to be the volume at the time of 50% mass fraction burned, $V_{CA50}$. $\dot{p}$ is taken as the $PRR_{max}$, as in Equation 5.5.

$$\tau = (\gamma - 1)LHV \frac{m_f}{V_{CA50}\left(dp/dt\right)_{max}} \tag{5.5}$$

$\tau$ or $1/\tau$ can serve as metric for the high load limit. If $\tau$ increases, then the mass of fuel per cycle increased while the $PRR_{max}$ remains constant. Efficiency may change between operating conditions affecting the high load limit slightly without changing $\tau$. For simplicity, $\tau$ is presented as a function of fuel mass rather than NIMEP although NIMEP could be used for an alternate definition.

A salient feature of this $\tau$ is that it strongly correlates with the 10-90% burn duration for the acquired data, as shown in Figure 5.3. The metrics are also close to the same magnitude thus bolstering the physical meaning of $\tau$. Therefore, the high load knock limit can be increased by increasing the burn duration.

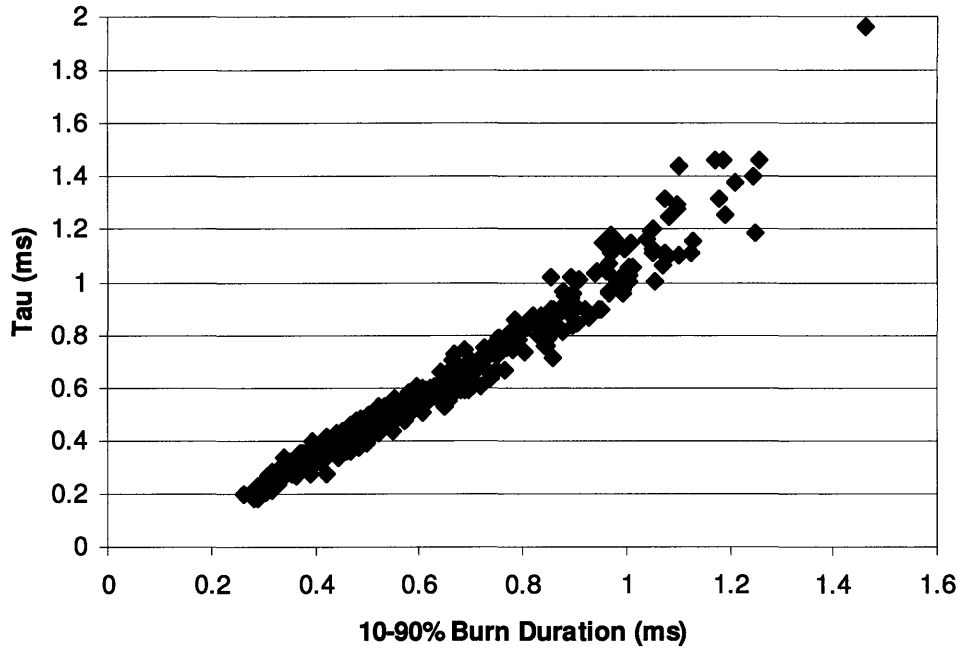


**Figure 5.3.** Tau vs. 10-90% Burn Duration. Stoichiometric, Lean, and EGR data.

## 5.3 A Correlation Based on Bulk Parameters

The $\tau$ burn duration metric can now be used to build a correlation based on bulk parameters that describe the charge. Since the experiment yields no data on temperature or concentration distributions, the model is expected to have limited accuracy. The state of the charge just before the start of the earliest combustion event was used as the point of reference, and this was decided to be 15°BTC. The five metrics used were oxygen fraction $x_{O2}$, equivalence ratio $\varphi$, the temperature at 15°BTC $T_{15BTC}$, the pressure at 15°BTC $P_{15BTC}$, and $R$ defined as the inverse of $\tau$. The ranges of values available in the data set are listed in Table 5.1.

**Table 5.1.** Ranges of Values for Burn Duration Correlations

| |
|---|
| $0.063 \le x_{O_2} \le 0.15$ |
| $0.80 \le \phi \le 1.01$ |
| $13.4bar \le P_{15BTC} \le 23.4bar$ |
| $832K \le T_{15BTC} \le 969K$ |
| $0.18ms \le \tau \le 1.96ms$ |
| $0.510ms^{-1} \le R \le 5.56ms^{-1}$ |

The correlation was formed as stated in Equation 5.6. This form is based on the Arrhenius formula for a reaction rate although it should be stressed that this form is meant to be purely phenomenological. The constants $a_1$ through $a_5$ were found via a least squares fit of the natural logarithm of Equation 5.6 as stated in Equation 5.7.

$$R = 1/Tau = a_1 \cdot x_{O_2}^{a_2} \cdot \phi^{a_3} \cdot P_{15BTC}^{a_4} \cdot \exp\left(a_5/T_{15BTC}\right) \tag{5.6}$$

$$\log(R) = \log(a_1) + a_2 \log(x_{O_2}) + a_3 \log(\phi) + a_4 \log(P_{15BTC}) + a_5/T_{15BTC} \tag{5.7}$$

Various other forms of this equation were evaluated that did not necessarily work with this linearization technique. The constants for these were found with MATLAB's "fminsearch" command, a nonlinear minimization algorithm using the Nelder-Mead technique.

The first correlation to be shown is as stated in Equation 5.6. The resulting $R$ is plotted against $R$ from the data for 568 points in Figure 5.4. The correlation shows promising agreement as $R^2 = 71.5\%$. The correlation clearly does not describe all of the phenomena at play; nevertheless, a clear trend is observable. The correlation coefficients yield some understanding regarding the behavior of the system. The exponent for oxygen fraction is 2.3, and the pressure exponent is 1.5. These are roughly consistent with previously presented data. Burn rate increases with both oxygen and with pressure. The temperature coefficient also features the correct sign. The exponent for equivalence ratio indicates that burn rate increases with excess air. While this effect is not explored in this work, the Ph.D. thesis of R.J. Scaringe features data and analysis supporting this [52].

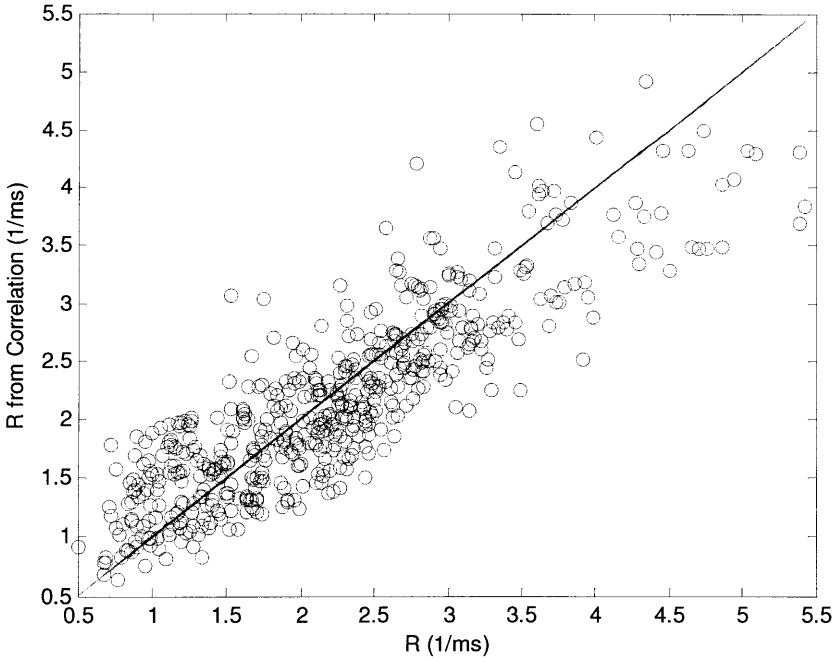


**Figure 5.4.** $R$ from the Correlation vs. $R$ from the Data. $x_{O2}$, $\varphi$, $P_{15BTC}$, and $T_{15BTC}$ were used in the correlation.

**Table 5.2.**
Correlation Parameters

| | |
|---|---|
| $R^2$ | 71.5% |
| $a_1$ | 71.41 |
| $a_2$ | 2.34 |
| $a_3$ | -1.41 |
| $a_4$ | 1.53 |
| $a_5$ | -2543 |

One consideration for improving this correlation is looking for where there might be substantial experimental error. The EVO sweeps yielded significant error for residual fraction estimates between the in-cylinder $CO_2$ measurements and the exhaust state technique. If the moles of residual gas were estimated poorly, this would affect both oxygen fraction and the bulk temperature. The next correlation, shown in Figure 5.5, shows the same formula but with these points omitted. $R^2$ increases to 72.7% for the 520 points plotted. The coefficient for temperature changes most significantly of the five coefficients.

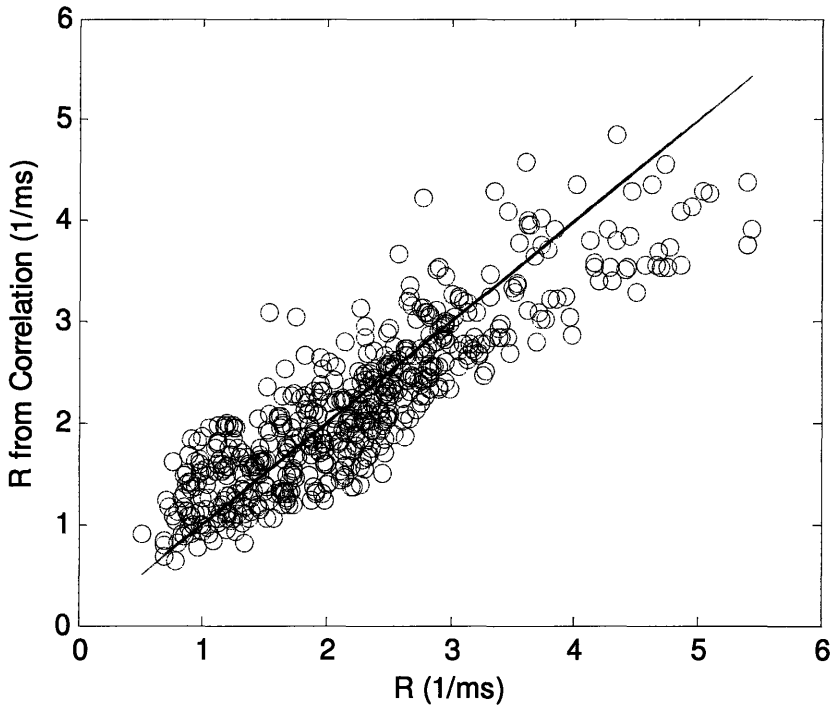


**Figure 5.5.** *R* from the Correlation vs. *R* from the Data. $x_{O2}$, $\varphi$, $P_{15BTC}$, and $T_{15BTC}$ were used in the correlation. EVO data was omitted.

**Table 5.3.**
Correlation Parameters

| | |
|---|---|
| $R^2$ | 72.7% |
| $a_1$ | 140.1 |
| $a_2$ | 2.30 |
| $a_3$ | -1.46 |
| $a_4$ | 1.39 |
| $a_5$ | -2876 |

Considerable spread persists in the correlation so different sweeps are overlaid with the correlation parameters to determine which data are well modeled and which are not. Figure 5.6 shows NVO sweeps with intake temperature set to 90°C at four different intake pressures overlaid on the correlation results. The variations in EVC timing seem to be well represented by the correlation. Since there are several NVO sweeps represented, with and without EGR, it is reasonable that they would dominate the points of the correlation and drive the form. Correlation results for intake temperature sweeps at five different pressures are overlaid the overall correlation result in Figure 5.7.

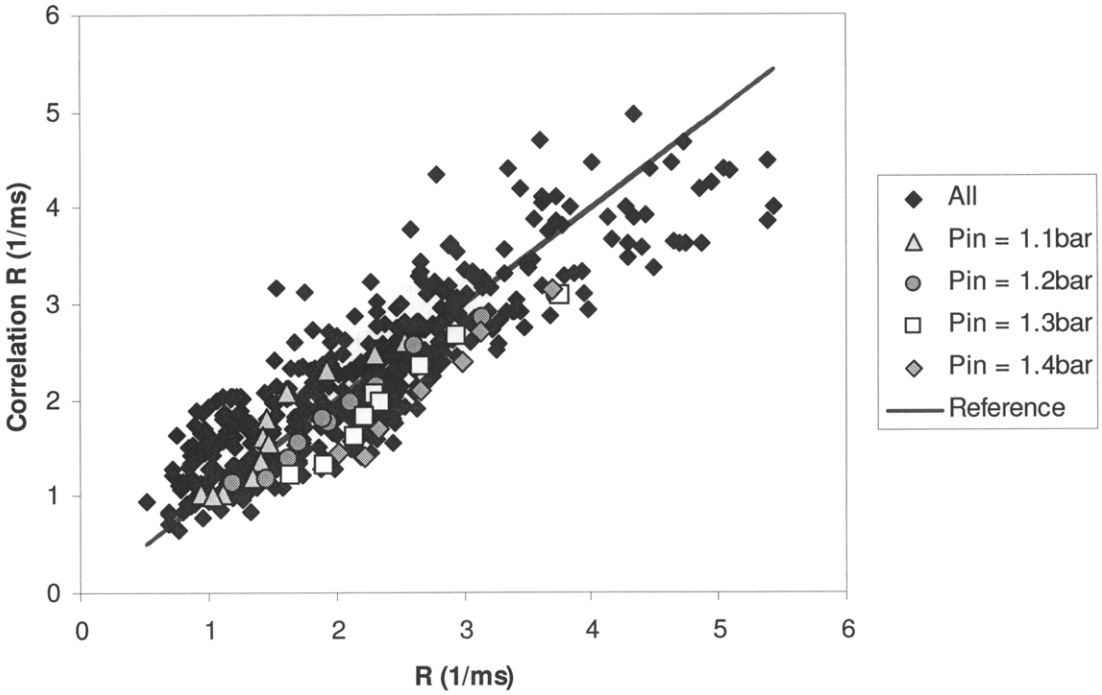


**Figure 5.6.** Correlation from Figure 5.5 with NVO Sweep ($T_{in}$ = 90°C) points overlaid.

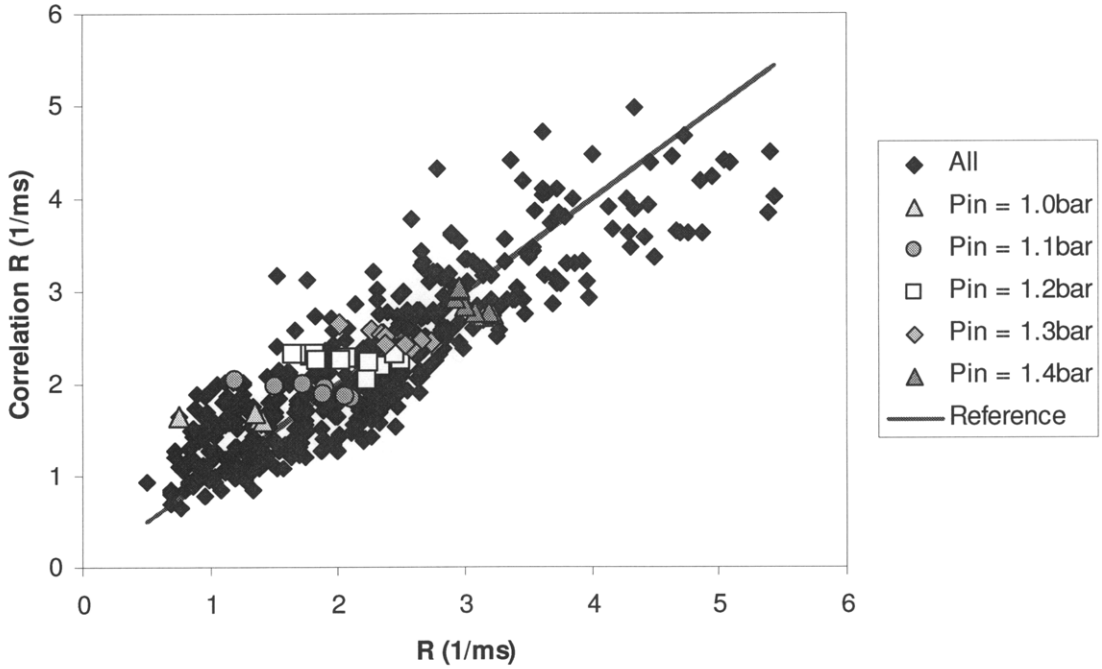


**Figure 5.7.** Correlation from Figure 5.5 with Intake Temperature Sweep Points Overlaid.

These sweeps are poorly represented by the correlation as the curves are almost perpendicular to the reference line. $T_{15BTC}$ changes in a different way with intake temperature than it does with residual trapping. This implies that the $T_{15BTC}$ term in the correlation is not helping the fit. $x_{res}/x_{burn}$ sweeps at constant total burned gas fraction, pressure, and intake temperature are

overlaid on the correlation result in Figure 5.8. The premise of flowing EGR rather than trapping residuals is that the bulk temperature is lower. Varying $x_{res}/x_{burn}$ is not well captured by the correlation so the bulk temperature term in the correlation is not describing this behavior either.

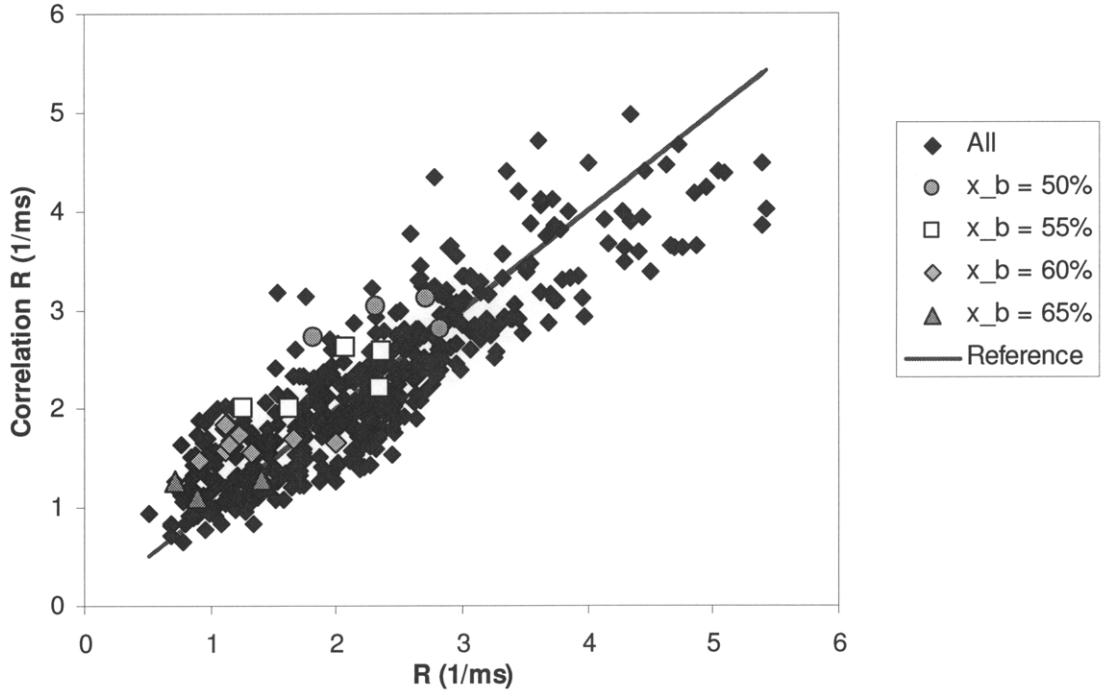


**Figure 5.8.** Correlation from Figure 5.5 with $x_{EGR}/x_{burn}$ Sweeps Overlaid. Total burned gas fraction is held constant for each color.

Since temperature effects were not captured in the correlation, the temperature term was omitted to evaluate the sensitivity of the correlation. This variation of the correlation is shown in Figure 5.9 for the formula in Equation 5.8.

$$R = {}^{1}/_{Tau} = a_1 \cdot x_{O_2}^{a_2} \cdot \phi^{a_3} \cdot P_{15BTC}^{a_4} \tag{5.8}$$

The resulting $R^2$ value features a modest drop to 70.8% indicating that the temperature term had little effect on the quality of fit. The exponents for oxygen fraction, pressure, and equivalence ratio have adjusted slightly as well.

Temperature is an integral part of a chemical kinetics reaction rate so the fact that average temperature does not help deserves some attention. First, it should be noted that in an NVO sweep, valve timing controls both oxygen fraction and bulk temperature since temperature is strongly affected by the amount of fuel and trapped residuals. Therefore, changing oxygen fraction accounts for changes in bulk temperature. Changing boost also affects bulk temperature, so the average temperature is already accounted for in some cases. It is possible that varying

intake temperature and EGR affect temperature and concentration stratifications in ways that conflict with the intuitive expectation of their effects on bulk temperature. The data provide no information on their effects on stratification characteristics so the discussion is relegated to speculation.

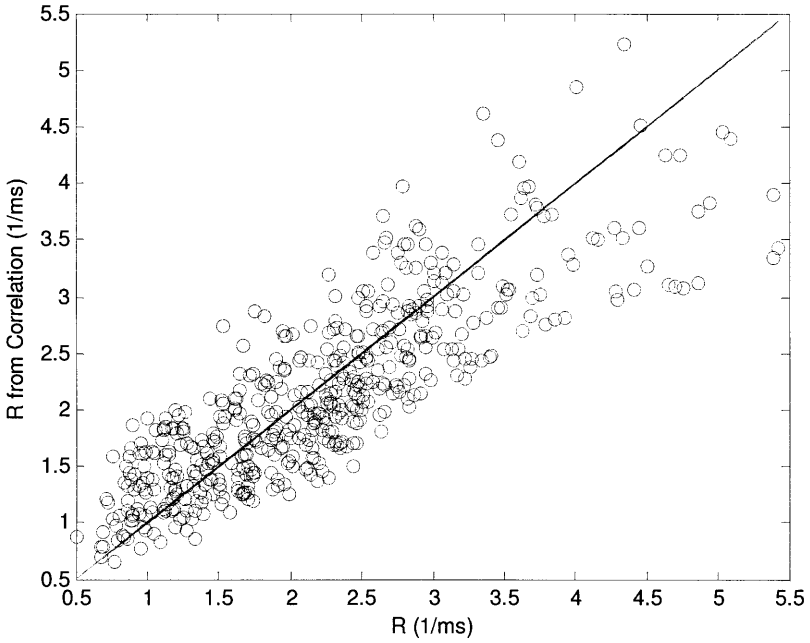


**Figure 5.9.** $R$ from the Correlation vs. $R$ from the Data. $x_{O2}$, $\varphi$, and $P_{15BTC}$ were used.

**Table 5.4.**
Correlation Parameters

| $R^2$ | 70.8% |
|---|---|
| $a_1$ | 2.02 |
| $a_2$ | 2.46 |
| $a_3$ | -1.63 |
| $a_4$ | 1.90 |

## 5.4 Correlations Including Corrections for Stratification Effects

As discussed in Section 1.4.2, stratification is a primary driver of burn duration. In this section, three different parameters will be considered as means to improve the correlation by accounting for differences in stratification characteristics from one operating condition to another. First, a temperature difference term of the form ($T_{IVO}$ - $T_{in}$) will be introduced to account for temperature stratification effects. This is meant to represent the temperature difference between inducted air with EGR and the trapped residual gas. Next, two different terms will be considered to account for concentration effects. ($1-x_{EGR}/x_{burned}$) is used to account for concentration stratification via EGR, and [$x_{res}(1-x_{res})$] is meant to represent concentration stratification effects caused by residual gas mixing.

Starting with the correlation shown in Figure 5.5 and Table 5.4 which includes bulk temperature, the three speculative terms are incorporated one at a time and then in combinations. The resulting $R^2$ values are listed in Table 5.5.

**Table 5.5.** Speculative Correlation Results

| Correlation Additions | $R^2$ |
|---|---|
| Baseline: $x_{O2}$, $\Phi$, $P_{15BTC}$, $T_{15BTC}$ | 72.7% |
| $T_{IVO}$ - $T_{in}$ | 77.7% |
| $(1\text{-}x_{EGR}/x_{burned})$ | 83.9% |
| $x_{res}(1\text{-}x_{res})$ | 72.8% |
| $T_{IVO}$ - $T_{in}$ & $(1\text{-}x_{EGR}/x_{burned})$ | 85.0% |
| $T_{IVO}$ - $T_{in}$ & $x_{res}(1\text{-}x_{res})$ | 77.8% |
| $(1\text{-}x_{EGR}/x_{burned})$ & $x_{res}(1\text{-}x_{res})$ | 86.5% |
| $T_{IVO}$ - $T_{in}$ & $(1\text{-}x_{EGR}/x_{burned})$ & $x_{res}(1\text{-}x_{res})$ | 86.9% |

The final correlation takes the form in Equation 5.9 and yields the plot in Figure 5.10.

$$R = a_1 \cdot x_{O_2}^{a_2} \cdot \phi^{a_3} \cdot P_{15BTC}^{a_4} \cdot \exp\left(a_5 / T_{15BTC}\right) \cdot \left(T_{IVO} - T_{in}\right)^{a_6} \cdot \left[x_{res}\left(1 - x_{res}\right)\right]^{a_7} \cdot \left(1 - x_{EGR}/x_{burned}\right)^{a_8} \quad (5.9)$$

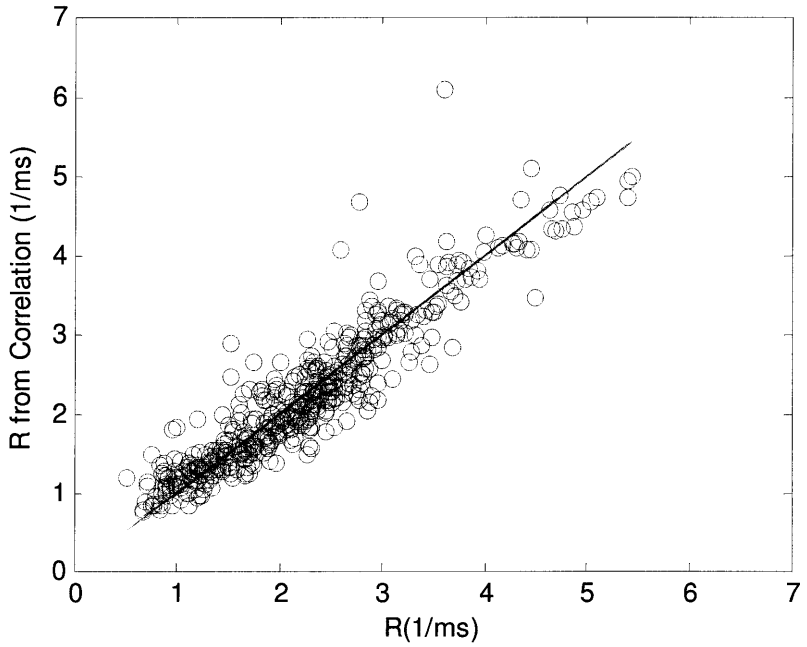


**Figure 5.10.** Burn Duration Correlation with Three Speculative Additions to Account for Stratification.

**Table 5.6.**
Correlation Parameters

| $R^2$ | 86.9% |
|---|---|
| $a_1$ | 20.44 |
| $a_2$ | 1.77 |
| $a_3$ | -0.11 |
| $a_4$ | 1.93 |
| $a_5$ | -4652 |
| $a_6$ | -3.00 |
| $a_7$ | 3.19 |
| $a_8$ | -0.47 |

The correlation features good agreement at this point, and it could be improved further by replacing $T_{IVO}$ with $T_{exhaust}$ or simply using $T_{in}$ rather than the temperature difference. The form presented has the strongest physical meaning. Exhaust temperature is determined, in part, by combustion phasing so using that metric would give information about phasing, which was

avoided in this section. Using $T_{in}$ does not really add insight; it only acknowledges that intake temperature was varied in the experiment.

## 5.5 Burn Duration Correlations Incorporating Combustion Phasing

A number of research groups view combustion phasing as a principle metric for combustion control of the CAI engine. If phasing is allowed to retard too much, misfire is encountered. If phasing in advanced, rate of pressure rise is believed to increase. Really, many of the same factors that affect rate of pressure rise also affect phasing. A caveat is that phasing determines the volume in which combustion takes place, and volume affects species concentration as well as bulk temperature. The metric $\tau$ incorporates volume during combustion to account for this though. The relationship between rate of pressure rise and combustion phasing could be useful to gain insight to combustion behavior and to help control the engine.

The relationships are illustrated between $PRR_{max}$ and CA10 in Figure 5.11 and $\tau$ and CA10 in Figure 5.12.

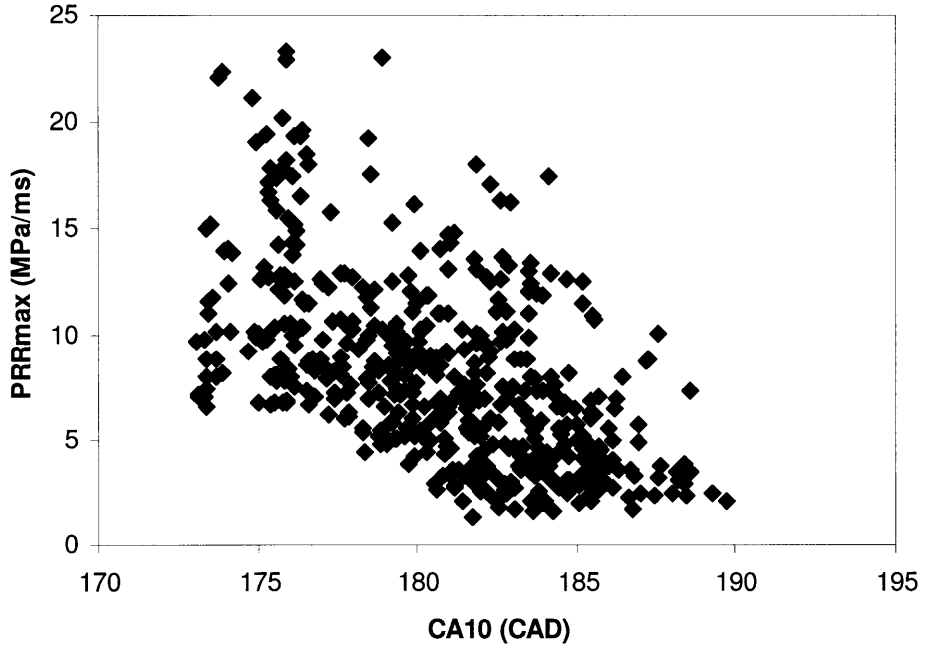


**Figure 5.11.** $PRR_{max}$ vs. CA10 for the Data Set.

Under certain circumstances, say varying intake temperature, it appears that $PRR_{max}$ correlates well with CA10; however, across the data set, it is evident that there is quite a spread. The same can be said for $\tau$ and CA10. It is apparently possible to achieve late-fast combustion as well as

early-slow combustion. There is a narrower range of durations at early timing than duration ranges at late timing.

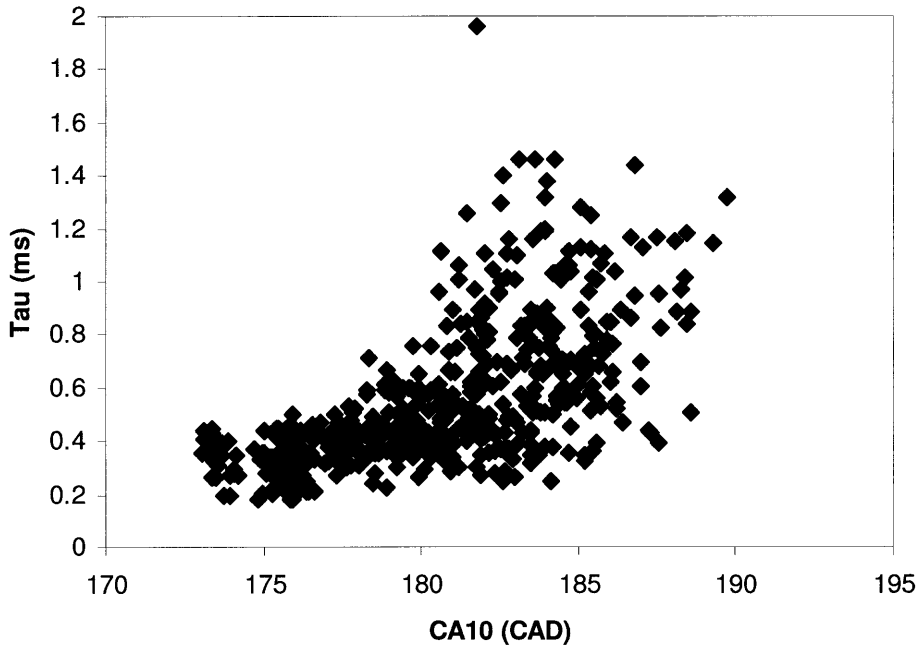


**Figure 5.12.** $\tau$ vs. CA10 for the Data Set.

The same least squares fit techniques used earlier will be used to related R = $1/\tau$ to oxygen fraction, equivalence ratio, pressure, temperature, and now also combustion phasing. An ignition delay is defined in milliseconds as the time after a reference point during compression, chosen at 165° ABC. The delay in crank angle degrees is divided by engine speed $N$ as in Equation 5.10.

$$\tau_{ig} \equiv \frac{(CA10 - 165)}{N}[ms] \tag{5.10}$$

$\tau_{ig}$ values ranged from 0.90ms to 2.74ms.

Correlation fits featured high $R^2$ values. A series of correlations with different terms were attempted with results noted in Table 5.7. The final correlation yielded a good fit with $R^2$ at 94.4%. The correlation is plotted in Figure 5.13 and the coefficients are listed in the Equation 5.11.

The correlation is strongest where $R$ is low. The correlation is expected to be strong because, as was noted in the cited spectroscopy work in Section 1.3.6, both combustion phasing and burn rate depend on the stratification of temperature and concentration in-cylinder. Phrasing burn duration in terms of phasing allows phasing to account for these stratification effects.

**Table 5.7.** Results for Correlation Incorporating $\tau_{ig}$

| Correlation Additions | $R^2$ |
|---|---|
| $x_{O2}$, $\tau_{ig}$ | 83.0% |
| $x_{O2}$, $\Phi$, $\tau_{ig}$ | 87.7% |
| $x_{O2}$, $\Phi$, $P_{15BTC}$, $\tau_{ig}$ | 93.4% |
| $x_{O2}$, $\Phi$, $P_{15BTC}$, $T_{15BTC}$, $\tau_{ig}$ | 94.4% |

$$R = 1/\tau = 810.5 \cdot x_{O_2}^{2.53} \cdot \phi^{2.69} \cdot P_{15BTC}^{1.31} \cdot \exp\left(2341/T_{15BTC}\right) \cdot \tau_{ig}^{-1.39} \tag{5.11}$$

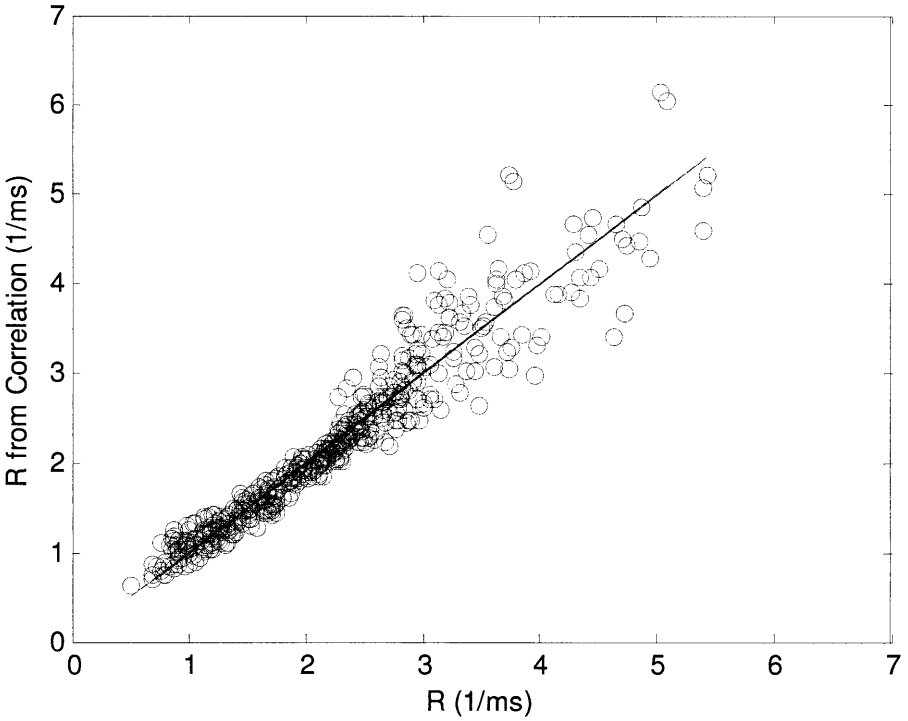


**Figure 5.13.** 1/τ Correlation Based on $x_{O2}$, $\Phi$, $P15_{BTC}$, $T15_{BTC}$, and $\tau_{ig}$.

## 5.6 Combustion Phasing Correlations

In Section 5.5, it was shown that the characteristic burn duration $\tau$ could be effectively described in terms of combustion phasing. To develop greater insight into the phenomena at play, correlations for combustion phasing are presented next. The simplest way to develop a correlation is to pick a reference point shortly before combustion begins to take place and to use the characteristics of the gas at this point. A formula can be used in the form shown in He et al.'s RCM ignition delay formula in Equation 1.13 [31]. Here, 15° BTC is used as the reference point during the compression stroke, and the terms of the correlation are oxygen fraction, equivalence ratio, pressure, and temperature as in Equation 5.12.

$$\tau_{ig} = a_1 \cdot x_{O_2}^{a_2} \cdot \phi^{a_3} \cdot P_{15BTC}^{a_4} \cdot \exp\left(a_5 / T_{15BTC}\right) \tag{5.12}$$

The resulting correlation shows promise with $R^2 = 65\%$, but does not properly capture the behavior of the system, as shown in Figure 5.14 and in Table 5.8.

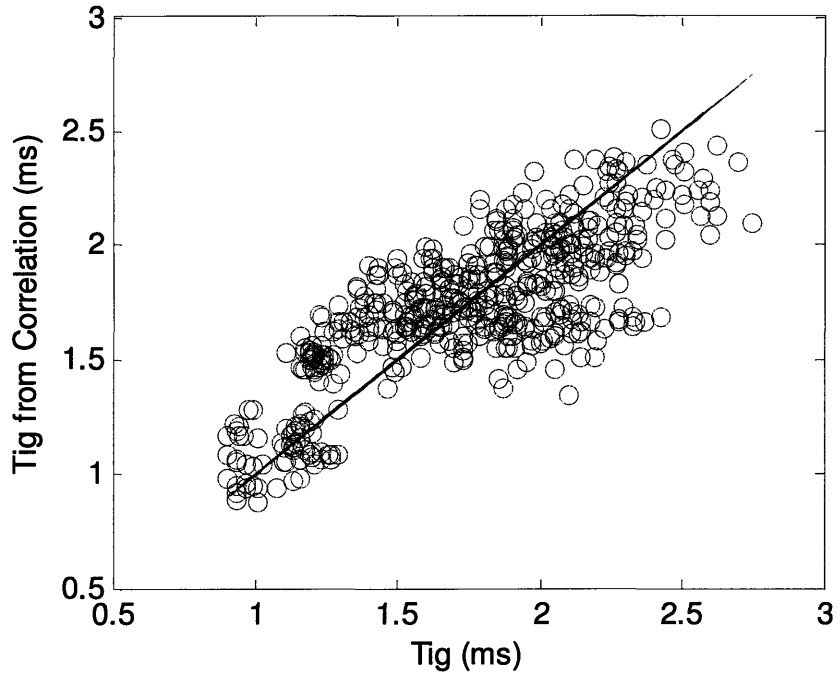


**Figure 5.14.** $\tau_{ig}$ from the Correlation vs. $\tau_{ig}$ from the Data. $x_{O2}$, $\varphi$, $P_{15BTC}$, and $T_{15BTC}$ were used in the correlation.

**Table 5.8.**
Correlation Parameters

| | |
|---|---|
| $R^2$ | 65.0% |
| $a_1$ | 0.049 |
| $a_2$ | 0.17 |
| $a_3$ | 2.99 |
| $a_4$ | -0.06 |
| $a_5$ | 3760 |

For this correlation to be very strong, a few assumptions need to be strong. First, the temperature, pressure, and concentrations of the first series of parcels to burn must be those at the reference point. This is not true, first, because the average properties of the charge continue to change temporally due to compression and heat transfer. Second, as was demonstrated in the cited spectroscopy studies, temperature stratification affects combustion phasing. The hottest parcels will burn first and will determine CA10. Since the average parameters are used in the correlation, the relationship between the temperatures of the hottest parcels to the average temperature ought to play a significant role in the correlation.

To account for temperature stratifications, the three correction factors applied in the burn duration correlation in Section 5.4 will be attempted here as well. First, ($T_{IVO}$ - $T_{in}$) will be introduced to account for temperature differences between intake and hot residual. Next, (1-$x_{EGR}/x_{burned}$) will be used to account for EGR effects, and [$x_{res}$(1-$x_{res}$)] is meant to represent

concentration stratification effects caused by residual gas mixing. The resulting $R^2$ values for each of these three plus combinations of them are listed in Table 5.9.

**Table 5.9.** Results for $\tau_{ig}$ Correlation

| Correlation Additions | $R^2$ |
|---|---|
| Baseline: $x_{O2}$, $\Phi$, $P_{15BTC}$, $T_{15BTC}$ | 65.0% |
| $(T_{IVO} - T_{in})$ | 71.2% |
| $(1-x_{EGR}/x_{burned})$ | 83.7% |
| $x_{res}(1-x_{res})$ | 67.0% |
| $(T_{IVO} - T_{in})$ & $(1-x_{EGR}/x_{burned})$ | 84.6% |
| $(T_{IVO} - T_{in})$ & $x_{res}(1-x_{res})$ | 73.4% |
| $(1-x_{EGR}/x_{burned})$ & $x_{res}(1-x_{res})$ | 84.4% |
| $(T_{IVO} - T_{in})$ & $(1-x_{EGR}/x_{burned})$ & $x_{res}(1-x_{res})$ | 84.9% |

The $(1-x_{EGR}/x_{burned})$ correction yields the most significant improvement as $R^2$ reaches 83.7%. The other two corrections each additionally improve $R^2$ by less than 1%. The correlation using the EGR correction with specific parameters is stated in Equation 5.13, and the correlation plot is shown in Figure 5.15.

$$\tau_{ig} = 0.24 \cdot x_{O_2}^{0.40} \cdot \phi^{2.09} \cdot P_{15BTC}^{-0.50} \cdot \exp\left(3840/T_{15BTC}\right) \cdot \left(1 - x_{EGR}/x_{burned}\right)^{-2.0} \quad (5.13)$$

The reason this correction results in such a benefit is that the volume of hot residuals becomes smaller as the $x_{EGR}/x_{burned}$ becomes larger. The first parcel of oxygen and fuel to burn must transfer heat from a pocket of hot residuals so access for oxygen to a hot pocket of residuals is vital to determining the beginning of combustion. By adding more and more inert exhaust gas that is at the same temperature as the oxygen, the oxygen's interaction with the small hot pocket of residual gas reduces.

The correlation plot in Figure 5.15 features a number of points far from the reference line. This error is due to poorly described phenomena as well as some experimental error. Varying intake error causes divergence from the reference line. Also, not all of the EGR data collapse to the reference line, and differences in behavior of some sweeps versus others imply a small but significant degree of experimental error.

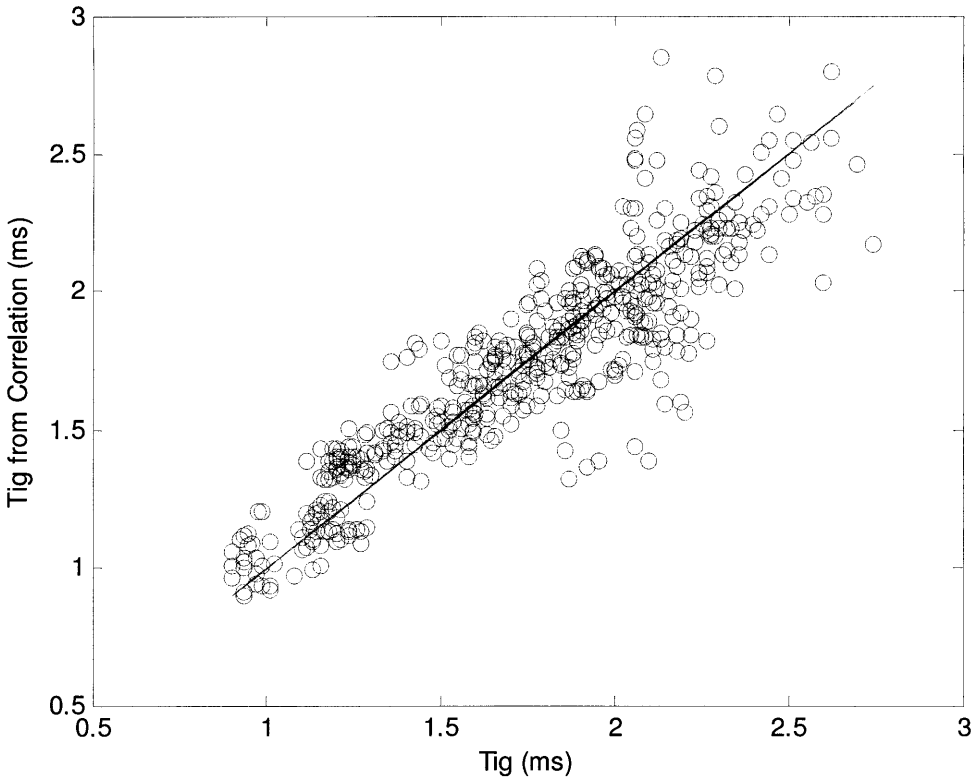


**Figure 5.15.** $\tau_{ig}$ from the Correlation vs. $\tau_{ig}$ from the Data. The EGR correction term is included.

# Chapter 6 Summary and Conclusions

This thesis seeks to add understanding to the high load limits of the controlled autoignition engine. An engine experiment was performed in which valve timing, intake temperature, intake and exhaust pressure held equal, and EGR flow were assessed for their effects on the high load knock limit and the high load misfire limit. The air fuel ratio was held stoichiometric, and the engine speed was set to 1500rpm for all tests.

## 6.1 Negative Valve Overlap

The effects on the high load limit of intake temperature, boost pressure, and negative valve overlap without EGR were explored. The high load limit was found to be always at the misfire limit where intake and exhaust pressures were low and residual fraction was also low. The misfire limit was optimal because the charge temperature was only high enough for consistent ignition. Excess charge temperature caused $PRR_{max}$ to increase without increasing NIMEP. Boost was shown to increase charge temperature considerably.

The high load limit was not very sensitive to the chosen $PRR_{max}$ limit. Doubling the $PRR_{max}$ limit would typically result in only a 25% increase in the load limit.

The misfire limit could be described well by CA10 and $P_{15BTC}$ and with slightly worse accuracy by $P_{in}$, $x_{res}$, and $T_{in}$.

Cycle-by-cycle data were investigated to assess the specific cause of misfire. It was observed that variations in combustion phasing resulted in variations in residual gas fraction and residual gas temperature on a cycle-by-cycle basis, which eventually led to a cycle with insufficient trapped enthalpy for ignition. On the time scale of 10 to 20 cycles, the air flow and the air-fuel ratio were observed to vary and to vary independently from one another. It was suggested that variations in fuel pooling in the intake port could be taking place. Both the 10-20 cycle phenomenon and the cycle-by-cycle variations were observed to be necessary for misfire.

## 6.2 IVC Timing

IVC timing and boost were varied with the other valve timings set to trap near 45% residual fraction. Exhaust pressure was held constant to intake pressure. $\lambda$ was fixed to 1. No EGR was used. It was shown that NIMEP could be increased while holding $PRR_{max}$ constant by boosting and retarding IVC timing. Retarding IVC timing reduced the effective compression ratio and charge density while boost increased charge density and temperature. By combining both IVC

retard and boost, the charge density could be increased without increasing the temperature at the end of compression.

## 6.3 EVO Timing

EVO timing was varied with the other three valve timings fixed such that between 40% and 45% residual fraction was achieved. Intake and exhaust pressure, held equal, were varied as well. It was shown that residual fraction followed a quadratic dependence on EVO timing reaching a maximum value when EVO timing was 20° BBC. This dependence appeared to be caused by pressure waves in the exhaust system during the exhaust event. Varying EVO timing also varied $T_{IVO}$, the temperature of the residual gas at the end of recompression. $T_{IVO}$ correlated with residual fraction, not with fuel mass as it does for an NVO sweep. The maximum load, constrained by $PRR_{max}$, was found to be where EVO timing was as advanced as possible since the fueling was increased while the charge temperature was decreased. EVO timing effects are expected to vary from engine to engine since they depend on exhaust pressure waves.

## 6.4 Exhaust Gas Recirculation

A study was conducted in which intake pressure, intake temperature, EGR flow rate, and NVO valve timing were varied. Exhaust pressure was held to be 30mbar above the intake pressure to drive the EGR flow. The equivalence ratio was set to 1.0.

Replacing trapped residuals with EGR gas had the effect of extending the high load limit by reducing charge temperature. The maximum rate of pressure rise was shown to vary with fuel rate and with $x_{res}/x_{burn}$ while the fuel mass did not vary with $x_{res}/x_{burn}$. The highest load for a given $PRR_{max}$ always occurred at the misfire limit. Boosting the engine, while also flowing EGR gas, provided no increase or decrease of the high load limit. EGR acted to offset the increase in charge temperature caused by boost. At the misfire limit, the engine produced the same $PRR_{max}$ at a given fuel rate regardless of boost. Increasing intake temperature allowed the engine to tolerate more EGR before misfire. This was simply a trade-off in the source of sensible energy, and the high load limit was unchanged. A correlation for the misfire limit under EGR operation was developed using $x_{O2}$, $P_{in}$, $x_{res}$, and $T_{in}$.

Cycle-by-cycle data was examined to understand misfire under EGR operation. Misfire appeared to be a result of large variations in $\lambda$ caused by variations of intake airflow rate. Periodically pulsed flow of the EGR may have led to variability in the air flow.

## 6.5 Phenomenological Correlations for the High Load Knock Limit

The entire data set was used to develop a correlation to describe the high-load knock limit. A characteristic burn duration $\tau$ was defined to take into account $PRR_{max}$ and fuel mass such that a larger $\tau$ would mean a lower $PRR_{max}$ at the same fuel mass. $\tau$ was found to correlated well with the 10-90% burn duration.

A correlation for $\tau$ based on the data was developed based on the bulk parameters, $x_{O2}$, $\Phi$, $P_{15BTC}$, and $T_{15BTC}$ yielding an $R^2$ of 72%. The primary source of error stemmed from thermal stratification effects and poorly represented variations in charge temperature. Three correction terms, $(T_{IVO} - Tin)$, $(1 - x_{EGR}/x_{burn})$, and $x_{res}(1 - x_{res})$, were added to account for poor accuracy in the temperature estimate and stratification effects. These terms increased the $R^2$ value to 87%.

A relationship between the characteristic burn duration and combustion phasing was developed based on $x_{O2}$, $\Phi$, $P_{15BTC}$, and $T_{15BTC}$ plus a term for CA10 yielded an $R^2$ of 94%. A correlation for combustion phasing was developed also. The bulk parameters, $x_{O2}$, $\Phi$, $P_{15BTC}$, and $T_{15BTC}$, featured poor agreement between predicted and actual CA10. Again, a correction term was added to account for thermal stratification. Adding $(1 - x_{EGR}/x_{burn})$ increased the $R^2$ value to 85%.

## 6.6 Conclusions

The high load limit of the controlled autoignition engine occurs where the fuel rate is maximized for a fixed maximum rate of pressure rise. For a given fuel rate, the $PRR_{max}$ is reduced by decreasing charge temperature and increasing thermal stratification. The limit to reducing $PRR_{max}$ is set by the misfire limit where the high load limit will always occur. Boost, EGR, intake temperature, and three types of valve timing sweeps have been presented as ways to vary the charge density and the charge temperature. These control parameters could be used to compensate for one another to increase load at a fixed $PRR_{max}$ until misfire. The high load limit was roughly uniform at 5bar NIMEP constrained at 5MPa/ms across all conditions.

Future work should focus on extending the misfire limit to increase the high load limit. By furthering the understanding of the misfire limit, the operating range constrained by the maximum rate of pressure rise can be expanded, and the CAI will step closer to entering production.

# References


1. Andreae, M., *Effect of Ambient Conditions and Fuel Properties on Homogeneous Charge Compression Ignition Engine Operation,* MIT Ph.D. Thesis, 2006.

2. Xu, H., Rudolph, S., Liu, Z., Wallace, S., Richardson, S., Wyszynski, M., and Megaritis, A., "An Investigation into the Operating Mode Transitions of a Homogeneous Charge Compression Ignition Engine Using EGR Trapping," SAE Paper 2004-01-1911, 2004.

3. Santoso, H., Matthews, J., Cheng W., "Managing SI/HCCI Dual-Mode Engine Operation," SAE Paper 2005-01-0162, 2005.

4. Zhao, H., Li, J., Ma, T. and Ladommatos, N., "Performance and Analysis of a 4-Stroke Mult-Cylinder Gasoline Engine with CAI Combustion," SAE Paper 2002-01-0420, 2002.

5. Yang, J. and Kenney, T., "Robustness and Performance Near the Boundary of HCCI Operating Regime of a Single-Cylinder OKP Engine," SAE Paper 2006-01-1082, 2006.

6. Yap, D., Wyszynski, M., Megaritis, A., and Xu, H., "Applying Boosting to Gasoline HCCI Operation with Residual Gas Trapping," SAE Paper 2005-01-2121, 2005.

7. Sjöberg, M. and Dec, J., "Effects of Engine Speed, Fueling Rate, and Combustion Phasing on the Thermal Stratification Required to Limit HCCI Knocking Intensity," SAE Paper 2005-01-2125, 2005.

8. Urata, Y., Awasaka, M., Takanashi, J., Kakinuma, T., Hakozaki, T., and Umemoto, A., "A Study of Gasoline-Fuelled HCCI Engine Equipped with an Electromagnetic Valve Train," SAE Paper 2004-01-1898, 2004.

9. Cairns, A. and Blaxill, H., "The Effects of Combined Internal and External Exhaust Gas Recirculation on Gasoline Controlled Auto-Ignition," SAE Paper 2005-01-0133, 2005.

10. Sjöberg, M., Dec, J., "EGR and Intake Boost for Managing HCCI Low-Temperature Heat Release over Wide Ranges of Engine Speed," SAE Paper 2007-01-0051, 2007.

11. Kaahaaina, N., Simon, A., Caton, P., and Edwards, C., "Use of Dynamic Valving to Achieve Residual-Affected Combustion," SAE Paper 2001-01-0549, 2001.

12. Caton, P, Simon, A., Gerdes, J., and Edwards, C., "Residual-Effected Homogeneous Charge Compression Ignition at a Low Compression Ratio Using Exhaust Reinduction," *International Journal of Engine Research*, Vol. 4, No. 3, pp. 163-177, 2002.

13. Caton, P., "Combustion Phasing of Residual-Effected Homogeneous Charge Compression Ignition," *International Journal of Engine Research*, Vol. 8, pp. 79-96, 2002.

14. Christensen, M., Johansson, B., Amneus, P., and Mauss., "Supercharged Homogeneous Charge Compression Ignition," SAE Paper 980787, 1998.

15. Olsson, J., Tunestål, P., Haraldsson, G., and Johansson, B., "A Turbo Charged Dual Fuel HCCI Engine," SAE Paper 2001-01-1896, 2001.

16. Heywood, J., *Internal Combustion Engine Fundamentals.* New York: McGraw-Hill, 1988.

17. Draper, C., "Pressure Waves Accompanying Detonation in the Internal Combustion Engine," J. Aeron. Sci. 5, 219, 1938.

18. Eng, J., "Characterization of Pressure Waves in HCCI Combustion," SAE Paper 2002-01-2859, 2002.

19. Vressner, A., Lundin, A., Christensen, M., Tunestål, and Johansson, B., "Pressure Oscillations during Rapid HCCI Combustion," SAE Paper 2003-01-3217, 2003.

20. Andreae, M., Cheng, W., Kenney, T., and Yang, J., "On HCCI Engine Knock," SAE Paper 2007-01-1858, 2007.

21. Aceves, S., Flowers, D., Westbrook, C., Smith, J., Pitz, W., Dibble, R., Christensen, M., and Johansson, B., "A Multi-Sone Model for Prediction of HCCI Combustion and Emissions," SAE Paper 2000-01-0327, 2000.

22. Yelvington, P. and Green, W., "Prediction of the Knock Limit and Viable Operating Range for a Homogeneous-Charge Compression-Ignition (HCCI) Engine," SAE Paper 2003-01-1092, 2003.

23. Oakley, A., Zhao, H., Ladommatos, N., and Ma, T., "Dilution Effects on the Controlled Auto-Ignition (CAI) Combustion of Hydrocarbon and Alcohol Fuels," SAE Paper 2001-01-3606, 2001.

24. Angelos, J., Puignou, M., Andreae, M., Cheng, W., Green, W., and Singer, M., "Detailed Chemical Kinetic Simulations of Homogeneous Charge Compression Ignition Engine Transients," *International Journal of Engine Research*, Vol. 9, pp. 149-164, 2008.

25. Turns, Stephen. *An Introduction to Combustion: Concepts and Applications.* Singapore: McGraw-Hill, 1996.

26. Vincenti, Walter, and Kruger, Charles. *Introduction to Physical Gas Dynamics.* Malabar, FL: Krieger Publishing Company, 1965.

27. Beckers, A. Motortechnische Zeitschrift, Vol. 14, No. 12, 1953.

28. Schmidt, F., *Verbrennungsmotoren Thermodynamische und Versuchsmässige Grundlagen Unter Besonderer Berücksichtigung der Flugmotoren.* Berlin: Springer-Verlag, 1945.

29. Livengood, J., and Wu, P., "Correlation of Auto-Ignition Phenomena in Internal Combustion Engines and Rapid Compression Machines," Fifth International Symposium on Combustion, p.347, 1955.

30. Douaud, A., and Eyzat, P., "Four-Octane-Number Method for Predicting the Anti-Knock Behavior of Fuels and Engines," SAE Paper 780080, 1978.

31. He, X., Donovan, M., Zigler, B., Palmer, T., Walton, S., Wooldridge, M., and Atreya, A., "An Experimental and Modeling Study of Iso-octane Ignition Delay Times Under Homogeneous Charge Compression Ignition Conditions," *Combustion and Flame*, Vol. 142, 2005, p.266-275.

32. Shahbakhti, M., Lupul, R., Koch, C., "Predicting HCCI Auto-Ignition Timing by Extending a Modified Knock-Integral Method," SAE Paper 2007-01-0222, 2007.

33. Yates, A., and Viljoen, C., "An Improved Empirical Model for Describing Auto-Ignition," SAE Paper 2008-01-1629, 2008.

34. Dryer, F. and Glassman, I., "High Temperature Oxidation of CO and $CH_4$," *Fourteenth Symposium (International) and Combustion,* The Combustion Institute, Pittsburgh, PA, pp. 987, 1973.

35. Sjöberg, M., Dec, J., "Combined Effects of Fuel-Type and Engine Speed on Intake Temperature Requirements and Completeness of Bulk-Gas Reactions for HCCI Combustion," SAE Paper 2003-01-3173, 2003.

36. Najt, P. and Foster, D., "Compression-Ignition Homogeneous Charge Combustion," SAE Paper 830264, 1983.

37. Rothamer, D., Snyder, J., Hanson, R., Steeper, R., and Fitzgerald, R., "Simultaneous Imaging of Exhaust Gas Residuals and Temperature During HCCI Combustion," *Proceedings of the Combustion Institute,* Vol. 32, pp. 2869-2876, 2009.

38. Lim, O., Nakano, H., and Iida, N., "The Research About the Effects of Thermal Stratification on *n*-Heptane/*iso*-Octane-Air Mixture HCCI Combustion Using a Rapid Compression Machine," SAE Paper 2006-01-3319, 2006.

39. Kakuho, A., Nagamine, M., Amenomori, Y., Urushihara, T., and Itoh, T., "In-Cylinder Temperature Distribution Measurement and Its Application to HCCI Combustion," SAE Paper 2006-01-1202, 2006.

40. Dec, J., Hwang, W., and Sjöberg, M., "An Investigation of Thermal Stratification in HCCI Engines Using Chemiluminescence Imaging," SAE Paper 2006-01-1518, 2006.

41. Hultqvist, A., Engdar, U., Johansson, B., and Klingmann, J., "Reacting Boundary Layers in a Homogeneous Charge Compression Ignition (HCCI) Engine," SAE Paper 2001-01-1032, 2001.

42. Borman, G. and Nishiwaki, K., "Internal-Combustion Engine Heat Transfer," *Progress Energy Combustion Science*," Vol. 13, pp. 1-46, 1987.

43. Sjöberg, M., Dec, J., Babajimopoulos, A., and Assanis, D., "Comparing Enhanced Natural Thermal Stratification Against Retarded Combustion Phasing for Smoothing of HCCI Heat-Release Rates," SAE Paper 2004-01-2994, 2004.

44. Woschni, G. and Fieger, J., "Experimentelle Untersuchungen zum Warmeubergang bei Normaler und Klopfender Verbrennung in Ottomotor," *MTZ*, Vol. 43, 2, pp. 63-67, 1982.

45. Chang, J., Güralp, O., Filipi, Z., Assanis, D., Kuo, T., Najt, P., and Rask, R., "New Heat Transfer Correlation for an HCCI Engine Derived from Measurements of Instantaneous Surface Heat Flux," SAE Paper 2004-01-2996, 2004.

46. Chang, K., Babajimopoulos, A., Lavoie, G., Filipi, Z., and Assanis, D., "Analysis of Load and Speed Transitions in an HCCI Engine Using 1-D Cycle Simulation and Thermal Networks, SAE Paper 2006-01-1087, 2006.

47. Richter, M., Engström, K., Franke, A., Alden, M., Hultqvist, A., and Johansson, B., "The Influence of Charge Inhomogeneity on the HCCI Combustion Process," SAE Paper 2000-01-2868, 2000.

48. Herold, R., Foster, D., Ghandhi, J., Iverson, R., Eng, J., and Najt, P., "Fuel Unmixedness Effects in a Gasoline Homogeneous Charge Compression Ignition Engine," *International Journal of Engine Research,* Vol. 8, No. 3, 2007.

49. Davis, P. and Peckham, M., "Cycle-by-cycle Gasoline Engine Cold Start Measurement of Residual Gas and AFR Using a Fast-Response CO&$CO_2$ Analyzer," SAE Paper 2008-01-1649, 2008.

50. Iizuka, M., Kato, N., Kasashima, K., and Muto, H., "Carbon Dioxide Measuring Technology in Engine Combustion Chambers," SAE Paper 2004-01-1430, 2004.

51. Pope, S. *Turbulent Flows,* Cambridge University Press: Cambridge, England, 2000.

52. Scaringe, R. and Cheng, W., "Influence of Intake Port Charge-Motion-Control-Valve on Mixture Preparation in a Port-Fuel-Injection Engine," SAE Paper 2007-01-4013, 2007.

53. Scaringe, R., *Extension of the High Load Limit in the Homogenous Charge Compression Ignition Engine*, Ph.D. Thesis, Dept. of Mech. Eng., MIT, 2009.

54. Cheng, W., "Notes on HCCI Pressure Rise Rate," personal notes, Mar. 18, 2008.

55. "Specialty Chemicals," Chevron-Phillips Chemical Company, LLC, May 4, 2009. <http://www.cpchem.com/enu/specialty_chemicals_p_performance_fuels.asp>.

56. Rassweiler, G., and Withrow, L., "Motion Pictures of Engine Flames Correlated with Pressure Cards," *Industrial Engineering and Chemistry*, pp.672-677, June 1936.

57. Wildman, C. "Late-Robust Combustion in a Spark-Ignition Engine," M.S. Thesis, Dept. of Mech. Eng., MIT, 2005.

# Appendix

## A.1 Fuel Specifications

Fuel Type: UTG-91
Fuel data from the Chevron-Phillips Chemical Company website [55].

| Property | Typical Value | Specification | Test Method |
|---|---|---|---|
| Copper Corrosion, 3 h at 50 °C | 1 | 1 max | ASTM D 130 |
| Specific Gravity at 60/60 °F | 0.735 | 0.734 – 0.744 | ASTM D 1250 |
| API Gravity at 60 °F | 61 | 58.7 – 61.2 | ASTM D 4052 |
| Oxidation Stability | 1440+ | 1440 min | ASTM D 525 |
| Existent Gum, mg/100 mL | 2 | 5 max | ASTM D 381 |
| Lead Content, g/gal | 0.001 | 0.05 max | ASTM D 3237 Mod. |
| Sulfur Content, wt % | 0.013 | 0.1 max | ASTM D 3120 |
| Phosphorus, g/gal | 0.001 | 0.005 max | ASTM D 3231 |
| Total Alcohol Content, vol % | 0.00 | 0.00 max | EPA Procedure 10 |
| Reid Vapor Pressure at 100 °F, psia | 9.0 | 8.8 – 9.2 | ASTM D 323 |
| Research Octane Number | 90.8 | 90.3 – 91.7 | ASTM D 2699 |
| Motor Octane Number | 83.0 | | ASTM D 2700 |
| Sensitivity | 7.8 | 7.5 min | ASTM D 2700 |
| Distillation Range at 760 mmHg, °F | | | ASTM D 86 |
| Initial Boiling Point | 88 | 75 – 95 | |
| 10% | 122 | 120 – 135 | |
| 50% | 212 | 200 – 230 | |
| 90% | 321 | 300 – 325 | |
| End Point | 399 | 415 max | |
| Composition, vol % | | | ASTM D 1319 |
| Olefins | 6 | 10 max | |
| Aromatics | 24 | 35 max | |
| Saturates | 70 | Remainder | |
| Heat of Combustion, Net, Btu/lb | 18500 | | ASTM D 3338 |
| Carbon Content, wt % | 86.3 | | |
| Hydrogen Content, wt % | 13.7 | | |
| Anti-Knock Index, (R+M)/2 | 86.8 | 87.0 max | Calculated |

## A.2 Burn Duration Calculations

The burn duration was calculated using the Rassweiler and Withrow method [56]. This method requires only the pressure at a given crank angle degree $p(\theta)$, the pressure at ignition $p_0$, the pressure at the end of combustion, $p_f$ and the exponent $n$ from the polytropic relation in Equation A-1.

$$pV^n = k \tag{A.1}$$

$k$ is a constant. This equation is used to relate the pressure and volume of the initial unburned gas to those of the unburned gas during combustion and the pressure and volume of the final burned gas to those of the burned gas during combustion as follows.

$$p_0 V_{u,0}^n = pV_u^n \tag{A.2}$$

$$V_{u,0} = V_u\left(\frac{p}{p_0}\right)^{1/n} \tag{A.3}$$

$$p_f V_{f,b}^n = pV_b^n \tag{A.4}$$

$$V_{b,f} = V_b\left(\frac{p}{p_f}\right)^{1/n} \tag{A.5}$$

Next, burned mass fraction is related to volume fraction. The in-cylinder pressure rise is due to a combustion component $\Delta p_c$ and a compression component $\Delta p_v$.

$$\Delta p = \Delta p_c + \Delta p_v \tag{A.5}$$

The pressure and volume change due to the compression component are estimated using an isentropic relation.

$$p_i V_i^n = p_j V_j^n \tag{A.6}$$

Incorporating this into Equation A-5 yields Equation A-7.

$$\Delta p_v = p_i\left[\left(\frac{V_i}{V_j}\right)^n - 1\right] \tag{A.7}$$

The assumption is made that for a given mass of mixture burned, a corresponding pressure rise results.

$$\frac{m_{b(i)}}{m_{b(total)}} = \frac{\sum_0^i \Delta p_c}{\sum_0^N \Delta p_c} \tag{A.8}$$

Here, $N$ is the total number of crank angles considered. Using Equations A.5 to A.8, burned mass fraction is related to volume change.

$$x_b = 1 - \frac{V_{u,0}}{V_0} = \frac{V_{b,f}}{V_f} \tag{A.9}$$

By relating Equations A.4 and A.9, an equation relating burned mass fraction to in-cylinder pressure, $n$, volume, pressure at ignition, and pressure at the end of combustion results [55].

$$x_b = \frac{p^{1/n}V - p_0^{1/n}V_0}{p_f^{1/n}V_f - p_0^{1/n}V_0} \tag{A.10}$$

## A.3 Combustion Phasing and Exhaust Gas Temperature

The relationship between combustion phasing and exhaust temperature was explored to understand the dependencies of the exhaust temperature toward understanding $T_{IVO}$. A strong relationship between these variables would also allow the combustion phasing to be estimated without any in-cylinder measurement device. Previous work with a spark ignition engine showed that CA50 and exhaust temperature correlated very well under a fixed load, fixed speed, and fixed valve timing [57].

Varying fuel rate would change the amount of energy in the exhaust so this factor would have to be considered. Exhaust valve timing would also affect the amount of work extracted from the exhaust gas and the heat transfer from the gas before it reached the thermocouple in the exhaust.

A correlation was developed to describe CA90 in terms of fuel mass, exhaust temperature, and EVC timing as in Equation A.11.

$$CA90 = 5.45e-19 \cdot m_f^{-1.51} Texh^{14.02} EVC^{-7.39} \tag{A.11}$$

The correlation showed good agreement with $R^2$ = 88%. Figure A.1 shows CA90 vs. CA90 predicted by the correlation.

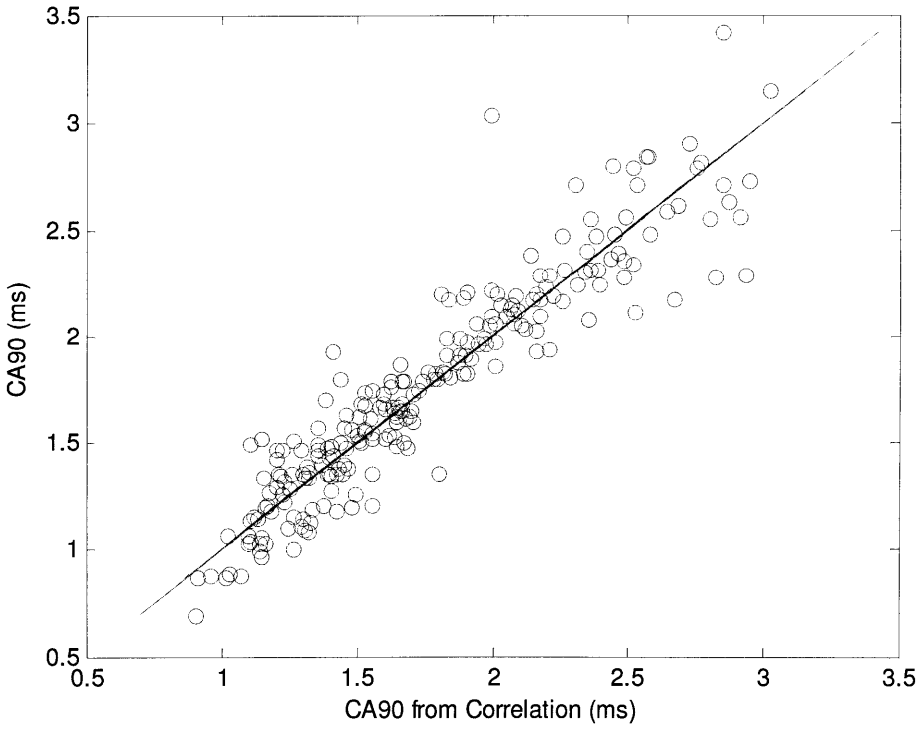


**Figure A.1.** Correlation for CA90 Delay Based on Fuel Mass, Texh, and EVC Timing.